HEMATOPOIESIS: LEARNING FROM IN VITRO AND IN VIVO MODELS

EDITED BY: Jon Frampton, Anskar Y. H. Leung, Xiaotian Zhang, Jianwei Wang and Yiyue Zhang

PUBLISHED IN: Frontiers in Cell and Developmental Biology

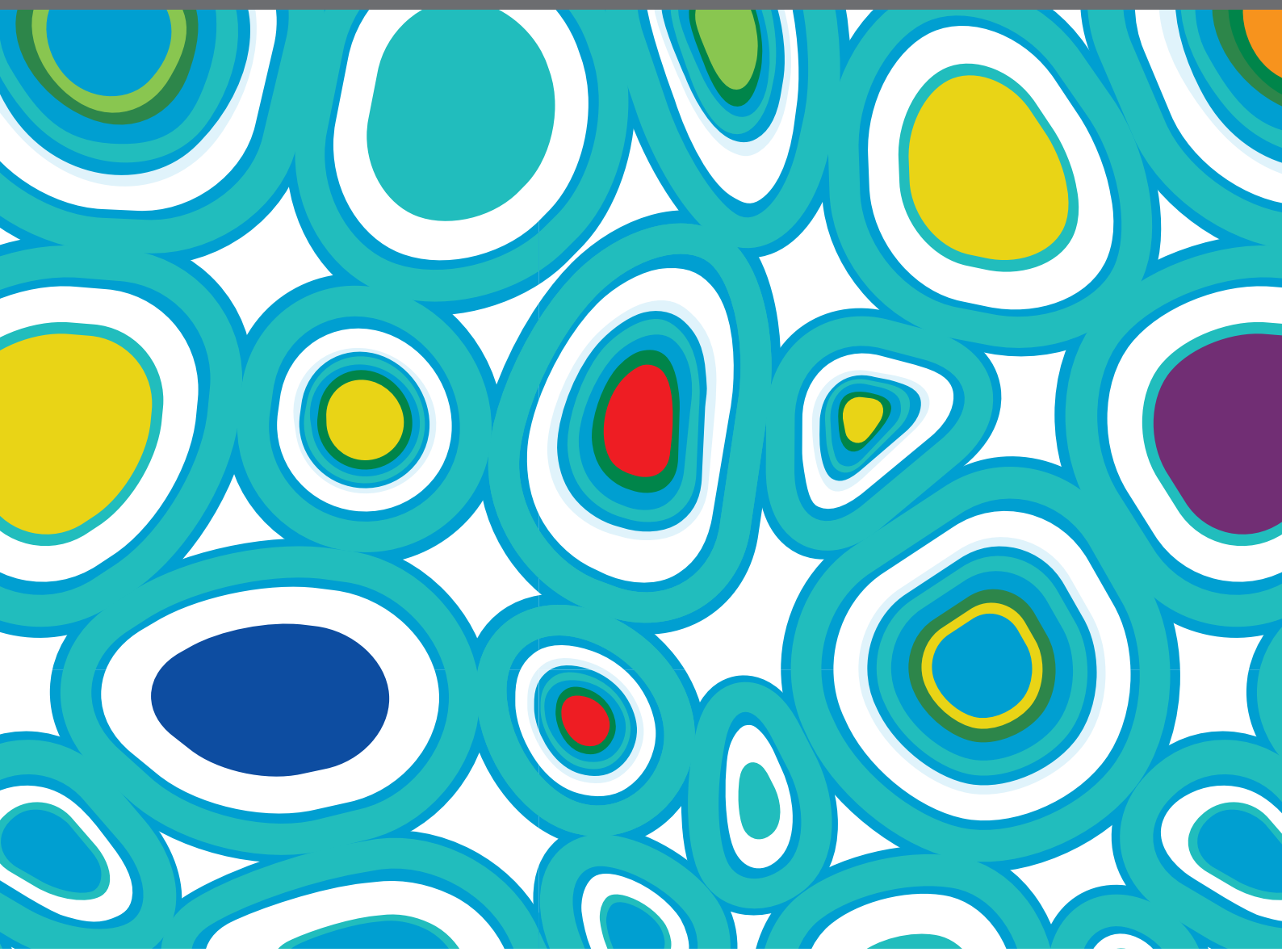

frontiers Research Topics

frontiers

ISSN 1664-8714
ISBN 978-2-88976-023-7
DOI 10.3389/978-2-88976-023-7

About Frontiers

Frontiers is more than just an open-access publisher of scholarly articles: it is a pioneering approach to the world of academia, radically improving the way scholarly research is managed. The grand vision of Frontiers is a world where all people have an equal opportunity to seek, share and generate knowledge. Frontiers provides immediate and permanent online open access to all its publications, but this alone is not enough to realize our grand goals.

Frontiers Journal Series

The Frontiers Journal Series is a multi-tier and interdisciplinary set of open-access, online journals, promising a paradigm shift from the current review, selection and dissemination processes in academic publishing. All Frontiers journals are driven by researchers for researchers; therefore, they constitute a service to the scholarly community. At the same time, the Frontiers Journal Series operates on a revolutionary invention, the tiered publishing system, initially addressing specific communities of scholars, and gradually climbing up to broader public understanding, thus serving the interests of the lay society, too.

Dedication to Quality

Each Frontiers article is a landmark of the highest quality, thanks to genuinely collaborative interactions between authors and review editors, who include some of the world's best academicians. Research must be certified by peers before entering a stream of knowledge that may eventually reach the public - and shape society; therefore, Frontiers only applies the most rigorous and unbiased reviews.
Frontiers revolutionizes research publishing by freely delivering the most outstanding research, evaluated with no bias from both the academic and social point of view. By applying the most advanced information technologies, Frontiers is catapulting scholarly publishing into a new generation.

What are Frontiers Research Topics?

Frontiers Research Topics are very popular trademarks of the Frontiers Journals Series: they are collections of at least ten articles, all centered on a particular subject. With their unique mix of varied contributions from Original Research to Review Articles, Frontiers Research Topics unify the most influential researchers, the latest key findings and historical advances in a hot research area! Find out more on how to host your own Frontiers Research Topic or contribute to one as an author by contacting the Frontiers Editorial Office: frontiersin.org/about/contact

HEMATOPOIESIS: LEARNING FROM IN VITRO AND IN VIVO MODELS

Topic Editors:
Jon Frampton, University of Birmingham, United Kingdom
Anskar Y. H. Leung, The University of Hong Kong, SAR China
Xiaotian Zhang, The University of Michigan, United States
Jianwei Wang, Tsinghua University, China
Yiyue Zhang, South China University of Technology, China

Citation: Frampton, J., Leung, A. Y. H., Zhang, X., Wang, J., Zhang, Y., eds. (2022). Hematopoiesis: Learning From in vitro and in vivo Models. Lausanne: Frontiers Media SA. doi: 10.3389/978-2-88976-023-7

Table of Contents

frontiers in Cell and Developmental Biology

ORIGINAL RESEARCH
published: 25 January 2021
doi: 10.3389/fcell.2020.622190

Deficiency of Rbpj Leads to Defective Stress-Induced Hematopoietic Stem Cell Functions and Hif Mediated Activation of Non-canonical Notch Signaling Pathways

*Ram Lakhan[1] and Chozha V. Rathinam[1,2]**

[1] Institute of Human Virology, University of Maryland School of Medicine, Baltimore, MD, United States, [2] Center for Stem Cell and Regenerative Medicine, University of Maryland School of Medicine, Baltimore, MD, United States

OPEN ACCESS

Edited by:
Anskar Y. H. Leung,
The University of Hong Kong,
Hong Kong

Reviewed by:
Takahiko Hara,
Tokyo Metropolitan Institute of Medical Science, Japan
Frank Staal,
Leiden University Medical Center, Netherlands
Masahiro Marshall Nakagawa,
Kyoto University, Japan

***Correspondence:**
Chozha V. Rathinam
crathinam@ihv.umaryland.edu

Specialty section:
This article was submitted to Stem Cell Research, a section of the journal Frontiers in Cell and Developmental Biology

Received: 27 October 2020
Accepted: 31 December 2020
Published: 25 January 2021

Citation:
Lakhan R and Rathinam CV (2021) Deficiency of Rbpj Leads to Defective Stress-Induced Hematopoietic Stem Cell Functions and Hif Mediated Activation of Non-canonical Notch Signaling Pathways. Front. Cell Dev. Biol. 8:622190. doi: 10.3389/fcell.2020.622190

Deregulated notch signaling has been associated with human pathobiology. However, functions of notch pathways in hematopoiesis remain incompletely understood. Here, we ablated canonical notch pathways, through genetic deletion of Rbpj, in hematopoietic stem cells (HSCs). Our data identified that loss of canonical notch results in normal adult HSC pool, at steady state conditions. However, HSC maintenance and functions in response to radiation-, chemotherapy-, and cytokine- induced stress were compromised in the absence of canonical notch. Rbpj deficient HSCs exhibit decreased proliferation rates and elevated expression of $p57^{Kip2}$. Surprisingly, loss of Rbpj resulted in upregulation of key notch target genes and augmented binding of Hes1 to *p57* and *Gata2* promoters. Further molecular analyses identified an increase in notch activity, elevated expression and nuclear translocation of Hif proteins, and augmented binding of Hif1α to *Hes1* promoter in the absence of Rbpj. These studies, for the first time, identify a previously unknown role for non-canonical notch signaling and establish a functional link between Hif and Notch pathways in hematopoiesis.

Keywords: hematopoiesis, hematopoietic stem cells, notch signaling, Hes1, stress hematopoiesis

INTRODUCTION

Notch signaling pathway is highly conserved and plays a vital role in development and adulthood. There are essentially four classes of molecules; Notch receptors, ligands, positive, and negative regulators, and transcription factors, that control notch signaling network (Pajcini et al., 2011; Lobry et al., 2014). Mammalian system contains four Notch receptors (Notch1-4) that can be activated by five ligands (Delt-like 1, 3, and 4 and Jagged 1 and 2) (Gordon et al., 2008; Kopan and Ilagan, 2009; Radtke et al., 2010). Upon engagement with its ligand, from the neighboring cell, the extracellular domain of notch receptor induces a conformation change that ultimately results in liberation of the intracellular domain (ICD) of Notch receptor (NICD) and subsequent translocation to the nucleus. Under the canonical scheme of notch signaling, NICD

heterodimerizes with the DNA binding transcription factor-recombination signal binding protein for immunoglobulin k J region (Rbpj, also known as CSL/CBF-1) and recruits additional co-factors, including mastermind proteins (MAML 1–3), to activate target genes, such as members of the Hairy enhancer of split (Hes) and Hairy related (Hey or Hrt) gene families (Gordon et al., 2008; Kopan and Ilagan, 2009; Radtke et al., 2010; Pajcini et al., 2011; Lobry et al., 2014).

Loss of functions studies have indicated the possible involvement of Notch signals in hematopoiesis (Radtke et al., 2010; Pajcini et al., 2011; Bigas and Espinosa, 2012). In particular, notch signals are essential for intra-embryonic hematopoiesis (Robert-Moreno et al., 2005), emergence of definitive hematopoietic stem cells (HSCs) from endothelial cells (Kumano et al., 2003), and maintenance of fetal liver HSC pool and functions (Gerhardt et al., 2014). Within the adult hematopoietic system, notch signals control T cell development in the thymus (Pui et al., 1999; Wilson et al., 2001; Chen et al., 2019), differentiation of M1 Vs. M2 macrophages (Wang et al., 2010), Megakaryocyte development (Mercher et al., 2008), Erythrocyte differentiation (Oh et al., 2013) and Dendritic cells (Caton et al., 2007; Kirkling et al., 2018). However, functions of notch in the maintenance of adult HSCs remain controversial.

Earlier studies, including our own (Rathinam et al., 2006), established that augmented notch signals through retroviral mediated overexpression of notch in both human and mouse HSCs causes immortalization and/or unlimited expansion without compromised self-renewal under *in vitro* culture conditions (Pui et al., 1999; Varnum-Finney et al., 2000; Stier et al., 2002; Duncan et al., 2005; Francis et al., 2017). In agreement with these data, we have shown that physiological events leading to accumulation of notch1 levels in HSCs, due to loss of a E3 ubiquitin ligase-itch, results in enhanced HSC maintenance and functions (Rathinam et al., 2011). These findings have unequivocally demonstrated the gain-of-functions role of notch signals in HSCs. Surprisingly, a series of loss-of-functions studies, through retroviral mediated overexpression of the dominant negative (dn) form of MAML (Maillard et al., 2008; Benveniste et al., 2014), Vav^{cre} mediated genetic activation of dnMAML (Francis et al., 2017) and $MX1^{cre}$ mediated deletion of Jagged1, *Notch1*, *Notch2*, and *Rbpj* (Mancini et al., 2005; Maillard et al., 2008; Varnum-Finney et al., 2011), suggested a dispensable role for notch in the maintenance of adult HSCs. Taken together, these studies established that exaggerated notch signals play key roles in HSCs, even though its deficiency may not affect HSC physiology.

To understand the complex roles by notch pathway in HSCs and explain this molecular paradox, we ablated Rbpj mediated canonical notch signals in HSCs and studied the downstream consequences on HSC maintenance and functions. Our data specify that canonical notch signals play indispensable roles in the differentiation of lymphoid-primed multipotent progenitors (MPP4) and hematopoietic recovery following radiation-, genotoxic- and cytokine- induced stress. Unexpectedly, our studies identified that Rbpj deficiency leads to activation of notch target genes through Hif1α mediated non-canonical notch pathways in HSCs.

MATERIALS AND METHODS

Mice

Rbpj Floxed mice (Han et al., 2002) (kind gift of Dr. Tasuku Honjo), Vav-iCre (B6.Cg-Commd10$^{Tg(Vav1-icre)A2Kio}$/J) mice and R26-CreERT2 (B6.129-*Gt (ROSA) 26Sor*$^{tm1(cre/ERT2)Tyj}$/J) mice were purchased from the Jackson Laboratory. CD45.1 congenic animals were purchased from the National Cancer Institute. The Institutional Animal Care and Use Committee approved all mouse experiments.

Cell Preparation

Mice were analyzed between 4–12 weeks after birth, unless otherwise specified. RBCs were lysed with ammonium chloride (STEMCELL Technologies). Trypan blue (Amresco)–negative cells were counted as live cells.

Flow Cytometry

Cells were analyzed by flow cytometry with Attune Nxt (Thermofisher) and FlowJo software (Tree Star). The following monoclonal antibodies were used: anti- CD34 (RAM34), anti-CD45.1 (A20), anti-CD45.2 (104), anti-CD48 (HM48-1), anti-CD117 (2B8), anti-Flt3 (A2F10.1), anti-Sca-1 (D7), anti-B220 (RA3-6B2), anti- CD19 (1D3), anti-CD3 (145-2C11), anti-CD4 (GK1.5), anti-CD8 (53-6.7), anti-CD11b (M1/70), anti– Gr-1 (RB6-8C5), and anti-Ter119 (TER119; from BD Biosciences); anti-CD150 (TC15-12F12.2) from Biolegend; anti-CD16/32 (93) from eBioscience. Cells incubated with biotinylated monoclonal antibodies were incubated with fluorochrome-conjugated streptavidin–peridinin chlorophyll protein–cyanine 5.5 (551419; BD), streptavidin-allophycocyanin-Cy7 (554063; BD), streptavidin-super bright 650 (Biolegend). In all the FACS plots, indicated are the percentages (%) of the gated fraction.

BMT Experiments

1×10^6 of bone marrow cells were injected into lethally irradiated (10 Gy) congenic ($CD45.1^+$) recipient mice. For competitive-repopulation experiments, 5×10^5 BM cells from either control or KO mice were mixed with 5×10^5 of WT ($CD45.1^+$) BM cells (to obtain a ratio of 1:1) and were injected into lethally irradiated congenic WT ($CD45.1^+$) recipient mice.

For serial transplantation assays, 1×10^6 of bone marrow cells were injected into lethally irradiated (10 Gy) WT congenic ($CD45.1^+$) recipient mice. After 12 weeks of transplantation, 1×10^6 BM cells of primary recipients were injected into lethally irradiated WT congenic secondary recipients.

RNA Extraction, PCR, and Real-Time PCR

Total RNA was isolated with an RNeasy Mini kit or RNeasy Micro kit (QIAGEN). cDNA was synthesized with Oligo (dT) primer and Superscript IVReverse Transcriptase (Thermo Fisher Scientific). PCR was performed with T100 thermal cycler (Bio-Rad Laboratories) and TSG Taq (Lamda Biotech). Real-time PCR was performed in duplicates with a CFX-connect real-time PCR system (Bio-Rad Laboratories) and SsoAd- vanced

SYBR Green Supermix (Bio-Rad Laboratories) according to the manufacturer's instructions. Relative expression was normalized to the expression levels of the internal control (housekeeping gene) HPRT/GAPDH.

ChIP Assay

ChIP assay was performed with Pierce Agarose ChIP Kit (Pierce) according to the manufacturer's instructions. In brief, 5×10^6 Lineage negative BM cells were fixed and immunoprecipitated with anti-Hes1 (abcam ab49170) and anti-Hif1 α (Novusbio NB100-105) antibody or control-IgG antibodies. Immunoprecipitated DNA fragments were quantified by real-time PCR with the use of primers which amplify Gata2 and p57 promoter regions containing Hes1 binding sites and Hes1 promoter region containing Hif1 α binding sites. Fold enrichment was normalized to goat IgG-precipitated samples.

Western Blot Analysis

For immunoblot analyses, cells were lysed with cell lysis buffer (Cell Signaling Technology) with protease inhibitor cocktail (Complete; Roche) and 1 mM PMSF (Santa Cruz Biotechnology, Inc.). Cell lysates were boiled with sample buffer (NuPAGE; Life Technologies) containing 1% 2-Mercaptoethanol (Sigma-Aldrich). In some experiments, cytoplasmic and nuclear proteins were fractionated using Subcellular Protein Fractionation Kit (Thermo Fischer). Proteins were subjected to 8–12% SDS-PAGE and transferred to PVDF membranes (Bio-Rad Laboratories). The membranes were blocked with either 5% bovine serum albumin (Life Technologies) or 5% skim milk and then treated with primary and secondary antibodies, respectively. The blots were visualized using the ECL (Pierce) and C300 (Azure Biosystems) western blot imaging unit. Antibodies used were as follows: anti-P57 (Novusbio NBP2-44488), anti-Hes1 (abcam ab49170), anti–ICN1 (Novusbio NB100-78486), anti-actin (I-19; Santa Cruz Biotechnology, Inc.), anti-Histone3 (Cell Signaling Technology 96C10) HRP-conjugated anti–mouse and anti–rabbit IgG (Cell Signaling Technology), and HRP-conjugated anti–goat IgG (Santa Cruz Biotechnology, Inc.).

Measuring ROS Levels

BM cells were stained with cell surface markers and then incubated with 2 mM CM-H_2DCFDA (Life Technologies C6827) in pre-warmed HBSS at 37C for 15 min. The cells were then pelleted and resuspended in PBS before acquisition.

In vitro Culture

Lineage depleted BM cells were placed in culture with 10%FBS/DMEM + 50 ng/ml stem cell cytokines (Flt3l, SCF, TPO, IL3, and IL6; Peprotech). After indicated period of culture, cells were harvested, stained with antibodies and analyzed by flow cytometry.

Confocal Microscopy

Freshly sorted Lin- BM cells were plated onto poly-D-lysine (Sigma) coated chamber slides and incubated at 37°C in 10%FBS/DMEM + 50 ng/ml stem cell cytokines (IL3, SCF, TPO, Flt3l, and IL6) for 2 h-overnight before fixing for 10 min with 4%PFA at RT. Cells were permeabilized in 0.15% Triton-X100 for 2 min at RT and then blocked overnight in 1%BSA/PBS at 4°C. Cells were incubated with primary in blocking solution for 2 h at 37°C and then with secondary for 1 h at 37°C. For nuclear stain, Sytox blue (Thermofisher) was added for 6 min at RT and then slides were mounted with VectaShield and imaged on a Zeiss 710 Confocal using a 100× objective. Florescence quantification was performed by ImageJ (NIH) analysis similar to Mccloy et al., 2014 except that the values for the background were obtained from the surrounding cells and *p*-values were obtained by performing a two-tailed unpaired Student's *t*-test. For these experiments, cells stained only with secondary were used to determine the specificity and intensity of fluorescence.

5-FU and Cell Proliferation Assay

A single dose (150 mg/kg) of 5-Fluorouracil (5-FU; Sigma-Aldrich) was injected intraperitoneally and mice were analyzed after 14 days. For *in vivo* bromodeoxyuridine (BrdU) assay, 1 mg BrdU (BD) was injected intraperitoneally. After 24 h of injection, mice were sacrificed and bone marrow cells were stained for BrdU, following the BrdU Flow Kit manufacturer's instructions (BD Pharmingen). For Ki67 analysis, BM cells were stained for cell surface markers, fixed, and permeabilized with BD Fix/Perm kit. Cells were stained with anti-Ki67—APC (BD558615) for 30 min on ice and analyzed by flow cytometry.

Statistics

Data represent mean and SEM. Two-tailed student's *t*-tests were used to assess statistical significance ($^*P < 0.05$, $^{**}P < 0.01$, $^{***}P < 0.001$). For survival curve analysis, log rank test was used to assess statistical significance ($^*P < 0.05$, $^{**}P < 0.01$, $^{***}P < 0.001$, $^{****}P < 0.0001$).

RESULTS

Loss of Rbpj Results in Altered MPP Pool

To study the role of Rbpj mediated signals in the hematopoiesis, we analyzed $Rbpj^{F/F}$ $Vav^{cre/+}$ mice (henceforth referred to as $Rbpj^{Hem-KO}$), as expression of cre through Vav promoter results in faithful deletion of transgenes in all hematopoietic cells, including LT-HSCs. To investigate the contribution of Rbpj mediated canonical notch pathway to the maintenance of HSPC pool, we enumerated the frequencies of HSPC subsets in the bone marrow (BM) of $Rbpj^{Hem-KO}$ mice. Our analysis of $Rbpj^{Hem-KO}$ mice indicated normal cellularity of the BM (**Figure 1A**). Immunophenotyping studies on HSPCs of BM documented a decrease in the relative frequency, but normal absolute numbers, of lineage$^-$ (Lin^-) hematopoietic cells, and a relative increase, but normal absolute numbers, of Lin^- c-Kit^+ $Sca1^+$ (LSK) cells of $Rbpj^{Hem-KO}$ mice (**Figures 1B,C**), as reported earlier (Duarte et al., 2018). To assess if Rbpj deficiency affects the distribution of specific HSPC subsets, we further analyzed the BM LSK cells of $Rbpj^{Hem-KO}$ mice through previously established immunophenotyping strategies; (1) according to the scheme established Yang et al. (2005) we identified normal

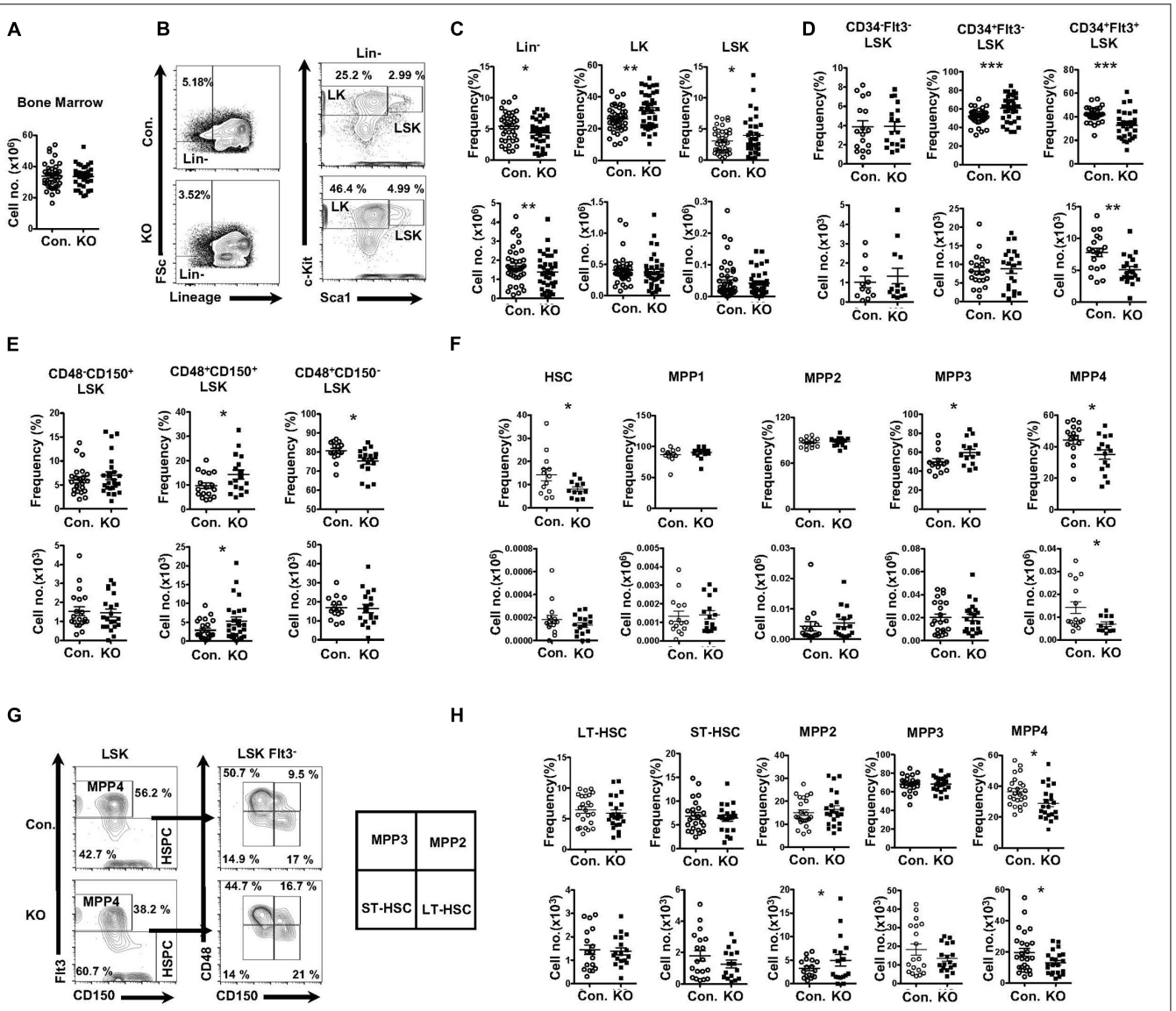

FIGURE 1 | Deficiency of Rbpj affects lymphoid- and erythroid- biased progenitors. **(A)** Absolute cell number of BM from KO and Control mice (n = 35–40). **(B)** FACS plots of Lin$^-$, LK, and LSK subsets of BM (two femurs and two tibias) from KO and control mice. Data are representative of seven independent experiments. **(C)** Frequencies (top) and absolute numbers (bottom) of Lin-, LK, and LSK subsets of BM (two femurs and two tibias) from KO and control mice (n = 16–25). **(D)** Frequencies (top) and absolute numbers (bottom) of LT-HSC, ST-HSC, and MPP subsets of BM (two femurs and two tibias) from KO and control mice (n = 16–25). **(E)** Frequencies (top) and absolute numbers (bottom) of CD150$^+$CD48$^-$LSK **(**LT-HSC), CD150$^+$CD48$^+$LSK and CD150$^-$CD48$^+$LSK subsets of BM (two femurs and two tibias) from KO and control mice (n = 16–25). **(F)** Frequencies (top) and absolute numbers (bottom) of HSC, MPP1, MPP2, MPP3, and MPP4 analysis of BM (two femurs and two tibias) from KO and control mice (n = 14–20). **(G)** FACS plots of LT-HSCs, ST-HSCs, MPP2, MPP3, and MPP4 subsets of BM (two femurs and two tibias) from KO and control mice. Data are representative of seven independent experiments. **(H)** Frequencies (top) and absolute numbers (bottom) of LT-HSCs, ST-HSCs, MPP2, MPP3, and MPP4 subsets of BM (two femurs and two tibias) from KO and control mice (n = 16–25). All data represent mean ± SEM. Two-tailed Student's t-tests were used to assess statistical significance (*P < 0.05; **P < 0.01; ***P < 0.001).

relative and absolute numbers of LT-HSCs (CD34$^-$Flt3$^-$LSK), increased relative, but normal absolute numbers of Short-Term HSCs (ST-HSCs; CD34$^+$Flt3$^-$LSK), and decreased relative and absolute numbers of Multipotent Progenitors (MPPs; CD34$^+$Flt3$^+$LSK) (**Figure 1D** and **Supplementary Figure 1A**); (2) immunophenotyping approach of Oguro et al. (2013) revealed normal relative and absolute numbers of LT-HSCs (CD150$^+$CD48$^-$LSK), increased relative, but normal absolute, numbers of CD150$^+$CD48$^+$LSK subset, and decreased relative, but normal absolute, numbers of CD150$^-$CD48$^+$LSK subset (**Figure 1E** and **Supplementary Figure 1B**); (3) HSPC characterization, established by Wilson et al. (2008) identified normal relative and absolute numbers of HSCs (CD34$^-$Flt3$^-$CD150$^+$CD48$^-$LSK), modestly increased relative, but normal absolute, numbers of MPP1 (CD34$^+$Flt3$^-$CD150$^+$CD48$^-$LSK), normal relative and

absolute numbers of MPP2 ($CD34^+Flt3^-CD150^+CD48^+LSK$), modestly increased relative, but normal absolute, numbers of MPP3 ($CD34^+Flt3^-CD150^-CD48^-LSK$), and a consistent decrease in both relative and absolute numbers of MPP4 ($CD34^+Flt3^+CD150^-CD48^-LSK$) (**Figure 1F** and **Supplementary Figure 1C**); and (4) through an immunophenotyping scheme established by Pietras et al. (2011) we identified that the relative and absolute numbers of LT-HSCs ($Flt3^-CD150^+CD48^-LSK$), ST-HSCs ($Flt3^-CD150^+CD48^-LSK$), and granulocyte/monocyte lineage biased MPP3 ($Flt3^-CD150^-CD48^+LSK$) fraction were normal. Normal relative, but increased absolute, numbers of megakaryocyte/erythroid lineage biased MPP2 ($Flt3^-CD150^+CD48^-LSK$) fraction were identified. Consistent with the other HSPC identification strategies, both relative and absolute numbers of the lymphoid biased MPP4 ($Flt3^+CD150^-CD48^+LSK$) fraction were decreased (**Figures 1G,H**). Taken together, these data unequivocally demonstrate that Rbpj deficiency selectively affects the differentiation and/or maintenance of the MPP subsets, under steady state conditions.

Rbpj Deficiency Leads to Defective Erythroid and Lymphoid Differentiation

To assess the functions of Rbpj mediated notch signals and impact of altered MPP pool in $Rbpj^{Hem-KO}$ to multi-lineage differentiation, we determined the frequencies of myeloid-, erythroid- and lymphoid- lineage cells in $Rbpj^{Hem-KO}$ mice. Analysis of lineage committed progenitors (**Figures 2A,B** and **Supplementary Figures 2A,B**), revealed an increase in relative, but normal absolute, numbers of Common myeloid progenitors (CMPs; $Lin^-Sca1^-c\text{-}Kit^+$ $CD34^+CD16/32^-$) and Granulocyte/Monocyte Progenitors (GMPs; $Lin^-Sca1^-c\text{-}Kit^+$ $CD34^+CD16/32^+$). However, both relative and absolute numbers of Megakaryocyte/Erythroid Progenitors (MEPs; $Lin^-Sca1^-c\text{-}Kit^+$ $CD34^-CD16/32^-$) were decreased. Analysis of Common Lymphoid Progenitors (CLPs; $Lin^-IL7R\alpha^+Sca1^{low}c\text{-}Kit^{low}$) revealed that their relative frequencies were increased, but absolute numbers were decreased. Next, enumeration of myeloid, erythroid and lymphoid lineage cells in BM of $Rbpj^{Hem-KO}$ mice indicated (**Figure 2C**) normal frequencies and absolute numbers of $CD11b^+$ myeloid- and $CD19^+$ B- lineage cells, and reduced frequencies and absolute numbers of $Ter119^+$ erythroid lineage cells. Consistent with previous reports (Pui et al., 1999; Wilson et al., 2001), our analysis of $Rbpj^{Hem-KO}$ mice revealed a remarkable reduction of thymic size and cellularity (**Figure 2D,E**). These studies establish that ablation of Rbpj mediated canonical notch signals in HSCs leads to defective erythroid and lymphoid differentiation.

Lack of Rbpj Affects Radiation Stress-Induced Hematopoietic Recovery

To identify functions of HSPCs in the absence of Rbpj, we performed total and mixed bone marrow transplantation (BMT) experiments. Transfer of RBC depleted total BM from $Rbpj^{Hem-KO}$ mice into lethally irradiated wildtype (WT; $CD45.1^+$) congenic recipients resulted in reduced donor ($CD45.2^+$) derived hematopoiesis in the peripheral blood at 6, 12, and 18 weeks of transplantation (**Figure 3A**). Donor derived multi-lineage analysis indicated normal frequencies of donor myeloid and B cell, but reduced $CD4^+$ and $CD8^+$ T cell fractions in the peripheral blood of recipients at 18 weeks of BMT (**Supplementary Figures 3A,B**). Analysis of BM of these recipients, after 20 weeks of BMT, revealed a significant reduction in both absolute and relative numbers of $Rbpj^{Hem-KO}$ donor ($CD45.2^+$) derived hematopoiesis, even though the total BM cellularity of recipients was comparable between control and $Rbpj^{Hem-KO}$ recipients (**Figure 3B**). To evaluate if the reduced $Rbpj^{Hem-KO}$ donor derived hematopoiesis in irradiated hosts is caused by HSPC defects, we analyzed the HSPC pool. Our analysis identified; normal relative, but reduced absolute, numbers of Lin^-, LK, and LSK subsets; reduced frequencies and numbers of LT-HSC and MPP4 fractions; increased relative, but normal absolute, numbers of MPP2; and normal frequencies and numbers of ST-HSC and MPP3 subsets (**Figures 3C,D**). Consistently, multi-lineage analysis indicated reduced absolute numbers of $Rbpj^{Hem-KO}$ donor derived myeloid, erythroid B and T lineage cells in the BM (**Figure 3E** and **Supplementary Figure 3C**). Analysis of spleen from recipients that received $Rbpj^{Hem-KO}$ BM suggested a reduction in overall donor derived hematopoiesis, increased frequencies of $CD19^+$ B cells, and reduced frequencies of $CD4^+$ and $CD8^+$ T cells (**Figure 3F**). Next, we assessed the capacities of Rbpj mutant BM to generate hematopoiesis in the presence of WT competitor BM. Analysis of lethally irradiated recipients that received mixed BM ($Rbpj^{Hem-KO}$: wildtype at a ratio of 1:1) indicated that the contribution of $Rbpj^{Hem-KO}$ derived hematopoiesis was reduced at 6, 12, and 18 weeks of transplantation in the peripheral blood (**Figure 3G**) and at 18 weeks in BM and spleen (**Figure 3H**). Further analysis of $Rbpj^{Hem-KO}$ derived HSPC compartments specified a consistent reduction of LSK, LK, LT-HSC, MPP3 and MPP4 fractions in the BM (**Figures 3I,J** and **Supplementary Figure 3D**). Finally, we transferred the BM of primary recipients from mixed chimera experiments into lethally irradiated secondary recipients and analysis indicated a remarkable reduction of $Rbpj^{Hem-KO}$ derived hematopoiesis at 8 weeks of transplantation (**Figure 3K**). Overall, these data specify that $Rbpj^{Hem-KO}$ HSPCs have reduced capacities to respond to radiation induced stress and that the HSPC defects of $Rbpj^{Hem-KO}$ mice are caused by cell intrinsic mechanisms.

Rbpj Deletion Causes Diminished Hematopoietic Responses to Genotoxic and Cytokine Stress

To measure the responses of Rbpj deficient HSPCs to hematopoietic stress mediated by 5-Fluorouracil (5-FU) (Van Zant, 1984), we injected *i. p.* a single dose of 5-FU and hematopoietic compartments were analyzed after 14 days. Analysis of hematopoietic organs of 5-FU injected $Rbpj^{Hem-KO}$ mice revealed reduced cellularity of the BM, increased cellularity of the spleen and normal cellularity of the thymus (**Figure 4A**). Multi-lineage analysis of peripheral blood indicated normal

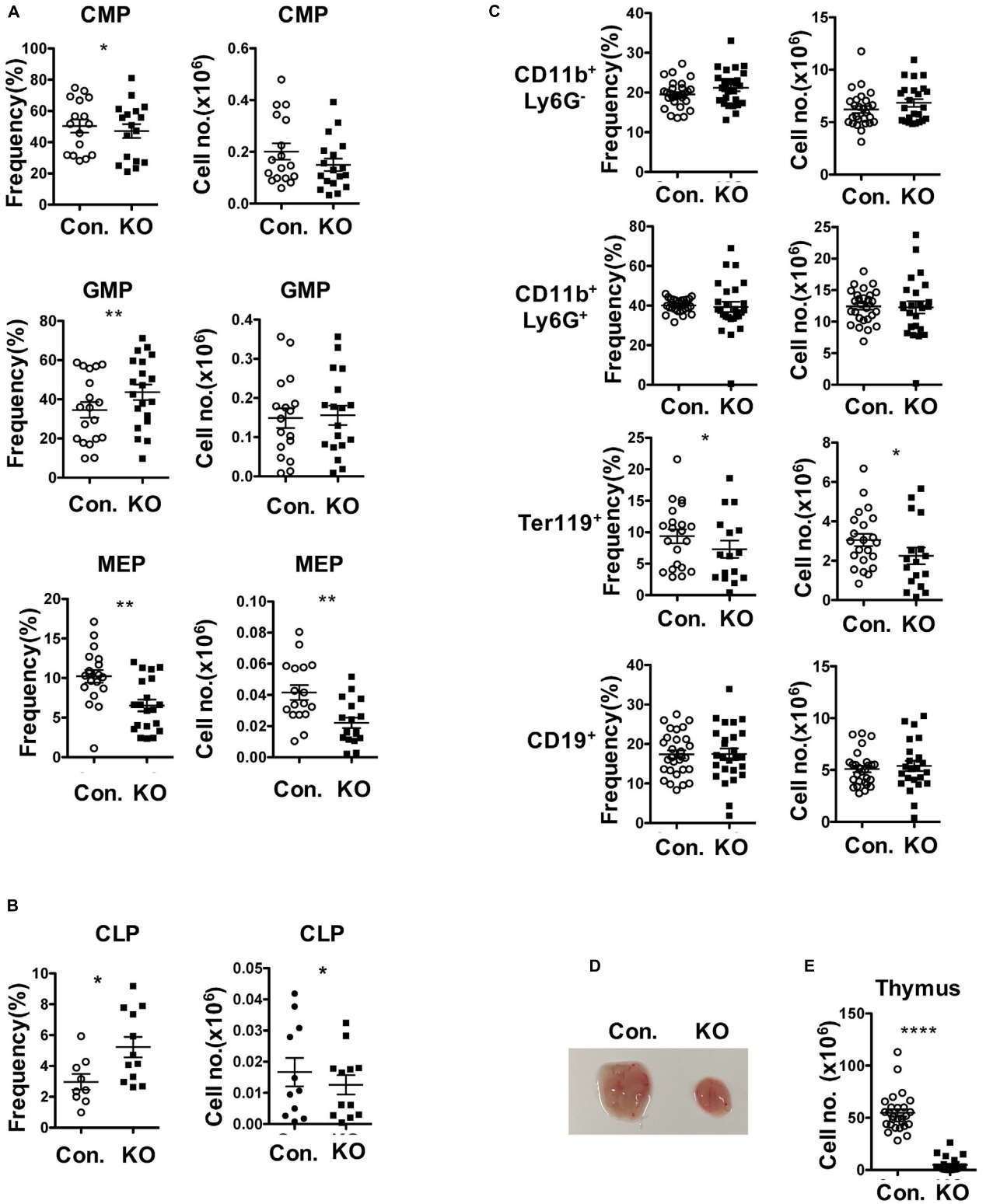

FIGURE 2 | Loss of Rbpj affects lymphoid and erythroid differentiation. **(A,B)** Frequencies (left) and absolute numbers (right) of CMPs, GMPs and MEPs **(A)** and CLPs **(B)** of BM (two femurs and two tibias) from KO and control mice (n = 10–20). **(C)** Frequencies (left) and absolute numbers (right) of $CD11b^+Ly6G^-$, $CD11b^+Ly6G^+$, $Ter119^+$, and $CD19^+$ subsets in the BM of (two femurs and two tibias) from KO and control mice (n = 12–25). **(D,E)** Representative picture showing size **(D)** and cellularity **(E)** of thymus from KO and control mice (n = 25–30). All data represent mean ± SEM. Two-tailed Student's t-tests were used to assess statistical significance (*$P < 0.05$; **$P < 0.01$; ****$P < 0.0001$).

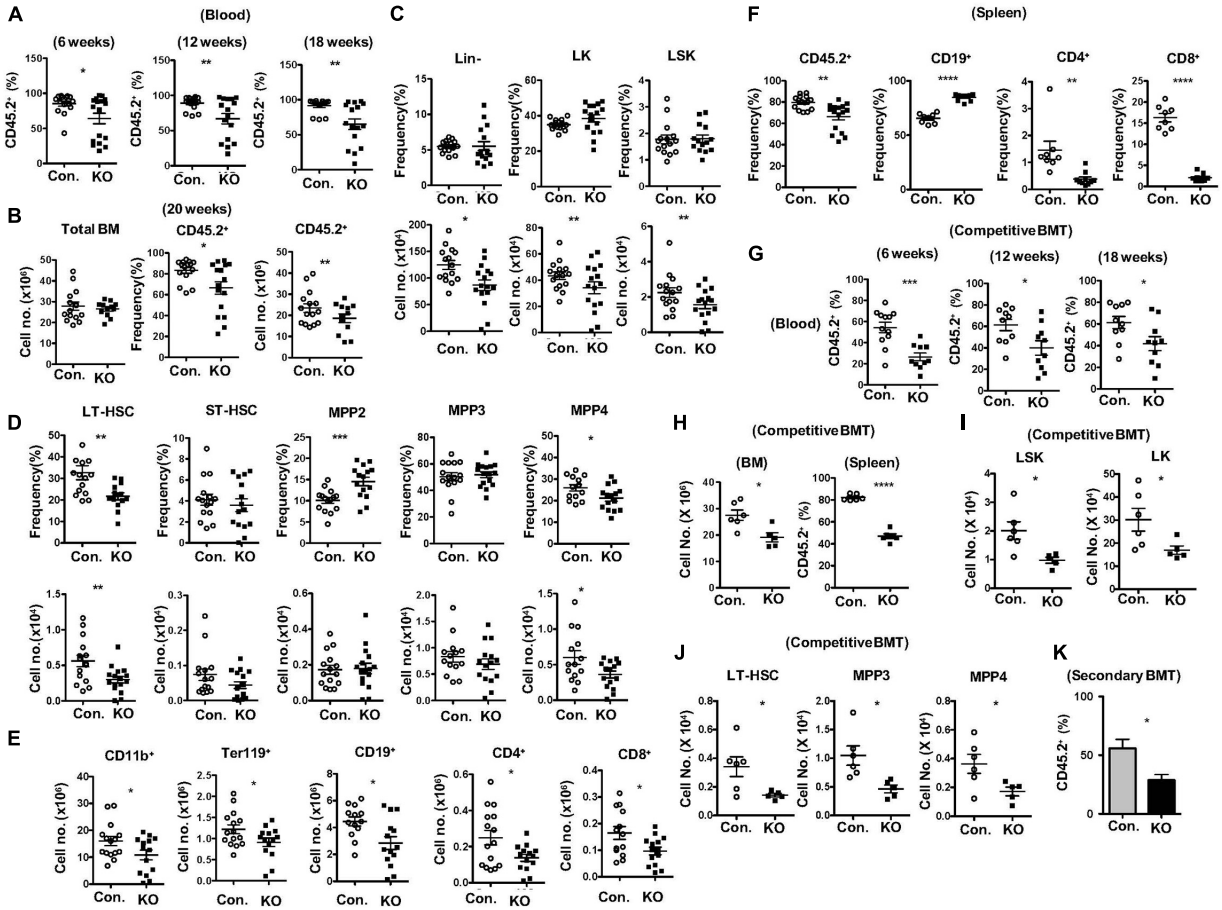

FIGURE 3 | Lack of Rbpj leads to compromised radiation stress induced HSC functions. **(A)** Frequencies of donor derived chimera ($CD45.2^+$) in the peripheral blood of lethally irradiated congenic recipients that received total BM of either KO or control mice at 6, 12, and 18 weeks of transplantation. **(B)** Absolute cell number of total BM (left) and frequencies (middle) and absolute cell numbers (right) of donor derived chimera ($CD45.2^+$) from KO and Control recipient mice (n = 12–25) at 20 weeks of transplantation. **(C,D)** Frequencies (top) and absolute numbers (bottom) of Lin-, LK, LSK, LT-HSCs, ST-HSCs, MPP2, MPP3, and MPP4 subsets of BM (two femurs and two tibias) from KO and Control recipient mice (n = 12–15) at 20 weeks of transplantation. **(E)** Frequencies of donor derived ($CD45.2^+$) $CD11b^+$, $Ter119^+$, $CD19^+$, $CD4^+$, and $CD8^+$ cells in the BM (two femurs and two tibias) from KO and Control recipient mice (n = 10–13) at 20 weeks of transplantation. **(F)** Frequencies of donor derived ($CD45.2^+$) splenocytes and $CD19^+$, $CD4^+$, and $CD8^+$ subsets in the spleen from KO and Control recipient mice (n = 8–12) at 20 weeks of transplantation. **(G)** Frequencies of KO and Control derived ($CD45.2^+$) chimera in the peripheral blood of lethally irradiated congenic recipients that received mixed BM of either KO or control + competitor (1:1) at 6, 12, and 18 weeks of transplantation. **(H)** $CD45.2^+$KO and Control derived cell counts in the BM and frequencies in the spleen of recipients (n = 6) that received mixed BM of either KO or control + competitor (1:1) at 20 weeks of transplantation. **(I,J)** Absolute numbers of KO and control ($CD45.2^+$) derived LK, LSK, LT-HSC, MPP3, and MPP4 subsets in the BM of recipients (n = 6) that received mixed BM of either KO or control + competitor (1:1) at 20 weeks of transplantation. **(K)** Frequencies of donor derived ($CD45.2^+$) chimera in the peripheral blood of secondary recipients that received total BM of primary recipients from **(G)** at 8 weeks of secondary transplantation. All data represent mean ± SEM. Two-tailed Student's t-tests were used to assess statistical significance (*$P < 0.05$; **$P < 0.01$; ***$P < 0.001$; ****$P < 0.0001$).

frequencies of $CD11b^+$ myeloid cells, but decreased frequencies of $CD19^+$ B cells, $CD4^+$ T cells and $CD8^+$ T cells (**Figure 4B**) and of BM documented increased relative, but normal absolute, numbers of myeloid, reduced relative and absolute numbers of erythroid-, B-, and T- lineage cells (**Figure 4C**) in 5-FU injected $Rbpj^{Hem-KO}$ mice. Multi-lineage analysis of spleen from 5-FU injected $Rbpj^{Hem-KO}$ mice revealed; normal numbers of myeloid cells and $CD4^+$ T cells; normal relative, but increased absolute, numbers of $CD19^+$ cells; and reduced relative, but normal absolute, numbers of $CD8^+$ T cells (**Supplementary Figures 4A,B**). Finally, immunophenotyping of BM HSPC compartments from 5-FU injected $Rbpj^{Hem-KO}$ mice identified reduced relative and absolute numbers of Lin^- cells and normal relative, but reduced absolute, numbers of LSK and LK cells (**Figure 4D**). Further characterization of LSK compartment indicated; normal relative and absolute numbers of LT-HSC and MPP2 fractions; reduced relative and absolute numbers of ST-HSCs; normal frequencies, but reduced absolute numbers, of MPP3 fraction; and reduced relative and absolute numbers of MPP4 fraction in the BM of 5-FU treated $Rbpj^{Hem-KO}$ mice (**Figure 4E**).

To evaluate the capacities of Rbpj deficient HSPCs to respond to cytokine induced stress (Zhao and Baltimore, 2015) we cultured BM lin^- cells in the presence of HSPC cytokine cocktail

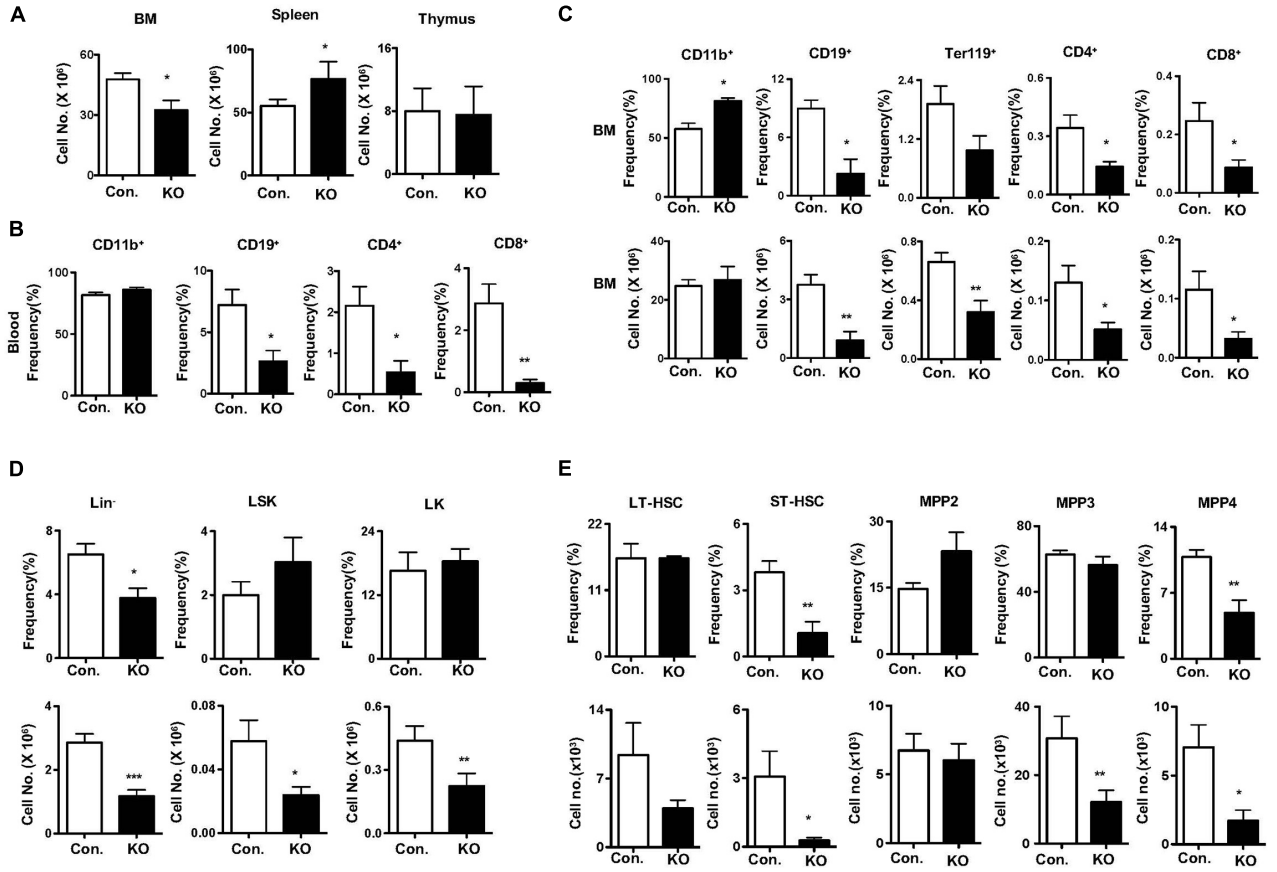

FIGURE 4 | Rbpj deficiency causes defective five-Fluorouracil and cytokine induced HSC response. **(A)** Total cell counts of BM, spleen and thymus from KO and control mice after 14 days of five-FU injection (n = 5–7). **(B)** Frequencies of CD11b$^+$, CD19$^+$, CD4$^+$, and CD8$^+$ cells in the peripheral blood of KO and control mice after 14 days of five-FU injection (n = 5–7). **(C)** Frequencies (top) and absolute numbers (bottom) of CD11b$^+$, CD19$^+$, Ter119, CD4$^+$, and CD8$^+$ cells in the BM of KO and control mice after 14 days of five-FU injection (n = 5–7). **(D,E)** Frequencies (top) and absolute numbers (bottom) of Lin$^-$, LK, LSK, LT-HSCs, ST-HSCs, MPP2, MPP3, and MPP4 subsets of BM from KO and control mice after 14 days of five-FU injection (n = 5–7). All data represent mean ± SEM. Two-tailed Student's t-tests were used to assess statistical significance (*P < 0.05; **P < 0.01; ***P < 0.001).

(IL3 + SCF + TPO + IL6 + Flt3L). Immunophenotyping analysis indicated an altered frequencies of HSPCs in the absence of Rbpj (**Supplementary Figures 4C,D**). Together, these results demonstrate that the hematopoietic responses to 5-FU and cytokine-induced induced stress are compromised in the absence of Rbpj mediated notch signals.

Disruption of Rbpj Mediated Signals Leads to Increased HSC Quiescence and p57^{Kip2} Levels

To identify the cellular mechanisms responsible for diminished stress-induced hematopoietic response, we focused on the proliferation kinetics of HSPCs. Indeed, capacities of HSCs to exit quiescence and enter an active proliferative state is vital for the demand-adapted regulation of hematopoiesis under severe stress conditions (Takizawa et al., 2012). First, we assessed the *in vitro* proliferative capacities of Rbpj deficient HSPCs through BrdU pulsing studies. Data indicated that the frequencies of BrdU$^+$ (**Figure 5A**) and BrdU^{high} (**Figure 5B**) Rbpj mutant LSK cells were reduced, even though their viability rates were normal (**Supplementary Figure 5A**). Further quantitative analysis suggested a reduction in the amount of incorporated BrdU within BrdU$^+$ Rbpj mutant LSK cells (**Figure 5C**), but not in Lin$^-$ and LK cells (**Supplementary Figures 5B,C**). To further verify these data, through an independent approach, we performed CFSE dilution assays and data confirmed that Rbpj mutant LSK cells exhibit reduced proliferation capacities *in vitro* in the presence of HSPC cytokines (**Figure 5D**).

Based on these data, we hypothesized that loss of Rbpj leads to decreased proliferative responses in HSPCs. To validate this and further strengthen our findings, we performed short-term *in vivo* BrdU pulsing experiments. Rbpj^{Hem-KO} mice were injected *i.p* with BrdU and BM HSPCs were analyzed after 24 h. Whereas the proliferation rates were normal in Lin$^-$ cells, the frequencies of proliferating (BrdU$^+$) LSK and LK cells were reduced in the BM of Rbpj^{Hem-KO} mice (**Figure 5E**). Further analysis specified decreased proliferation of LT-HSCs (CD150$^+$CD48$^-$LSK), Flt3$^-$LSK, and Flt3$^+$ LSK cells from Rbpj^{Hem-KO} mice (**Figure 5F**). To corroborate these

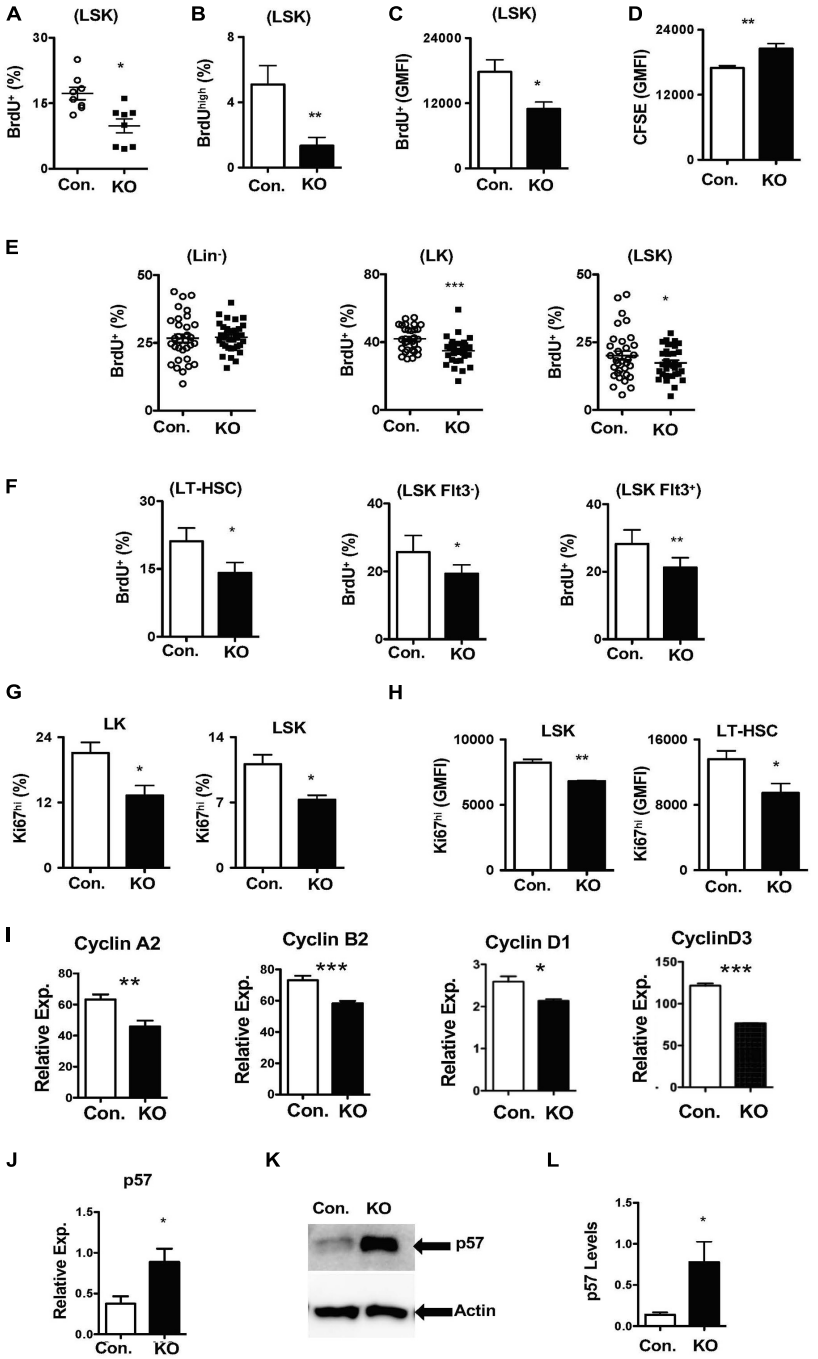

FIGURE 5 | Loss of Rbpj results in increased HSC quiescence. **(A,B)** Frequencies of BrdU^{+} **(A)** and BrdU^{high} **(B)** LSK cells following *in vitro* culture of purified Lin^{-} BM cells from KO and Control mice in the presence of HSPC cytokine cocktail for 24 h. Data are pool of two independent experiments (n = 8–12). **(C)** Geomean fluorescence Intensity (GMFI) of BrdU^{+} LSK cells following *in vitro* culture of purified Lin^{-} BM cells from KO and Control mice in the presence of HSPC cytokine cocktail for 24 h. Data are pool of two independent experiments (n = 8–12). **(D)** GMFI of CFSE in LSK cells following *in vitro* culture of purified Lin^{-} BM cells from KO and Control mice in the presence of HSPC cytokine cocktail for 72 h. Data are pool of two independent experiments (n = 5–7). **(E,F)** Frequencies of BrdU^{+} Lin^{-}, LK, LSK, LT-HSCs, Flt3^{-}LSK and Flt3^{+}LSK subsets in the BM of KO and Control mice (n = 20–22). Mice were injected i.p., with BrdU and analyzed after 24 h. **(G,H)** Frequencies of Ki67^{+} LK and LSK cells **(G)** and GMFI of Ki67^{high} LSK cells and LT-HSCs **(H)** in the BM of KO and Control mice (n = 10–12). **(I)** Real time PCR data for *Cyclin A2, Cyclin B2, Cyclin D1*, and *Cyclin D3* expression levels in Lin^{-} cells from the BM of KO and Control mice. Expression levels of target genes were normalized to HPRT levels. Data are representative of two independent experiments. **(J)** Real time PCR data for *p57^{Kip2}* expression levels in Lin^{-} cells from the BM of KO and Control mice. Expression levels were normalized to HPRT levels. Data are representative of three independent experiments. **(K)** Western blot analysis of p57^{Kip2} protein in Lin^{-} BM cells of KO and control mice. Data are representative of three independent experiments. **(L)** Quantification of proteins from western blots shown in **(K)** p57^{Kip2} protein levels were normalized to actin protein levels in each lane, respectively. Data are pool of three independent experiments. All data represent mean ± SEM. Two-tailed Student's *t*-tests were used to assess statistical significance (*$P < 0.05$; **$P < 0.01$; ***$P < 0.001$).

findings, we quantified Ki67 levels, a faithful marker of cell proliferation, in $Rbpj^{Hem-KO}$ HSPCs. Data indicated that the frequencies of $Ki67^{+}$ LK, and LSK cells (**Figure 5G** and **Supplementary Figure 5D**) and expression levels of Ki67 within $Ki67^{+}$ LSK cells and LT-HSCs (**Figure 5H** and **Supplementary Figure 5E**) were reduced.

To explain these findings at a molecular level, we quantified expression levels of both positive (Cyclins) and negative [cyclin dependent kinase inhibitors (CDKIs)] regulators of cell cycle in Rbpj deficient Lin- BM cells. Real-time PCR assays documented reduced mRNA levels of key cyclins, such as *CyclinA2*, *CyclinB2*, *CyclinD1*, and *CyclinD3* (**Figure 5I**). On the other hand, mRNA and protein expression levels of $p57^{Kip2}$, a key CDKI and positive regulator of HSC quiescence (Matsumoto et al., 2011; Zou et al., 2011), were augmented in the absence of Rbpj (**Figures 5J–L**). However, mRNA levels of other CDKIs, including *p16*, *p18*, and *p27*, were reduced in Rbpj mutant cells Lin- BM cells (**Supplementary Figure 5F**). Taken together, these studies suggest that Rbpj mediated signaling pathways are essential for proper transition of HSCs from a quiescent state to proliferative state and finetuning the balance between cyclins and CDKIs.

Loss of Rbpj Causes Augmented Expression Notch Target Genes and Hes1 Functions

To identify molecular mechanisms responsible for the HSPC phenotype of $Rbpj^{Hem-KO}$ mice, we assessed the expression levels of notch target genes in the absence of Rbpj. In view of the fact that Rbpj is the key downstream mediator and indispensable for the canonical notch pathway (Kopan and Ilagan, 2009; Pajcini et al., 2011; Bigas and Espinosa, 2012; Bray, 2016), we anticipated that expression of notch targets might be reduced in Rbpj mutant HSPCs. Unexpectedly, our studies identified that the expression levels of key downstream targets of Notch pathway (Kopan and Ilagan, 2009; Pajcini et al., 2011; Bigas and Espinosa, 2012; Bray, 2016), including *Hes1*, *Hes5*, *Hey1*, and *HeyL*, were elevated in Rbpj mutant HSPCs (**Figures 6A,B**). We were especially intrigued by the elevated expression of *Hes1* in Rbpj deficient HSPCs, as Hes1 has been considered as the key and major target gene of canonical Notch pathway in hematopoietic cells (Gordon et al., 2008; Kopan and Ilagan, 2009; Radtke et al., 2010; Pajcini et al., 2011; Lobry et al., 2014). To strengthen these results, we quantified the expression levels of Hes1 protein. Our western blot studies concluded that Hes1 protein levels were elevated in both cytoplasm and nucleus of Rbpj deficient hematopoietic progenitors (**Figures 6C,D**). To further corroborate these data, we performed confocal microscopy studies. Consistent with our observations, a remarkably increased levels of Hes1 protein were detected in the nucleus of Rbpj mutant HSPCs (**Figures 6E,F**).

All data represent mean ± SEM. Two-tailed Student's *t*-tests were used to assess statistical significance ($^{*}P < 0.05$; $^{**}P < 0.01$; $^{***}P < 0.001$; $^{****}P < 0.0001$).

To identify the functional consequences of elevated *Hes1*, we analyzed if expression of transcription factors, such as *Gata1, Gata2, c-Myc, HoxA9, Cebpα*, and *Gfi1*, that play key roles in hematopoiesis is altered in $Rbpj^{Hem-KO}$ HSPCs. These studies identified normal expression of *Gata1* and *c-Myc* and increased expression of *Gata2* and *Gfi1* in Lin^{-} cells, normal expression of *Gata1* and *Cebpα* and increased expression of *Gata2* and *HoxA9* in LK cells, and reduced expression of *Gata1*, increased expression of *Gata2* and normal expression of *HoxA9* and *Cebpα* in $LSKFlt3^{-}$ cells (**Figure 6G** and **Supplementary Figures 6A–C**). Among these candidate transcription factors, we were intrigued by deregulated expression of Gata2 because; (1) Gata2 is consistently upregulated in Lin^{-}, LK and $LSKFlt3^{-}$ cells of $Rbpj^{Hem-KO}$ mice; (2) overexpression of Gata2 in mouse and human HSCs (Tipping et al., 2009; Nandakumar et al., 2015) has been shown to block hematopoietic reconstitution in irradiated hosts, inhibit cell cycle entry/promote quiescence and suppress lymphoid differentiation, very similar to the phenotype of Rbpj deficient HSPCs; and (3) Hes1 has been suggested to regulate *Gata2* expression during embryogenesis (Guiu et al., 2013).

To test if increased expression levels of *Gata2* (**Figure 6G**) and $p57^{Kip2}$ (**Figures 5J–L**) in Rbpj mutant HSPCs are in response to augmented binding of Hes1 to their promoters, we performed *in silico* analysis. Indeed, a single Hes1 binding site (CACGCA) is present in $p57^{Kip2}$ promoter (**Figure 6H**) and four Hes1 binding sites (Guiu et al., 2013) in the regulatory regions of both generic and hematopoietic specific promoters of *Gata2* (**Figure 6I**). Finally, data of Chromatin immunoprecipitation (ChIP) experiments documented an increased binding of Hes1 to the promoters of $p57^{Kip2}$ and *Gata2* in Lin- BM cells of $Rbpj^{Hem-KO}$ mice (**Figures 6J–L**). Overall, these molecular studies established that Rbpj deficiency causes elevated expression of notch target genes and increased binding of Hes1 to the regulatory regions of $p57^{Kip2}$ and *Gata2.*

Loss of Rbpj Induces Hif1α Mediated Upregulation of Hes1

To investigate pathways leading to elevated expression of notch target genes, we assessed if notch activity is intact in the absence of Rbpj. Real-Time PCR assays revealed that expression levels of *Notch1* and *Notch2* mRNA were increased in LK and $Flt3^{-}LSK$ cells of $Rbpj^{Hem-KO}$ mice (**Figures 7A,B**). While western blot analysis indicated normal levels of cleaved Notch1 (ICN1) protein (**Figures 7C,D**), confocal microscopy studies documented an augmented levels of Notch1 in the nucleus of Rbpj mutant progenitor cells (**Figures 7E,F**). These findings were unexpected, because it has been believed that Rbpj deficiency ablates all canonical notch signaling pathways.

To further understand and possibly explain these findings, we assessed if non-canonical notch pathways are altered in $Rbpj^{Hem-KO}$ mice. First, we explored if NF-κB signaling is augmented in the absence of Rbpj, as signaling cross talks exist between notch and NF-κB pathways (Andersen et al., 2012; Ayaz and Osborne, 2014). Real-time PCR analysis indicated rather reduced expression levels of NF-κB target genes, such as *NF-κB1α, NF-κB2, Rela,* and *Relb*, even though expression levels of *NF-κB1ε* was elevated, in Rbpj mutant progenitor cells (**Figure 7G**). Next, we tested if expression levels of Hypoxia inducible factor (Hif) family members are altered in Rbpj mutant cells. Even though Hif proteins are implicated

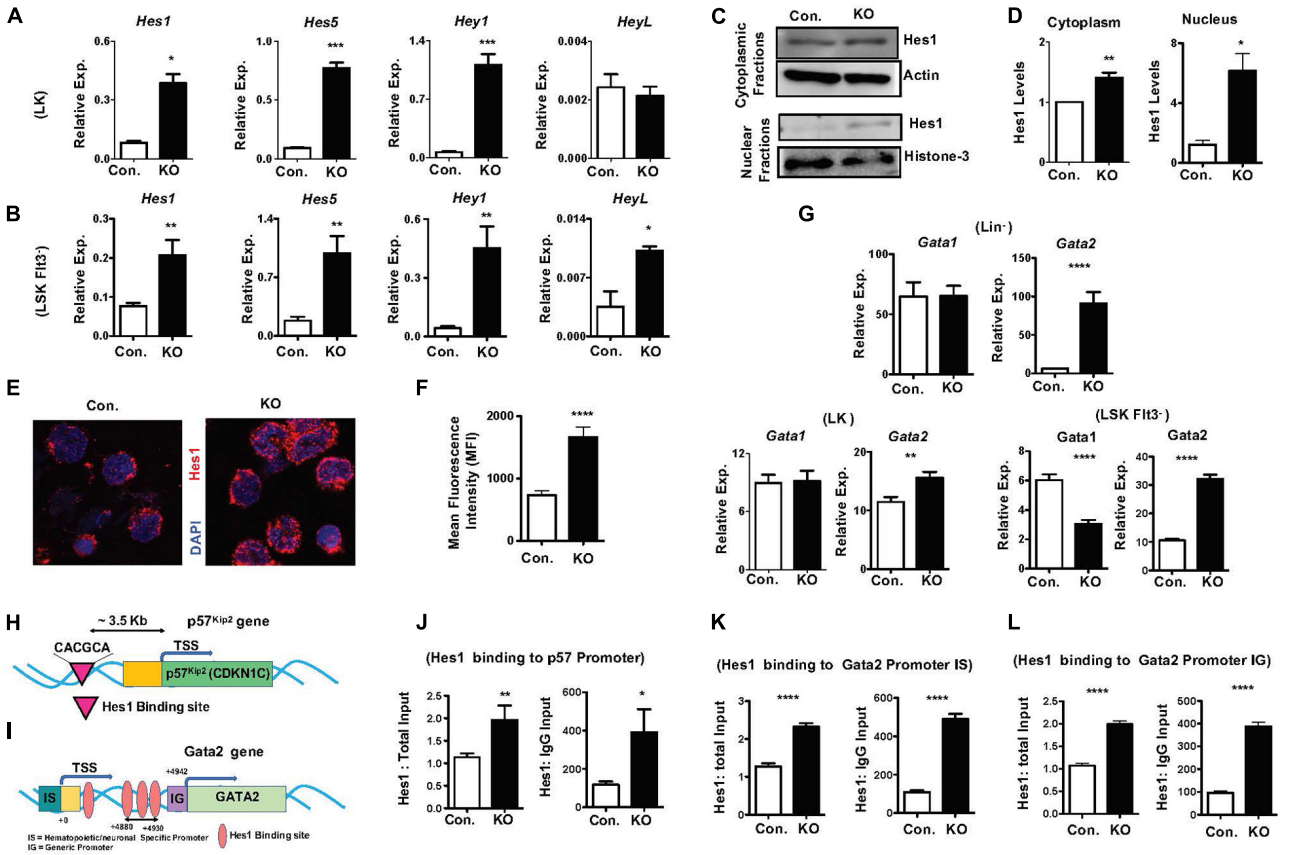

FIGURE 6 | Lack of Rbpj leads to augmented expression and activity of notch target genes. **(A,B)** Real time PCR analysis of notch target genes in purified LK **(A)** and Flt3$^-$LSK **(B)** cells of BM from KO and control mice. Expression levels were normalized to HPRT levels. Data are representative of three independent experiments. **(C)** Western blot analysis of Hes1 proteins in the cytoplasm and nucleus of Lin$^-$ BM cells of KO and control mice. Data are representative of three independent experiments. **(D)** Quantification of proteins from western blots shown in **(C)** cytoplasmic Hes1 protein levels were normalized to actin protein levels and nuclear Hes1 protein levels were normalized to Histone-3 protein levels in each lane, respectively. Data are pool of three independent experiments. **(E)** Representative immunofluorescence images of Hes1 and DAPI in purified Lin$^-$c-Kit$^+$ BM cells of KO and control mice. **(F)** Quantification of nuclear Hes1 levels from **(E)**. Data points include n = 30–40 individual cells from two independent experiments. **(G)** Real time PCR analysis of *Gata1* and *Gata2* mRNA levels in purified Lin$^-$, LK and Flt3$^-$LSK cells of BM from KO and control mice. Expression levels were normalized to HPRT levels. Data are representative of two independent experiments. **(H)** Diagrammatic representation of *p57^{Kip2}* gene indicating the presence of Hes1 binding site in the 5′ upstream of its promoter. **(I)** Diagrammatic representation of *Gata2* gene indicating the presence of four Hes1 binding sites in both hematopoietic/neuronal specific promoter (IS) and generic promoter (IG) regions of *Gata2*. **(J)** ChIP analysis of Hes1 binding to the regulatory regions of *p57^{Kip2}* in purified Lin$^-$ cells of BM from KO and control mice. Shown are the real-time PCR data of Hes1 immunoprecipitates, which were normalized to either total input (left) or IgG control (right) immunoprecipitates. Data are representative of two independent experiments. **(K,L)** ChIP analysis of Hes1 binding to the IS **(K)** and IG **(L)** promoter regions of *Gata2* in purified Lin$^-$ cells of BM from KO and control mice. Shown are the real-time PCR data of Hes1 immunoprecipitates, which were normalized to either total input (left) or IgG control (right) immunoprecipitates. Data are representative of two independent experiments. All data represent mean SEM. Two-tailed Student's *t*-tests were used to assess statistical significance (*$P < 0.05$; **$P < 0.01$; ***$P < 0.001$; ****$P < 0.0001$).

in non-canonical Notch pathways (Gustafsson et al., 2005; Johnson, 2011; Mukherjee et al., 2011; Hu et al., 2014), it remained totally unknown if Hif proteins mediated non-canonical notch pathway plays any functions in hematopoiesis, particularly in HSPCs. Our gene expression studies documented an upregulation of *Hif1α* and *Hif2α* mRNA, downregulation of *Hif1β* and normal expression of *Hif3α* mRNA in Rbpj deficient progenitor cells (**Figure 7H**). Consistently, confocal microscopy studies documented an increased presence of Hif1α and Hif2α proteins in the nucleus of Rbpj deficient progenitor cells (**Figures 7I–L**). Despite increased expression of Hif1α and Hif2α, intracellular reactive oxygen species (ROS) levels in Rbpj mutant HSPCs remain normal (**Supplementary Figures 7A,B**), suggesting that the increased expression Hif1α and Hif2α are not in response to hypoxia. Finally, to determine the functional consequences of elevated levels of Hif proteins, we assessed if Hes1 is a direct transcriptional target of Hif1α in HSPCs. *In silico* studies suggested the presence of two Hif binding (HRE) sites (Zheng et al., 2017), one in the promoter and the other in the 5′ regulatory region, of *Hes1* gene (**Figure 7M**). ChIP assays documented an elevated Hif1α binding to both proximal and distal Hypoxia Responsive Element (HRE) sites of *Hes1* (**Figures 7N,O**) in BM progenitor cells. Taken together, these studies documented that Rbpj deficiency

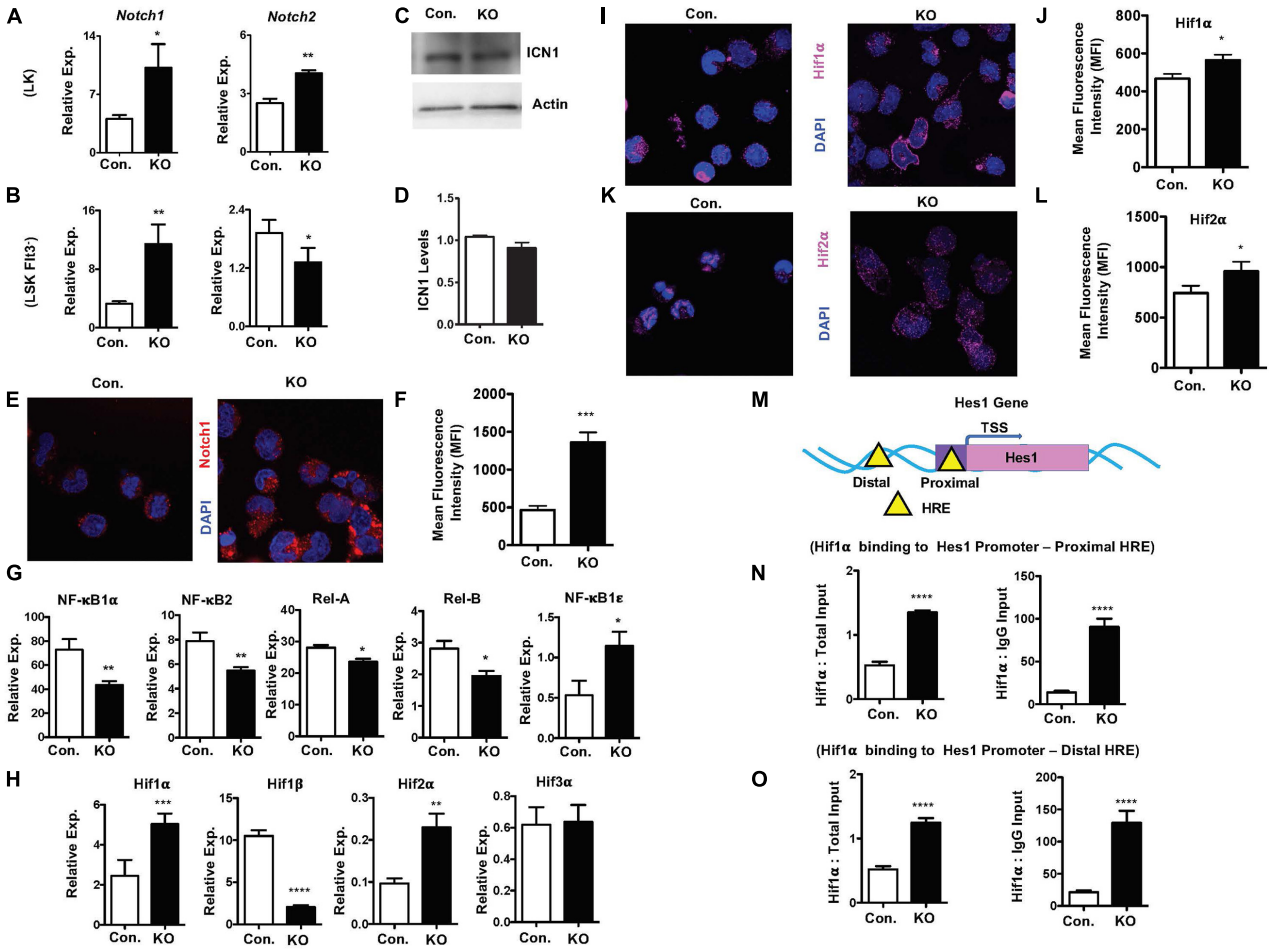

FIGURE 7 | Rbpj loss results in elevated Hif expression and functions. **(A,B)** Real time PCR analysis of *notch1* and *notch2* mRNA expression in purified LK **(A)** and Flt3$^-$LSK **(B)** cells of the BM from KO and control mice. Expression levels were normalized to HPRT levels. Data are representative of three independent experiments. **(C)** Western blot analysis of Notch1 protein in Lin$^-$ BM cells of KO and control mice. Data are representative of three independent experiments. **(D)** Quantification of proteins from western blots shown in **(C)**. Notch1 protein levels were normalized to actin protein levels in each lane, respectively. Data are pool of two independent experiments. **(E)** Representative immunofluorescence images of Notch1 and DAPI in purified Lin$^-$ BM cells of KO and control mice. **(F)** Quantification of nuclear Notch levels from **(E)**. Data points include $n = 30$ individual cells from two independent experiments. **(G)** Real time PCR analysis of NF-κB target genes in purified Lin$^-$ BM cells from KO and control mice. Expression levels were normalized to HPRT levels. Data are representative of three independent experiments. **(H)** Real time PCR analysis of *Hif1α*, *Hif2α*, *Hif3α*, and *Hif1β* target genes in purified Lin$^-$ BM cells from KO and control mice. Expression levels were normalized to HPRT levels. Data are representative of three independent experiments. **(I,K)** Representative immunofluorescence images of Hif1α and DAPI **(I)** and Hif2α and DAPI **(K)** in purified Lin$^-$ BM cells of KO and control mice. **(J,L)** Quantification of nuclear Hif1α levels **(J)** from **(I)** and Hif2α levels **(L)** from **K**. Data points include $n = 60$ **(J)** and $n = 30$ **(L)** individual cells from two independent experiments. **(M)** Diagrammatic representation of *Hes1* gene indicating the presence of Hif binding HRE sites in both the promoter (proximal) and 5′ upstream (distal) regulatory regions. **(N,O)** ChIP analysis of Hif1α binding to the promoter **(N)** and 5′ upstream regulatory **(O)** regions of *Hes1* in purified Lin$^-$ cells of BM from KO and control mice. Shown are the real-time PCR data of Hif1α immunoprecipitates, which were normalized to either total input (left) or IgG control (right) immunoprecipitates. Data are representative of two independent experiments. All data represent mean ± SEM. Two-tailed Student's *t*-tests were used to assess statistical significance (*$P < 0.05$; **$P < 0.01$; ***$P < 0.001$; ****$P < 0.0001$).

leads to increased expression and functional activity of Hif proteins in HSPCs.

DISCUSSION

Functional relevance of Notch signaling in the maintenance of adult HSCs remains a controversial subject. *In vitro* studies based on overexpression of Notch receptors and treatment of HSCs with notch ligands have provided a compelling evidence on the positive role of notch in HSCs (Pui et al., 1999; Varnum-Finney et al., 2000; Stier et al., 2002; Duncan et al., 2005; Rathinam et al., 2006; Francis et al., 2017). On the other hand, studies mainly based on the loss-of-functions approach have concluded that notch signaling is dispensable for the maintenance and functions of adult HSCs (Mancini et al., 2005; Maillard et al., 2008; Varnum-Finney et al., 2011; Benveniste et al., 2014; Francis et al., 2017). Even though there appears to be an obvious disagreement regarding the functions of notch in HSCs, these differences are likely multifactorial and possible explanations for

these discrepancies could be as follows; (1) In view of the fact that are multiple notch receptors and their ligands in the mammalian system, it remains possible that deletion of an individual notch receptor/ligand can be compensated by the other notch receptors. Indeed, multiple notch receptors; Notch1 (Varnum-Finney et al., 2000; Rathinam et al., 2006), Notch2 (Varnum-Finney et al., 2011; Wang et al., 2017) and Notch4 (Vercauteren and Sutherland, 2004) have been shown to play roles in HSCs and hematopoiesis, (2) To overcome the possible functional redundancies amongst notch receptors/ligand, studies were conducted based on global ablation of notch signals, through either retroviral mediated overexpression/genetic activation of dnMAML (Maillard et al., 2008; Benveniste et al., 2014; Francis et al., 2017) or genetic ablation of Rbpj (Maillard et al., 2008). Data of these studies have suggested a dispensable role for notch in HSCs. While inhibiting MAML and Rbpj can efficiently block canonical notch pathways, mounting evidences suggest an existence of Rbpj independent functions of notch pathway (Turkoz et al., 2016), and (3) Notch signaling is controlled at multiple levels and through various mechanisms. Even though deletion of individual notch receptors did not affect adult HSC maintenance or functions, conditional loss of O-fucosylglycans on Notch EGF-like repeats, which results in defective binding of all Notch ligands, in adult HSCs caused reduced pool size, loss of quiescence, altered niche distribution and increased mobilization of HSPCs (Wang et al., 2017). In the present study we document that loss of canonical notch pathway leads to reduced capacities of HSCs to differentiate into lymphoid-primed multipotent progenitors. Even though both long-term and short-term HSC pool was largely normal in Rbpj mutant mice under steady state conditions, their functions are severely compromised in response to radiation and chemotherapy induced hematopoietic stress. Interestingly, earlier studies by Duarte et al. (2018) concluded that canonical notch signals are dispensable for adult steady-state and stress myelo-erythropoiesis. In contrast, data obtained from our studies unequivocally demonstrate that Rbpj mediated canonical notch signaling is critical for stress-induced hematopoiesis. Even though the conclusions of our studies and of Daurte *et al.* were based on Rbpj conditional KO mice, the Cre-deleter strains used in these two studies are completely different. Daurte et al. conducted most of their studies, including their BM transplantation experiments, using Mx1-cre deleter strain. However, it has become apparent in the recent years that Mx1-cre based deletion of transgenes has some potential pitfalls (Velasco-Hernandez et al., 2016). More importantly, in view of the fact that injection of poly I:C, necessary to induce expression of Cre in Mx1-Cre mouse strain, activates the interferon system and that interferons alter hematopoiesis and HSC physiology (Essers et al., 2009; Passegue and Ernst, 2009), it is unclear to what extent the studies and conclusion of Daurte et al. were influenced by the interferon mediated "effects". To overcome these technical hurdles, in the present study we genetically ablated Rbpj signals using Vav-cre deleter strain and this strategy allowed us to constitutively ablate canonical notch signals in all hematopoietic cells from embryo throughout adulthood. Moreover, Duarte et al. (2018) particularly focused on stress erythropoiesis, mediated by Phenyl-hydrazine (PHZ), and concluded that Rbpj has a dispensable role in their model. In contrast, we studied global stress responses of HSCs, induced by 5-Fluorouracil (5-FU), and our data identified that Rbpj has an indispensable role in HSC mediated stress response. Taken together, these studies warrant a need for careful interpretation of data on notch functions in HSCs and for thorough research, involving additional and more sophisticated models to ablate global notch signals.

Mounting evidences document the existence of RBPJ independent non-canonical Notch signaling pathways (Andersen et al., 2012; Ayaz and Osborne, 2014). Intriguingly, most often non-canonical notch signals are associated with pathological conditions, including myeloproliferative disorders (Wang et al., 2014) human myeloid leukemia (Liao et al., 2007) and T cell leukemia (Ayaz and Osborne, 2014). While these studies established the significance of non-canonical notch signals in pathophysiology, to date nothing is known about their roles and downstream molecular consequences in HSCs. Our data on Rbpj deficient mice, for the first time, suggest that loss of canonical notch pathway in HSPCs, leads to activation of Hif1α mediated regulation of notch targets. Earlier studies documented an interesting role for Hifα proteins in the activation of non-canonical notch pathways. According to our current understanding, Hif proteins physically interact with notch receptors and colocalized in endocytic vesicles (Johnson, 2011; Mukherjee et al., 2011). This interaction causes ligand independent cleavage of ICD of notch from the cell membrane and stabilization of Hifα proteins (Johnson, 2011; Mukherjee et al., 2011) and causes transcriptional activation of notch target genes in the nucleus, including *Hes1* (Gustafsson et al., 2005; Pistollato et al., 2010; Zheng et al., 2017). Non-canonical notch activation by Hifα has been reported to exist in cells under both normoxic and hypoxic conditions, and pathological states (Gustafsson et al., 2005; Pistollato et al., 2010; Hu et al., 2014; Zheng et al., 2017). Even though Rbpj has been identified as the key and major component of the notch induced transcriptional activation complex, Hifα/notch mediated transcriptional activation of notch target genes is independent of Rbpj (Gustafsson et al., 2005; Pistollato et al., 2010; Hu et al., 2014; Zheng et al., 2017). Furthermore, earlier studies identified that Rbpj physically interacts with Hif proteins and suppresses Hif activity under steady state conditions (Diaz-Trelles et al., 2016). Consistent with these observations, data from our current study document that Rbpj deficiency causes an augmented Hifα activity in hematopoietic progenitor cells. Based on these studies, and our current findings, it is tempting to hypothesize that loss of Rbpj leads to defective suppression of Hif activity, which in results in exaggerated non-canonical activation of notch pathways in hematopoietic cells. We believe that exaggerated Hif activity may compensate for the loss of canonical notch signals under steady state conditions. However, this compensatory role by Hif1α is insufficient for initiating effective stress induced-hematopoietic recovery. In addition, it is currently unclear to what extent Hif1α compensates for the loss of Rbpj signals. Even though more studies are necessary for understanding the molecular interactions and targets of Hif1α in these settings, our data document the existence and highlight

the functions of Hif1α mediated non-canonical notch signaling pathways in HSCs.

Even though our mechanistic studies provide novel insights and rationale as how and why loss of canonical notch signals might result in normal hematopoiesis (under steady state hematopoiesis), we believe that additional mechanisms might be involved in the phenotype of Rbpj mutant HSCs. More thorough investigations, particularly, focused on Rbpj/Notch dependent and independent (but Hif1α dependent) activation of Hes1 might be necessary for understanding the complex roles played by notch signaling pathways in HSPCs.

DATA AVAILABILITY STATEMENT

The raw data supporting the conclusions of this article will be made available by the authors, without undue reservation.

ETHICS STATEMENT

The animal study was reviewed and approved by the Institutional Animal Care and Use Committee.

AUTHOR CONTRIBUTIONS

RL performed experiments, collected the data, and analyzed the data. CR designed and performed research, analyzed and interpreted the data, and wrote and corrected the manuscript. Both authors contributed to the article and approved the submitted version.

FUNDING

This work was supported by grants from the NHLBI HL132194 (CR).

SUPPLEMENTARY MATERIAL

The Supplementary Material for this article can be found online at: https://www.frontiersin.org/articles/10.3389/fcell.2020.622190/full#supplementary-material

REFERENCES

Andersen, P., Uosaki, H., Shenje, L. T., and Kwon, C. (2012). Non-canonical Notch signaling: emerging role and mechanism. *Trends Cell Biol.* 22, 257–265. doi: 10.1016/j.tcb.2012.02.003

Ayaz, F., and Osborne, B. A. (2014). Non-canonical notch signaling in cancer and immunity. *Front. Oncol.* 4:345. doi: 10.3389/fonc.2014.00345

Benveniste, P., Serra, P., Dervovic, D., Herer, E., Knowles, G., Mohtashami, M., et al. (2014). Notch signals are required for in vitro but not in vivo maintenance of human hematopoietic stem cells and delay the appearance of multipotent progenitors. *Blood* 123, 1167–1177. doi: 10.1182/blood-2013-07-505099

Bigas, A., and Espinosa, L. (2012). Hematopoietic stem cells: to be or Notch to be. *Blood* 119, 3226–3235. doi: 10.1182/blood-2011-10-355826

Bray, S. J. (2016). Notch signalling in context. *Nat. Rev. Mol. Cell Biol.* 17, 722–735. doi: 10.1038/nrm.2016.94

Caton, M. L., Smith-Raska, M. R., and Reizis, B. (2007). Notch-RBP-J signaling controls the homeostasis of CD8- dendritic cells in the spleen. *J. Exp. Med.* 204, 1653–1664. doi: 10.1084/jem.20062648

Chen, E. L. Y., Thompson, P. K., and Zuniga-Pflucker, J. C. (2019). RBPJ-dependent Notch signaling initiates the T cell program in a subset of thymus-seeding progenitors. *Nat. Immunol.* 20, 1456–1468. doi: 10.1038/s41590-019-0518-7

Diaz-Trelles, R., Scimia, M. C., Bushway, P., Tran, D., Monosov, A., Monosov, E., et al. (2016). Notch-independent RBPJ controls angiogenesis in the adult heart. *Nat. Commun.* 7:12088.

Duarte, S., Woll, P. S., Buza-Vidas, N., Chin, D. W. L., Boukarabila, H., Luis, T. C., et al. (2018). Canonical Notch signaling is dispensable for adult steady-state and stress myelo-erythropoiesis. *Blood* 131, 1712–1719. doi: 10.1182/blood-2017-06-788505

Duncan, A. W., Rattis, F. M., Dimascio, L. N., Congdon, K. L., Pazianos, G., Zhao, C., et al. (2005). Integration of Notch and Wnt signaling in hematopoietic stem cell maintenance. *Nat. Immunol.* 6, 314–322. doi: 10.1038/ni1164

Essers, M. A., Offner, S., Blanco-Bose, W. E., Waibler, Z., Kalinke, U., Duchosal, M. A., et al. (2009). IFNalpha activates dormant haematopoietic stem cells in vivo. *Nature* 458, 904–908. doi: 10.1038/nature07815

Francis, O. L., Chaudhry, K. K., Lamprecht, T., and Klco, J. M. (2017). Impact of notch disruption on myeloid development. *Blood Cancer J.* 7:e598. doi: 10.1038/bcj.2017.73

Gerhardt, D. M., Pajcini, K. V., D'altri, T., Tu, L., Jain, R., Xu, L., et al. (2014). The Notch1 transcriptional activation domain is required for development and reveals a novel role for Notch1 signaling in fetal hematopoietic stem cells. *Genes Dev.* 28, 576–593. doi: 10.1101/gad.227496.113

Gordon, W. R., Arnett, K. L., and Blacklow, S. C. (2008). The molecular logic of Notch signaling–a structural and biochemical perspective. *J. Cell Sci.* 121, 3109–3119. doi: 10.1242/jcs.035683

Guiu, J., Shimizu, R., D'altri, T., Fraser, S. T., Hatakeyama, J., Bresnick, E. H., et al. (2013). Hes repressors are essential regulators of hematopoietic stem cell development downstream of Notch signaling. *J. Exp. Med.* 210, 71–84. doi: 10.1084/jem.20120993

Gustafsson, M. V., Zheng, X., Pereira, T., Gradin, K., Jin, S., Lundkvist, J., et al. (2005). Hypoxia requires notch signaling to maintain the undifferentiated cell state. *Dev. Cell* 9, 617–628. doi: 10.1016/j.devcel.2005.09.010

Han, H., Tanigaki, K., Yamamoto, N., Kuroda, K., Yoshimoto, M., Nakahata, T., et al. (2002). Inducible gene knockout of transcription factor recombination signal binding protein-J reveals its essential role in T versus B lineage decision. *Int. Immunol.* 14, 637–645. doi: 10.1093/intimm/dxf030

Hu, Y. Y., Fu, L. A., Li, S. Z., Chen, Y., Li, J. C., Han, J., et al. (2014). Hif-1alpha and Hif-2alpha differentially regulate Notch signaling through competitive interaction with the intracellular domain of Notch receptors in glioma stem cells. *Cancer Lett.* 349, 67–76. doi: 10.1016/j.canlet.2014.03.035

Johnson, E. A. (2011). HIF takes it up a notch. *Sci. Signal.* 4:e33.

Kirkling, M. E., Cytlak, U., Lau, C. M., Lewis, K. L., Resteu, A., Khodadadi-Jamayran, A., et al. (2018). Notch signaling facilitates in vitro generation of cross-presenting classical dendritic cells. *Cell Rep.* 23, 3658.e6–3672.e6.

Kopan, R., and Ilagan, M. X. (2009). The canonical Notch signaling pathway: unfolding the activation mechanism. *Cell* 137, 216–233. doi: 10.1016/j.cell.2009.03.045

Kumano, K., Chiba, S., Kunisato, A., Sata, M., Saito, T., Nakagami-Yamaguchi, E., et al. (2003). Notch1 but not Notch2 is essential for generating hematopoietic stem cells from endothelial cells. *Immunity* 18, 699–711. doi: 10.1016/s1074-7613(03)00117-1

Liao, W. R., Hsieh, R. H., Hsu, K. W., Wu, M. Z., Tseng, M. J., Mai, R. T., et al. (2007). The CBF1-independent Notch1 signal pathway activates human c-myc expression partially via transcription factor YY1. *Carcinogenesis* 28, 1867–1876. doi: 10.1093/carcin/bgm092

Lobry, C., Oh, P., Mansour, M. R., Look, A. T., and Aifantis, I. (2014). Notch signaling: switching an oncogene to a tumor suppressor. *Blood* 123, 2451–2459. doi: 10.1182/blood-2013-08-355818

Maillard, I., Koch, U., Dumortier, A., Shestova, O., Xu, L., Sai, H., et al. (2008). Canonical notch signaling is dispensable for the maintenance of adult

hematopoietic stem cells. *Cell Stem Cell* 2, 356–366. doi: 10.1016/j.stem.2008.02.011

Mancini, S. J., Mantei, N., Dumortier, A., Suter, U., Macdonald, H. R., and Radtke, F. (2005). Jagged1-dependent Notch signaling is dispensable for hematopoietic stem cell self-renewal and differentiation. *Blood* 105, 2340–2342. doi: 10.1182/blood-2004-08-3207

Matsumoto, A., Takeishi, S., Kanie, T., Susaki, E., Onoyama, I., Tateishi, Y., et al. (2011). p57 is required for quiescence and maintenance of adult hematopoietic stem cells. *Cell Stem Cell* 9, 262–271. doi: 10.1016/j.stem.2011.06.014

Mccloy, R. A., Rogers, S., Caldon, C. E., Lorca, T., Castro, A., and Burgess, A. (2014). Partial inhibition of Cdk1 in G 2 phase overrides the SAC and decouples mitotic events. *Cell Cycle* 13, 1400–1412. doi: 10.4161/cc.28401

Mercher, T., Cornejo, M. G., Sears, C., Kindler, T., Moore, S. A., Maillard, I., et al. (2008). Notch signaling specifies megakaryocyte development from hematopoietic stem cells. *Cell Stem Cell* 3, 314–326. doi: 10.1016/j.stem.2008.07.010

Mukherjee, T., Kim, W. S., Mandal, L., and Banerjee, U. (2011). Interaction between Notch and Hif-alpha in development and survival of *Drosophila* blood cells. *Science* 332, 1210–1213. doi: 10.1126/science.1199643

Nandakumar, S. K., Johnson, K., Throm, S. L., Pestina, T. I., Neale, G., and Persons, D. A. (2015). Low-level GATA2 overexpression promotes myeloid progenitor self-renewal and blocks lymphoid differentiation in mice. *Exp. Hematol.* 43, .565–577.e1–10.

Oguro, H., Ding, L., and Morrison, S. J. (2013). SLAM family markers resolve functionally distinct subpopulations of hematopoietic stem cells and multipotent progenitors. *Cell Stem Cell* 13, 102–116. doi: 10.1016/j.stem.2013.05.014

Oh, P., Lobry, C., Gao, J., Tikhonova, A., Loizou, E., Manet, J., et al. (2013). In vivo mapping of notch pathway activity in normal and stress hematopoiesis. *Cell Stem Cell* 13, 190–204. doi: 10.1016/j.stem.2013.05.015

Pajcini, K. V., Speck, N. A., and Pear, W. S. (2011). Notch signaling in mammalian hematopoietic stem cells. *Leukemia* 25, 1525–1532. doi: 10.1038/leu.2011.127

Passegue, E., and Ernst, P. (2009). IFN-alpha wakes up sleeping hematopoietic stem cells. *Nat. Med.* 15, 612–613. doi: 10.1038/nm0609-612

Pietras, E. M., Warr, M. R., and Passegue, E. (2011). Cell cycle regulation in hematopoietic stem cells. *J. Cell Biol.* 195, 709–720.

Pistollato, F., Rampazzo, E., Persano, L., Abbadi, S., Frasson, C., Denaro, L., et al. (2010). Interaction of hypoxia-inducible factor-1alpha and Notch signaling regulates medulloblastoma precursor proliferation and fate. *Stem Cells* 28, 1918–1929. doi: 10.1002/stem.518

Pui, J. C., Allman, D., Xu, L., Derocco, S., Karnell, F. G., Bakkour, S., et al. (1999). Notch1 expression in early lymphopoiesis influences B versus T lineage determination. *Immunity* 11, 299–308. doi: 10.1016/s1074-7613(00)80105-3

Radtke, F., Fasnacht, N., and Macdonald, H. R. (2010). Notch signaling in the immune system. *Immunity* 32, 14–27. doi: 10.1016/j.immuni.2010.01.004

Rathinam, C., Matesic, L. E., and Flavell, R. A. (2011). The E3 ligase Itch is a negative regulator of the homeostasis and function of hematopoietic stem cells. *Nat. Immunol.* 12, 399–407. doi: 10.1038/ni.2021

Rathinam, C., Sauer, M., Ghosh, A., Rudolph, C., Hegazy, A., Schlegelberger, B., et al. (2006). Generation and characterization of a novel hematopoietic progenitor cell line with DC differentiation potential. *Leukemia* 20, 870–876. doi: 10.1038/sj.leu.2404157

Robert-Moreno, A., Espinosa, L., De La Pompa, J. L., and Bigas, A. (2005). RBPjkappa-dependent Notch function regulates Gata2 and is essential for the formation of intra-embryonic hematopoietic cells. *Development* 132, 1117–1126. doi: 10.1242/dev.01660

Stier, S., Cheng, T., Dombkowski, D., Carlesso, N., and Scadden, D. T. (2002). Notch1 activation increases hematopoietic stem cell self-renewal in vivo and favors lymphoid over myeloid lineage outcome. *Blood* 99, 2369–2378. doi: 10.1182/blood.v99.7.2369

Takizawa, H., Boettcher, S., and Manz, M. G. (2012). Demand-adapted regulation of early hematopoiesis in infection and inflammation. *Blood* 119, 2991–3002. doi: 10.1182/blood-2011-12-380113

Tipping, A. J., Pina, C., Castor, A., Hong, D., Rodrigues, N. P., Lazzari, L., et al. (2009). High GATA-2 expression inhibits human hematopoietic stem and progenitor cell function by effects on cell cycle. *Blood* 113, 2661–2672. doi: 10.1182/blood-2008-06-161117

Turkoz, M., Townsend, R. R., and Kopan, R. (2016). The notch intracellular domain has an rbpj-independent role during mouse hair follicular development. *J. Invest. Dermatol.* 136, 1106–1115. doi: 10.1016/j.jid.2016.02.018

Van Zant, G. (1984). Studies of hematopoietic stem cells spared by 5-fluorouracil. *J. Exp. Med.* 159, 679–690. doi: 10.1084/jem.159.3.679

Varnum-Finney, B., Halasz, L. M., Sun, M., Gridley, T., Radtke, F., and Bernstein, I. D. (2011). Notch2 governs the rate of generation of mouse long- and short-term repopulating stem cells. *J. Clin. Invest.* 121, 1207–1216. doi: 10.1172/jci43868

Varnum-Finney, B., Xu, L., Brashem-Stein, C., Nourigat, C., Flowers, D., Bakkour, S., et al. (2000). Pluripotent, cytokine-dependent, hematopoietic stem cells are immortalized by constitutive Notch1 signaling. *Nat. Med.* 6, 1278–1281. doi: 10.1038/81390

Velasco-Hernandez, T., Sawen, P., Bryder, D., and Cammenga, J. (2016). Potential pitfalls of the Mx1-Cre system: implications for experimental modeling of normal and malignant hematopoiesis. *Stem Cell Rep.* 7, 11–18. doi: 10.1016/j.stemcr.2016.06.002

Vercauteren, S. M., and Sutherland, H. J. (2004). Constitutively active Notch4 promotes early human hematopoietic progenitor cell maintenance while inhibiting differentiation and causes lymphoid abnormalities in vivo. *Blood* 104, 2315–2322. doi: 10.1182/blood-2004-01-0204

Wang, L., Zhang, H., Rodriguez, S., Cao, L., Parish, J., Mumaw, C., et al. (2014). Notch-dependent repression of miR-155 in the bone marrow niche regulates hematopoiesis in an NF-kappaB-dependent manner. *Cell Stem Cell* 15, 51–65. doi: 10.1016/j.stem.2014.04.021

Wang, W., Yu, S., Myers, J., Wang, Y., Xin, W. W., Albakri, M., et al. (2017). Notch2 blockade enhances hematopoietic stem cell mobilization and homing. *Haematologica* 102, 1785–1795. doi: 10.3324/haematol.2017.168674

Wang, Y. C., He, F., Feng, F., Liu, X. W., Dong, G. Y., Qin, H. Y., et al. (2010). Notch signaling determines the M1 versus M2 polarization of macrophages in antitumor immune responses. *Cancer Res.* 70, 4840–4849. doi: 10.1158/0008-5472.can-10-0269

Wilson, A., Laurenti, E., Oser, G., Van Der Wath, R. C., Blanco-Bose, W., Jaworski, M., et al. (2008). Hematopoietic stem cells reversibly switch from dormancy to self-renewal during homeostasis and repair. *Cell* 135, 1118–1129. doi: 10.1016/j.cell.2008.10.048

Wilson, A., Macdonald, H. R., and Radtke, F. (2001). Notch 1-deficient common lymphoid precursors adopt a B cell fate in the thymus. *J. Exp. Med.* 194, 1003–1012. doi: 10.1084/jem.194.7.1003

Yang, L., Bryder, D., Adolfsson, J., Nygren, J., Mansson, R., Sigvardsson, M., et al. (2005). Identification of Lin(-)Sca1(+)kit(+)CD34(+)Flt3- short-term hematopoietic stem cells capable of rapidly reconstituting and rescuing myeloablated transplant recipients. *Blood* 105, 2717–2723. doi: 10.1182/blood-2004-06-2159

Zhao, J. L., and Baltimore, D. (2015). Regulation of stress-induced hematopoiesis. *Curr. Opin. Hematol.* 22, 286–292. doi: 10.1097/moh.0000000000000149

Zheng, X., Narayanan, S., Zheng, X., Luecke-Johansson, S., Gradin, K., Catrina, S. B., et al. (2017). A Notch-independent mechanism contributes to the induction of Hes1 gene expression in response to hypoxia in P19 cells. *Exp. Cell Res.* 358, 129–139. doi: 10.1016/j.yexcr.2017.06.006

Zou, P., Yoshihara, H., Hosokawa, K., Tai, I., Shinmyozu, K., Tsukahara, F., et al. (2011). p57(Kip2) and p27(Kip1) cooperate to maintain hematopoietic stem cell quiescence through interactions with Hsc70. *Cell Stem Cell* 9, 247–261. doi: 10.1016/j.stem.2011.07.003

Conflict of Interest: The authors declare that the research was conducted in the absence of any commercial or financial relationships that could be construed as a potential conflict of interest.

The reviewer, MN, declared a past co-authorship with one of the authors, CR, to the handling editor.

frontiers in Cell and Developmental Biology

BRIEF RESEARCH REPORT
published: 30 April 2021
doi: 10.3389/fcell.2021.670654

Mutation of Gemin5 Causes Defective Hematopoietic Stem/Progenitor Cells Proliferation in Zebrafish Embryonic Hematopoiesis

Xiaofen Liu[1], Wenjuan Zhang[2], Changbin Jing[2], Lei Gao[2], Cong Fu[2], Chunguang Ren[2], Yimei Hao[2], Mengye Cao[2], Ke Ma[2,3], Weijun Pan[1,2]* and Dantong Li[1,2]**

[1] Shanghai Jiao Tong University School of Medicine, Shanghai, China, [2] Shanghai Institute of Nutrition and Health, Chinese Academy of Sciences, Shanghai, China, [3] Clinical Research and Translation Center, The First Affiliated Hospital of Fujian Medical University, Fujian, China

OPEN ACCESS

Edited by:
Yiyue Zhang,
South China University of Technology, China

Reviewed by:
Mugen Liu,
Huazhong University of Science and Technology, China
Zilong Wen,
Hong Kong University of Science and Technology, Hong Kong

***Correspondence:**
Ke Ma
MKE2002@163.com
Weijun Pan
weijunpan@sibs.ac.cn
Dantong Li
dtli@sibs.ac.cn

Specialty section:
This article was submitted to Stem Cell Research, a section of the journal Frontiers in Cell and Developmental Biology

Received: 22 February 2021
Accepted: 13 April 2021
Published: 30 April 2021

Citation:
Liu X, Zhang W, Jing C, Gao L, Fu C, Ren C, Hao Y, Cao M, Ma K, Pan W and Li D (2021) Mutation of Gemin5 Causes Defective Hematopoietic Stem/Progenitor Cells Proliferation in Zebrafish Embryonic Hematopoiesis. Front. Cell Dev. Biol. 9:670654. doi: 10.3389/fcell.2021.670654

Fate determination and expansion of Hematopoietic Stem and Progenitor Cells (HSPCs) is tightly regulated on both transcriptional and post-transcriptional level. Although transcriptional regulation of HSPCs have achieved a lot of advances, its post-transcriptional regulation remains largely underexplored. The small size and high fecundity of zebrafish makes it extraordinarily suitable to explore novel genes playing key roles in definitive hematopoiesis by large-scale forward genetics screening. Here, we reported a novel zebrafish mutant line *gemin5*^{cas008} with a point mutation in *gemin5* gene obtained by ENU mutagenesis and genetic screening, causing an earlier stop codon next to the fifth WD repeat. Gemin5 is an RNA-binding protein with multifunction in post-transcriptional regulation, such as regulating the biogenesis of snRNPs, alternative splicing, stress response, and translation control. The mutants displayed specific deficiency in definitive hematopoiesis without obvious defects during primitive hematopoiesis. Further analysis showed the impaired definitive hematopoiesis was due to defective proliferation of HSPCs. Overall, our results indicate that Gemin5 performs an essential role in regulating HSPCs proliferation.

Keywords: Gemin5, Hematopoietic stem/progenitor cells, cell proliferation, zebrafish, definitive hematopoiesis, forward genetic screening, positional cloning

INTRODUCTION

In vertebrates, embryonic development of blood system involves two waves of hematopoiesis: the primitive hematopoiesis and the definitive hematopoiesis. In definitive wave, the fate of Hematopoietic Stem and Progenitor Cells (HSPCs) is determined in the aorta-gonad-mesonephros (AGM) region, and then generating all blood lineages throughout the life (Galloway and Zon, 2003). Ontogeny from HSPCs fate determination to expansion and then terminal differentiation of types of blood cells requires an orchestrated regulation of transcriptional networks and signaling pathways, however, its underlying mechanism remains largely unknown.

Recently, zebrafish as a wonderful vertebrate model system, has become popular in hematopoiesis research. With high fecundity and small size, zebrafish extremely suits large-scale forward genetics screening (Gao et al., 2015). Taking the benefit of the external fertilization, we

can observe and manipulate on zebrafish embryos as early as the one-cell stage. In addition, definitive hematopoiesis is highly conserved between zebrafish and mammals (Song et al., 2004; Gore et al., 2018). In zebrafish, HSPCs emerge from the ventral wall of the dorsal aorta, equals to the AGM in mammals, through endothelium to hematopoietic transition (Kissa and Herbomel, 2010). Then they migrate and colonize in the caudal hematopoietic tissue (CHT), which is similar to mammalian fetal liver, for HSPCs rapid expansion and the differentiation of erythroid and myeloid cells (Ciau-Uitz et al., 2014). By 4 days post-fertilization (dpf), the HSPCs migrate to the kidney marrow, analogous to the bone marrow of mammals (Murayama et al., 2006). Although the main hematopoietic sites are different in zebrafish and mammals, both of them share the same major blood cell types arising from common hematopoietic lineages (Traver et al., 2003), which means findings of blood development in zebrafish could be translated to mammalian systems.

Normal function of HSPCs is sustained through an orchestrated regulation at transcriptional and post-transcriptional level. Major advances have been achieved in the understanding of transcriptional regulation of HSPCs; however, it remains underexplored for the post-transcriptional regulation. RNA-binding proteins (RBPs) take control of post-transcriptional regulation in hematopoiesis through modulating RNA properties including RNA splicing, localization, degradation, or translation (de Rooij et al., 2019). It has been reported RBPs have essential roles in regulating cell fate determination and cell proliferation in stem cell biology (Grech and von Lindern, 2012; de Rooij et al., 2019). Gemin5, an RBP with multidomain, consists of the *N*-terminal tryptophan-aspartic acid (WD) repeat domains, a dimerization domain in the middle, and a non-canonical RNA-binding domain in the *C*-terminal region (Martinez-Salas et al., 2020). Its WD repeat motifs recognize the small nuclear RNAs (snRNAs), allowing assembly of the survival of motor neurons (SMN) complex into small nuclear ribonucleoproteins (snRNPs; Pineiro et al., 2015; Martinez-Salas et al., 2020). Structure analyses show the dimerization module of Gemin5 acts a fundamental part in its architecture and essential for its activity (Martinez-Salas et al., 2020). The non-canonical RNA-binding domain allows Gemin5 to interact with its mRNA targets and play a key role in translation. Research on Gemin5 is emerging but far from enough to understand the consequence of its multifunction.

Since ENU-mutagenesis combined with forward genetic screening is a powerful approach to unbiasedly uncover novel genetic and molecular pathways, we conducted it in zebrafish model organism to dissect the sophisticated mechanisms of definitive hematopoiesis (Gao et al., 2015; Jia et al., 2015). We first generated mutants by mutagen ethylnitrosourea (ENU). Then we did whole mount *in situ* hybridization (WISH) on the embryos of F2 families with *myb* probe, a crucial marker and transcription factor of HSPCs. We obtained a new mutant *cas008* showing severe hematopoietic defects. Then we accomplished positional cloning and located the mutation in gene *gemin5*. Furthermore, we found abnormal definitive hematopoiesis was due to defective proliferation of HSPCs. To sum up, we reported a zebrafish mutant family carrying Gemin5 point mutation with severe definitive hematopoiesis defects due to HSPCs proliferation failure.

MATERIALS AND METHODS

Zebrafish Husbandry

The zebrafish facility and studies were approved by the Animal Research Advisory Committee of Shanghai Institute of Nutrition and Health, CAS. Zebrafish were kept in accordance with the guidelines of the Institutional Animal Care and Use Committee (Li et al., 2018).

The transgenic zebrafish line Tg(*myb*: eGFP; North et al., 2007) was described previously. For the forward genetics screen, Wild-type (WT) TU zebrafish line was treated with ENU, Sigma (Gao et al., 2015; Jia et al., 2015). For positional cloning, we first outcrossed heterozygous *mutant*^{cas008} in Tu background with wild-type in polymorphic WIK background and then mapped the *mutant*^{cas008} allele in Tu background as described previously (Bahary et al., 2004).

Mapping and Identification of Mutation in Zebrafish *cas008* Mutant

Based on the *myb* expression in zebrafish embryos at 5 dpf, the *mutant*^{cas008} line was identified among numerous ENU-mutagenized F2 families. We carried on the ENU screen and positional cloning as mentioned before (Bahary et al., 2004; Gao et al., 2015; Jia et al., 2015). By bulk segregation analysis with sequence length polymorphism (SSLP) markers, the mutation was first mapped to chromosome 21. To narrow down the genetic interval, fine mapping was performed and identified the mutation flanked by two SSLP markers, zK189O20 and zC153M12. Then, we cloned the cDNAs of candidate genes in the range and sequenced from siblings and mutants separately. Finally, we sequenced genomic DNA of individual mutant embryos to confirm the putative mutation.

Plasmid Construction and Microinjection

We cloned the zebrafish Gemin5 (accession number: ZDB-GENE-031112-9) and inserted it into the Tol2 backbone between the promoter UAS and p2A (primer F: atgcacgaaagacatctgcc; primer R: gtgtatgagtctcctcacag) (Schematic diagram in **Figure 2C**). For transient transgene, Tol2 transposase mRNA (40 pg) and the Gemin5 construct or Tol2 vector (40 pg) were microinjected into one-cell-stage embryos (Suster et al., 2009).

WISH, FISH, TUNEL Assay and Immunofluorescence Staining

The *myb*, *ae1-globin*, *lyz*, *mpx*, *rag1*, *gata1*, *pu.1,* and *kdrl* probe were transcribed by polymerase T3 or T7 (Ambion) with Digoxigenin RNA Labeling Mix (Roche) *in vitro* (Li et al., 2018). WISH was carried out as described before using NBT/BCIP (Sigma) as substrates. To detect HSPCs proliferation, we performed fluorescence whole mount *in situ* hybridization (FISH) and pH3 immunofluorescence double-staining as described previously (Gao et al., 2015; Jia et al., 2015).

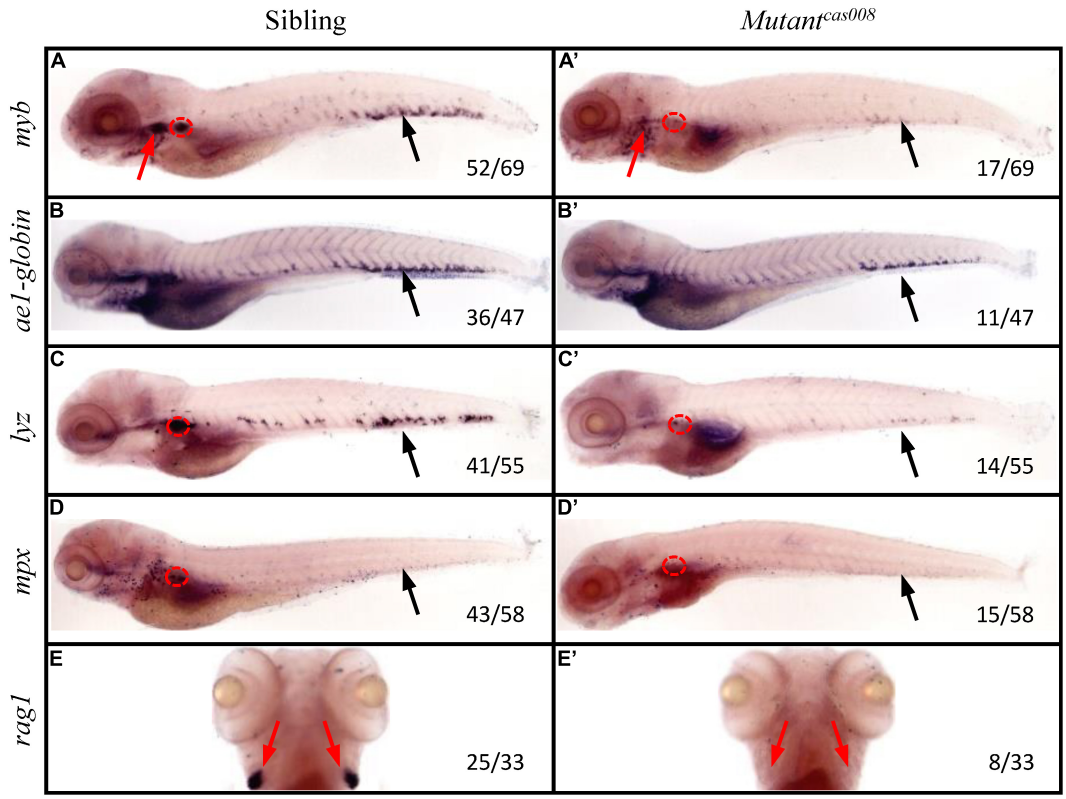

FIGURE 1 | The *mutant*^{cas008} line showed defective definitive hematopoiesis. WISH analysis of *myb* **(A,A')**, *ae1-globin* **(B,B')**, *lyz* **(C,C')**, *mpx* **(D,D')**, and *rag1* **(E,E')** expression in sibling **(A–E)** and *mutant*^{cas008} **(A'–E')** embryos at 5 dpf. The penetrance of the indicated phenotype is shown in the bottom right of each panel. Black arrows indicate the position of CHT, while red arrows and circles show the position of thymus and kidney, respectively.

We first stained embryos with cy3 (TSA system, Perkin Elmer), and used anti-pH3 (ser10) antibody (1:500; Santa Cruz) for pH3 immunofluorescence staining, and then imaged by Olympus FV1000 Fluoview scanning confocal microscope. With *in situ* Cell Death Detection Kit and TMR Red Kit (Roche), TUNEL assay was conducted according to manufacturer's instruction. Embryos in Tg(*myb*:eGFP) background were fixed with 4% PFA. After pretreatment, the embryos were stained at 37°C for 2 h using the TUNEL Kit (100 μl, enzyme: labeling solution = 1:9). Next, the immunostaining of eGFP was performed with incubation of anti-GFP (Rabbit, 1:500, Invitrogen) and secondary antibody goat-Alexa Fluore488-conjugated anti-rabbit (1:500, Invitrogen). Then, the embryos were imaged by confocal microscope Olympus FV1000 Fluoview scanning.

Imaging

Images of zebrafish immunofluorescence staining (**Figures 3A,B** and **Supplementary Figure 3A**) were taken by Olympus FV1000 Fluoview scanning confocal microscope. 1% low-melt agarose was used to mount the embryos. These confocal images were captured by UPLSAPO 20X objective. Scale bars, 50 μm.

Statistical Analysis

Data were analyzed with the two-tailed Student's *t*-test using the software Graphpad Prism 8. Error values in the plots were calculated by standard error of the mean (SEM). In this study, all data were repeated for at least twice.

RESULTS

Obtained Zebrafish *Mutant*^{cas008} Line in a Large-Scale Forward Genetics Screen

To explore novel genes which played essential roles in definitive hematopoiesis, we used zebrafish model organism to perform a large-scale forward genetics screen (Gao et al., 2015; Jia et al., 2015). First of all, we generated mutants by crossing zebrafish previously treated with ENU mutagen. Then we tested *myb* expression by WISH on the embryos of F2 families. As a key transcription factor and marker of HSPCs, *myb* was expressed in all hematopoietic tissues of sibling embryos at 5 dpf, including CHT, thymus and kidney tested by WISH (**Figure 1A**). While *mutant*^{cas008} displayed dramatically decreased *myb* expression in CHT, thymus and kidney suggesting defective definitive hematopoiesis (**Figure 1A'**). The cell marker of downstream hematopoietic lineages, including *ae1-globin* (erythrocyte marker), *lyz* (macrophage marker), *mpx* (granulocyte marker), and *rag1* (lymphocyte marker) were also examined. Comparing with siblings, *mutant*^{cas008} expressed

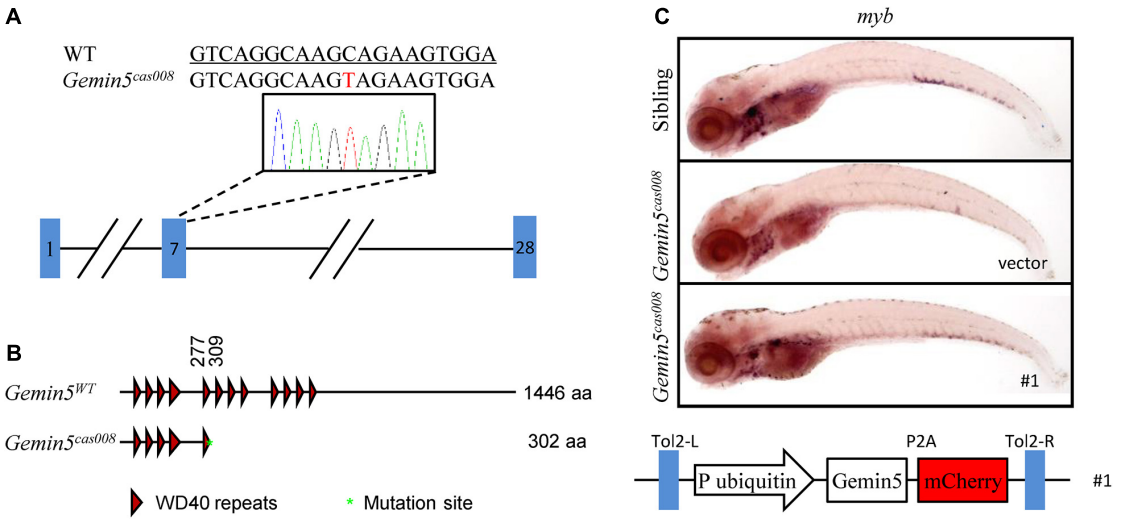

FIGURE 2 | The mutation was mapped to a point mutation in gene *gemin5*. **(A)** The alignment of WT (underlined) and NC_007132.7: g.36404684 C > T (*gemin5*^{008}) sequences are listed. The mutation by ENU is indicated in red (a C to T nonsense mutation causes an immediate stop codon in *gemin5* in *mutant*^{cas008}). **(B)** According to the stop codon in the genome, SMART software was used to predict the structure of Gemin5^{WT} and XP_001339880.4:p.Gln303_His1440del (Gemin5^{008}) presumed protein. The molecular sizes of the presumed protein are indicated on the right. **(C)** WISH analysis with *myb* probe in the CHT region (at 6 dpf) of sibling and *gemin5*^{008} with transient transgenesis of vector (only plasmid backbone) or ubi: gemin5 (#1, The construction of the plasmid is shown below).

decreased *ae1-globin* and barely expressed *lyz*, *mpx*, and *rag1* (**Figures 1B–E,B′–E′**). All these results showed definitive HSPCs in the CHT are severely disrupted and downstream differentiation of HSPCs were blocked in *mutant*^{cas008} embryos.

Furthermore, we tested the primitive hematopoiesis in *mutant*^{cas008} by WISH. The results showed the expression of primitive hematopoietic cell markers, including *gata1* (erythrocyte progenitor marker) and *pu.1* (myeloid progenitor marker; **Supplementary Figures 1A,B,A′,B′**) were identical between siblings and *mutant*^{cas008} at 22 hpf. As mentioned, in the developing dorsal aorta HSPCs emerge from endothelial cells during 33–54 hpf (Kissa and Herbomel, 2010), thus vascular morphogenesis is essential for HSPCs initiation and maintenance (Burns et al., 2009). The expression of the pan-endothelial cell marker *kdrl* at 26 hpf before HSPCs emergence was examined and it was intact in *mutant*^{cas008} as well (**Supplementary Figures 1C,C′**). We also examined the expression of *runx1* at 36 hpf, required for HSPCs emergence and showed no defects in *mutant*^{cas008} comparing with sibling embryos (**Supplementary Figures 1D,D′**). Taken together, we obtained *mutant*^{cas008} displayed specific deficiency in definitive hematopoiesis without obvious defects during primitive hematopoiesis, vasculogenesis and HSPCs emergence.

Positional Cloning

We carried out positional cloning to elucidate the mechanism underlying the hematopoietic failure in *mutant*^{cas008}. According to the previously reported procedure (Gao et al., 2015; Jia et al., 2015), by bulk segregation analysis (BSA) the mutation was first mapped to chromosome 21. Then a high-resolution mapping approach was performed and it identified the mutation was flanked by two linked SSLP markers, zK189O20 and zC153M12. There were four candidate genes in the flanked region (**Supplementary Figure 2A**). Among them, we identified a C to T nonsense mutation causing an immediate stop codon in *gemin5* in *mutant*^{cas008} by sequencing cDNA of the four genes (NC_007132.7: g.36404684 C > T, **Figure 2A**). Next, the result was verified by genomic sequencing. The earlier stop codon caused by this mutation was next to the end of the fifth WD repeats domain of Gemin5 protein (XP_001339880.4:p.Gln303_His1440del, **Figure 2B**). Hence, we changed the name of *mutant*^{cas008} into NC_007132.7: g.36404684 C > T, *gemin5*^{cas008} for short. To further confirm our results, we performed a rescue experiment by employing a Tol2 transposase-mediated transgenic approach to express wild-type (WT) *gemin5* gene in *gemin5*^{cas008} embryos. In the construction of transgenic plasmid, the ubiquitin promoter drove ubiquitous expression of wildtype *gemin5*, followed by P2A peptide-mCherry fusion protein to indicate transgenic efficiency (P2A peptide allows self-cleavage to avoid influencing Gemin5 function). This plasmid element was flanked by Tol2 arms (**Figure 2C**). After co-injection of the plasmid and Tol2 transposase mRNA into one-cell stage *gemin5*^{cas008} embryos, ubiquitous expression of wild-type *gemin5* could rescue *gemin5*^{cas008} phenotype to a large extend at 6 dpf (**Figure 2C**). Taken together, the nonsense mutation in *gemin5* caused the defective hematopoietic phenotypes in *gemin5*^{cas008}.

Gemin5, as an RBP with multidomain consists of the *N*-terminal WD repeat domains, a dimerization domain in the middle, and a non-canonical RNA-binding domain in the *C*-terminal region (Martinez-Salas et al., 2020). Its WD repeat motifs recognize the snRNAs, allowing assembly of the SMN complex into snRNPs (Pineiro et al., 2015; Martinez-Salas et al., 2020). Structure analyses show the dimerization module of Gemin5 is fundamental for its architecture and plays an essential

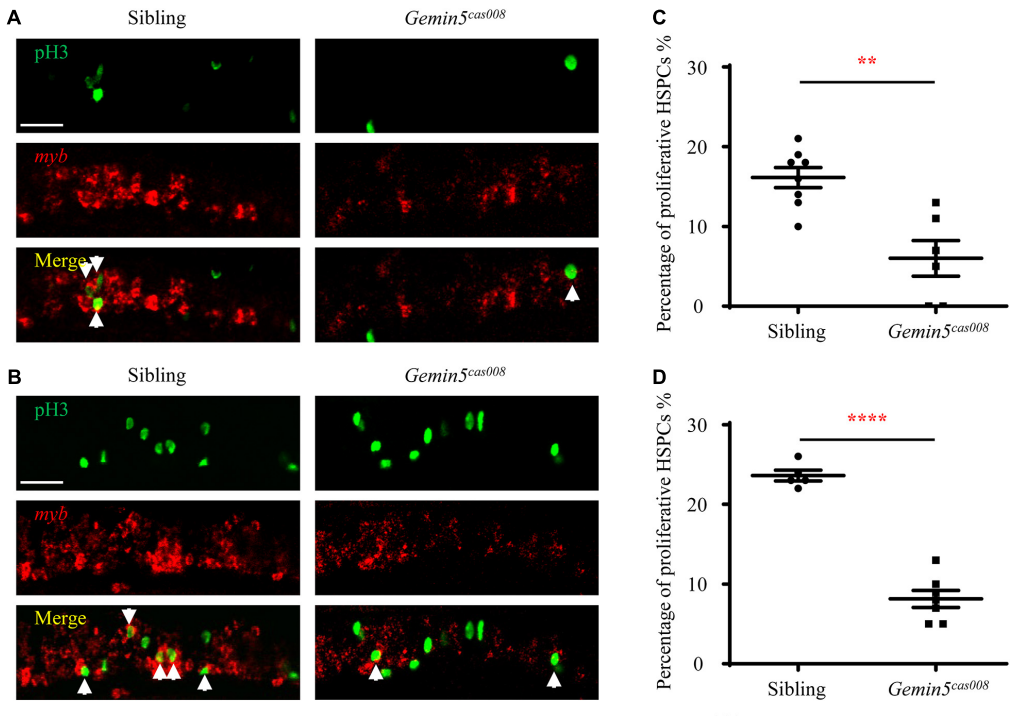

FIGURE 3 | Decreased HSPCs proliferation in mutant *gemin5*^{cas008}. **(A,B)** Representative confocal images of double staining of pH3 protein (green) and *myb* RNA (red) in the CHT at 4 dpf **(A)** and 5 dpf **(B)**. Arrows point at proliferative HSPCs. Scale bars, 50 μm. **(C,D)** Percentage of proliferative HSPCs (pH3+myb+)/ total HSPCs (myb+) in sibling and *gemin5*^{cas008} embryos at 4 dpf **(C)** and 5 dpf **(D)**. **(C)** $t = 4.202$, df = 12, and $P = 0.0012$. **(D)** $t = 10.96$, df = 10, and $P < 0.0001$.

role in its activity (Martinez-Salas et al., 2020). The non-canonical RNA-binding domain allows Gemin5 to interact with its mRNA targets and play a key role in translation. Research on Gemin5 is emerging but far from enough to understand the consequence of its multifunction, including its canonical role in the biogenesis of snRNPs, and its control on alternative splicing and translation, etc. (Pineiro et al., 2015).

HSPCs Failed in Proliferation in *Gemin5*^{cas008}

To elucidate the reason of HSPCs abrogation, we first examined HSPCs proliferation during hematopoietic development by combination of fluorescence *in situ* hybridization (FISH) and phospho-histone 3 (pH3) immunostaining. We calculated the percentage of proliferative HSPCs (pH3 + *myb*+) in total HSPCs (*myb*+). At both 4 and 5 dpf, the percentage of proliferative HSPCs (pH3^{+} *myb*$^{+}$) in the CHT in *gemin5*^{cas008} was significantly decreased (**Figures 3A–D**, 4 dpf $P = 0.0012$, and 5 dpf $P < 0.0001$). Next, we examined the apoptosis of HSPCs by terminal-transferase dUTP Nick End Labeling (TUNEL) assays in transgenic background Tg(*myb*:eGFP) and calculated the percentage of apoptotic HSPCs (TUNEL+ GFP+) in total HSPCs (GFP+). Apoptotic signals of HSPCs in the CHT region had no significant difference between sibling and *gemin5*^{cas008} at 4 dpf (**Supplementary Figures 3A,B**, $P = 0.1430$), which indicated there was no excessive HSPCs apoptosis in mutant *gemin5*^{cas008}. In brief, impaired definitive hematopoiesis in *gemin5*^{cas008} was due to defective proliferation of HSPCs.

In brief, we obtained a zebrafish mutant family with Gemin5 point mutation. Mutant *gemin5*^{cas008} showed no obvious defects during primitive hematopoiesis or vasculogenesis. However, the reductive HSPCs proliferation caused severe definitive hematopoiesis failure in the *gemin5*^{cas008}.

DISCUSSION

The basis of stem cells' self-maintenance and differentiation could be described as genetically programmed and integrated circuits (Yuan and Muljo, 2013). In the hematopoietic system, major advances have been achieved in elucidating the regulatory networks which orchestrate gene expression programs and direct cell-fate determinations. Among them, much work has focused on elucidating signaling pathways and transcriptional programs. However, the post-transcriptional regulation of HSPCs is far from well-explored. This "RNA centric" level of regulation precisely and quickly tunes protein expression by regulating splicing, localization, degradation, or translation of mRNA (de Rooij et al., 2019). As one of the key players, RBPs perform their function by interaction with existent transcriptional networks in the cell. They interact with their target mRNAs which are based on RNA sequence, strongly influencing their downstream processing. It has been reported different changes of RBPs will cause the disruption

of hematopoietic homeostasis (Yuan and Muljo, 2013). For instance, the RBP Rbm15 regulates splicing of Mpl-TR, the truncated isoform of the c-Mpl receptor, which affects thrombopoietin signaling and subsequently influences HSCs quiescence and proliferation (Xiao et al., 2015). The oncogenic fusion gene BCR-ABL markedly increased the expression of the RBPs La/SSB, multiple hnRNPs and TLS/FUS and interfered mRNA processing, nuclear-cytoplasmic export and translation, resulting in the unbalance of HSCs proliferation and differentiation (Perrotti and Calabretta, 2002).

In this study, we obtained a zebrafish mutant family with Gemin5 point mutation through a large-scale forward genetics screen. Gemin5 is an RBP described as a peripheral component of the SMN complex, first identified in 2002 (Gubitz et al., 2002). In eukaryotic cells, the SMN complex acts as an assemblyosome, mediating the biogenesis and function of spliceosomal snRNPs. It is intensive in nuclear Gems (Gemini of Cajal bodies), though it is dispersed throughout the cytoplasm. The SMN complex is composed of nine members, including SMN, Gemins2–8 and the unr-interacting protein (unrip) in human (Martinez-Salas et al., 2020). Gemin5 comprises WD repeat domains at the *N*-terminal, recognizing the snRNAs, delivering them to the SMN complex and allowing assembly of the SMN complex and snRNAs into snRNPs in the cytoplasm. Gemin5 is predominantly distributed in the cell cytoplasm (Gubitz et al., 2002). However, a large fraction of Gemin5 is found outside of the SMN complex (Battle et al., 2007), which suggests there may be additional functions of Gemin5. In accordance with this, it has been detected Gemin5 and the SMN complex colocalize in nuclear gems, rather than in nuclear Cajal bodies. Gemin5 may participate in tumor cell motility through the alternative splicing process. For instance, analyze the global mRNA splicing profile of the MDA-MB-435 tumor cell line at metastatic state or suppression state, showing a distinct splicing profile between different cellular states in dependence on Gemin5 (Lee et al., 2008, 2009). In addition, it has been reported that Gemin5 may interact with signal recognition particle or ribosome, and regulate the translation or *trans*-splicing of several mRNAs. More recently, structural analyses have unveiled there is a robust dimerization module in Gemin5, helping understand the functional role of the middle region (Moreno-Morcillo et al., 2020). The dimerization module of Gemin5 is fundamental in its architecture and essential for its activity. At the *C*-terminal region, it has a non-canonical RNA-binding site (RBS) with two parts named as RBS1 and RBS2, not only determining the interaction with IRES (viral internal ribosome entry site) of the FMDV (foot-and-mouth disease virus), but also harboring the capacity to downregulate translation (Fernandez-Chamorro et al., 2014). In sum, Gemin5 plays an essential role in the snRNPs biogenesis. Moreover, with the analysis of its structure, its function involved in alternative splicing, stress response and translation control has been uncovered. Although genetic evidence shown defective Gemin5 might link to neuron degeneration, its role in other tissues/organs remains unknown.

In mutant *gemin5*^{cas008}, we identified a C to T nonsense mutation causing an earlier stop codon next to the end of the fifth WD repeats domain of Gemin5 protein (**Figures 2A,B**). Mutant *gemin5*^{cas008} had intact primitive hematopoiesis, while showed specific deficiency in definitive hematopoiesis. FISH and pH3 immunostaining results showed the percentage of proliferative HSPCs dramatically decreased in *gemin5*^{cas008} (**Figures 3A–D**). However, the percentage of apoptotic HSPCs had no significant difference (**Supplementary Figures 3A,B**). In accordance, inhibiting p53 dependent apoptosis pathway by p53 MO or bcl2 mRNA injection at one-cell stage could not rescue the phenotype of *gemin5*^{cas008} (similar experiments could rescue another mutant due to increased apoptosis in Gao et al., 2015). So, we concluded that impaired definitive hematopoiesis in *gemin5*^{cas008} was due to defective proliferation of HSPCs. It has been reported that in human cells, Gemin5 interact with snRNAs through the WD repeat domain. Particularly, RNA-mediated radical probing and mass spectrometry results showed the fifth WD repeat contributes to the interaction (Lau et al., 2009). In addition, the establishment of the interaction depends on the structural integrity of this domain, for even a point mutation at the W286 residue (human) would disrupt the interaction shown by mutational experiment. This residue in zebrafish Gemin5 orthologs (W270) is conserved and might be preserved in mutant *gemin5*^{cas008}. Considering the intact primitive hematopoiesis and specific deficient definitive hematopoiesis, we speculate the truncated Gemin5 protein can still recognize snRNAs through its residual domain for there is no large-scale transcriptional splicing disorder in the cell. However, the efficiency of the interaction may be reduced, and its target may even be biased toward certain snRNAs, eventually leading to the appearance of specific transcription and splicing disorders, thereby targeting the hematopoietic process.

In addition, Gemin5 has cap-binding capacity in the WD repeat domains and may influence translation initiation in a cap-dependent manner (Pineiro et al., 2015). W286 and F338 (human), as the putative cap-interacting residues, are identified by combination of the protein homology/analogy recognition engine (PHYRE) algorithm and site-directed mutagenesis. These sites are conserved in zebrafish (W270 and F322), and W270 might be preserved while F322 was not in the mutant. As mentioned, truncated Gemin5 protein lacked C-terminal which interacts with IRES and regulates transition. It's reasonable to believe the regulation of Gemin5 in translation initiation was partially preserved in the mutants. The defective Gemin5 might still maintain various basic functions to let the mutants survive early development without obvious defects, however, the biological processes during definitive hematopoiesis were beyond the ability of truncated Gemin5 and drove abnormal development. Based on reported researches about the regulation of Gemin5 on the ASK1-JNK1 signaling pathway (Kim et al., 2007) and its cooperation with nuclear receptor to transmit ecdysone signaling (Gates et al., 2004), we speculate some relatively sensitive signal pathways of HSPCs or the transcriptional regulatory network required for proliferation depending on Gemin5 were specifically disrupted in mutant *gemin5*^{cas008}.

Questions remain open regarding how Gemin5 regulates hematopoiesis. First of all, the location and the protein level of

the mutant Gemin5 protein need to be determined. Secondly, HSPC-specific re-expression of WT Gemin5 in *gemin5*^{cas008} need to be carried out to elucidate its requirement in a stem cell or niche cell manner. Lack of zebrafish Gemin5 antibody and lack of efficient HSPC-specific promoter for transgenesis need be overcome in future study. Thirdly, the pathogenic mechanism downstream of the mutated Gemin5 needs to be elucidated. It needs to be described which signal pathways of HSPCs or which transcriptional regulatory network required for proliferation depending on Gemin5 are essential. It will also be interesting to figure out the function of diverse regions of Gemin5 in the regulation of HSPCs. At last, it is worth identifying whether there are human hematopoietic diseases caused by Gemin5 mutations and what extent of Gemin5 involved in human diseases in blood system. It is very likely that the extend of other components in the SMN complex, as well as other RBPs, need be studied in hematopoiesis.

DATA AVAILABILITY STATEMENT

The original contributions presented in the study are included in the article/**Supplementary Material**, further inquiries can be directed to the corresponding author/s.

ETHICS STATEMENT

The animal study was reviewed and approved by the Animal Research Advisory Committee of Shanghai Institute of Nutrition and Health, CAS.

AUTHOR CONTRIBUTIONS

XL, KM, WP, and DL designed the experiments. XL and KM carried on the experiments and analyzed data. CJ, LG, CF, and CR assisted with ENU screening and positional cloning. WZ, YH, and MC assisted with imaging with Olympus FV1000 Fluoview scanning confocal microscope. All the authors provided ideas and discussions throughout the project. WP and DL wrote the manuscript. KM, WP, and DL supervised the project.

FUNDING

The National Science Fund for Distinguished Young Scholars (Grant No. E034J11381), China National Postdoctoral Program for Innovative Talents (Grant No. BX20200347), and Shanghai Post-doctoral Excellence Program (Grant No. 2020505).

ACKNOWLEDGMENTS

We thank Yi Chen, Yi Jin, Min Deng, Mei Dong, Peili Ni, and Yan Hao for zebrafish husbandry and technical support.

SUPPLEMENTARY MATERIAL

The Supplementary Material for this article can be found online at: https://www.frontiersin.org/articles/10.3389/fcell.2021.670654/full#supplementary-material

REFERENCES

Bahary, N., Davidson, A., Ransom, D., Shepard, J., Stern, H., Trede, N., et al. (2004). The zon laboratory guide to positional cloning in zebrafish. *Methods Cell. Biol.* 77, 305–329. doi: 10.1016/s0091-679x(04)77017-x

Battle, D. J., Kasim, M., Wang, J., and Dreyfuss, G. (2007). SMN-independent subunits of the SMN complex. Identification of a small nuclear ribonucleoprotein assembly intermediate. *J. Biol. Chem.* 282, 27953–27959. doi: 10.1074/jbc.m702317200

Burns, C. E., Galloway, J. L., Smith, A. C., Keefe, M. D., Cashman, T. J., Paik, E. J., et al. (2009). A genetic screen in zebrafish defines a hierarchical network of pathways required for hematopoietic stem cell emergence. *Blood* 113, 5776–5782. doi: 10.1182/blood-2008-12-193607

Ciau-Uitz, A., Monteiro, R., Kirmizitas, A., and Patient, R. (2014). Developmental hematopoiesis: ontogeny, genetic programming and conservation. *Exp. Hematol.* 42, 669–683. doi: 10.1016/j.exphem.2014.06.001

de Rooij, L., Chan, D. C. H., Keyvani Chahi, A., and Hope, K. J. (2019). Post-transcriptional regulation in hematopoiesis: RNA binding proteins take control (1). *Biochem. Cell. Biol.* 97, 10–20.

Fernandez-Chamorro, J., Pineiro, D., Gordon, J. M., Ramajo, J., Francisco-Velilla, R., Macias, M. J., et al. (2014). Identification of novel non-canonical RNA-binding sites in Gemin5 involved in internal initiation of translation. *Nucleic Acids Res.* 42, 5742–5754.

Galloway, J. L., and Zon, L. I. (2003). Ontogeny of hematopoiesis: examining the emergence of hematopoietic cells in the vertebrate embryo. *Curr. Top Dev. Biol.* 53, 139–158. doi: 10.1016/s0070-2153(03)53004-6

Gao, L., Li, D., Ma, K., Zhang, W., Xu, T., Fu, C., et al. (2015). TopBP1 governs hematopoietic stem/progenitor cells survival in zebrafish definitive hematopoiesis. *PLoS Genet.* 11:e1005346. doi: 10.1371/journal.pgen.1005346

Gates, J., Lam, G., Ortiz, J. A., Losson, R., and Thummel, C. S. (2004). Rigor mortis encodes a novel nuclear receptor interacting protein required for ecdysone signaling during drosophila larval development. *Development* 131, 25–36. doi: 10.1242/dev.00920

Gore, A. V., Pillay, L. M., Venero Galanternik, M., and Weinstein, B. M. (2018). The zebrafish: a fintastic model for hematopoietic development and disease. *Wiley Interdiscip. Rev. Dev. Biol.* 7:e312. doi: 10.1002/wdev.312

Grech, G., and von Lindern, M. (2012). The role of translation initiation regulation in haematopoiesis. *Comp. Funct. Genom.* 2012:576540.

Gubitz, A. K., Mourelatos, Z., Abel, L., Rappsilber, J., Mann, M., and Dreyfuss, G. (2002). Gemin5, a novel WD repeat protein component of the SMN complex that binds Sm proteins. *J. Biol. Chem.* 277, 5631–5636. doi: 10.1074/jbc.m109448200

Jia, X. E., Ma, K., Xu, T., Gao, L., Wu, S., Fu, C., et al. (2015). Mutation of kri1l causes definitive hematopoiesis failure via PERK-dependent excessive autophagy induction. *Cell. Res.* 25, 946–962. doi: 10.1038/cr.2015.81

Kim, E. K., Noh, K. T., Yoon, J. H., Cho, J. H., Yoon, K. W., Dreyfuss, G., et al. (2007). Positive regulation of ASK1-mediated c-Jun NH(2)-terminal kinase signaling pathway by the WD-repeat protein Gemin5. *Cell. Death Differ.* 14, 1518–1528. doi: 10.1038/sj.cdd.4402157

Kissa, K., and Herbomel, P. (2010). Blood stem cells emerge from aortic endothelium by a novel type of cell transition. *Nature* 464, 112–125. doi: 10.1038/nature08761

Lau, C. K., Bachorik, J. L., and Dreyfuss, G. (2009). Gemin5-snRNA interaction reveals an RNA binding function for WD repeat domains. *Nat. Struct. Mol. Biol.* 16, 486–491. doi: 10.1038/nsmb.1584

Lee, J. H., Horak, C. E., Khanna, C., Meng, Z., Yu, L. R., Veenstra, T. D., et al. (2008). Alterations in Gemin5 expression contribute to alternative mRNA splicing patterns and tumor cell motility. *Cancer Res.* 68, 639–644. doi: 10.1158/0008-5472.can-07-2632

Lee, J. H., Marshall, J. C., Steeg, P. S., and Horak, C. E. (2009). Altered gene and protein expression by Nm23-H1 in metastasis suppression. *Mol. Cell. Biochem.* 329, 141–148. doi: 10.1007/s11010-009-0124-3

Li, D., Xue, W., Li, M., Dong, M., Wang, J., Wang, X., et al. (2018). VCAM-1(+) macrophages guide the homing of HSPCs to a vascular niche. *Nature* 564, 119–124. doi: 10.1038/s41586-018-0709-7

Martinez-Salas, E., Embarc-Buh, A., and Francisco-Velilla, R. (2020). Emerging roles of gemin5: from snRNPs assembly to translation control. *Int. J. Mol. Sci.* 21:3868. doi: 10.3390/ijms21113868

Moreno-Morcillo, M., Francisco-Velilla, R., Embarc-Buh, A., Fernandez-Chamorro, J., Ramon-Maiques, S., and Martinez-Salas, E. (2020). Structural basis for the dimerization of Gemin5 and its role in protein recruitment and translation control. *Nucleic Acids Res.* 48, 788–801. doi: 10.1093/nar/gkz1126

Murayama, E., Kissa, K., Zapata, A., Mordelet, E., Briolat, V., Lin, H. F., et al. (2006). Tracing hematopoietic precursor migration to successive hematopoietic organs during zebrafish development. *Immunity* 25, 963–975. doi: 10.1016/j.immuni.2006.10.015

North, T. E., Goessling, W., Walkley, C. R., Lengerke, C., Kopani, K. R., Lord, A. M., et al. (2007). Prostaglandin E2 regulates vertebrate haematopoietic stem cell homeostasis. *Nature* 447, 1007–1011. doi: 10.1038/nature05883

Perrotti, D., and Calabretta, B. (2002). Post-transcriptional mechanisms in BCR/ABL leukemogenesis: role of shuttling RNA-binding proteins. *Oncogene* 21, 8577–8583. doi: 10.1038/sj.onc.1206085

Pineiro, D., Fernandez-Chamorro, J., Francisco-Velilla, R., and Martinez-Salas, E. (2015). Gemin5: a multitasking RNA-binding protein involved in translation control. *Biomolecules* 5, 528–544. doi: 10.3390/biom5020528

Song, H. D., Sun, X. J., Deng, M., Zhang, G. W., Zhou, Y., Wu, X. Y., et al. (2004). Hematopoietic gene expression profile in zebrafish kidney marrow. *Proc. Natl. Acad. Sci. U S A* 101, 16240–16245. doi: 10.1073/pnas.0407241101

Suster, M. L., Kikuta, H., Urasaki, A., Asakawa, K., and Kawakami, K. (2009). Transgenesis in zebrafish with the tol2 transposon system. *Methods Mol. Biol.* 561, 41–63. doi: 10.1007/978-1-60327-019-9_3

Traver, D., Paw, B. H., Poss, K. D., Penberthy, W. T., Lin, S., and Zon, L. I. (2003). Transplantation and in vivo imaging of multilineage engraftment in zebrafish bloodless mutants. *Nat. Immunol.* 4, 1238–1246. doi: 10.1038/ni1007

Xiao, N., Laha, S., Das, S. P., Morlock, K., Jesneck, J. L., and Raffel, G. D. (2015). Ott1 (Rbm15) regulates thrombopoietin response in hematopoietic stem cells through alternative splicing of c-Mpl. *Blood* 125, 941–948. doi: 10.1182/blood-2014-08-593392

Yuan, J., and Muljo, S. A. (2013). Exploring the RNA world in hematopoietic cells through the lens of RNA-binding proteins. *Immunol. Rev.* 253, 290–303. doi: 10.1111/imr.12048

Conflict of Interest: The authors declare that the research was conducted in the absence of any commercial or financial relationships that could be construed as a potential conflict of interest.

frontiers in Cell and Developmental Biology

ORIGINAL RESEARCH
published: 27 May 2021
doi: 10.3389/fcell.2021.650599

Rheb1-Deficient Neutrophils Promote Hematopoietic Stem/Progenitor Cell Proliferation *via* Mesenchymal Stem Cells

Juan Gao[1,2†], Shuaibing Hou[1†], Shengnan Yuan[1], Yuxia Wang[1], Yanan Gao[1,3], Xiaolu Sun[1], Weili Wang[1], Yajing Chu[1], Yuan Zhou[1], Xiaoming Feng[1], Hongbo R. Luo[4], Tao Cheng[1], Jun Shi[1], Weiping Yuan[1] and Xiaomin Wang[1,5]**

[1] State Key Laboratory of Experimental Hematology, National Clinical Research Center for Blood Diseases, Institute of Hematology and Blood Diseases Hospital, Chinese Academy of Medical Sciences & Peking Union Medical College, Tianjin, China, [2] Tianjin Key Laboratory of Ophthalmology and Visual Science, Tianjin Eye Hospital, Clinical College of Ophthalmology, Tianjin Eye Institute, Tianjin Medical University, Nankai University Affiliated Eye Hospital, Tianjin, China, [3] Department of Pathology, Tianjin Medical University Cancer Institute and Hospital, Tianjin Medical University, Tianjin, China, [4] Department of Pathology, Dana-Farber/Harvard Cancer Center, Harvard Medical School, Boston, MA, United States, [5] Department of Neuro-Oncology, Cancer Center, Beijing Tiantan Hospital, Capital Medical University, Beijing, China

OPEN ACCESS

Edited by:
Jon Frampton,
University of Birmingham,
United Kingdom

Reviewed by:
Toshiyuki Yamane,
Mie University, Japan
Chen Xu,
Fudan University, China

***Correspondence:**
Xiaomin Wang
wangxiaomin@ihcams.ac.cn
Weiping Yuan
wpyuan@ihcams.ac.cn

[†] These authors have contributed equally to this work

Specialty section:
This article was submitted to Stem Cell Research, a section of the journal Frontiers in Cell and Developmental Biology

Received: 07 January 2021
Accepted: 19 April 2021
Published: 27 May 2021

Citation:
Gao J, Hou S, Yuan S, Wang Y, Gao Y, Sun X, Wang W, Chu Y, Zhou Y, Feng X, Luo HR, Cheng T, Shi J, Yuan W and Wang X (2021) Rheb1-Deficient Neutrophils Promote Hematopoietic Stem/Progenitor Cell Proliferation via Mesenchymal Stem Cells. Front. Cell Dev. Biol. 9:650599. doi: 10.3389/fcell.2021.650599

Myeloid cells have been identified as hematopoietic stem cell (HSC)-regulating cells. However, the mechanisms by which myeloid cells regulate the function of HSCs are not fully defined. Our previous study indicated that the HSCs are over-expanded in *Vav1-Cre;Rheb1$^{fl/fl}$* mice. Here, using *in vivo* and *in vitro* models, we found that *Rheb1*-deficient neutrophils remodeled the bone marrow environment and induced expansion of HSCs *in vivo*. Further studies showed that loss of Rheb1 impaired neutrophils' ability to secrete IL-6, led mesenchymal stem cells (MSCs) to produce more SCF, and promote HSC proliferation. We further found that IL-6 suppressed SCF mRNA expression in human MSCs. Interesting, the high level of IL-6 was also related with poor survival of chronic myeloid leukemia (CML) patients, and higher expression of IL-6 in CML cells is associated with the lower expression of SCF in MSCs in patients. Our studies suggested that blocking IL-6 signaling pathway might stimulate MSCs to secrete more SCF, and to support hematopoietic stem/progenitor cells proliferation.

Keywords: *Rheb1*-deficient neutrophils, hematopoietic stem/progenitor cell, proliferation, mesenchymal stem cells, IL-6

INTRODUCTION

Hematopoietic stem cells (HSCs) play an important role in the regulation of hematopoietic homeostasis. They can self-renew and differentiate into all cell types of the hematopoietic system according to proliferative or stress cues throughout life (Feng et al., 2008; Rathinam and Flavell, 2008). This process requires fine regulation by intra- and extracellular signaling in the bone

Abbreviations: BMCs, whole bone marrow cells; BM, bone marrow; MNCs, mononuclear cells; PB, peripheral blood; HSC, hematopoietic stem cell; HPC, hematopoietic progenitor cell; LKS$^{\pm}$, Lin^{-}c-kit^{+}Sca-1$^{\pm}$; LK^{+}, Lin^{-}c-kit^{+}; MSC, mesenchymal stem cell; OBC, osteoblast cell; *wt*, wild-type; SCF, stem cell factor; CML, chronic myeloid leukemia; PBS, Phosphate Buffer Solution; FBS, fetal bovine serum; HBSS, Hanks' Balanced Salt Solution.

marrow microenvironment. HSCs primarily reside in the bone marrow cavity (or niche), where they interact with a variety of cell types, including perivascular cells, osteoblast cells (OBCs) and mesenchymal stem cells (MSCs). HSCs directly adhere to mesenchymal cells and possibly to osteoblasts in the bone marrow stroma that express important regulatory molecules including stem cell factor (SCF) and C-X-C motif chemokine 12 (CXCL-12) (Frenette et al., 2013; Greenbaum et al., 2013). In addition, differentiated hematopoietic cells have been proposed to regulate HSCs. For example, macrophages have been shown to indirectly promote the retention of HSCs by regulating mesenchymal cells and osteoblasts (Chow et al., 2011). Megakaryocytes (MK) are physically associated with HSCs in the bone marrow. MK ablation leads to the activation of quiescent HSCs and increases proliferation of HSCs (Meng et al., 2014). Neutrophils can produce ROS to stimulate the proliferation of myeloid progenitors (Kwak et al., 2015). These studies suggested that the hematopoietic cells and niche cells interact with HSCs, regulate HSCs division and proliferation, and maintain hematopoietic system balance *in vivo*.

It has been known that the change of normal hematopoietic niche to a hostile HSC growth environment is the tipping point for the development of myelodysplastic syndromes (MDS) and leukemia (Raaijmakers, 2012). For example, study has shown that leukemia cells could secrete more proinflammatory cytokines and establish a feedback loop that drive over-expansion of immature myeloid cells and chronic myeloid leukemia (CML) development (Reynaud et al., 2011). Additionally, leukemia cells could also stimulate MSCs to differentiate into OBCs to support LSC proliferation (Schepers et al., 2013), while MSCs may accelerate abnormal HSCs over-proliferation through secreting more SDF-1 in myeloproliferative neoplasm (MPN) patients (Arranz et al., 2014).

mTOR is a serine/threonine protein kinase that responds to multiple signals and maintains homeostasis. Increased or decreased mTORC1 activity can alter HSC function and cause hematological disorders (Wang et al., 2016a). Rheb1 acts as a key activator of mTOR to play vital roles in maintaining proper hematopoiesis and myeloid differentiation (Aspuria and Tamanoi, 2004). Previously, we reported that *Rheb1*-deficient mice showed increased phenotypic HSCs, immature neutrophils in bone marrow, and splenomegaly, which are reminiscent of the hematopoiesis seen in MPNs (Wang et al., 2018). Meanwhile, *Rheb1* deficiency inhibits the development of macrophages and neutrophils, thus impairing their phagocytic ability (Wang et al., 2016b). Rheb1 cooperated with MLL-AF9 to promote acute myeloid leukemia progression, and deletion of *Rheb1* in the MLL-AF9 acute myeloid leukemia mouse model prolonged the survival of mice by inhibiting the mTORC1 signaling pathway (Gao et al., 2016).

Interestingly, our study found that the absolute number of HSCs were increased in *Vav1-Cre;Rheb1*$^{fl/fl}$ mice, while HSCs were not over expanded under *in vitro* culture conditions (Wang et al., 2018). This suggested that the expansion of these HSPCs in the bone marrow of *Vav1-Cre;Rheb1*$^{fl/fl}$ mice might be caused by additional extrinsic factors rather than intrinsic factors. Here in this study, we found that loss of *Rheb1* impaired neutrophils ability to secrete IL-6, and this in turn stimulated MSCs to produce more SCF, leading to HSPCs over proliferation.

MATERIALS AND METHODS

Mice and Genotyping

Vav1-Cre mice (JAX stock #008610, background CD45.2) were purchased from Jackson Lab. *Rheb1*$^{fl/fl}$ mice (background CD45.2) were kindly provided by Dr. Bo Xiao (Zou et al., 2011). The mice were crossed with *B6.SJL* mice (background CD45.1) and were backcrossed, respectively, to generate CD45.1 congenital *Vav1-Cre* mice and *Rheb1*$^{fl/fl}$ mice (**Supplementary Figure 1A**). Then the *Vav1-Cre* mice and *Rheb1*$^{fl/fl}$ mice were crossed to generated mice in which *Rheb1* was specifically deleted in the hematopoietic system (*Vav1-Cre;Rheb1*$^{fl/fl}$ or *Rheb1*$^{\Delta/\Delta}$, CD45.1). C57BL/6 mice (6–8 weeks old, CD45.2) were the recipient mice in transplantation experiments. Mice were maintained at the specific pathogen-free (SPF) animal facility of the State Key Laboratory of Experimental Hematology (SKLEH). All animal surgeries were approved by the Institutional Animal Care and Use Committee (IACUC), Institute of Hematology and Blood Diseases Hospital, CAMS/PUMC. All efforts were made to minimize mouse suffering.

Flow Cytometry Analysis

A 15 μl peripheral blood (PB) sample was obtained from either the tail vein or retroorbital bleeding and diluted with PBE (PBS with 2% fetal bovine serum and 2 mM EDTA). Before staining, ammonium chloride-potassium bicarbonate was used to lyse the red blood cells (RBCs). Bone marrow (BM) cells were flushed out from tibias, femurs and ilia with PBE. The cells were stained with the following antibodies: anti-mouse CD3 biotin, anti-mouse CD4 biotin, anti-mouse CD8a biotin, anti-mouse TER-119 biotin, anti-human/mouse CD45R (B220) biotin, anti-mouse CD11b BIOTIN, STREPTAVIDIN APC-Cy7, anti-mouse CD34 FITC, anti-mouse CD117 (c-Kit) APC, anti-mouse Ly-6A/E (Sca-1) PE-Cyanine7, anti-mouse CD45.2 PE, and anti-mouse CD45.1 Percp-Cy5.5 for HSPCs or anti-mouse CD45.1 FITC, anti-mouse CD45.2 PE, anti-mouse CD11b APC, and anti-mouse Ly-6G (Gr-1) PE-Cyanine7 for neutrophils. All antibodies were purchased from either eBioscience or Invitrogen (United States). The detail information for the antibodies was listed in the **Supplementary Table 1**. The samples were analyzed with a BD Canto II flow cytometer, more than 10,000 cells were collected and the results were analyzed with FlowJo software.

Isolation of Neutrophils From Bone Marrow

Percoll-based (GE Healthcare, 17144003, Little Chalfont, United Kingdom) density gradient centrifugation was used for the purification of neutrophils from bone marrow cells (Swamydas et al., 2015). A "100% Percoll" solution is generated by adding 5 ml of 10X HBSS (Gibco, 14065056, United States) to 45 ml of Percoll. Percoll dilutions of 52, 62, and 76% were

generated from the "100% Percoll" solution using 1X HBSS-EDTA (Thermo Fisher Scientific, 14025092, United States). The 76, 62, and 52% Percoll separation solutions were successively added to a 15 ml centrifuge tube (avoiding mixing of the three concentrations of Percoll separation solutions). The bone marrow cell suspension was overlaid on the Percoll separation layer, followed by centrifugation for 30 min at 2,800 rpm (1,420 g) at room temperature without braking. Cells were harvested from the 76 and 62% Percoll interface and washed twice with 1X HBSS buffer. 3 ml of Histopaque-1119 (Sigma-Aldrich, 11191, United States) was added to a 15-ml conical centrifuge tube, which was then overlaid with the cell suspension, followed by centrifugation for 30 min at 2,000 rpm (724 g) at room temperature without braking. The neutrophils were then collected at the Histopaque-1119 interface. The surface markers of neutrophils (Ly-6G$^+$CD11b$^+$) were analyzed by flow cytometry.

Isolation of MSCs From Bone and MSCs Culture

Mesenchymal stem cells (MSCs) from the compact bones of mice were obtained as previously described (Zhu et al., 2010). To deplete hematopoietic cells from the tibiae and femurs, the bone cavities were washed thoroughly at three times using a syringe until the bones become pale. Hold the humeri, tibiae and femurs with forceps and excise the compact bones carefully into chips of approximately 1–3 mm^3 with scissors. The bone chips were transferred into a 25-cm^2 plastic culture flask with forceps, then suspend the chips in 3 ml of α-MEM (Hyclone, SH30265.01, United States) containing 10% (vol/vol) FBS (Gibco, 16000-044, United States) in the presence of 1 mg/ml (wt/vol) of collagenase II (Gibco, 17101015, United States). The chips were digested for 1–2 h in a shaking incubator at 37°C with a shaking speed of 200 rpm. The collagenase digestion was stopped when the bone chips become loosely attached to each other. The digestion medium and released cells were aspirated and discarded. Enzyme-treated bone chips were placed in a 10-cm^2 dish containing 6 ml of α-MEM supplemented with 10% FBS. Each replanting was considered a passage. Passage 3 MSCs were used for all experiments. The surfaces marker of MSCs (Lin$^-$CD45$^-$CD31$^-$CD51$^+$Sca-1$^+$) were analyzed by Flow cytometry.

Lin$^-$c-kit$^+$ (LK$^+$) Isolation and Cocultured With MSCs

BM cells were isolated from the tibias, femurs and ilia of 8-week-old *B6.SJL* mice. *wt* LK$^+$ cells were sorted with a c-Kit (CD117) Microbead Kit (MACS, 130-091-224, German) and a Lineage Cell Depletion Kit (MACS, 130-090-858, German) according to the manufacturer's protocol. 1×10^6 LK$^+$ cells cultured with 6×10^4 MSCs from *Rheb1*$^{\Delta/\Delta}$ or *Rheb1*$^{fl/fl}$ mice for 24 h and counted the number of LK$^+$ cells. For the SCF/c-kit blocking experiment, 1×10^5 LK$^+$ cells cultured with 6×10^4 MSCs from *Rheb1*$^{\Delta/\Delta}$ or *Rheb1*$^{fl/fl}$ mice. SCF inhibitor (MCE, HY-101443, China) was added to the coculture system at 0.5 μM. After 24 h of coculture, counted the number of LK$^+$ cells.

LKS$^+$ Isolation and Culture

Rheb1$^{fl/fl}$ or *Rheb*$^{\Delta/\Delta}$ BM cells were isolated from the tibias, femurs and ilia of 8-week-old mice. LKS$^+$ cells were stained with the antibodies indicated above and sorted with a BD FACS Aria III flow cytometer (BD Bioscience, United States). Lin$^-$ cells and Lin$^-$c-kit$^+$ (LK$^+$) cells were sorted with a c-Kit (CD117) Microbead Kit (MACS, 130-091-224, Germany) and a Lineage Cell Depletion Kit (MACS, 130-090-858, Germany) according to the manufacturer's protocol. 2×10^5 *wt* Lin$^-$ cells were co-cultured with 2×10^7 *Rheb1*$^{fl/fl}$ or *Rheb1*$^{\Delta/\Delta}$ BMCs. The total cells were analyzed for the percentage of CD45.2$^+$/CD45.1$^+$ cells by flow cytometry.

MSCs Coculture With Neutrophils

For the neutrophils and MSCs coculture assay, 1×10^5 MSCs were cultured in 24-well plate in a volume of 500 μl α-MEM with 15% FBS. After 24h of culture, the MSCs were cultured with 1×10^6 *Rheb1*$^{fl/fl}$ or *Rheb1*$^{\Delta/\Delta}$ neutrophils using cell culture inserts (FALCON, 353095, United States). After 24 h of coculture, the MSCs were harvested, and the relative expression of stem cell factor (SCF) was measured. For the IL-6 neutralization experiment, IL-6 antibody (R&D, MAB406-SP, United States) was added to the coculture system at 10 ng/ml. After 24 h of coculture, MSCs were harvested, and the relative expression of SCF was measured. All cells were incubated at 37°C in a 5% CO_2 incubator.

Whole Bone Marrow Transplantation

For *wt* BMC transplantation, BMCs (CD45.2$^+$) were obtained from C57BL/6 mice, and 1×10^6 BMCs were intravenously injected into lethally irradiated 6–8-week-old *Rheb1*$^{fl/fl}$ or *Rheb1*$^{\Delta/\Delta}$ recipient mice (CD45.1$^+$). For *wt* BMC and *Rheb1*$^{\Delta/\Delta}$ or *Rheb1*$^{fl/fl}$ BMC co-transplantation, 5×10^5 *wt* BMCs (CD45.2$^+$), 1×10^6 *Rheb1*$^{\Delta/\Delta}$ or *Rheb1*$^{fl/fl}$ BMCs (CD45.1$^+$) and 7.5×10^5 *wt* MSCs were intravenously injected into lethally irradiated mice (CD45.2$^+$) (**Figure 1**).

HSPCs Transplantation

200 *wt* LKS$^+$ cells (from *B6.SJL* mice, CD45.1$^+$) were cocultured with MSCs from *Rheb1*$^{fl/fl}$ mice or *Rheb1*$^{\Delta/\Delta}$ mice for 24 h. The cultured LKS$^+$ cells (CD45.1$^+$) were harvested and intravenously injected into lethally irradiated recipient mice (CD45.2$^+$) with 5×10^5 BMCs (CD45.2$^+$). The reconstitution of PB cells was analyzed every 4 weeks after transplantation for 4 months, and the reconstitution of BM cells was analyzed at 4 months after transplantation (**Figure 4**).

Isolation of MSCs and MNCs From CML Patients

CML patients' BM cells were obtained from the Blood Bank of the State Key Laboratory of Experimental Hematology, Institute of Hematology and Blood Diseases Hospital, CAMS/PUMC. Specimen acquisition was approved by the Ethics Committee of Blood Diseases Hospital, Chinese Academy of Medical Sciences. All donors signed informed consent forms. One-fifth the volume of hydroxyethyl starch was added to the patient samples, and

let stand for 1 h at room temperature to allow the red blood cells to fully sediment. Gently suck the supernatant and divide it into two according to the volume of 3:1. A large volume of supernatant fluid was selected to culture MSC in containing 6 ml of α-MEM supplemented with 10% (vol/vol) FBS. The other was separated using a Ficoll (GE, United States) gradient to generated mononuclear cells (MNCs).

Quantitative Real-Time PCR

RNA was extracted using the RNeasy Mini Kit (QIAGEN, 74106, Germany) according to the manufacturer's protocol. cDNA synthesis was performed using a cDNA reverse transcription kit (Takara, RR047A, Japan) according to the manufacturer's protocol. Quantitative PCR assays were performed in 96-well Micro Amp Fast Optical Reaction Plates (Applied Biosystems, 4344904, United States) using SYBR Green Mix (Roche, 04913914001, Switzerland). The signal was detected using the Step-One Plus Real-Time PCR System (QuantStudio5). GAPDH was used as an endogenous control for gene expression assays.

ELISA

500 μl PB was obtained from the retro-orbital bleeding of mice and clotted for 1 h at room temperature, then centrifuged at 5,915 rpm (3,000 g) for 10 min, and the serum was collected for determination. Then ELISA was performed using the Mouse SCF ELISA Kit (Quantikine, MCK00, United States) and the Mouse IL-6 ELISA Kit (NRC, TAE-385, Canada) according to the manufacturer's protocols. A total of 5×10^6 *Rheb1*$^{fl/fl}$ or *Rheb1*$^{\Delta/\Delta}$ neutrophils in 200 μl of PBS were frozen and thawed three times and centrifuged at 5,915 rpm (3,000 g) for 10 min, and the liquid supernatants were collected for IL-6 determination. The cell culture medium was concentrated with an ultra-gentrification device (Merck, UFC900308, Germany). The ELISA tests were read on a Synergy^{H4} Hybrid Reader at 450 nm.

Statistical Analysis

GraphPad Prism 6.0 was used for statistical analyses. Every experiment was compared as two groups. The data are presented as the mean ± standard deviation (SD). The unpaired two-tailed Student's *t*-test was used to compute the *P*-values. $P < 0.05$ was considered significant. Significant differences are indicated with asterisks ($^*P < 0.05$; $^{**}P < 0.01$; $^{***}P < 0.001$).

RESULTS

HSPCs Are Expanded in the *Rheb1*$^{\Delta/\Delta}$ Blood Cell-Remodeled Bone Marrow Environment

We have shown that *Vav1-Cre;Rheb1*$^{fl/fl}$ mice present HSCs and immature myeloid cells expansion in BM, which resemble the phenotype of MPN patients (Wang et al., 2018). To investigate whether *Rheb1*-deficient cells regulate the proliferation of HSPCs, we established a chimeric mouse model with *wt* HSPCs and a *Rheb1*$^{\Delta/\Delta}$ blood cell-remodeled bone marrow environment. We isolated MSCs from bone of *wt* mice (*wt* MSCs, **Supplementary Figure 1B**), and transplanted 5×10^5 *wt* BMCs (CD45.2$^+$) together with 7.5×10^5 *wt* MSCs and 1×10^6 *Rheb1*$^{\Delta/\Delta}$ or *Rheb1*$^{fl/fl}$ BMCs (CD45.1$^+$) into lethally irradiated recipient *wt* mice (CD45.2) (**Figure 1A**). The percentage of *Rheb1*$^{\Delta/\Delta}$ and *Rheb1*$^{fl/fl}$ BMC-derived cells (CD45.1$^+$) in PB was approximately 80%, 4 months after the transplantation, and the percentage of *wt* BMC-derived cells (CD45.2$^+$) in PB was close to 20% in mice after the transplantation (**Figure 1B** and **Supplementary Figure 1C**). The absolute number of *Rheb1*$^{\Delta/\Delta}$ -derived LKS$^+$ and LKS$^-$ cells (CD45.1$^+$) were significantly increased when compared with those of *Rheb1*$^{fl/fl}$-derived LKS$^+$ and LKS$^-$ cells (CD45.1$^+$), respectively (**Figures 1C,D**). *Rheb1*$^{\Delta/\Delta}$ BMC-derived myeloid cells were also increased in the PB of mice (**Supplementary Figure 1D**). Moreover, the percentage of *Rheb1*$^{\Delta/\Delta}$ Ly-6G^{low}CD11b$^+$ immature neutrophils (CD45.1$^+$) was increased in mice when compared with that of *Rheb1*$^{fl/fl}$ Ly-6G^{low}CD11b$^+$ immature neutrophils (**Figures 1E,F**). These phenotypes were similar with *Rheb1*$^{\Delta/\Delta}$ mouse (Wang et al., 2018). Then we analyzed the absolute number of *wt* HSPCs (CD45.2$^+$) in the *Rheb1*$^{\Delta/\Delta}$ blood cell-remodeled bone marrow environment in the chimeric mouse model, and found that the absolute number of *wt* LKS$^+$ cells (CD45.2$^+$) transplanted with *Rheb1*$^{\Delta/\Delta}$ BMCs were higher than those of the cells transplanted with *Rheb1*$^{fl/fl}$ BMCs (**Figures 1G–I**). The percentage of *wt* BMC-derived myeloid cells (CD45.2$^+$) was increased in PB, while the ratio of *wt* BMC-derived Ly-6G^{high}CD11b$^+$ and Ly-6G^{low}CD11b$^+$ neutrophils (CD45.2$^+$) was not changed in the BM of mice co-transplanted with *Rheb1*$^{\Delta/\Delta}$ BMCs (**Supplementary Figures 1E,F**). It indicated that *Rheb1*$^{\Delta/\Delta}$ blood cell remodeled bone marrow environment and promoted HSPC proliferation. To explore whether *Rheb1*$^{\Delta/\Delta}$ BM cells directly promoted phenotypic HSPCs over proliferation, we cocultured *wt* Lin$^-$ cells (CD45.2$^+$) with BMCs from *Rheb1*$^{fl/fl}$ and *Rheb1*$^{\Delta/\Delta}$ mice (CD45.1$^+$) (**Supplementary Figure 2A**). Interestingly, the number of *wt* Lin$^-$ cells cocultured with BMCs from *Rheb1*$^{\Delta/\Delta}$ mice was similar with that in the control group at 24 h (**Supplementary Figure 2B**). These data suggested that *Rheb1*$^{\Delta/\Delta}$ BM cells indirectly promoted HSPCs over-proliferation.

The Proliferation of *wt* HSPCs Was Normal in *Rheb1*$^{\Delta/\Delta}$ Recipient Mice After Transplantation

To investigate whether the niche cells affect the expansion of HSPCs in *Rheb1*$^{\Delta/\Delta}$ mice, we transplanted *wt* whole bone marrow cells (CD45.2$^+$) into lethally irradiated *Rheb1*$^{\Delta/\Delta}$ or *Rheb1*$^{fl/fl}$ recipient mice (CD45.1$^+$) and analyzed the donor-derived HSPCs (CD45.2$^+$) at 4 months after transplantation (**Figure 2A**). The rate of donor chimerism was approximately 80% in both *Rheb1*$^{\Delta/\Delta}$ and control mice (**Figure 2B**). The absolute number of donor-derived LKS$^+$ cells and LKS$^-$ cells (CD45.2$^+$) in *Rheb1*$^{\Delta/\Delta}$ mice were similar when compared with those in the control mice (**Figures 2C,D**). Since *Rheb1* deletion caused increased number and immaturity of neutrophils in steady condition (Wang et al., 2018), we also analyzed neutrophils by flow cytometry (FACS) with CD11b and Ly-6G

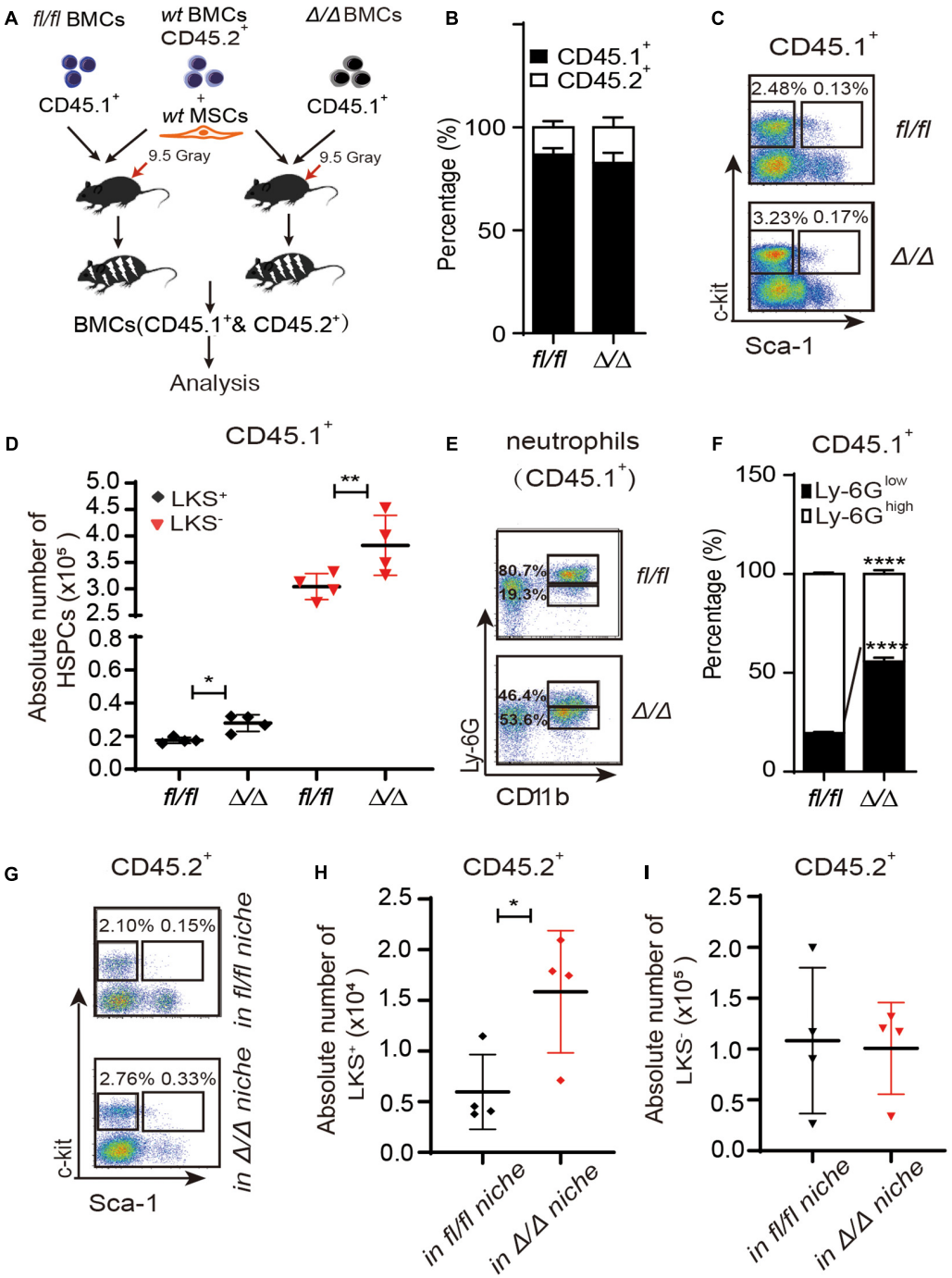

FIGURE 1 | HSPCs are expanded in the *Rheb1*$^{\Delta/\Delta}$ blood cell-remodeled bone marrow environment. **(A)** *WT* BMCs (CD45.2$^+$) together with *wt* MSCs and *Rheb1*$^{\Delta/\Delta}$ or *Rheb1*$^{fl/fl}$ BMCs (CD45.1$^+$) were transplanted into lethally irradiated recipient *wt* mice. **(B)** The percentages of CD45.1$^+$ cells and CD45.2$^+$ cells in BM 4 months after transplantation. **(C,D)** The absolute number of CD45.1$^+$LKS$^+$ cells and CD45.1$^+$LKS$^-$ cells in BM 4 months after transplantation. **(E,F)** The percentages of CD45.1$^+$CD11b$^+$Ly-6G$^{high/low}$ neutrophils in BM 4 months after transplantation. **(G–I)** The absolute number of CD45.2$^+$LKS$^+$ cells and CD45.2$^+$LKS$^-$ cells in BM 4 months after transplantation. The data are presented as the mean ± SD, $n = 4$. *$P < 0.05$; **$P < 0.01$; ***$P < 0.001$.

antibodies, that have been used as neutrophil subpopulation markers for the identification of myelocytes or promyelocytes, as well as immature or mature neutrophils. The CD11b$^+$Ly-6G$^+$ subpopulation of donor-derived cells (*wt*) in *Rheb1*$^{\Delta/\Delta}$ mice was similar to that in the control mice (**Figure 2E,F**). These data indicated that niche cells in *Rheb1*$^{\Delta/\Delta}$ mice contributed little to HSCs proliferation *in vivo*, while *Rheb1*$^{\Delta/\Delta}$ BM cells cooperated with niche cells to promote HSCs proliferation.

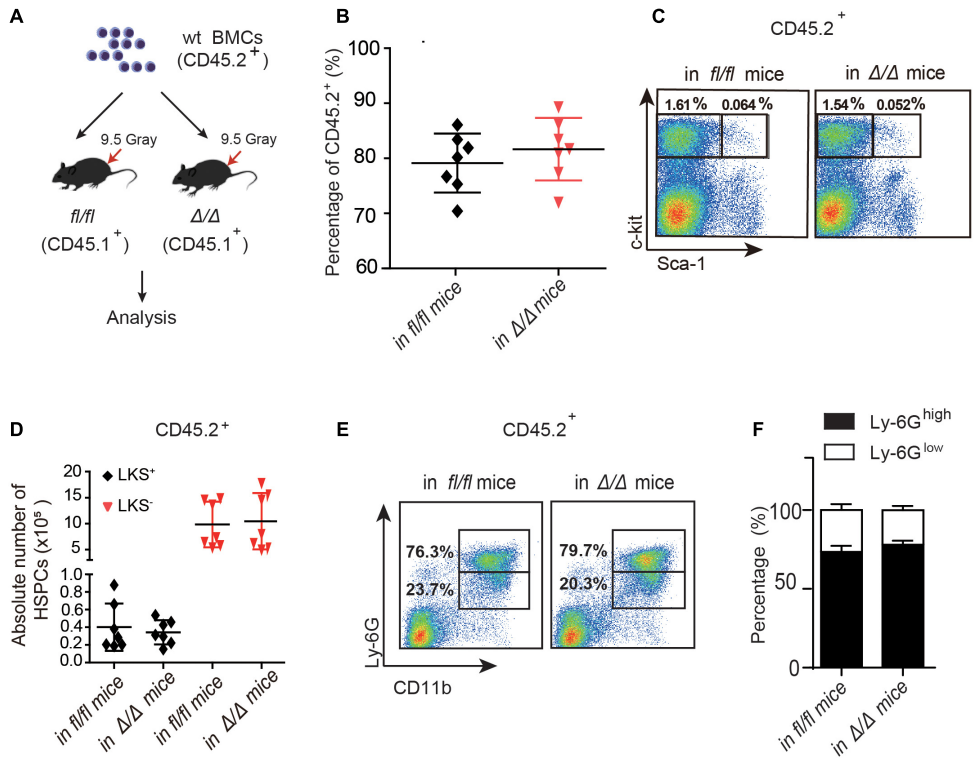

FIGURE 2 | The number of *wt* HSPCs showed no change in *Rheb1*$^{\Delta/\Delta}$ and *Rheb1*$^{fl/fl}$ mice at 4 months after transplantation. **(A)** Wild-type (*wt*) whole bone marrow cells (CD45.2$^+$) were transplantation into lethally irradiated *Rheb1*$^{\Delta/\Delta}$ or *Rheb1*$^{fl/fl}$ mice. **(B)** The percentage of donor-derived cells (CD45.2$^+$) in PB 4 months after transplantation. **(C,D)** The absolute number of donor-derived LKS$^+$ and LKS$^+$ cells (CD45.2$^+$) in BM 4 months after transplantation. **(E,F)** The percentage of donor-derived CD11b$^+$Ly-6G$^{high/low}$ cells (CD45.2$^+$) in BM 4 months after transplantation. The data are presented as the mean ± SD, $n = 7$.

Rheb1-Deficient Neutrophils Stimulate MSCs to Secrete More SCF

To investigate whether *Rheb1*-deficient BM cells interacted with MSCs and stimulated HSCs expansion, we evaluated the expression of Rheb1 and SCF in MSCs from *Rheb1*$^{\Delta/\Delta}$ mice. We found that the mRNA expression of SCF was higher in primary MSCs from *Rheb1*$^{\Delta/\Delta}$ mice than that from *Rheb1*$^{fl/fl}$ mice, while Rheb1 expression was equal in these two cell types (**Figure 3A**). The SCF level in serum was also increased in *Rheb1*$^{\Delta/\Delta}$ mice when compared with that in *Rheb1*$^{fl/fl}$ mice (**Figure 3B**), while the expression of EPO, G-CSF, TPO IL-3 and IL-6 showed no difference between two groups (**Supplementary Figure 3A**). Furthermore, we cultured MSCs derived from *Rheb1*$^{fl/fl}$ and *Rheb1*$^{\Delta/\Delta}$ mice *in vitro* and analyzed the expression of SCF in MSCs after serial passages. We found that in comparison with the MSCs from *Rheb1*$^{fl/fl}$ mice, the expression of SCF remained at a higher level in MSCs from *Rheb1*$^{\Delta/\Delta}$ mice at passage 3 and then decreased to about the same level as in MSCs from that of *Rheb1*$^{fl/fl}$ mice at passage 5 (**Figure 3C**). Interestingly, when *wt* BMCs were transplanted into lethally irradiated *Rheb1*$^{fl/fl}$ and *Rheb1*$^{\Delta/\Delta}$ mice (**Figure 2A**), SCF mRNA expression in MSCs and SCF serum levels were restored to normal levels (**Figures 3D–E**). These results demonstrated that the higher expression of SCF in MSCs from *Rheb1*$^{\Delta/\Delta}$ mice was caused by extrinsic factors from the bone marrow cells of *Rheb1*$^{\Delta/\Delta}$ mice and was reversible under native conditions.

To evaluate the specific role(s) of *Rheb1*$^{\Delta/\Delta}$ BMCs in influencing MSCs, we cocultured *wt* MSCs with *Rheb1*$^{\Delta/\Delta}$ or *Rheb1*$^{fl/f}$ T cells, B cells and myeloid cells for 12 h and then analyzed the expression of SCF in MSCs under each condition. Interestingly, the expression of SCF was higher in MSCs in the presence of *Rheb1*$^{\Delta/\Delta}$ myeloid cells than in the presence of *Rheb1*$^{\Delta/\Delta}$ T cells or B cells (**Supplementary Figure 3B**). In our previous study, we showed that the differentiation of neutrophils was abnormal in the BM of *Rheb1*$^{\Delta/\Delta}$ mice. Hence, we isolated neutrophils (**Supplementary Figure 3C**) from bone marrow cells and cocultured *wt* MSCs with *Rheb1*$^{fl/fl}$ and *Rheb1*$^{\Delta/\Delta}$ neutrophils for 24 h. We found that the expression of SCF was significantly increased in MSCs in the presence of *Rheb1*$^{\Delta/\Delta}$ neutrophils after cultured for 24 h when compared with the control (**Figure 3F**). Taken together, our results suggested that *Rheb1*$^{\Delta/\Delta}$ neutrophils stimulated MSCs to produce more SCF.

Rheb1-Deficient Neutrophil-Trained-MSCs Promote *wt* HSPCs Expansion

We then cocultured 1 × 10^6 LK$^+$ cells with 6 × 10^4 MSCs from *Rheb1*$^{\Delta/\Delta}$ or *Rheb1*$^{fl/fl}$ mice for 24 h and found that the

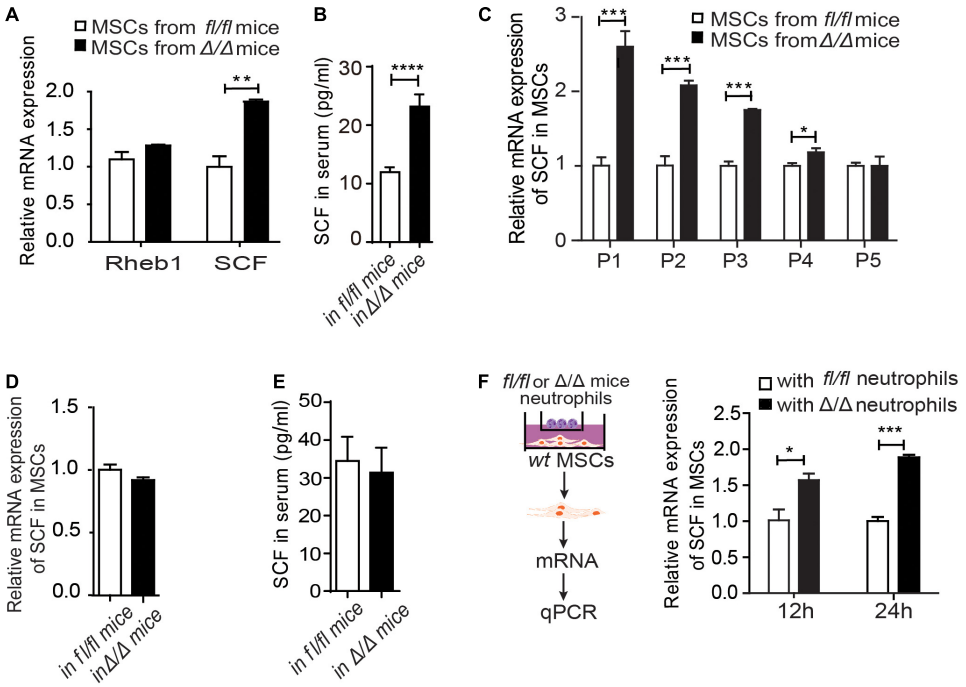

FIGURE 3 | *Rheb1*-deficient neutrophils stimulate MSCs to secrete more SCF. **(A)** The relative mRNA expression of Rheb1 and SCF in primary MSCs from *Rheb1*$^{fl/fl}$ and *Rheb1*$^{\Delta/\Delta}$ mice (n = 3). **(B)** The serum levels of SCF in *Rheb1*$^{fl/fl}$ and *Rheb1*$^{\Delta/\Delta}$ mice (n = 4). **(C)** The relative mRNA expression of SCF in passage 1 (P1) to P5 cultured MSCs from *Rheb1*$^{fl/fl}$ and *Rheb1*$^{\Delta/\Delta}$ mice (n = 3). **(D)** The relative mRNA expression of SCF in MSCs from *Rheb1*$^{fl/fl}$ and *Rheb1*$^{\Delta/\Delta}$ mice 4 months after *wt* BMC transplantation (n = 3). **(E)** The serum level of SCF in *Rheb1*$^{fl/fl}$ or *Rheb1*$^{\Delta/\Delta}$ mice 4 months after *wt* BMC transplantation (n = 3). **(F)** The relative mRNA expression of SCF in *wt* MSCs cocultured with *Rheb1*$^{fl/fl}$ or *Rheb1*$^{\Delta/\Delta}$ neutrophils after 12 h and 24 h (n = 3). The data are presented as the mean ± SD. $^{*}P < 0.05$; $^{**}P < 0.01$; $^{***}P < 0.001$; $^{****}P < 0.0001$.

number of LK^{+} cells cocultured with MSCs from *Rheb1*$^{\Delta/\Delta}$ mice was more than the number of LK^{+} cells cocultured with MSCs from *Rheb1*$^{fl/fl}$ mice (**Figures 4A,B**). Next, we blocked SCF/c-kit signaling by adding a SCF inhibitor in the culture medium. We found that the number of LK^{+} cells was equally decreased in coculturing with MSCs from *Rheb1*$^{\Delta/\Delta}$ or *Rheb1*$^{fl/fl}$ mice in medium with SCF inhibitor (**Supplementary Figures 3D,E**). These results indicated that *Rheb1*-deficient neutrophil-trained MSCs could promote *wt* HSPCs expansion through SCF signaling pathway.

We further cocultured 200 *wt* LKS^{+} (CD45.1^{+}) with 2×10^4 MSCs from *Rheb1*$^{\Delta/\Delta}$ or *Rheb1*$^{fl/fl}$ mice for 24 h, then transplanted the cultured LKS^{+} (CD45.1^{+}) cells with 5×10^5 newly isolated *wt* WBMCs (CD45.2^{+}) into lethally irradiated recipient mice by intravenously injection respectively (**Figure 4C**). We found that the percentage of chimerism was higher in mice transplanted with LKS^{+} cells cocultured with MSCs from *Rheb1*$^{\Delta/\Delta}$ mice when compared with those from *Rheb1*$^{fl/fl}$ mice (**Figure 4D**). Accordingly, the absolute number of LKS^{+} (CD45.1^{+}) cells treated with MSCs from *Rheb1*$^{\Delta/\Delta}$ mice was significantly increased in comparison with the controls at 4 months after transplantation (**Figures 4E,F**). However, the percentage of CD11b^{+} (CD45.1^{+}) myeloid cells was similar in the PB of the two groups (**Figure 4G**). The ratio of Ly-6G^{high}CD11b^{+} and Ly-6G^{low}CD11b^{+} neutrophils was also not changed between the two groups (**Figures 4H,I**). These data indicated that HSPCs cocultured with MSCs from *Rheb1*$^{\Delta/\Delta}$ mice exhibited a higher expansion capacity while their ability to differentiate into myeloid cells was not changed. MSCs educated by *Rheb1*-deficient neutrophils induced LKS^{+} over proliferation but not myeloid differentiation.

Rheb1-Deficient Neutrophils Stimulate MSCs to Produce More SCF by Decreasing IL-6 Expression

To investigate the underlying mechanisms by which *Rheb1*-deficient neutrophils stimulate MSCs to increase SCF production, we measured the mRNA expression of several potential interleukin and chemokine candidates secreted by neutrophils (**Supplementary Figure 3F**). We found that the mRNA and protein expression levels of IL-6 were decreased in *Rheb1*$^{\Delta/\Delta}$ neutrophils when compared with those from the control (**Figures 5A,B**, 0 h). We confirmed that IL-6 is mainly expressed in myeloid cells (**Supplementary Figure 3G**), and found that IL-6 mRNA and protein expression levels in *Rheb1*$^{\Delta/\Delta}$ neutrophils remained lower after cultured with *wt* MSCs for 24 h *in vitro* (**Figures 5A,B**, 24 h). In addition, the level of IL-6 in the *Rheb1*$^{\Delta/\Delta}$ neutrophil coculture medium was also lower than that in the control (**Figure 5C**). These data indicated that *Rheb1*$^{\Delta/\Delta}$ neutrophils expressed and secreted less IL-6 than *Rheb1*$^{fl/fl}$ neutrophils. Since MSCs are immunomodulatory cells

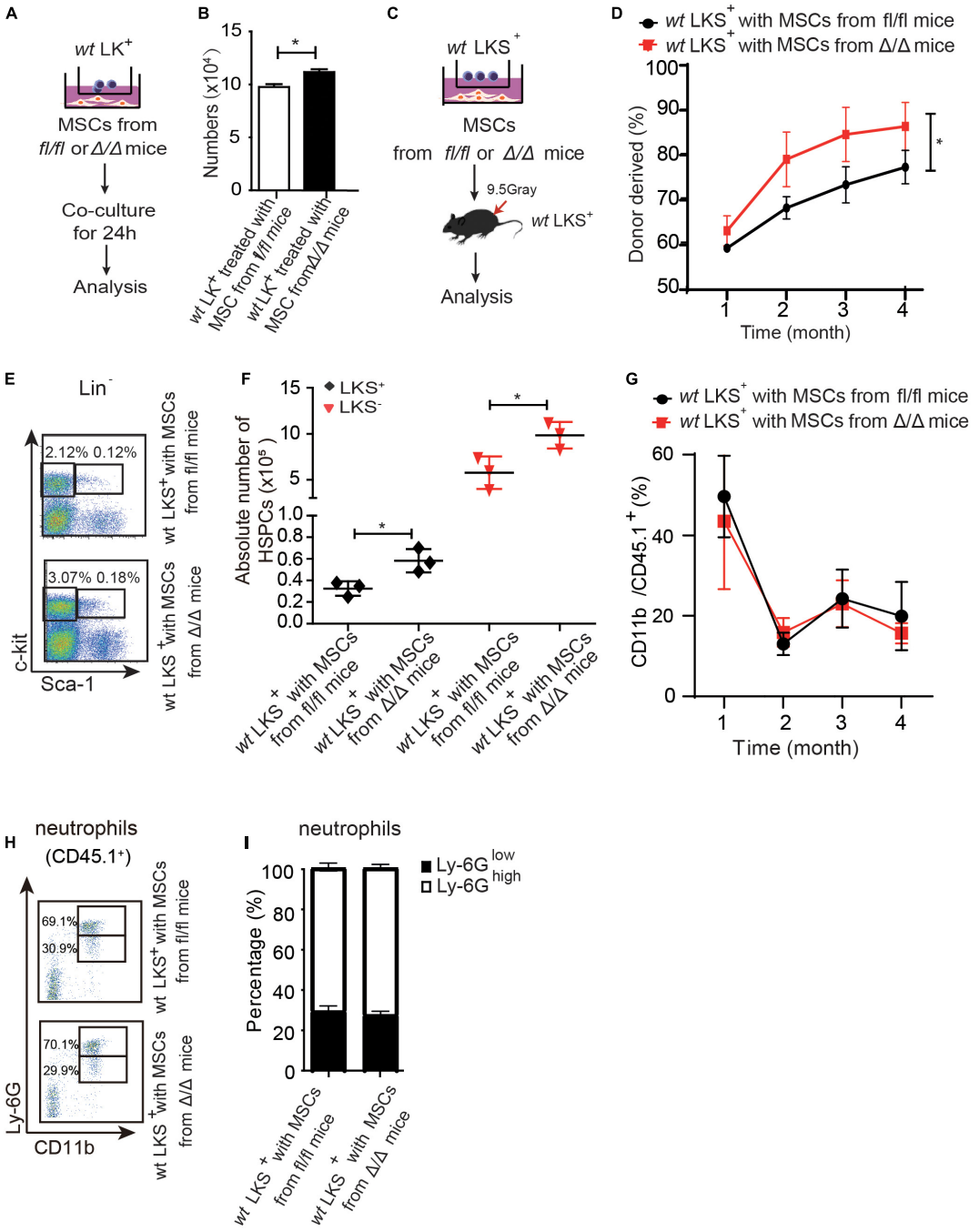

FIGURE 4 | *Rheb1*-deficient neutrophil trained-MSCs promote *wt* HSPCs expansion. **(A,B)** The number of LK$^+$ cells after coculturing with MSCs from *Rheb1*$^{fl/fl}$ and *Rheb1*$^{\Delta/\Delta}$ mice for 24 h. **(C)** *wt* LKS$^+$ (CD45.1$^+$) were cultured with MSCs from *Rheb1*$^{\Delta/\Delta}$ or *Rheb1*$^{fl/fl}$ mice for 24 h, and the cultured LKS$^+$ (CD45.1$^+$) cells and newly isolated *wt* WBMCs (CD45.2$^+$) were transplanted into lethally irradiated recipient mice by intravenously injection. **(D)** The percentage of donor-derived LKS$^+$ cells (CD45.1$^+$) in PB 4 months after transplantation. The data are presented as the mean ± SD, $n = 5$. **(E,F)** The absolute number of donor-derived LKS$^+$ cells (CD45.1$^+$) in BM ($n = 3$). **(G)** The percentage of donor-derived CD11b$^+$ cells (CD45.1$^+$) in PB. The data are presented as the mean ± SD, $n = 5$. **(H,I)** The percentage of donor-derived CD11b$^+$Ly-6G$^{high/low}$ neutrophils (CD45.1$^+$) in BM 4 months after transplantation. The data are presented as the mean ± SD. $^*P < 0.05$.

and secrete a variety of cytokines, including IL-6, we measured the mRNA expression of IL-6 in MSCs and found that its expression in MSCs from *Rheb1*$^{\Delta/\Delta}$ mice was similar to that in MSCs isolated from *Rheb1*$^{fl/fl}$ mice (**Supplementary Figure 3H**). To determine the role of IL-6 in MSCs, we cultured *wt* MSCs with different concentrations of IL-6 and analyzed the relative

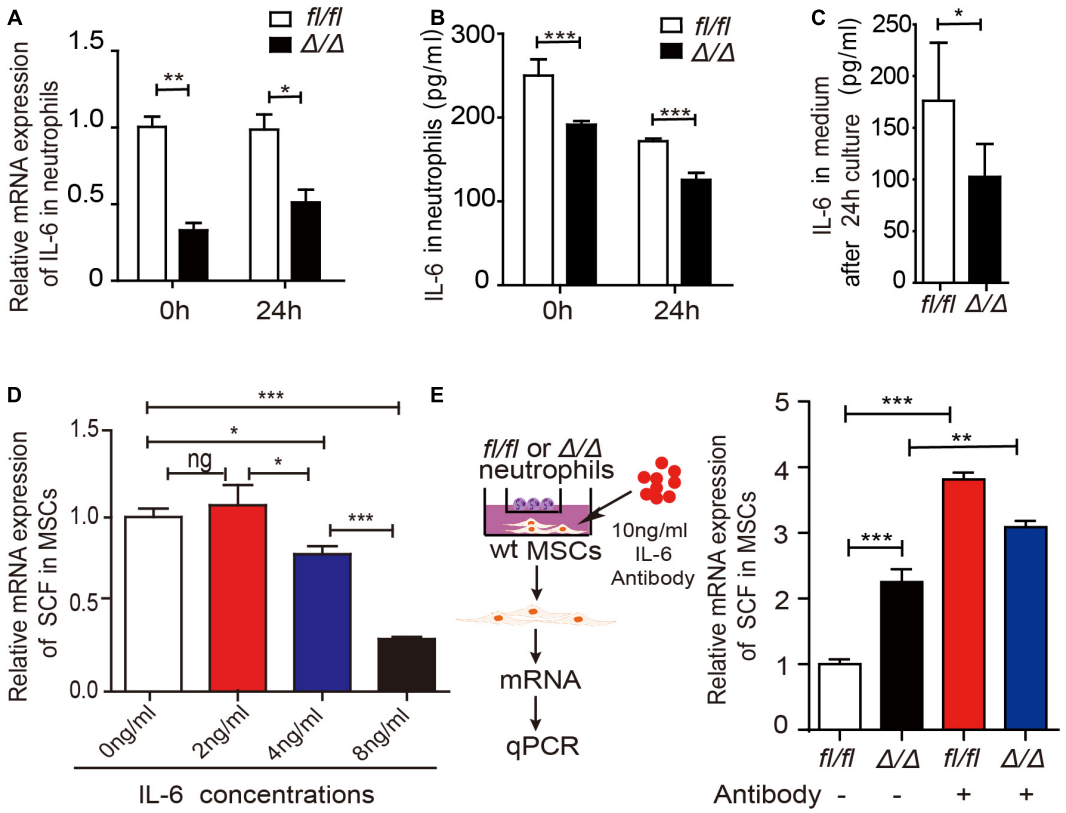

FIGURE 5 | *Rheb1*-deficient neutrophils stimulate MSCs to produce more SCF by decreasing IL-6 expression. **(A)** The relative mRNA expression of IL-6 in *Rheb1*$^{fl/fl}$ or *Rheb1*$^{\Delta/\Delta}$ neutrophils when separated from BM (0 h) or after 24 h of coculture with MSCs (n = 3). **(B)** The protein levels of IL-6 in the cell lysates of *Rheb1*$^{fl/fl}$ and *Rheb1*$^{\Delta/\Delta}$ neutrophils when separated from BM (0 h) or after 24 h of coculture with MSCs (n = 3). **(C)** The IL-6 levels in the media of *Rheb1*$^{fl/fl}$ or *Rheb1*$^{\Delta/\Delta}$ neutrophils cocultured with MSCs (n = 4). **(D)** The relative mRNA expression of SCF in *wt* MSCs after exposure to different concentrations IL-6 for 24 h (n = 3). **(E)** The relative mRNA expression of SCF in *wt* MSCs cocultured with *Rheb1*$^{fl/fl}$ or *Rheb1*$^{\Delta/\Delta}$ neutrophils after being exposed to an IL-6 antibody at 10 ng/ml for 24 h (n = 3). *P < 0.05; **P < 0.01; ***P < 0.001.

SCF mRNA expression in MSCs at 24 h. We found that higher IL-6 treatment suppressed SCF mRNA expression in MSCs (**Figure 5D**). We then blocked IL-6 signaling by adding an IL-6 neutralizing antibody in the media in which *Rheb1*$^{\Delta/\Delta}$ or *Rheb1*$^{fl/fl}$ neutrophils were cocultured with *wt* MSCs, and measured the expression of SCF mRNA in MSCs (**Figure 5E**, left panel). We found that the mRNA expression of SCF was significantly increased in MSCs after treatment with the IL-6-neutralizing antibody in coculture with either *Rheb1*$^{fl/fl}$ or *Rheb1*$^{\Delta/\Delta}$ neutrophils (**Figure 5E**, right panel). These data suggested that the lower expression of IL-6 in *Rheb1*$^{\Delta/\Delta}$ neutrophils stimulated the expression of SCF in MSCs.

IL-6 Regulates SCF Expression in Human MSCs

It has been reported that IL-6 was higher in CML patients (Panteli et al., 2005) and higher level of IL-6 is associated with poor prognosis in CML patients (Nievergall et al., 2016). To evaluate the relationship of IL-6 and SCF expression level in human cells, we first investigated whether IL-6 regulates SCF expression in human MSCs. We cultured MSCs from human umbilical cord blood with different concentrations of IL-6 and analyzed the relative SCF mRNA expression in MSCs at 24 h. The result showed that higher IL-6 treatment suppressed SCF mRNA expression in human MSCs (**Figure 6A**). Next we isolated MNCs and MSCs from the BM of 39 CML patients, and measured the expression of IL-6 in mononuclear cells and the expression of SCF in MSCs in patients (**Figure 6B**, left panel). We found a negative correlation of SCF and IL-6 by analyzing the relationship of IL-6 and SCF expression in CML patients (n = 39) (**Figure 6B**, right panel). The data indicated that higher expression of IL-6 in myeloid cells is associated with the lower expression of SCF in MSCs in CML patients.

DISCUSSION

We previously found that the HSPCs were over-expanded in *Vav1-Cre;Rheb1*$^{fl/fl}$ mice (Wang et al., 2018). Here, using *in vivo* and *in vitro* models, we found that loss of *Rheb1* impaired neutrophils' ability to secrete IL-6, which stimulated MSCs to secrete more SCF and in turn stimulated HSPCs to proliferate (**Figure 6C**).

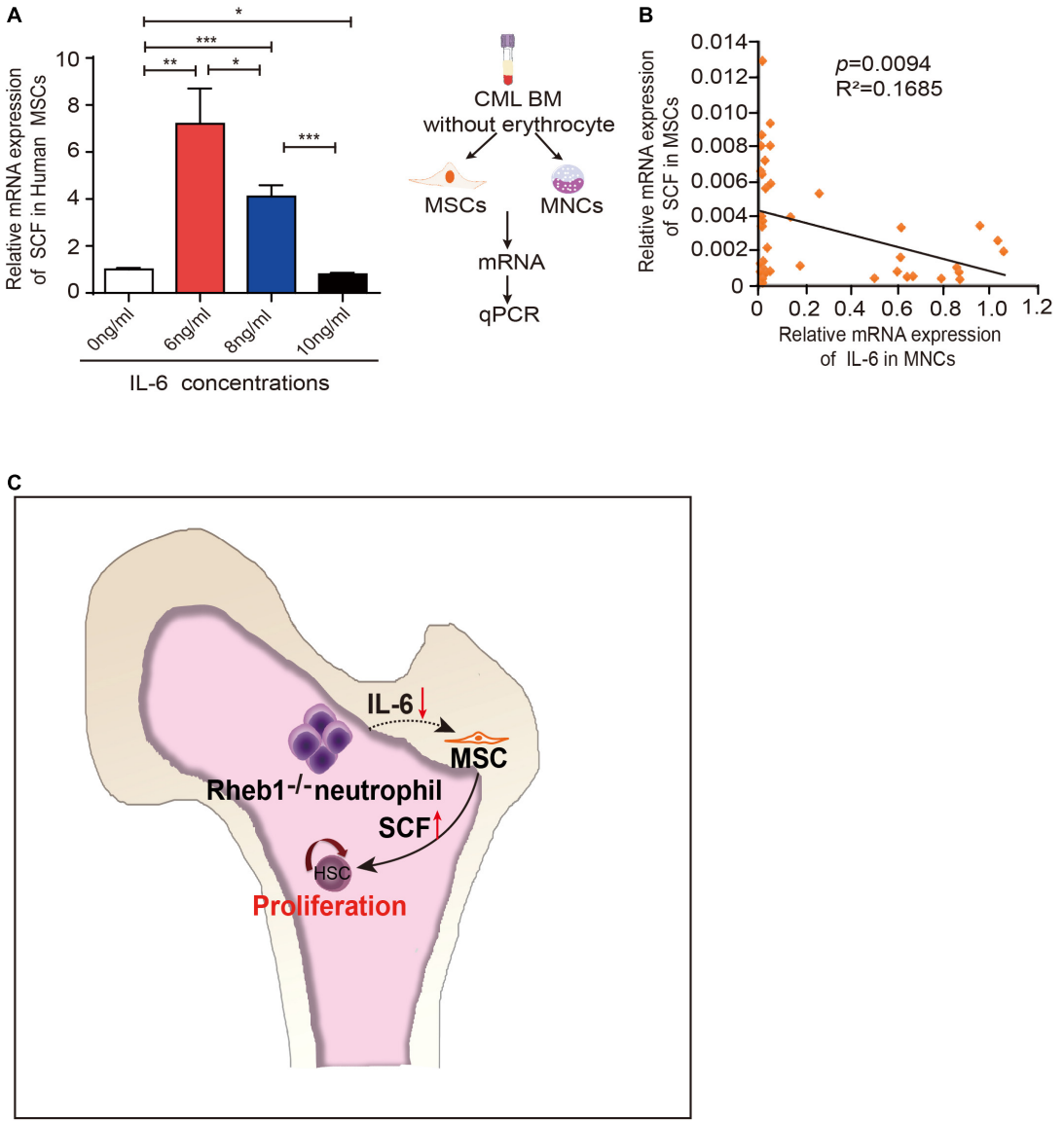

FIGURE 6 | IL-6 regulates SCF expression in human MSCs. **(A)** The relative mRNA expression of SCF in H-MSCs after exposure to different concentrations IL-6 for 24 h (n = 3). The data are presented as the mean ± SD. **(B)** Correlation analysis for SCF and IL-6 mRNA expression in CML patients (n = 39) (p = 0.0094). R: Pearson correlation coefficients; R^2: indicates "the goodness of fit." Statistical significance was calculated by Pearson correlation coefficients. **(C)** Model depicting hematopoietic regulation in the absence of *Rheb1*. *P < 0.05; **P < 0.01; ***P < 0.001.

The microenvironment in BM comprises multipotent stromal cells (MSCs), osteoblasts, endothelial cells, mature blood cells and the cytokines that they produced (Gao et al., 2018). We previously showed that the differentiation and maturation of neutrophils in BM were abnormal in *Rheb1*$^{\Delta/\Delta}$ HSCs, leading aged *Rheb1*$^{\Delta/\Delta}$ mice to show MPN-like symptoms (Wang et al., 2018). Neutrophils and their progenitors have been shown to secrete a variety of cytokines to influence the development and proliferation of HSCs either directly or indirectly. For example, apoptotic neutrophils can stimulate macrophages to secrete G-CSF and regulate HSCs indirectly in zebrafish (Hall et al., 2016). Gr-1^{+} neutrophils in mouse bone marrow produce ROS during acute infection, which contributes to the proliferation of HSPCs via a paracrine mechanism (Kwak et al., 2015). Senescent neutrophils are markedly increased in aged mice and promote an increase in platelet-biased HSCs via IL-1β (Frisch et al., 2019). Our results demonstrated that *Rheb1*$^{\Delta/\Delta}$ neutrophils remodeled the BM niche, and induced HSPCs to undergo overexpansion in BM (**Figure 3**) probably via a feedback in MSC through the proinflammatory factor IL-6 (**Figures 4**, **5**). This partially supported that the abnormal myeloid cells could regulate the proliferation of HSCs in MPN patients (Schepers et al., 2013).

IL-6 was higher in CML patients and was elevated during the transformation phase of CML (Panteli et al., 2005), while blocking

IL-6 signaling could delay CML development in mouse model (Reynaud et al., 2011). More importantly, higher level of IL-6 is shown to be associated with poor prognosis in CML patients (Nievergall et al., 2016). We found there is a negative correlation of SCF with IL-6 in CML patients (**Figure 6B**), indicating that higher IL-6 could inhibit MSCs to secrete SCF and impair normal HSPC proliferation, thus promote CML progression. It suggested that blocking IL-6 signaling might be benefit for the restoration of HSC proliferation in CML patients.

Rheb1 has been implicated in many metabolic processes via the canonical TSC/Rheb/mTOR signaling pathway and/or non-canonical signaling pathways. We previously reported that *Rheb1* deficiency inhibited neutrophil maturation through the mTOR signaling pathway (Wang et al., 2018). We found mTORC1 inhibitor Rapamycin could reduce p-S6 level and IL-6 RNA expression level in neutrophils (data not shown), which was consistent with blocking Rheb1-mTORC1 signaling pathway decreased IL-6 expression in IL-33 stimulated type 2 innate lymphoid cells (ILC2) (Petrova et al., 2020). Since IL-6 is a pleiotropic cytokine and a strong activator of Mammalian Target of Rapamycin (mTOR) (Pinno et al., 2016), it is possible that *Rheb1* regulates IL-6 expression through a negative feedback loop affecting mTORC1. Several studies revealed that the inhibition of B-Raf and Dyneinor activation of the Notch signaling pathway by *Rheb1* is independent of the mTORC1 pathway (Neuman and Henske, 2011), and increased Notch signaling increases IL-6 expression, leading to the activation of IL-6/JAK/STAT signaling (Jin et al., 2013). The specific role and mechanism of *Rheb1* in the IL-6 signaling pathway in neutrophils need to be further investigated.

DATA AVAILABILITY STATEMENT

The original contributions presented in the study are included in the article/**Supplementary Material**, further inquiries can be directed to the corresponding author/s.

ETHICS STATEMENT

The studies involving human participants were reviewed and approved by the Ethics Committee of Blood Diseases Hospital, Chinese Academy of Medical Sciences. The patients/participants provided their written informed consent to participate in this study. The animal study was reviewed and approved by Institutional Animal Care and Use Committee (IACUC), Institute of Hematology and Blood Diseases Hospital (CAMS/PUMC).

AUTHOR CONTRIBUTIONS

JG, SH, and XW performed the experiments, analyzed the data, and wrote the manuscript. SY, YW, YG, and XS helped with the *in vivo* experiments and data collection. WW, YC, YZ, XF, HL, TC, and JS contributed to the data analyses and manuscript discussion. XW and WY conceived and directed the research project and revised the manuscript. All authors contributed to the article and approved the submitted version.

FUNDING

This work was supported by funds from the Ministry of Science and Technology of China (2018YFA0107801 and 2017YFA0103402), the Chinese Academy of Medical Sciences Innovation Fund for Medical Sciences, CIFMS (2017-I2M-3-015, 2016-I2M-1-017, and 2017-I2M-3-018), and the National Natural Science Foundation of China (81870088, 81700103, 81770105, 81670120, 81629001, and 81421002).

SUPPLEMENTARY MATERIAL

The Supplementary Material for this article can be found online at: https://www.frontiersin.org/articles/10.3389/fcell.2021.650599/full#supplementary-material

REFERENCES

Arranz, L., Sanchez-Aguilera, A., Martin-Perez, D., Isern, J., Langa, X., Tzankov, A., et al. (2014). Neuropathy of haematopoietic stem cell niche is essential for myeloproliferative neoplasms. *Nature* 512, 78–81. doi: 10.1038/nature13383

Aspuria, P. J., and Tamanoi, F. (2004). The Rheb family of GTP-binding proteins. *Cell. Signal.* 16, 1105. doi: 10.1016/j.cellsig.2004.03.019

Chow, A., Lucas, D., Hidalgo, A., Mendez-Ferrer, S., Hashimoto, D., Scheiermann, C., et al. (2011). Bone marrow CD169+ macrophages promote the retention of hematopoietic stem and progenitor cells in the mesenchymal stem cell niche. *J. Exp. Med.* 208, 261–271. doi: 10.1084/jem.20101688

Feng, C. G., Weksberg, D. C., Taylor, G. A., Sher, A., and Goodell, M. A. (2008). The p47 GTPase Lrg-47 (Irgm1) links host defense and hematopoietic stem cell proliferation. *Cell Stem Cell* 2, 83–89. doi: 10.1016/j.stem.2007.10.007

Frenette, P. S., Pinho, S., Lucas, D., and Scheiermann, C. (2013). Mesenchymal stem cell: keystone of the hematopoietic stem cell niche and a stepping-stone for regenerative medicine. *Annu. Rev. Immunol.* 31, 285–316. doi: 10.1146/annurev-immunol-032712-095919

Frisch, B. J., Hoffman, C. M., Latchney, S. E., LaMere, M. W., Myers, J., Ashton, J., et al. (2019). Aged marrow macrophages expand platelet-biased hematopoietic stem cells via Interleukin1. *JCI Insight* 5:e124213.

Gao, X., Xu, C., Asada, N., and Frenette, P. S. (2018). The hematopoietic stem cell niche: from embryo to adult. *Development* 145:dev139691. doi: 10.1242/dev.139691

Gao, Y., Gao, J., Li, M., Zheng, Y., Wang, Y., Zhang, H., et al. (2016). Rheb1 promotes tumor progression through mTORC1 in MLL-AF9-initiated murine acute myeloid leukemia. *J. Hematol. Oncol.* 9:36.

Greenbaum, A., Hsu, Y. M., Day, R. B., Schuettpelz, L. G., Christopher, M. J., Borgerding, J. N., et al. (2013). CXCL12 in early mesenchymal progenitors is required for haematopoietic stem-cell maintenance. *Nature* 495, 227–230. doi: 10.1038/nature11926

Hall, C., Crosier, P., and Crosier, K. (2016). Inflammatory cytokines provide both infection-responsive and developmental signals for blood development: lessons from the zebrafish. *Mol. Immunol.* 69, 113–122. doi: 10.1016/j.molimm.2015.10.020

Jin, S., Mutvei, A. P., Chivukula, I. V., Andersson, E. R., Ramskold, D., Sandberg, R., et al. (2013). Non-canonical Notch signaling activates

IL-6/JAK/STAT signaling in breast tumor cells and is controlled by p53 and IKKalpha/IKKbeta. *Oncogene* 32, 4892–4902. doi: 10.1038/onc.2012.517

Kwak, H. J., Liu, P., Bajrami, B., Xu, Y., Park, S. Y., Nombela-Arrieta, C., et al. (2015). Myeloid cell-derived reactive oxygen species externally regulate the proliferation of myeloid progenitors in emergency granulopoiesis. *Immunity* 42, 159–171. doi: 10.1016/j.immuni.2014.12.017

Meng, Z., Perry, J. M., Heather, M., Aparna, V., Pengxu, Q., He, X. C., et al. (2014). Megakaryocytes maintain homeostatic quiescence and promote post-injury regeneration of hematopoietic stem cells. *Nat. Med.* 20, 1321–1326. doi: 10.1038/nm.3706

Neuman, N. A., and Henske, E. P. (2011). Non-canonical functions of the tuberous sclerosis complex-Rheb signalling axis. *EMBO Mol. Med.* 3, 189–200. doi: 10.1002/emmm.201100131

Nievergall, E., Reynolds, J., Kok, C. H., Watkins, D. B., Biondo, M., Busfield, S. J., et al. (2016). TGF-α and IL-6 plasma levels selectively identify CML patients who fail to achieve an early molecular response or progress in the first year of therapy. *Leukemia* 30, 1263–1272. doi: 10.1038/leu.2016.34

Panteli, K. E., Hatzimichael, E. C., Bouranta, P. K., Katsaraki, A., Seferiadis, K., Stebbing, J., et al. (2005). Serum interleukin (IL)-1, IL-2, sIL-2Ra, IL-6 and thrombopoietin levels in patients with chronic myeloproliferative diseases. *Br. J. Haematol.* 130, 709–715. doi: 10.1111/j.1365-2141.2005.05674.x

Petrova, T., Pesic, J., Pardali, K., Gaestel, M., and Arthur, J. S. C. (2020). p38 MAPK signalling regulates cytokine production in IL-33 stimulated Type 2 Innate Lymphoid cells. *Sci. Rep.* 10:3479.

Pinno, J., Bongartz, H., Klepsch, O., Wundrack, N., Poli, V., Schaper, F., et al. (2016). Interleukin-6 influences stress-signalling by reducing the expression of the mTOR-inhibitor REDD1 in a STAT3-dependent manner. *Cell. Signal.* 28, 907–916. doi: 10.1016/j.cellsig.2016.04.004

Raaijmakers, M. H. (2012). Myelodysplastic syndromes: revisiting the role of the bone marrow microenvironment in disease pathogenesis. *Int. J. Hematol.* 95, 17–25. doi: 10.1007/s12185-011-1001-x

Rathinam, C., and Flavell, R. A. (2008). The hematopoiesis paradigm: Clarity or ambiguity? *Blood* 112, 3534–3535. doi: 10.1182/blood-2008-07-167759

Reynaud, D., Pietras, E., Barry-Holson, K., Mir, A., Binnewies, M., Jeanne, M., et al. (2011). IL-6 controls leukemic multipotent progenitor cell fate and contributes to chronic myelogenous leukemia development. *Cancer Cell* 20, 661–673. doi: 10.1016/j.ccr.2011.10.012

Schepers, K., Pietras, E. M., Reynaud, D., Flach, J., Binnewies, M., Garg, T., et al. (2013). Myeloproliferative neoplasia remodels the endosteal bone marrow niche into a self-reinforcing leukemic niche. *Cell Stem Cell* 13, 285–299. doi: 10.1016/j.stem.2013.06.009

Swamydas, M., Luo, Y., Dorf, M. E., and Lionakis, M. S. (2015). Isolation of mouse neutrophils. *Curr. Protoc. Immunol.* 110, 3.20.1–3.20.15.

Wang, X., Chu, Y., Wang, W., and Yuan, W. (2016a). mTORC signaling in hematopoiesis. *Int. J. Hematol.* 103, 510–518.

Wang, X., Gao, Y., Gao, J., Li, M., Zhou, M., Wang, J., et al. (2018). Rheb1 loss leads to increased hematopoietic stem cell proliferation and myeloid-biased differentiation in vivo. *Haematologica* 104, 245–255. doi: 10.3324/haematol.2018.194811

Wang, X., Li, M., Gao, Y., Gao, J., Yang, W., Liang, H., et al. (2016b). Rheb1-mTORC1 maintains macrophage differentiation and phagocytosis in mice. *Exp. Cell Res.* 344, 219–228. doi: 10.1016/j.yexcr.2016.04.017

Zhu, H., Guo, Z. K., Jiang, X. X., Li, H., Wang, X. Y., Yao, H. Y., et al. (2010). A protocol for isolation and culture of mesenchymal stem cells from mouse compact bone. *Nat. Protoc.* 5, 550–560. doi: 10.1038/nprot.2009.238

Zou, J., Zhou, L., Du, X. X., Ji, Y., Xu, J., Tian, J., et al. (2011). Rheb1 is required for mTORC1 and myelination in postnatal brain development. *Dev. Cell* 20, 97–108. doi: 10.1016/j.devcel.2010.11.020

Conflict of Interest: The authors declare that the research was conducted in the absence of any commercial or financial relationships that could be construed as a potential conflict of interest.

frontiers in Cell and Developmental Biology

ORIGINAL RESEARCH
published: 11 August 2021
doi: 10.3389/fcell.2021.699263

Spatiotemporal and Functional Heterogeneity of Hematopoietic Stem Cell-Competent Hemogenic Endothelial Cells in Mouse Embryos

Yun-Qiao Li[1], Yandong Gong[2], Siyuan Hou[3], Tao Huang[1], Haizhen Wang[3], Di Liu[4], Yanli Ni[2], Chaojie Wang[3], Junliang Wang[5], Jun Hou[6], Ruichuang Yang[6], Jing Yan[1], Guangyu Zhang[1], Bing Liu[1,2,3] and Yu Lan[3]**

[1] State Key Laboratory of Proteomics, Academy of Military Medical Sciences, Academy of Military Sciences, Beijing, China, [2] State Key Laboratory of Experimental Hematology, Fifth Medical Center of Chinese PLA General Hospital, Institute of Hematology, Beijing, China, [3] Key Laboratory for Regenerative Medicine of Ministry of Education, School of Medicine, Institute of Hematology, Jinan University, Guangzhou, China, [4] Peking-Tsinghua Center for Life Sciences, Peking University, Beijing, China, [5] Department of Radiotherapy, The Fifth Medical Center of Chinese PLA General Hospital, Beijing, China, [6] The Fifth Medical Center of PLA General Hospital, National Clinical Research Center for Infectious Diseases, Beijing, China

Hematopoietic stem cells (HSCs) are derived from hemogenic endothelial cells (HECs) during embryogenesis. The HSC-primed HECs increased to the peak at embryonic day (E) 10 and have been efficiently captured by the marker combination $CD41^{-}CD43^{-}CD45^{-}CD31^{+}CD201^{+}Kit^{+}CD44^{+}$ (PK44) in the aorta-gonad-mesonephros (AGM) region of mouse embryos most recently. In the present study, we investigated the spatiotemporal and functional heterogeneity of PK44 cells around the time of emergence of HSCs. First, PK44 cells in the E10.0 AGM region could be further divided into three molecularly different populations showing endothelial- or hematopoietic-biased characteristics. Specifically, with the combination of Kit, the expression of CD93 or CD146 could divide PK44 cells into endothelial- and hematopoietic-feature biased populations, which was further functionally validated at the single-cell level. Next, the PK44 population could also be detected in the yolk sac, showing similar developmental dynamics and functional diversification with those in the AGM region. Importantly, PK44 cells in the yolk sac demonstrated an unambiguous multilineage reconstitution capacity after *in vitro* incubation. Regardless of the functional similarity, PK44 cells in the yolk sac displayed transcriptional features different from those in the AGM region. Taken together, our work delineates the spatiotemporal characteristics of HECs represented by PK44 and reveals a previously unknown HSC competence of HECs in the yolk sac. These findings provide a fundamental basis for in-depth study of the different origins and molecular programs of HSC generation in the future.

Keywords: hematopoietic stem cells, hemogenic endothelial cells, heterogeneity, developmental hematopoiesis, single-cell RNA-sequencing

OPEN ACCESS

Edited by:
Yiyue Zhang,
South China University of Technology, China

Reviewed by:
James Palis,
University of Rochester, United States
Eirini Trompouki,
Max Planck Institute for Immunobiology and Epigenetics, Germany
Chunjiang He,
Huazhong Agricultural University, China

****Correspondence:***
Bing Liu
bingliu17@126.com
Yu Lan
rainyblue_1999@126.com

Specialty section:
This article was submitted to Stem Cell Research, a section of the journal Frontiers in Cell and Developmental Biology

Received: *23 April 2021*
Accepted: *19 July 2021*
Published: *11 August 2021*

Citation:
Li Y-Q, Gong Y, Hou S, Huang T, Wang H, Liu D, Ni Y, Wang C, Wang J, Hou J, Yang R, Yan J, Zhang G, Liu B and Lan Y (2021) Spatiotemporal and Functional Heterogeneity of Hematopoietic Stem Cell-Competent Hemogenic Endothelial Cells in Mouse Embryos. Front. Cell Dev. Biol. 9:699263. doi: 10.3389/fcell.2021.699263

INTRODUCTION

As the cornerstone of the adult hematopoietic system, self-renewal and multilineage hematopoietic differentiation are the dominant features of hematopoietic stem cells (HSCs). HSCs are widely proposed to be derived from a special subgroup of endothelial cells, called hemogenic endothelial cells (HECs), in the aorta-gonad-mesonephros (AGM) region around embryonic day (E) 10.0 through the endothelial-to-hematopoietic transition (EHT) process. It is widely proposed that HECs express CD47, CD61, and Dll4 (Huang et al., 2016; Zhou et al., 2016) in addition to pan-endothelial markers such as Flk1 and VE-Cadherin (Yamashita et al., 2000; Yokomizo and Dzierzak, 2010; Hadland et al., 2017) but lack the expression of hematopoietic markers CD41, CD43, and CD45 (Taoudi et al., 2005; Swiers et al., 2013). The expression of Runx1, a transcription factor critically required for the process of EHT (Chen et al., 2009; Swiers et al., 2013; Gao et al., 2018; Lie et al., 2018), represents a hallmark of HECs. Based on this, *Runx1 + 23GFP* (GFP transgene on the Runx1 + 23 enhancer locus) transgenic reporter mouse model has been established to enrich HECs for molecular/phenotypic and functional analyses (Swiers et al., 2013). Similarly, *Gfi1-Tomato* transgenic mice are used to delineate the process of EHT (Thambyrajah et al., 2016). However, the enrichment with the surface markers or transgenic reporters mentioned above is insufficient, and the HSC competence of HECs has not been directly confirmed.

Recently, we elucidated the precise identity of HSC-primed HECs by high-precision single-cell transcriptomic profiling. With *in vivo* functional validation, we identified the PK44 ($CD41^-CD43^-CD45^-CD31^+CD201^+Kit^+CD44^+$) population as HSC-competent HECs (Hou et al., 2020). Additionally, functional heterogeneity of the PK44 population was revealed *in vitro* at the single-cell level, involving three kinds of differentiation potentials, namely, only endothelial potential, endothelial-hematopoietic dual potential, and only hematopoietic potential (Hou et al., 2020). Nevertheless, the characteristics of these heterogeneous subpopulations within immunophenotypic PK44 cells remain unclear and deserve further investigation.

Whether the hematopoietic cells produced by the extra-embryonic yolk sac can sustain hematopoiesis during the lifespan has long been debated (Samokhvalov et al., 2007; Lee et al., 2016). The blood circulation in embryos precludes the possibility of precisely addressing if the yolk sac can *in situ* produce HSCs (Cumano et al., 2001). It is known that HECs also exist in the extra-embryonic yolk sac besides the intra-embryonic AGM region (Frame et al., 2016; Lee et al., 2016). Considering that PK44 efficiently enriches HSC-primed HECs in AGM, the performance of the immunophenotypic PK44 population in the yolk sac is worthy of investigation.

Index sorting is a very innovative mode of flow cytometry that can capture the expression profiles of multiple proteins of each sorted cell (Schulte et al., 2015). The characteristics of index sorting make it useful in exploring immunophenotypes of populations with a specific functional readout. In this study, we focus on the hematopoietic potential of PK44 cells, and we achieved further enrichment of the hematopoietic potential within PK44 cells in the AGM region using additional surface markers by the index sorting function. We also explored the spatiotemporal and functional heterogeneity of AGM and yolk sac PK44 populations. Our findings in total shed light on the in-depth understanding of HSC emergence during embryogenesis.

MATERIALS AND METHODS

Mice

All the mice used in the experiment were raised in the Laboratory Animal Center of Academy of Military Medical Sciences. The experimental operation of mice was carried out with the approval of the Animal Care and Use Committee of the Institute. All mice were maintained on C57BL/6 background. Embryos were staged by somite pair (sp) counting: E9.5, 21-30 sp; E10.0, 31-35 sp; E10.5, 36-40 sp; and E11.0, 41-45 sp. For E9.5 embryos, the caudal half was dissected under the heart with the limbs removed. For embryos older than E10.0, the AGM region was dissected as previously reported (Hou et al., 2020).

Flow Cytometry

Cells were analyzed and sorted by flow cytometers FACS Aria 2 and Calibur (BD Biosciences), and the data were analyzed with FlowJo software (Tree Star). Cells were stained by the following antibodies: B220 (eBioscience, RA3-6B2), CD3 (eBioscience, 145-2C11), CD4 (eBioscience, GK1.5), CD8 (eBioscience, 53-6.7), CD19 (eBioscience, eBio1D3), CD31 (BD or BioLegend, MEC13.3), CD34 (eBioscience, RAM34), CD41 (BD or eBioscience, MWReg30), CD43 (BD, S7), CD44 (eBioscience or BioLegend, IM7), CD45 (eBioscience, 30-F11), CD45.1 (eBioscience, A20), CD45.2 (eBioscience, 104), CD47 (eBioscience, miap301), CD49d (Biolegend, R1-2), CD93 (eBioscience, AA4.1), CD133 (Biolegend, 315-2C11), CD146 (BD, ME-9F1), CD201 (eBioscience, eBio1560), CD304 (Biolegend, 3E12), Flk1 (eBioscience, Avas12a1), Flk2 (Biolegend, A2F10), F4/80 (Biolegend, 93), Kit (eBioscience, 2B8), Ly-6G (BioLegend, 1A8), Mac-1 (eBioscience, M1/70), Sca-1 (eBioscience, D7), Ter119 (BD, TER-119), and 7-amino-actinomycin D (7-AAD; eBioscience).

Colony Forming Unit-Culture (CFU-C) Assay

Cells were sorted by flow cytometry and cultured in a 35 mm Petri dish containing 2.5 mL methylcellulose-based medium with recombinant cytokines (MethoCult GF M3434, STEMCELL Technologies) for 7 days for the colony-forming assay. Hematopoietic colonies were scored individually by microscope.

In vitro Hematopoietic and Endothelial Potential Assay

Cells were sorted by the FACS Diva 8 "index sorting" function in single-cell mode and were then individually plated on OP9-DL1 stromal cells in IMDM (Hyclone) containing 1% bovine serum albumin (Sigma), 10 μg/mL insulin (Macgene), 15% fetal bovine

serum (Hyclone), 5.5×10^{-5} mol/L 2-mercaptoethanol (Gibco), and 200 μg/mL transferrin (Sigma), 50 ng/mL SCF (PeproTech) and 100 ng/mL rhVEGF-165 (PeproTech). After 7 days co-culture with OP9-DL1, cells were fixed in 2% paraformaldehyde for 20 min and then stained with CD45 antibody (BD Biosciences). Subsequently, CD31 (BD Pharmingen, MEC13.3) immunohistochemistry staining was performed. When only $CD31^+$ endothelial tubes were detected, the single cell plated in the well was considered to have only endothelial potential. When $CD45^+$ round cells but no $CD31^+$ endothelial tubes were detected, the single cell plated in the well was considered to have only hematopoietic potential. When both $CD31^+$ endothelial tubes and $CD45^+$ round cells were simultaneously detected in the same single-cell well, the plated cell was considered to have both endothelial and hematopoietic potential (Hou et al., 2020).

OP9-DL1 Co-culture and HSC Transplantation Assay

To investigate the HSC potential of the PK44 population in E10.0 AGM and yolk sac, male CD45.1/1 mice were mated with female CD45.2/2 mice to obtain CD45.1/2 embryos, which were used as donors for PK44 cells. PK44 cells were sorted and plated on OP9-DL1 stromal cells in α-MEM (Gibco) containing 10% fetal bovine serum (Hyclone), 2 mM glutamine (Hyclone), 100 U/mL penicillin, and 100 mg/mL streptomycin (Hyclone) and cytokines (100 ng/mL SCF, 100 ng/mL Flt3 ligand, and 100 ng/mL IL-3, all from PeproTech) as we previously reported (Hou et al., 2020). After 7 days of co-culture, all cells in each well were collected (with trypsin digestion), and the culture progenies together with 2×10^4 nucleated fresh bone marrow carrier cells (CD45.1/1 background) were injected into 10- to 12-week female recipients (CD45.2/2 background), which were exposed to a split dose of 9 Gy γ-irradiation (^{60}Co) via tail vein. Peripheral blood cells of recipients were detected by flow cytometry at 4, 8, 12, and 16 weeks post-transplantation, respectively, to determine the chimerism. The recipients demonstrating ≥5% donor-derived chimerism in $CD45^+$cells of peripheral blood were counted as successfully reconstituted. Multiorgan and multilineage reconstitution were analyzed as reported (Hou et al., 2020).

Preprocessing Single-Cell RNA-Seq Data

For scRNA-seq data from modified STRT-seq, raw reads of each cell were first split by a specific barcode sequence attached in Read 2. The template switch oligo (TSO) sequence and polyA tail sequence were trimmed for the corresponding Read 1 after UMI information was aligned to it. Subsequently, reads with adapter contaminants or low-quality bases (N > 10%) were discarded. Next, the stripped Read 1 sequences were aligned to mm10 mouse transcriptome (UCSC) using Hisat2 (version 2.1.0) (Kim et al., 2015). Uniquely mapped reads were counted by HTSeq package (Anders et al., 2015) and grouped by the cell-specific barcodes. Duplicated transcripts were removed based on the UMI information for each gene. Finally, for each individual cell, the copy number of transcripts of a given gene was the number of the distinct UMIs of that gene. To filter low-quality cells, count values for each cell were first grouped in an expression matrix, and only cells with more than 2000 genes and 10,000 transcripts detected were retained. Also, cells with too many raw reads (> 1,000,000) and genes (> 10,000) were excluded because these cells might not be real single cells.

Cell Type Detection and Dimensionality Reduction

Downstream analysis for well-based modified STRT-seq—such as data normalization, clustering, differential expression analysis, principal component analysis (PCA), and Uniform Manifold Approximation and Projection (UMAP) analysis—were implemented using the R package Seurat 2 and monocle 2. Harmony was employed to integrate AGM and yolk sac data.

Differentially Expressed Genes (DEGs) and Cluster Biomarker Identification

DEGs were identified by running the "FindAllMarkers" function using ROC test (**Figure 2**) or Wilcoxon rank sum test (**Figure 5**) in Seurat 2. High-confidence surfaceome proteins identified in the Cell Surface Protein Atlas were marked as surface molecules. All DEGs of specific clusters and the surface proteins list are listed in the **Supplementary Tables 1, 2**.

Gene Ontology (GO) Analysis

To interpret the biological meaning of DEGs, GO analyses were performed by clusterProfiler using all the DEGs, and then, the top 10 GO terms with P value < 0.05 were selected for visualization using bar plots.

Endothelial and Hematopoietic Feature Score

The endothelial and hematopoietic feature score was assigned to each cell by using the "AddModuleScore" function in Seurat. Fifteen representative endothelial genes (*Gja4*, *Unc5b*, *Mecom*, *Hey1*, *Efnb2*, *Dll4*, *Vegfc*, *Epas1*, *Cxcr4*, *Igfbp3*, *Nr2f2*, *Aplnr*, *Nrp1*, *Nrp2*, *Pecam1*) (Chong et al., 2011; Corada et al., 2014; Simons and Eichmann, 2015; Su et al., 2018) and eight representative hematopoietic genes (*Adgrg1*, *Ikzf2*, *Bcl11a*, *Runx1*, *Neurl3*, *Angpt1*, *Gfi1*, *Hlf*) (Zhou et al., 2016; Hou et al., 2020) were selected to calculate the endothelial and hematopoietic feature score for each cell, respectively.

Statistical Analysis

All statistical analyses were conducted in R version 3.5.0. ROC analysis and two sample Wilcoxon rank sum tests were employed for comparisons of gene expression levels between two clusters of cells. GO biological process enrichment analyses were performed using clusterProfiler. We referred to statistically significant as $P < 0.05$ (if not specified).

RESULTS

Transcriptomically Different Subpopulations in AGM PK44 Cells

According to a graph-based unsupervised clustering approach from Seurat software, 93 E10.0 AGM PK44 cells from our previous scRNA-seq dataset that had passed rigorous quality control were separated into three clusters (Hou et al., 2020) (**Figure 1A**). The endothelial-biased subpopulation was readily recognized by the obvious *Nrp1* and *Gja4* expression (Chong et al., 2011; Corada et al., 2014; Simons and Eichmann, 2015; Su et al., 2018). The hematopoietic-biased cluster was featured by its relatively high expression of *Spi1* (Thambyrajah et al., 2016; Hou et al., 2020). The remaining one was named the transitional population given its moderate expression level of endothelial and hematopoietic genes (**Figure 1A–C**). Then, the three subpopulations were analyzed by Gene Ontology, and it was found that the endothelial-biased subpopulation enriched genes were mainly involved in angiogenesis and regulation of vasculature, and the genes enriched in hematopoietic-biased subpopulation were mainly related to positive regulation of cell adhesion, B cell differentiation, and regulation of T cell activation (**Figure 1D**). Taken together, these results suggested the existence of molecular heterogeneity within AGM PK44 population.

Further Enrichment of Hematopoietic Potential by Additional Marker Within AGM PK44 Cells

Based on the transcriptomic analysis, we explored whether the endothelial- or hematopoietic-biased subpopulation could be further enriched by additional surface markers. First, we ranked the differentially expressed surface markers according to ROC power and fold change for antibody screening (**Figure 2A**). Among these molecules, endothelial markers *Nrp1*, *Kdr*, and *Tek* were highly expressed in the endothelial-biased subpopulation (Shalaby et al., 1997; Takakura et al., 1998; Yamashita et al., 2000; Simons and Eichmann, 2015), whereas *CD47* and *Kit* were overrepresented in the hematopoietic-biased subpopulation (North et al., 2002; Taoudi et al., 2005; Zhou et al., 2016; Hou et al., 2020). No surface marker was screened out being highly expressed in the transitional subpopulation (**Figure 2A**).

Next, we tried several predicated surface markers in the following functional assays, including the ones highly expressed in the endothelial-biased subpopulation, CD304, Flk1, CD93, and CD146, and those highly expressed in the hematopoietic-biased subpopulation, CD47 and CD49d (**Figure 2A**). We, respectively, added each of these selected surface markers to PK44 combination and used the index sorting function to sort individual PK44 cells into 48-well plates with one cell per well (**Figures 2B,C**). After co-culture with OP9-DL1 for 7 days, the cultures were stained with CD45 and CD31 to determine the presence of hematopoietic clusters and endothelial tubes, respectively (**Supplementary Figure 1A**) (Hou et al., 2020). The number and proportion of cells with only endothelial potential, endothelial-hematopoietic dual potential, and only hematopoietic potential were counted (**Supplementary Figure 1A**), and these were generally in line with that in our previous report (Hou et al., 2020). By retrospectively analyzing the corresponding expression of the selected markers on each cell via index sorting data (**Figure 2B**), we identified CD93 and CD146 as candidates, which could further distinguish the cells with different potentials within PK44 population (**Figures 2D,E** and **Supplementary Figure 1B**), and excluded Flk1, CD304, CD47, and CD49d given their poor performance in further discriminating endothelial- or hematopoietic-biased subpopulations (**Supplementary Figure 1D**). In detail, cells with different potentials were basically separated on the plots when displaying the expression of Kit and one other candidate (CD93 or CD146) (**Figure 2D**). The cells with hematopoietic potential showed relatively high expression of Kit and low expression of the two candidates (CD93 or CD146) and were, thus, abbreviated as $Kit^{hi}CD93^{lo}$ and $Kit^{hi}CD146^{lo}$. On the other hand, the endothelial potential was concentrated in the subpopulation with relatively high expression of the candidates (CD93 or CD146) and low expression of Kit (abbreviated as $CD93^{hi}Kit^{lo}$ and $CD146^{hi}Kit^{lo}$) (**Figures 2D,E** and **Supplementary Figures 1B,E**).

To determine whether these two combinations could prospectively enrich potential-biased subpopulations, we, respectively, sorted $Kit^{hi}CD93^{lo}$, $CD93^{hi}Kit^{lo}$, $Kit^{hi}CD146^{lo}$, and $CD146^{hi}Kit^{lo}$ subpopulations within the PK44 population according to their expression patterns on FACS for *in vitro* single-cell functional evaluation (**Figure 2F**). When the differentiation potential of these cells was retrospectively projected on the FACS plots, the bias of potential for the subpopulations was clearly observed (**Figures 2F,G**). In detail, the proportions of cells with hematopoietic progenies in the $Kit^{hi}CD93^{lo}$ (52/124 $\approx$ 41.9%) and $Kit^{hi}CD146^{lo}$ (79/138 $\approx$ 57.2%) subpopulations were about 3.9- and 2.6-fold higher than those in the $CD93^{hi}Kit^{lo}$ (13/120 $\approx$ 10.8%) and $CD146^{hi}Kit^{lo}$ (26/120 $\approx$ 21.7%) subpopulations, respectively (**Figure 2G** and **Supplementary Figures 1C,F**). Compared with that of PK44 population without subdividing (**Supplementary Figure 1A**), the enrichment efficiency of the $Kit^{hi}CD93^{lo}$ and $Kit^{hi}CD146^{lo}$ combinations for the hematopoietic potential increased about 1.3- and 1.7-fold, respectively (**Supplementary Figure 1F**). Expectedly, the similarity between Kit&CD93 and Kit&CD146 combinations to discriminate two potential-biased subpopulations was observed (**Figure 2H**). Interestingly, both endothelial- and hematopoietic-biased subpopulations, either index-sorted or prospectively isolated, comprise a small proportion of cells with endothelial-hematopoietic dual potential (1.7%–4.8%), which stood for a transient intermediate state of the cells undergoing fate choice (Hou et al., 2020) (**Figures 2E,G**). The existence of this rare potential suggests that the PK44 population is a continuum for the EHT process. Collectively, we further caught the subpopulations with either endothelial- or hematopoietic-biased characteristics by markers screened out from transcriptomic data.

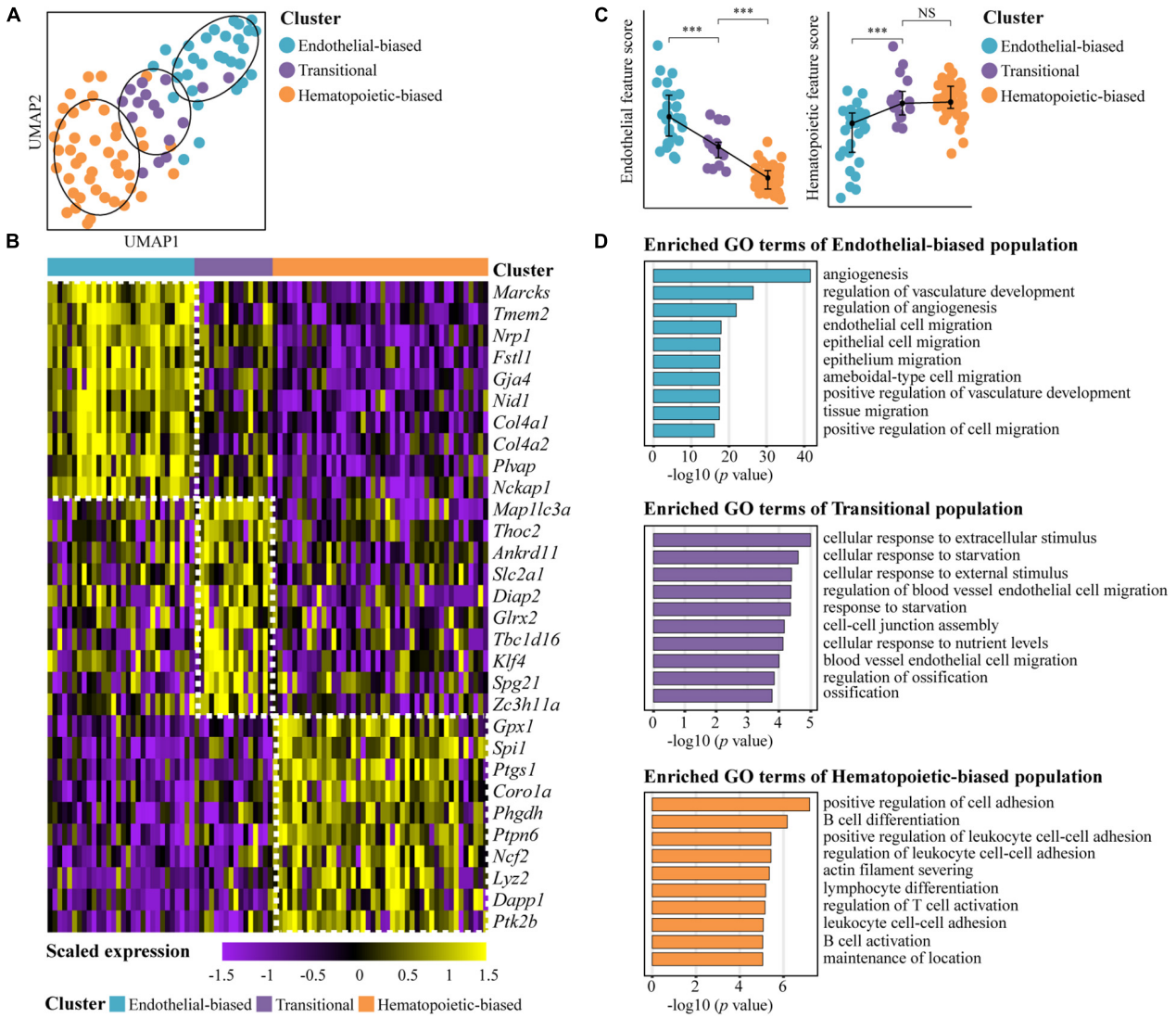

FIGURE 1 | Transcriptomically different subpopulations in E10.0 AGM PK44 cells. **(A)** UMAP plots of the E10.0 AGM PK44 cells with clusters mapped onto it. **(B)** Heatmap showing top 10 DEGs of three subpopulations (endothelial-biased, transitional, and hematopoietic-biased population) in E10.0 AGM PK44 cells. DEGs were sorted by ROC power calculated through FindallMarkers function (test.use = "roc") in Seurat2. **(C)** Dot plot showing the endothelial and hematopoietic scores of E10.0 AGM PK44 cells in three subpopulations to, respectively, represent the endothelial and hematopoietic characteristics molecularly. The statistical significance of differences was determined using Wilcox test. ***$P < 0.001$. **(D)** Enriched GO terms of three subpopulations in E10.0 AGM PK44 cells and top 10 terms with P value < 0.05 are shown.

Developmental Dynamics of the Immunophenotypic PK44 Cells in AGM and Yolk Sac

We then analyzed the spatiotemporal expression characteristics of the immunophenotypic PK44 populations in AGM and yolk sac from E9.5 to E11.0 at an interval of half a day, around the time of emergence of HSCs (**Figure 3A**). The proportion of the PK44 population in the AGM/caudal half region increased from E9.5 to a peak at E10.0, reaching 0.45% (1:222), and then decreased gradually. In comparison, this proportion in the yolk sac was highest at E9.5, reaching 0.43% (1:233) (**Figures 3A,B**). For absolute quantities, both AGM and yolk sac PK44 populations reached the peak at E10.0, which were 95 ± 5 and 135 ± 13 and then met a gradual drop (**Figure 3B**). The previously unknown expression profile of the immunophenotypic PK44 cells in yolk sac provide a basis for the following *in vitro* and *in vivo* functional experiments.

Functional Differences of the Immunophenotypic PK44 Cells Between AGM and Yolk Sac

With the aim of further exploring whether the yolk sac PK44 cells are HECs transitioning into hematopoietic fate and have endothelial-hematopoietic dual potential like that in the AGM

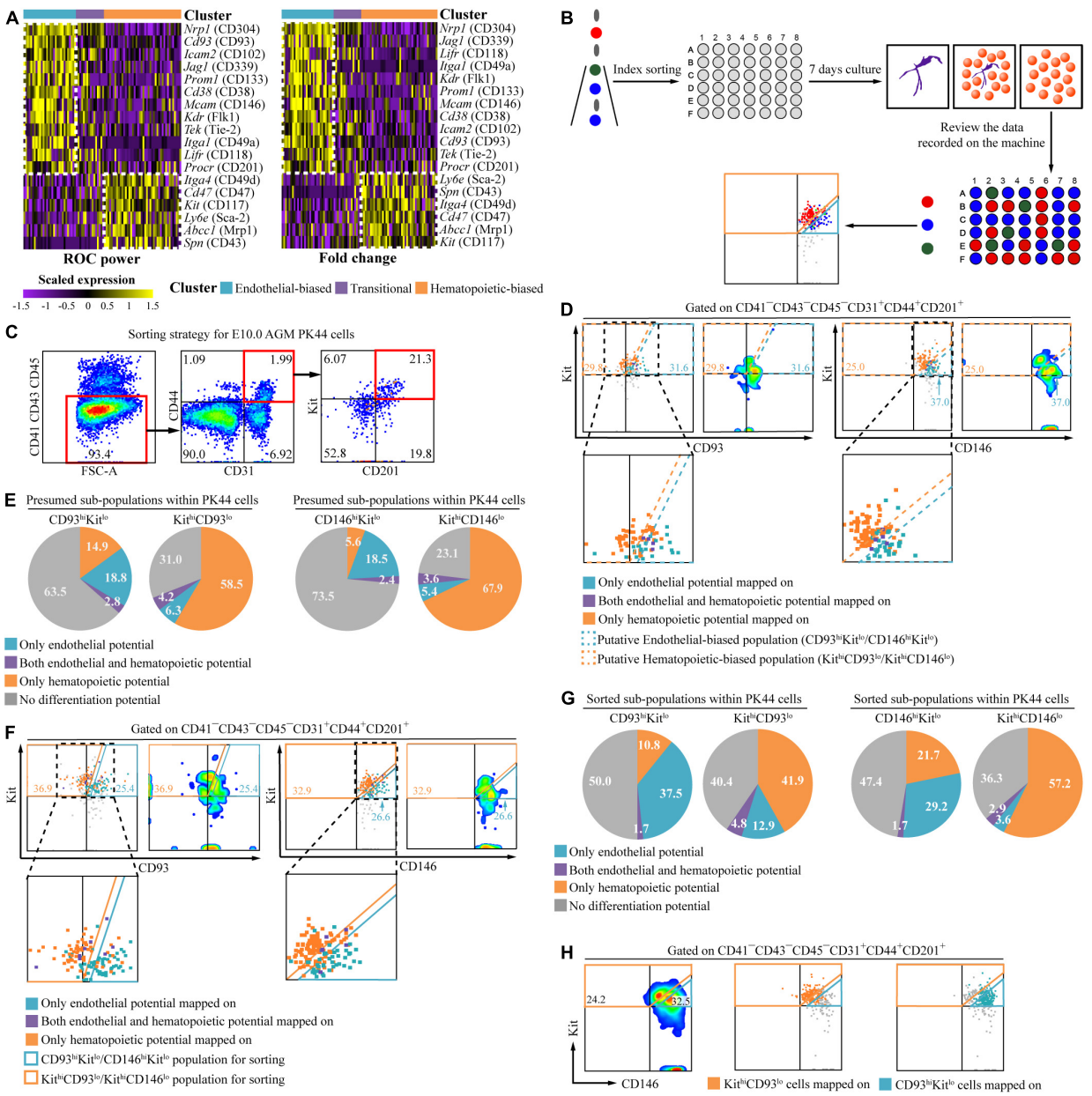

FIGURE 2 | Functionally different subpopulations within E10.0 AGM PK44 cells. **(A)** Heatmap showing the differentially expressed surface marker coding genes of the subpopulations in E10.0 AGM PK44 cells arranged by ROC power (left) and fold change (right), respectively. For the convenience of FACS labeling and live cell sorting, only genes coding cell surface proteins whose antibodies for FACS labeling are also commercially available in China within the DEG list are displayed. **(B)** Schematic experimental design of screening candidate molecules by index sorting. **(C)** Flow cytometry gating strategy for isolating PK44 population ($CD41^{-}CD43^{-}CD45^{-}CD31^{+}CD44^{+}$ $Kit^{+}CD201^{+}$) from the E10.0 AGM region. **(D)** FACS plots showing expression of Kit and CD93/CD146 on the index-sorted E10.0 AGM PK44 cells. Cells with different kinds of potentials based on *in vitro* functional evaluation (color dots) are mapped onto the reference FACS plots (gray dots). Data are from four independent experiments. The enlarged views of dashed black boxes are shown below. **(E)** Pie charts showing the proportions of four differentiation potentials in the putative subpopulations. **(F)** FACS plots showing expression of Kit and CD93/CD146 on the index-sorted candidate subpopulations of E10.0 AGM PK44 cells. Cells with different potentials based on *in vitro* functional evaluation (color dots) are mapped onto the reference FACS plots (gray dots). Data are from four independent experiments. The enlarged views of dashed black boxes are shown below. **(G)** Pie charts showing the proportions of four differentiation potentials in each of the isolated subpopulations. **(H)** FACS plots of Kit and CD146 expression with the indicated subpopulations mapped on. Orange boxes indicate the gates of the $Kit^{hi}CD146^{lo}$ subpopulation; cyan boxes indicate the gates of the $CD146^{hi}Kit^{lo}$ subpopulation.

region, we first performed the *in vitro* hematopoietic and endothelial differentiation assays at the single-cell level of E9.5 and E10.0 yolk sac PK44 cells with E9.5 caudal half and E10.0 AGM PK44 cells as positive controls. Interestingly, yolk sac PK44 cells also possessed the three differentiation potentials, namely, only endothelial potential (E9.5: 22/350 ≈ 6.29%, E10.0: 91/384

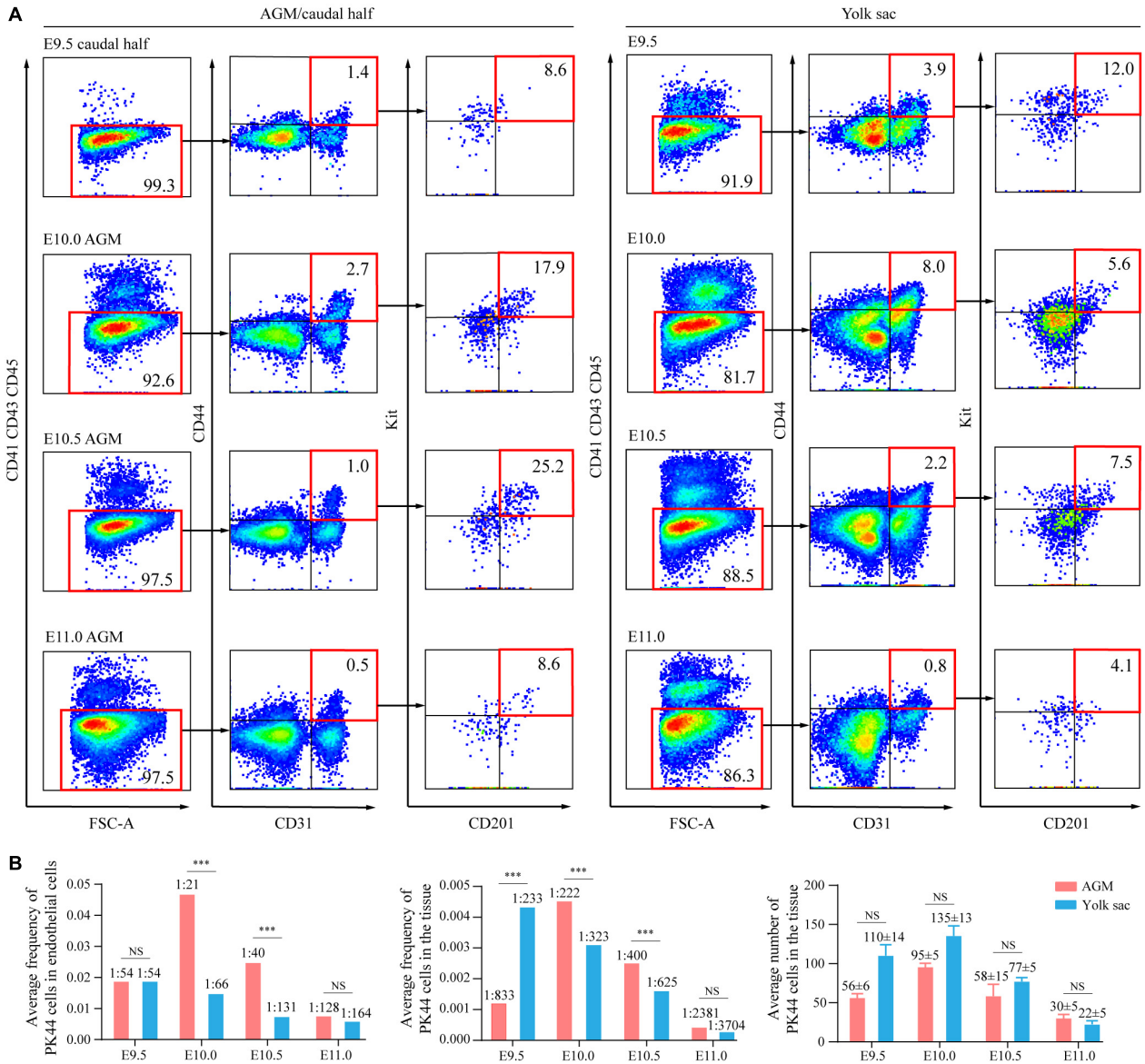

FIGURE 3 | Developmental dynamics of the immunophenotypic PK44 cells in AGM and yolk sac. **(A)** Representative FACS plots for AGM/caudal half and yolk sac PK44 cells from E9.5 to E11.0. **(B)** Graphs showing the proportions of PK44 cells in endothelial cells ($CD41^-CD43^-CD45^-CD31^+$) (left) and in total cells of the corresponding tissues (middle). The statistical significance of differences was determined using Fisher's exact test. ***$P < 0.001$. NS, not significant. The average numbers of PK44 cells in corresponding tissues are shown to the right. Data are means ± SD. Data are from three independent experiments. The statistical significance of differences was determined using Mann–Whitney test. NS, not significant.

≈ 23.70%), endothelial-hematopoietic dual potential (E9.5: 1/350 ≈ 0.29%, E10.0: 3/384 ≈ 0.78%), and only hematopoietic potential (E9.5: 75/350 ≈ 21.43%, E10.0: 19/384 ≈ 4.95%) (**Figures 4A,B**). From E9.5 to E10.0, the proportion of cells with hematopoietic potential in yolk sac PK44 cells sharply decreased in contrast to that in the intra-embryonic PK44 cells which showed an obvious increase (**Figure 4A**). The methylcellulose-based culture system supports hematopoietic differentiation from hematopoietic progenitors rather than blood generation from endothelial precursors. Similar to AGM PK44 cells (Hou et al., 2020), yolk sac PK44 cells did not form hematopoietic colonies in methylcellulose (**Figure 4C**), confirming their identity as endothelial cells rather than hematopoietic progenitors. Using index sorting data, we retrospectively analyzed the expression level of CD201, Kit, and CD44 of E9.5 yolk sac PK44 cells whose potential had been individually determined and found that no paired combinations of the three markers could effectively distinguish hematopoietic or endothelial potentials from one another (**Supplementary Figure 2**).

We next compared the hematopoietic potential of E10.0 AGM and yolk sac PK44 cells after co-cultured on OP9-DL1 under the culture condition for inducing HSCs (Zhou et al., 2016;

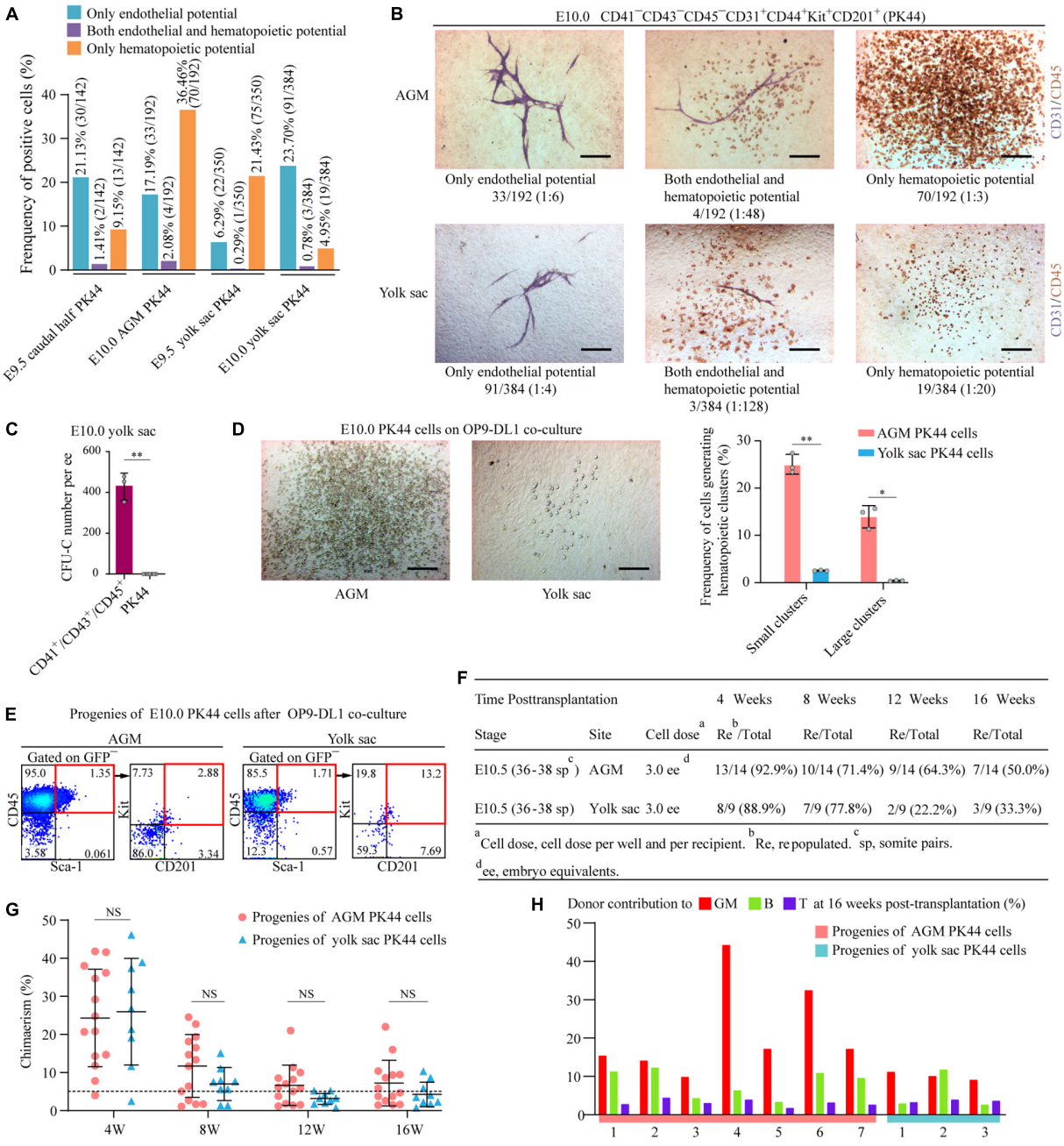

FIGURE 4 | Functional evaluation of yolk sac PK44 cells. **(A)** Column charts showing the frequencies of potential-positive cells in the indicated populations for each kind of differentiation potentials. Data are from three independent experiments. **(B)** Representative CD31 and CD45 immunostaining on the cultures of single PK44 cells from E10.0 AGM and yolk sac, showing typical morphologies regarding distinct differentiation potentials. Cell frequencies of each kind of potentials are shown. Data are from three independent experiments. Scale bars, 100 μm. **(C)** Number of hematopoietic progenitors per embryo equivalent (ee) in the indicated populations derived from E10.5 yolk sac measured by the methylcellulose CFU-C assay. Data are means ± SD. The statistical significance of differences was determined using the Wilcox test. $^{**}P < 0.01$. Data are from three independent experiments. **(D)** Morphology of hematopoietic progenies generated by AGM (left) and yolk sac (middle) PK44 cells after OP9-DL1 co-culture for 5 days. Scale bars, 100 μm. Column charts in the right showing the frequencies of AGM and yolk sac PK44 cells generating small or large hematopoietic clusters. Data are from three independent experiments. Data are means ± SD. The statistical significance of differences was determined using Pearson's chi-squared test. $^{*}P < 0.05$; $^{**}P < 0.01$. **(E)** Representative FACS plots of analyzing the progenies of E10.0 AGM and yolk sac PK44 cells following 7 days co-culture, showing a population of cells expressing putative HSC markers. **(F)** Detailed information of the transplantation assays performed with the progenies of E10.5 AGM and yolk sac PK44 cells. **(G)** Graphs showing the donor chimerism from 4 to 16 weeks after being transplanted with the progenies of the E10.5 AGM and yolk sac PK44 populations (three embryo equivalents per recipient), respectively. Data are means ± SD. The statistical significance of differences was determined using Mann–Whitney test. NS, not significant. **(H)** Bar plots showing the donor contribution to the granulocytes/monocytes (GM, red), B lymphocytes (green), and T lymphocytes (purple) in the peripheral blood of each of the primary recipients receiving the progenies of E10.5 AGM and yolk sac PK44 cells at 16 weeks post-transplantation.

Hou et al., 2020). Through morphological observation, a large hematopoietic cluster was defined as the one with diameter greater than or equal to 1.5 mm (McNiece et al., 1990) after 5 days co-culture. Under this criteria, yolk sac PK44 cells generated fewer hematopoietic clusters (yolk sac: 58/1729≈ 3.4%; AGM: 184/465 ≈ 39.6%) with a lower proportion of large ones (yolk sac: 10/58 ≈ 17.2%; AGM: 66/184 ≈ 35.9%) than AGM PK44 cells (**Figure 4D**). After co-culture for 7 days, the hematopoietic products in the cultures were assessed by FACS. Although the total hematopoietic cells generated by PK44 cells from yolk sac were much fewer than those from AGM (**Figure 4D**), both AGM and yolk sac PK44 cells were capable of giving rise to $CD45^+Sca\text{-}1^+Kit^+CD201^+$ immunophenotypic HSPCs, suggesting the yolk sac PK44 population as a potential origin for HSPCs (**Figure 4E**).

The *in vivo* repopulating capacity of the progenies of PK44 cells was further evaluated, and the multilineage reconstitution was found in 7/14 and 3/9 recipient mice 16 weeks after being transplanted with the culture products of AGM and yolk sac PK44 cells, respectively (**Figures 4F–H** and **Supplementary Figure 3A**). Moreover, the donor-derived immunophenotypic HSCs were detected in the bone marrow of recipients transplanted with the progenies of PK44 cells from both AGM and yolk sac (**Supplementary Figures 3B,C**). This finding revealed a previously unknown HSC competence of HECs represented by the PK44 population in the yolk sac around the time for HSC emergence during embryogenesis.

Analysis of Transcriptomic Characteristics of Yolk Sac PK44 Cells

To further investigate the molecular characteristics of the yolk sac PK44 population, we used STRT-seq to perform single-cell transcriptomic profiling of E10.0 yolk sac PK44 cells (**Figure 5A**). Of the 87 cells that passed the strict quality control, we detected, on average, 5139 genes and 248,722 transcripts for each cell. Of note, the well-known yolk sac endothelial markers *Lyve1* and *Stab2* were highly expressed in the PK44 cells from the yolk sac compared with those from AGM region (Nonaka et al., 2007; Lee et al., 2016; Ganuza et al., 2018; Shvartsman et al., 2019) (**Figure 5B**). The genes enriched in the yolk sac PK44 population compared with E10.0 AGM PK44 cells (Hou et al., 2020) were related to angiogenesis and vasculature development (**Figure 5C**). In comparison, those related to regulation of cell fate specification and mesodermal cell differentiation were enriched in the AGM PK44 population (**Figure 5C**). These data emphasize the distinct identities of PK44 cells from different sampling sites.

Similar to that from the AGM region, yolk sac PK44 cells could also be further separated into two subpopulations by unsupervised clustering, which were, respectively, annotated as endothelial- and hematopoietic-biased subpopulations according to their DEGs. *Nrp1*, *Tek*, *Cdh5*, *Gja5*, *Kdr*, were highly expressed in the endothelial-biased subpopulation of yolk sac PK44 cells (Shalaby et al., 1997; Nishikawa et al., 1998; Takakura et al., 1998; Simons and Eichmann, 2015), and the hematopoietic-biased subpopulation was featured by the obvious expression of *Kit*, *Adgrg1*, and transcription factor *Runx1* (North et al., 2002; Taoudi et al., 2005; Zilberberg et al., 2012; Swiers et al., 2013; Zhou et al., 2016; Hou et al., 2020) (**Figures 5D,E**). Gene Ontology terms related to angiogenesis were enriched in the endothelial-biased subpopulation, and ribosome biogenesis was enriched in the hematopoietic-biased subpopulation of yolk sac PK44 cells (**Figure 5F**). By further comparing the hematopoietic-biased subpopulations from the yolk sac and that from the AGM region, we detected a set of DEGs similar to those extracted from the comparison of PK44 cells between two sites (**Figure 5B**), including *Lyve1* and *Stab2*, which were relatively highly expressed in the former (Nonaka et al., 2007; Lee et al., 2016; Ganuza et al., 2018; Shvartsman et al., 2019) (**Figure 5G**). Considering the unambiguous repopulating capacity of the progenies of PK44 cells from both the yolk sac and AGM region (**Figures 4F–H** and **Supplementary Figure 3A**), these data together suggest the existence of spatially and molecularly distinct HECs with a multilineage hematopoietic potential.

Then, PK44 cells from the yolk sac and the AGM region in our previous dataset (Hou et al., 2020) were pooled for integrative analysis. Interestingly, PK44 cells from the yolk sac and AGM region were not initially distinguished by their sampling locations. Rather, they were clustered predominantly according to whether they presented endothelial- or hematopoietic-biased characteristics (**Figure 5H**). Featured by the relatively high expression of *Nrp1*, *Gja4*, and *Gja5*, the integrated endothelial-biased cluster was separated from the integrated hematopoietic-biased cluster, which was featured by *Adgrg1* and *Spi1* expression (**Figures 5H,I**). This finding further provides a molecular basis for the diverged potentials of PK44 cells from both the yolk sac and AGM region (**Figures 4A,B**).

DISCUSSION

In the present study, the existence of three molecularly different subpopulations within the AGM PK44 population were transcriptomically identified. Subsequently, the subpopulations with either endothelial- or hematopoietic-biased characteristics were functionally validated by using the marker combinations of Kit and CD93/CD146 within the PK44 population through flow cytometry index sorting. The finding complements the characteristics of heterogeneous subpopulations in HECs that were unknown before (Hou et al., 2020). Meanwhile, the concomitant presence of endothelial-hematopoietic dual potential cells in both endothelial- and hematopoietic-biased subpopulations suggests the PK44 population as a continuum for the EHT process.

Based on the functional validation, we further revealed a previously unknown HSC competence of HECs represented by the PK44 population in the yolk sac around the time of HSC emergence during embryogenesis. Unexpectedly, the three differentiation potentials such as that in AGM region PK44 cells were found within yolk sac PK44 cells. The capture of the endothelial-hematopoietic dual potential suggests that a part of PK44 cells in the yolk sac might be undergoing EHT.

Transcriptionally, two subpopulations characterized by endothelial or hematopoietic bias were separated by unsupervised clustering within yolk sac PK44 cells.

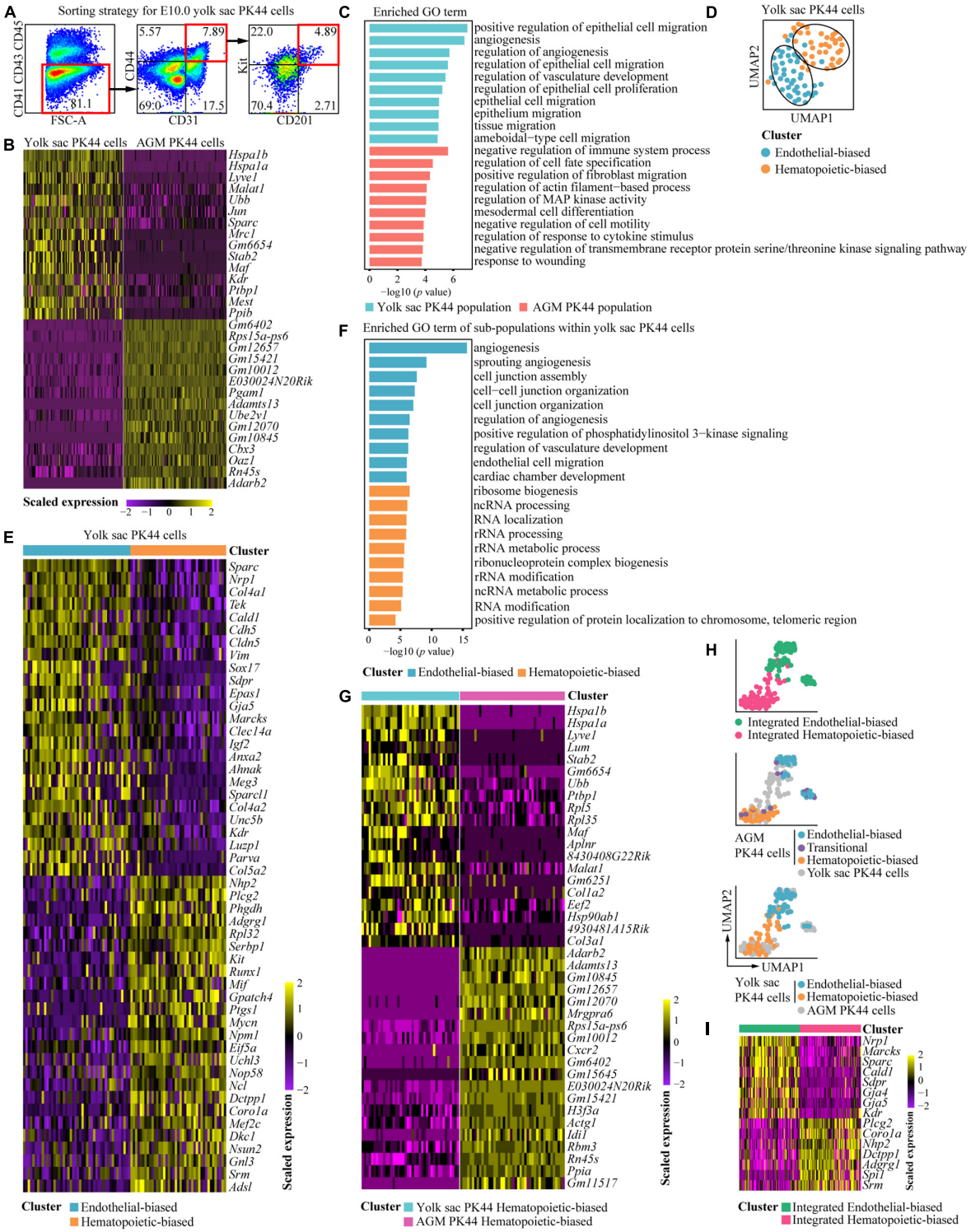

FIGURE 5 | Transcriptomic characteristics of E10.0 yolk sac PK44 cells. **(A)** Flow cytometry gating strategy for isolating PK44 cells in E10.0 yolk sac. **(B)** Heatmap showing the top 15 DEGs between E10.0 yolk sac and AGM PK44 cells. **(C)** Enriched GO terms of E10.0 yolk sac and AGM PK44 populations. **(D)** UMAP plots of the E10.0 yolk sac PK44 cells with clusters mapped on. **(E)** Heatmap showing top 25 DEGs between two subpopulations (endothelial- and hematopoietic-biased) in E10.0 yolk sac PK44 cells. **(F)** Enriched GO terms of two subpopulations (endothelial- and hematopoietic-biased) in E10.0 yolk sac PK44 cells. **(G)** Heatmap showing top 20 DEGs between hematopoietic-biased subpopulation in E10.0 yolk sac PK44 cells and that in E10.0 AGM PK44 cells. **(H)** UMAP of integrated data of E10.0 AGM and yolk sac PK44 cells with subpopulations (endothelial-biased, transitional, and hematopoietic-biased population) mapped on. **(I)** Heatmap showing DEGs between the integrated endothelial- and hematopoietic-biased populations.

Unexpectedly, when the yolk sac and AGM PK44 cells were pooled for integrative analysis, the cells gathered together according to their endothelial- or hematopoietic-biased characteristics rather than different embryonic sites, which provided a molecular basis for the diverged potentials of PK44 cells from both the yolk sac and AGM region.

Interestingly, unlike the AGM PK44 cells, the proportion of yolk sac PK44 cells with only hematopoietic potential at E9.5 was significantly higher than that at E10.0. A possible explanation is that part of the yolk sac PK44 cells differentiated into erythroid-myeloid progenitor cells, thus increasing the proportion of hematopoietic clusters. However, this hypothesis needs to be further verified by functional experiments. Our study also found that, the chimerism in the peripheral blood of adult recipient mice transplanted with progenies of AGM and yolk sac PK44 cells both peaked at 4 weeks post-transplantation and then decreased gradually, probably because most HSC-primed HECs have completed EHT by E10.5, and the remaining HECs, which could be obtained by our sorting strategy in the present study, only retain very limited potential to generate HSCs.

In summary, our study paves the way for further analysis of the developmental progress of HSCs and provides clues for the expansion of HSCs *in vitro*. In addition, a comprehensive understanding of the spatiotemporal and functional heterogeneity of HECs helps us to comprehend the process of hematopoietic development.

DATA AVAILABILITY STATEMENT

The scRNA-seq data of yolk sac PK44 cells have been deposited in NCBI's Gene Expression Omnibus (GEO) with the accession number GSE173833. The scRNA-seq data of AGM PK44 cells have already been deposited in the GEO under accession number GSE139389.

ETHICS STATEMENT

The animal study was reviewed and approved by the Academy of Military Medical Sciences (Fifth Medical Center of Chinese PLA General Hospital).

AUTHOR CONTRIBUTIONS

YL and BL designed the study. Y-QL performed cell sorting, culture, immunostaining, HSC transplantation assays with help from YN, SH, HW, CW, JW, JH, RY, JY, and GZ. TH performed scRNA-seq. YG and DL performed bioinformatics analysis. Y-QL, YL, BL, and SH wrote the manuscript and revision. All authors reviewed the manuscript.

FUNDING

This work was supported by the National Key R&D Program of China (2020YFA0112402 and 2017YFA0103401), the National Key Research and Development Plan Young Scientists Program (2017YFA0106000), the National Natural Science Foundation of China (81890991, 31871173, 31930054, and 81900115), the Program for Guangdong Introducing Innovative and Entrepreneurial Teams (2017ZT07S347), and the Key Research and Development Program of Guangdong Province (2019B020234002).

SUPPLEMENTARY MATERIAL

The Supplementary Material for this article can be found online at: https://www.frontiersin.org/articles/10.3389/fcell.2021.699263/full#supplementary-material

Supplementary Figure 1 | Functional experiments using index sorting. **(A)** Representative CD31 and CD45 immunostaining on the cultures of single PK44 cells from E10.0 AGM, showing typical morphologies regarding distinct differentiation potentials (left). Scale bars, 100 μm. Cell frequencies of each kind of potential within PK44 cells are shown (right). Data are from 20 independent experiments. **(B)** Cell numbers of each kind of potential in presumed subpopulations within E10.0 AGM PK44 cells. **(C)** Cell numbers of each kind of potential in sorted subpopulations within E10.0 AGM PK44 cells. **(D)** Expression of Kit, Flk1, CD304, CD47, and CD49d on the index-sorted single E10.0 AGM PK44 cells. Cells with different kinds of potentials based on *in vitro* functional evaluation (color dots) are mapped onto the reference FACS plots (gray dots). Data are from three independent experiments. The enlarged views of red boxes are shown below. **(E,F)** Column charts showing quantitative analyses of the differentiation potential of different presumed **(E)** or prospectively sorted **(F)** subpopulations as indicated. Data are means ± SD. The statistical significance of differences was determined using Pearson's chi-squared test. $^{*}P < 0.05$; $^{**}P < 0.01$, $^{***}P < 0.001$.

Supplementary Figure 2 | Expression of surface markers in the index-sorted single E9.5 yolk sac PK44 cells. Cells with different kinds of potentials based on *in vitro* functional evaluation (color dots) are mapped onto the reference FACS plots (gray dots). Data are from three independent experiments. The enlarged views of red boxes are shown below.

Supplementary Figure 3 | Multiorgan and multilineage repopulations at 16 weeks post-transplantation of primary recipients transplanted with the progenies of E10.5 AGM and yolk sac PK44 populations. **(A)** Representative FACS plots showing donor-derived ($CD45.1^+CD45.2^+$) myeloid ($Ly6G^+/Mac\text{-}1^+$), B lymphoid ($B220^+$), and T lymphoid ($CD3^+$) cells in peripheral blood and multiple hematopoietic organs. **(B,C)** Representative FACS plots of immunophenotypic HSCs ($Lin^-Kit^+Sca\text{-}1^+Flk2^-CD34^-$) in bone marrow of the primary recipients transplanted with the progenies of AGM (upper) and yolk sac (lower) PK44 cells.

REFERENCES

Anders, S., Pyl, P. T., and Huber, W. (2015). HTSeq–a python framework to work with high-throughput sequencing data. *Bioinformatics* 31, 166–169. doi: 10.1093/bioinformatics/btu638

Chen, M. J., Yokomizo, T., Zeigler, B. M., Dzierzak, E., and Speck, N. A. (2009). Runx1 is required for the endothelial to haematopoietic cell transition but not thereafter. *Nature* 457, 887–891. doi: 10.1038/nature07619

Chong, D. C., Koo, Y., Xu, K., Fu, S., and Cleaver, O. (2011). Stepwise arteriovenous fate acquisition during mammalian vasculogenesis. *Dev. Dyn.* 240, 2153–2165. doi: 10.1002/dvdy.22706

Corada, M., Morini, M. F., and Dejana, E. (2014). Signaling pathways in the specification of arteries and veins. *Arterioscler. Thromb. Vasc. Biol.* 34, 2372–2377. doi: 10.1161/ATVBAHA.114.303218

Cumano, A., Ferraz, J. C., Klaine, M., Di Santo, J. P., and Godin, I. (2001). Intraembryonic, but not yolk sac hematopoietic precursors, isolated before

circulation, provide long-term multilineage reconstitution. *Immunity* 15, 477–485. doi: 10.1016/s1074-7613(01)00190-x

Frame, J. M., Fegan, K. H., Conway, S. J., McGrath, K. E., and Palis, J. (2016). Definitive hematopoiesis in the yolk sac emerges from Wnt-responsive hemogenic endothelium independently of circulation and arterial identity. *Stem Cells* 34, 431–444. doi: 10.1002/stem.2213

Ganuza, M., Chabot, A., Tang, X., Bi, W., Natarajan, S., Carter, R., et al. (2018). Murine hematopoietic stem cell activity is derived from pre-circulation embryos but not yolk sacs. *Nat. Commun.* 9:5405. doi: 10.1038/s41467-018-07769-8

Gao, L., Tober, J., Gao, P., Chen, C., Tan, K., and Speck, N. A. (2018). RUNX1 and the endothelial origin of blood. *Exp. Hematol.* 68, 2–9. doi: 10.1016/j.exphem.2018.10.009

Hadland, B. K., Varnum-Finney, B., Mandal, P. K., Rossi, D. J., Poulos, M. G., Butler, J. M., et al. (2017). A common origin for B-1a and B-2 lymphocytes in clonal pre- hematopoietic stem cells. *Stem Cell Rep.* 8, 1563–1572. doi: 10.1016/j.stemcr.2017.04.007

Hou, S., Li, Z., Zheng, X., Gao, Y., Dong, J., Ni, Y., et al. (2020). Embryonic endothelial evolution towards first hematopoietic stem cells revealed by single-cell transcriptomic and functional analyses. *Cell Res.* 30, 376–392. doi: 10.1038/s41422-020-0300-2

Huang, K., Gao, J., Du, J., Ma, N., Zhu, Y., Wu, P., et al. (2016). Generation and analysis of GATA2(w/eGFP) human ESCs reveal ITGB3/CD61 as a reliable marker for defining hemogenic endothelial cells during hematopoiesis. *Stem Cell Rep.* 7, 854–868. doi: 10.1016/j.stemcr.2016.09.008

Kim, D., Langmead, B., and Salzberg, S. L. (2015). HISAT: a fast spliced aligner with low memory requirements. *Nat. Methods* 12, 357–360. doi: 10.1038/nmeth.3317

Lee, L. K., Ghorbanian, Y., Wang, W., Wang, Y., Kim, Y. J., Weissman, I. L., et al. (2016). LYVE1 marks the divergence of yolk sac definitive hemogenic endothelium from the primitive erythroid lineage. *Cell Rep.* 17, 2286–2298. doi: 10.1016/j.celrep.2016.10.080

Lie, A. L. M., Marinopoulou, E., Lilly, A. J., Challinor, M., Patel, R., Lancrin, C., et al. (2018). Regulation of RUNX1 dosage is crucial for efficient blood formation from hemogenic endothelium. *Development* 145:dev149419. doi: 10.1242/dev.149419

McNiece, I. K., Bertoncello, I., Kriegler, A. B., and Quesenberry, P. J. (1990). Colony-forming cells with high proliferative potential (HPP-CFC). *Int. J. Cell Cloning* 8, 146–160. doi: 10.1002/stem.5530080302

Nishikawa, S. I., Nishikawa, S., Hirashima, M., Matsuyoshi, N., and Kodama, H. (1998). Progressive lineage analysis by cell sorting and culture identifies FLK1+VE-cadherin+ cells at a diverging point of endothelial and hemopoietic lineages. *Development* 125, 1747–1757. doi: 10.1242/dev.125.9.1747

Nonaka, H., Tanaka, M., Suzuki, K., and Miyajima, A. (2007). Development of murine hepatic sinusoidal endothelial cells characterized by the expression of hyaluronan receptors. *Dev. Dyn.* 236, 2258–2267. doi: 10.1002/dvdy.21227

North, T. E., de Bruijn, M. F., Stacy, T., Talebian, L., Lind, E., Robin, C., et al. (2002). Runx1 expression marks long-term repopulating hematopoietic stem cells in the midgestation mouse embryo. *Immunity* 16, 661–672. doi: 10.1016/s1074-7613(02)00296-0

Samokhvalov, I. M., Samokhvalova, N. I., and Nishikawa, S. (2007). Cell tracing shows the contribution of the yolk sac to adult haematopoiesis. *Nature* 446, 1056–1061. doi: 10.1038/nature05725

Schulte, R., Wilson, N. K., Prick, J. C., Cossetti, C., Maj, M. K., Gottgens, B., et al. (2015). Index sorting resolves heterogeneous murine hematopoietic stem cell populations. *Exp. Hematol.* 43, 803–811. doi: 10.1016/j.exphem.2015.05.006

Shalaby, F., Ho, J., Stanford, W. L., Fischer, K. D., Schuh, A. C., Schwartz, L., et al. (1997). A requirement for Flk1 in primitive and definitive hematopoiesis and vasculogenesis. *Cell* 89, 981–990. doi: 10.1016/s0092-8674(00)80283-4

Shvartsman, M., Pavlovich, P. V., Oatley, M., Ganter, K., McKernan, R., Prialgauskaite, R., et al. (2019). Single-cell atlas of major haematopoietic tissues sheds light on blood cell formation from embryonic endothelium. *bioRxiv* [Preprint]. doi: 10.1101/774547

Simons, M., and Eichmann, A. (2015). Molecular controls of arterial morphogenesis. *Circ. Res.* 116, 1712–1724. doi: 10.1161/CIRCRESAHA.116.302953

Su, T., Stanley, G., Sinha, R., D'Amato, G., Das, S., Rhee, S., et al. (2018). Single-cell analysis of early progenitor cells that build coronary arteries. *Nature* 559, 356–362. doi: 10.1038/s41586-018-0288-7

Swiers, G., Baumann, C., O'Rourke, J., Giannoulatou, E., Taylor, S., Joshi, A., et al. (2013). Early dynamic fate changes in haemogenic endothelium characterized at the single-cell level. *Nat. Commun.* 4:2924. doi: 10.1038/ncomms3924

Takakura, N., Huang, X. L., Naruse, T., Hamaguchi, I., Dumont, D. J., Yancopoulos, G. D., et al. (1998). Critical role of the TIE2 endothelial cell receptor in the development of definitive hematopoiesis. *Immunity* 9, 677–686. doi: 10.1016/s1074-7613(00)80665-2

Taoudi, S., Morrison, A. M., Inoue, H., Gribi, R., Ure, J., and Medvinsky, A. (2005). Progressive divergence of definitive haematopoietic stem cells from the endothelial compartment does not depend on contact with the foetal liver. *Development* 132, 4179–4191. doi: 10.1242/dev.01974

Thambyrajah, R., Mazan, M., Patel, R., Moignard, V., Stefanska, M., Marinopoulou, E., et al. (2016). GFI1 proteins orchestrate the emergence of haematopoietic stem cells through recruitment of LSD1. *Nat. Cell Biol.* 18, 21–32. doi: 10.1038/ncb3276

Yamashita, J., Itoh, H., Hirashima, M., Ogawa, M., Nishikawa, S., Yurugi, T., et al. (2000). Flk1-positive cells derived from embryonic stem cells serve as vascular progenitors. *Nature* 408, 92–96. doi: 10.1038/35040568

Yokomizo, T., and Dzierzak, E. (2010). Three-dimensional cartography of hematopoietic clusters in the vasculature of whole mouse embryos. *Development* 137, 3651–3661. doi: 10.1242/dev.051094

Zhou, F., Li, X., Wang, W., Zhu, P., Zhou, J., He, W., et al. (2016). Tracing haematopoietic stem cell formation at single-cell resolution. *Nature* 533, 487–492. doi: 10.1038/nature17997

Zilberberg, L., Todorovic, V., Dabovic, B., Horiguchi, M., Courousse, T., Sakai, L. Y., et al. (2012). Specificity of latent TGF-beta binding protein (LTBP) incorporation into matrix: role of fibrillins and fibronectin. *J. Cell Physiol.* 227, 3828–3836. doi: 10.1002/jcp.24094

Conflict of Interest: The authors declare that the research was conducted in the absence of any commercial or financial relationships that could be construed as a potential conflict of interest.

Publisher's Note: All claims expressed in this article are solely those of the authors and do not necessarily represent those of their affiliated organizations, or those of the publisher, the editors and the reviewers. Any product that may be evaluated in this article, or claim that may be made by its manufacturer, is not guaranteed or endorsed by the publisher.

frontiers in Cell and Developmental Biology

ORIGINAL RESEARCH
published: 25 August 2021
doi: 10.3389/fcell.2021.734176

Absence of CD11a Expression Identifies Embryonic Hematopoietic Stem Cell Precursors *via* Competitive Neonatal Transplantation Assay

Alborz Karimzadeh[1,2†‡], Erika S. Varady[1,2†], Vanessa M. Scarfone[1], Connie Chao[1,2], Karin Grathwohl[1,2], Pauline U. Nguyen[1,2], Yasamine Ghorbanian[1,2], Irving L. Weissman[3], Thomas Serwold[4] and Matthew A. Inlay[1,2]*

[1] Sue and Bill Gross Stem Cell Research Center, University of California, Irvine, Irvine, CA, United States, [2] Department of Molecular Biology and Biochemistry, University of California, Irvine, Irvine, CA, United States, [3] Institute of Stem Cell Biology and Regenerative Medicine and Ludwig Center, Stanford University, Stanford, CA, United States, [4] Joslin Diabetes Center, Harvard Medical School, Boston, MA, United States

OPEN ACCESS

Edited by:
Jon Frampton,
University of Birmingham,
United Kingdom

Reviewed by:
Georges Lacaud,
The University of Manchester,
United Kingdom
Hannes Klump,
Essen University Hospital, Germany

***Correspondence:**
Matthew A. Inlay
minlay@uci.edu

[†] These authors share first authorship

[‡] ***Present address:***
Alborz Karimzadeh,
Joslin Diabetes Center, Harvard Medical School, Boston, MA,
United States

Specialty section:
This article was submitted to Stem Cell Research, a section of the journal Frontiers in Cell and Developmental Biology

Received: 30 June 2021
Accepted: 02 August 2021
Published: 25 August 2021

Citation:
Karimzadeh A, Varady ES, Scarfone VM, Chao C, Grathwohl K, Nguyen PU, Ghorbanian Y, Weissman IL, Serwold T and Inlay MA (2021) Absence of CD11a Expression Identifies Embryonic Hematopoietic Stem Cell Precursors via Competitive Neonatal Transplantation Assay. Front. Cell Dev. Biol. 9:734176. doi: 10.3389/fcell.2021.734176

Hematopoietic stem cells (HSCs) are defined by their self-renewal, multipotency, and bone marrow (BM) engraftment abilities. How HSCs emerge during embryonic development remains unclear, but are thought to arise from hemogenic endothelium through an intermediate precursor called "pre-HSCs." Pre-HSCs have self-renewal and multipotent activity, but lack BM engraftability. They can be identified functionally by transplantation into neonatal recipients, or by *in vitro* co-culture with cytokines and stroma followed by transplantation into adult recipients. While pre-HSCs express markers such as Kit and CD144, a precise surface marker identity for pre-HSCs has remained elusive due to the fluctuating expression of common HSC markers during embryonic development. We have previously determined that the lack of CD11a expression distinguishes HSCs in adults as well as multipotent progenitors in the embryo. Here, we use a neonatal transplantation assay to identify pre-HSC populations in the mouse embryo. We establish CD11a as a critical marker for the identification and enrichment of pre-HSCs in day 10.5 and 11.5 mouse embryos. Our proposed pre-HSC population, termed "11a- eKLS" (CD11a- Ter119- CD43+ Kit+ Sca1+ CD144+), contains all *in vivo* long-term engrafting embryonic progenitors. This population also displays a cell-cycle status expected of embryonic HSC precursors. Furthermore, we identify the neonatal liver as the likely source of signals that can mature pre-HSCs into BM-engraftable HSCs.

Keywords: embryo, flow cytometry, hematopoietic stem cell (HSC), hematopoietic stem cell transplantation, neonatal transplantation, embryonic hematopoiesis

INTRODUCTION

Hematopoietic stem cells (HSCs) in adults are the multipotent and self-renewable source of the entire blood system, and hold the regenerative capacity to engraft a myeloablated recipient upon transplantation (Hagedorn et al., 2014). While the identity, self-renewal ability, engraftment potential, and differentiation properties of adult HSCs has been extensively studied over the past

30 years, much less is known about the developmental origins of HSCs in the embryo. During early embryonic development and prior to the appearance of fully-functional HSCs, distinct waves of blood-forming cells emerge, likely initiated from specialized endothelial cells called "hemogenic endothelium" (Zovein et al., 2008; Lancrin et al., 2009). These waves overlap, with each wave functionally more mature than the last. In mice, the initial wave of hematopoiesis gives rise primarily to primitive nucleated erythrocytes and arises in the yolk sac (YS) blood islands starting from embryonic day (e) 7.5 (Moore and Metcalf, 1970). After establishment of a heartbeat, definitive hematopoiesis begins at e8.5 in the YS and placenta (PL) with a transient wave of erythro-myeloid progenitors (Palis et al., 1999; Alvarez-Silva et al., 2003; Palis, 2016). At e9.5, the first self-renewable and multipotent progenitors, that immediately precede HSCs, emerge in the YS, aorta-gonad-mesonephros (AGM), and PL, and are often called "pre-HSCs" (Yoder et al., 1997a; Taoudi et al., 2008; Arora et al., 2014; Inlay et al., 2014; Rybtsov et al., 2016; Zhou et al., 2016). After e11.5, the pre-HSC wave transitions into an expanding BM-engraftable HSC pool in the fetal liver (FL) (Kumaravelu et al., 2002; Gekas et al., 2005). The FL remains the major site of hematopoiesis until perinatal seeding of the BM (Muller et al., 1994; Beaudin et al., 2016).

In adult mice, multi-parameter fluorescence-activated cell sorting (FACS) coupled with transplantation assays have enabled the isolation of a highly purified bone marrow (BM) HSC population for functional and molecular characterization (Wiesmann et al., 2000; Kiel et al., 2005; Balazs et al., 2006; Karlsson et al., 2013). BM HSCs can be sorted, then transplanted intravenously into lethally-irradiated wild-type recipient mice, where they will home to the BM, engraft, and reconstitute the hematopoietic system for the life of the recipient. Pioneering work on the embryonic origins of HSCs led to the present definition of pre-HSCs as cells that have the self-renewal and lineage potential of adult HSCs, but lack the ability to engraft into the BM when transplanted intravenously into adult lethally-irradiated recipients (Weissman et al., 1978; Akashi and Weissman, 2001). However, two alternative assays have been developed to functionally identify pre-HSC activity in the embryo: *ex vivo* maturation and neonatal transplantation. In the former, candidate populations or tissues are harvested from the embryo and cultured *in vitro* with the addition of exogenous factors to induce *ex vivo* maturation of these cells into HSCs, which is then confirmed by adult transplantation (Taoudi et al., 2008; Rybtsov et al., 2011). However, these *ex vivo* maturation assays rely on the presence of cultured stromal lines as well as potent exogenous factors such as SCF, TPO, IL-3, and Flt3L. Accordingly, these assays can potentially drive HSC formation from cell-types that are more primitive than pre-HSCs, such as hemogenic endothelium (Hadland et al., 2017). An alternative approach to reveal pre-HSC activity is *via* intravenous injection of embryonic cells directly into irradiated *neonatal* recipients (Yoder and Hiatt, 1997; Yoder et al., 1997b,a). While less sensitive than *ex vivo* cultures, neonatal transplantation presents minimal risk of introducing artifacts by bypassing the non-physiological concentrations of cytokines and growth factors used *ex vivo* (Yoder et al., 1997a; Boisset et al., 2010; Arora et al., 2014).

Adult HSCs can be precisely identified by a combination of different markers expressed (or unexpressed) on their surface. While many different combinations can work, a commonly used definition for murine HSCs is Lineage- Kit+ Sca1+ CD150+ and CD34-. However, many adult HSC markers are not similarly expressed in the early embryo and can change depending on the tissue and timepoint examined (Cumano and Godin, 2007). Alternative assays have identified potential pre-HSC markers including hematopoietic markers CD41 (Rybtsov et al., 2011), CD43 (Inlay et al., 2014), and CD45 (Taoudi et al., 2008; Boisset et al., 2010), progenitor markers Kit (Boisset et al., 2010) and Sca1 (Inlay et al., 2014), and endothelial markers CD31 (Inlay et al., 2014), VE-Cadherin (CD144) (Taoudi et al., 2008), and EPCR (CD201) (Zhou et al., 2016). This has resulted in the identification of populations such as Type I (CD144+ CD41+ CD45-) and Type II (CD144+ CD45+) pre-HSCs (Rybtsov et al., 2011), or rarer $CD201^{hi}$ subsets within these populations (Zhou et al., 2016) or a CD27+ subset within Type II pre-HSCs (Li et al., 2017). However, a strictly-defined pre-HSC cell type has not been described to the same resolution as that in adult HSCs.

CD11a (integrin alpha L, or *Itgal*) forms the complex LFA-1 (leukocyte functional-associated antigen 1; $\alpha_L\beta_2$) upon dimerization with the β2-integrin CD18. LFA-1 interacts with ICAMs and has roles in lymphocyte activation, differentiation, and transendothelial migration (Kinashi, 2005; Shamri et al., 2005; Zhang and Wang, 2012). CD11a is highly expressed on all circulating immune cells, including BM progenitor populations (Fathman et al., 2014). However, our previous work found CD11a to be uniquely unexpressed in a subset of adult HSCs (defined as Lin- Kit+ Sca1+ CD150+ CD34-), and only the CD11a- fraction of adult HSCs displayed long-term multilineage reconstitution upon transplantation (Fathman et al., 2014; Karimzadeh et al., 2018). In a related study, we examined the potential of CD11a as a marker of embryonic multipotent progenitors in e9.5-11.5 embryos. Using a single-cell *in vitro* multipotency assay, we determined that only a rare CD11a- population we termed "CD11a- KLS" cells (defined as Ter119- CD43+ Kit+ Sca1+ CD144+ CD11a-) contained all multipotent progenitor activity, regardless of what timepoint or tissue it was isolated from Inlay et al. (2014). Neonatal transplantation demonstrated these cells produce a variety of lineages *in vivo,* though their long-term engraftment and ability to give rise to HSCs was never assessed. Thus, in both studies, the absence of CD11a expression was an important marker to identify adult HSCs by transplantation, and a candidate pre-HSC population in the embryo by *in vitro* multipotency.

In the present study, we use an *in vivo* neonatal NSG transplantation system to prospectively identify pre-HSCs in e10.5 and e11.5 tissues. In line with our previous work, the absence of CD11a expression on pre-HSCs (defined as Ter119- CD43+ Kit+ Sca1+ CD144+ CD11a-) was critical for distinguishing them from downstream progenitors which were all CD11a+. Moreover, our data suggest the neonatal liver serves as an essential temporary niche for the maturation of embryonic progenitors which lack the expression of the BM homing receptor CXCR4 prior to seeding the BM. These findings establish CD11a as a key marker to identify and isolate a highly

purified pre-HSC population, beyond what has been achieved, therefore paving the way for more detailed characterization of these immature progenitors.

MATERIALS AND METHODS

Antibodies

A detailed list of all antibodies used in this study is shown in **Supplementary Table 1**.

Mice

In our experiments, we used embryos from a *Rosa26*$^{Tomato/CFP}$ male crossed to a *Rosa26*$^{wt/wt}$ (C57Bl/6; Jackson Laboratory; stock no. 00664) female. *Rosa26*$^{Tomato/CFP}$ males were generated from a cross between *Rosa26*$^{Tomato/Tomato}$ (mT/mG; Jackson Laboratory; stock no. 007576) and *Rosa26*$^{CFP/CFP}$ (TM5; generous donation by Dr. Irving Weissman). NSG (NOD-*scid* IL-2Rγ^{null}; Jackson Laboratory; Stock no. 005557) mice were used as neonatal recipients. All strains were maintained at the Gross Hall and Med Sci A vivarium facilities at UCI and fed with standard chow and water. All animal procedures were approved by the International Animal Care and Use Committee (IACUC) and University Laboratory Animal Resources (ULAR) of University of California, Irvine.

Embryo Harvest and Tissue Processing

Mating cages were established and vaginal plugs were checked every morning to determine the time of pregnancy. The morning of plug detection was assigned as day 0.5. Pregnant mice were dissected and embryos harvested in PBS + 2% fetal bovine serum (FACS buffer) and kept on ice during tissue dissection. Somite pairs were counted and averaged for each experiment to determine dpc. Dpc designation is as follows: 15–29 somite pairs: e9.5; 30–39 somite pairs: e10.5; 40–50 somite pairs: e11.5. For tissue analyses and non-sorted transplants, CH, YS, and PL were harvested from e9.5 embryos. For e10.5 and e11.5 embryos, AGM and FL were harvested separately instead of together (e.g., CH). For sorted transplants, CH, YS, and PL were harvested from e10.5 donors and AGM, YS, PL, and FL from e11.5 donors. For non-sorted transplants, YS was harvested with the vitelline vessels, and PL was harvested with umbilical vessels. For sorted transplants, YS was separated without the vitelline vessels, and PL was harvested with umbilical vessels. Separated tissues were digested with 1 mg/mL Collagenase Type IV (ThermoFisher Scientific; cat. no. 17104019) for 30–45 min at 37°C. Tissues were pipetted up and down at 15-min intervals to aid with the digestion. Single cell suspension was filtered using a 40 μ mesh. We recommend using 40 μ (instead of 70 μ) mesh for donor cells to minimize clogging of blood vessels upon injection into neonatal recipients. Cells were washed twice and resuspended in FACS buffer for staining/transplantation.

Cell Sorting

Single cell suspensions of cells were typically stained for 20–30 min on ice. We recommend using ACK lysis buffer *after* completion of cell staining as pre-staining use can affect the VE-Cadherin signal. For sorting, a BD FACS-Aria II (Becton Dickinson) with FACSDiva software was used. For sorted transplants, the "purity" mode was used for cell sorting. Since opposing populations from differentially labeled embryo cells were pooled together, only embryo batches with close to 50–50% color distribution were used for the competitive sorted transplant. Therefore, physiological ratios of opposing populations were reflected in the final tube to be transplanted. For short-term homing sorts, the "yield" mode was used for cell sorting to maximize cell recovery.

In vivo Transplantation and Analysis

For non-sorted transplants, the embryo equivalent used for each timepoint is as follows: ≥4 ee for e9.5, ≤3 ee for e10.5, and ≤1 ee for e11.5. For all transplants, single cell suspensions were resuspended in 50–70 μL FACS buffer for injection with defined numbers of adult helper BM added. For neonatal transplants, cells were injected into the facial vein of sublethally irradiated (180–200 Rads; XRAD 320, Precision X-ray) P1-P4 NSG recipients. Nursing NSG mothers were fed an antibiotic chow of Trimethoprim Sulfa (Uniprim, Envigo) for 4 weeks post transplant to prevent bacterial infections. For secondary transplantation into adult recipients, recipient C57BL/6 mice were conditioned with 800 Rads, anesthetized by isoflurane, and retro-orbitally injected with 1–2 million whole BM harvested from primary recipients. For peripheral blood analysis, blood was obtained from the tail vein of transplanted mice at various timepoints, and red blood cells were depleted using ACK lysis buffer. For BM analysis, BM was harvested from tibias and femurs by flushing with ice-cold FACS buffer followed by ACK lysis and filtration. Cells were stained with lineage antibodies and analyzed on the BD FACS-Aria II. FlowJo software (Tree Star) was used for data analysis.

Cell Cycle Analysis

FoxP3/Transcription Factor Staining Buffer Kit (Tonbo Biosciences; cat. no. TNB-0607) is a paraformaldehyde/saponin based fixation/permeabilization buffer set for intracellular staining, and was adapted here for cell cycle analysis. Briefly, cells stained with extracellular antibodies were fixed with 1X Tonbo Foxp3/Transcription Factor Fix/Perm buffer for 45 min at 4°C, permeabilized/stained with PE anti-ki-67 antibody (Biolegend; cat. no. 652403) diluted in 1X Tonbo Flow Cytometry Perm Buffer for 45 min in the dark at room temperature. Cells were then washed and stained with 1 μM DAPI (Biolegend; cat. no. 422801) for 10 min prior to flow cytometric analysis. Ki-67 is a nuclear protein associated with cellular proliferation, and is expressed on cells that have entered the cell cycle, but not on quiescent G0 cells (Kim and Sederstrom, 2015). DAPI is a nuclear dye that can distinguish cells that have undergone DNA replication. We recommend avoiding separation of e10.5 tissues into fewer than 4 ee as the fix/perm process results in loss of cells.

Short-Term Homing Analysis

Neonatal recipients were sacrificed 15 h post-transplant for tissue dissection. Care was taken to harvest tissues in their entirety. All tissues except bones were harvested by crushing in between

slides followed by separation using a 28-gauge needle. Limb bones were crushed using a pestle and mortar. Crushed bone particles were passed through a 28-gauge needle for further separation. All tissues were filtered through a 40 μ mesh and ACK lysed prior to staining.

Statistical Analysis

Statistical analysis was performed with GraphPad Prism 5 software (La Jolla, CA, United States).

RESULTS

Establishing the NSG Neonatal Transplant System for *in vivo* Detection of Pre-HSCs

To functionally detect pre-HSC activity *in vivo*, we used immunodeficient NSG (NOD/SCID/IL2rγ$^{-/-}$) neonatal mice as transplantation recipients (Ishikawa, 2013; Verbiest et al., 2016; Dai et al., 2017). We first tested this system on unsorted embryonic cells harvested from e9.5 to e11.5 tissues, the stages when pre-HSCs are thought to emerge, expand, and mature. From e9.5 embryos we harvested the YS, PL, and caudal half (CH), which contains the AGM. From e10.5 and e11.5 embryos we harvested the YS, PL, AGM, and FL (**Figure 1A**). Cells from whole tissues of e9.5–11.5 donors along with adult helper BM were transplanted into irradiated NSG neonates followed by tissue analysis and secondary transplants (**Figure 1B** and **Supplementary Figure 1**). While donor chimerism from e9.5 donors was detected at extremely low rates, we consistently detected BM HSC engraftment from all tissues of e10.5 and e11.5 donors (**Figure 1C** and **Supplementary Figure 1**). To confirm that none of the transplanted cells were *already* HSCs, we separately transplanted e10.5 and e11.5 donor cells into *adult* recipients and did not find any long-term adult BM engraftment (**Supplementary Figure 2**). It should be noted that while e11.5 tissues can contain adult-engraftable HSCs, this activity is rare, often less than one HSC per embryo (Arora et al., 2014), and we did not find any HSC-engraftment in our transplants. Therefore, any engraftment in the neonatal recipients must have come from cells which lack adult engraftability, and are thereby pre-HSCs.

Establishment of an Embryonic Competitive Transplant System

We next used the NSG neonatal transplant system to assay sorted populations for pre-HSC activity. To allow us to directly compare sorted embryonic populations in a competitive setting, we bred mice to generate embryos that expressed either CFP or Tomato fluorescent reporters in the same litters. To accomplish this, males bearing two reporters, Tomato and CFP (*Rosa26*$^{Tomato/CFP}$), on different alleles of the *Rosa26* locus, were crossed to Wt females (*Rosa26*$^{wt/wt}$). Each offspring will receive only one reporter allele and be either Tomato+ (*Rosa26*$^{Tomato/wt}$) or CFP+ (*Rosa26*$^{CFP/wt}$). Therefore, age-matched littermates can be distinguished by color, sorted based on marker expression, and co-transplanted in a head-to-head competitive setting (**Figures 2A,B**). Provided equal numbers of embryos of each color are used, we can directly compare two populations to determine which contains more pre-HSCs by measuring donor chimerism in the recipient animals. Unlabeled adult B6 BM was used as helper (CD45.2+), and could be distinguished from host NSG recipients (CD45.1+). As the injection into the facial vein of neonatal mice is technically challenging, the inclusion of helper BM (which also contains HSCs) also served as an internal control to determine injection success.

All Pre-HSCs Are Within the CD11a- Fraction of Progenitors in e10.5 and e11.5 Embryos

Our previous study identified a population that contained all *in vitro* clonal multipotent activity in the early embryo (Inlay et al., 2014). These cells are within the CD144+ CD11a- fraction of "eKLS" cells (embryonic equivalent of the adult KLS population), which is defined as Ter119- CD43+ Kit+ Sca1+. To determine whether CD144+ CD11a- eKLS cells ("11a- eKLS"), contains pre-HSCs, we sorted and transplanted embryonic progenitors into neonatal recipients. Due to the low engraftment rate of e9.5 whole-tissue transplants (**Figure 1C** and **Supplementary Figure 1A**), we focused only on e10.5 and e11.5 tissues. We also sorted all other eKLS cells (not CD11a- CD144+ eKLS cells, or "Other eKLS"), to ensure that other potential sources of pre-HSCs were also examined. We sorted "11a- eKLS" from one color of embryo (e.g., Tomato+), and mixed it with "Other eKLS" sorted from the other color embryo (e.g., CFP+) and co-transplanted them along with helper BM into neonatal NSG recipients (**Figures 2A,B** and **Supplementary Figure 3**). We maintained the physiological ratios of the two populations, such that each recipient contained the equivalent of all eKLS cells from each embryo (**Figure 2B**). Thus, whichever fraction contained the most pre-HSCs would display greater donor chimerism in the recipients, regardless of how many non-pre-HSCs were contained in that fraction. On average, each recipient received 3–4 embryo equivalents (ee) of each population.

Blood analysis of recipients showed higher total CD45+ leukocyte chimerism (total blood chimerism) from the 11a- eKLS population compared to the "Other eKLS" source at both e10.5 and e11.5 timepoints and from all embryonic tissues examined (**Figure 2Ci** and **Supplementary Figure 4**). Within the short-lived granulocyte compartment, we found that only the 11a- eKLS cells gave rise to donor granulocytes in all recipients (**Figure 2Cii** and **Supplementary Figure 4**). BM analysis of recipients confirmed the presence of embryo-derived HSPCs (hematopoietic stem/progenitor cells, Ter119- CD27+ Kit+ Sca1+) only from the 11a- eKLS population with no contribution from the other eKLS source (**Figure 2Ciii**). We then performed secondary transplants and confirmed long-term engraftability of 11a- eKLS-derived HSCs (**Figure 2Civ**). We also examined the distribution of donor lineages to determine whether 11a- eKLS cells exhibited any

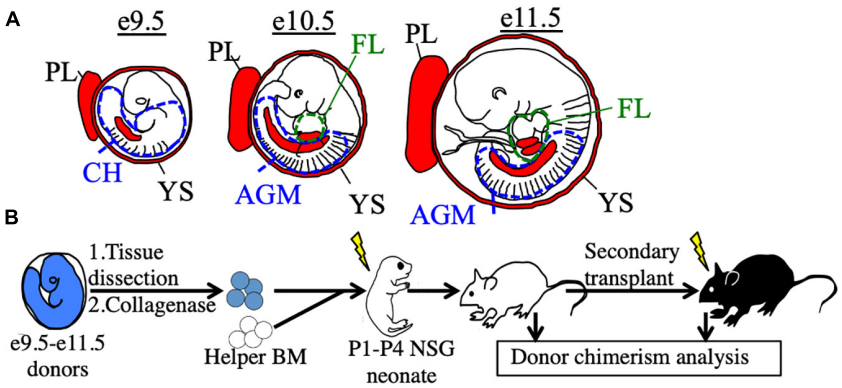

C

dpc	ee/ recipient	Helper BM	Donor tissue	LT-chimerism	Total blood chimerism	successful injections	LT-Engraftment efficiency
e8.5	4-8	none	WE	0	0	n.d.	NA
e9.5	4-8	0-500K	CH	2	6	16	0.12
			YS	0	8	16	NA
			PL	0	3	12	NA
e10.5	3	75-200K	AGM	4	10	16	0.25
			YS	9	16	20	0.45
			PL	2	6	12	0.17
			FL	1	2	10	0.10
e11.5	1	100-200K	AGM	6	7	7	0.86
			YS	6	11	12	0.50
			PL	5	8	8	0.63
			FL	6	12	12	0.50

FIGURE 1 | Utilization of the NSG neonatal transplant system to reveal pre-HSCs in e9.5–11.5 embryos. **(A)** Schematic representation of hematopoietic tissues (red) harvested from e9.5, e10.5, and e11.5 embryos. YS, yolk sac; PL, placenta; CH, caudal half; AGM, aorta-gonad-mesonephros; FL, fetal liver. Dissection sites of the CH/AGM and FL are shown in blue and green dashed lines, respectively. **(B)** Schematic representation of the neonatal transplant system. Harvested tissues from e9.5–11.5 donor CFP+ embryos are dissected, dissociated, and combined with CFP- adult helper BM. Donor cells are administered intravenously (i.v.) into irradiatated neonatal NSG recipients of 1–4 days of age (P1-P4). Recipients are bled for donor chimerism analysis at 4 week intervals and are then sacrificed for BM analysis and secondary transplants. **(C)** Compilation of whole-tissue transplants from e8.5–11.5 embryos. Number of successful tissue-specific long-term engraftment ("LT-chimerism") is determined by the presence of ≥1% embryo donor granulocyte chimerism (at the last bleed) and HSPC (hematopoietic stem/progenitor cell) chimerism in the BM. "Total blood chimerism" refers to the number of recipients with ≥1% embryo chimerism in total CD45+ compartment of blood. "Successful injection" is defined as engraftment of either embryo or helper adult BM donors. "Engraftment efficiency" is determined by # of successful embryo engraftment/total successful injections. dpc, days post conception; ee, embryo equivalent; WE, whole embryo.

lineage biases depending on which tissue they were sorted from **Supplementary Figures 4C,D**. While some recipients displayed a minor increase in T cells over B cells, there did not appear to be a consistent bias for any specific tissue source or timepoint. Notably, 11a- eKLS cells from e11.5 FL had a significantly decreased myeloid output relative to lymphoid output, due to increase T cell production. We also examined lineage output over time, but observed no trends that would indicate some tissues produce some lineages earlier or faster than others (data not shown).

While our data shows that up to e11.5, all pre-HSC activity is in the CD11a- fraction, at later timepoints, e13.5 and e14.5, we observed neonatal engraftment from both CD11a- and CD11a+ progenitors (**Supplementary Figure 5A**). At e14.5, we also observed adult engraftment from both CD11a- and CD11a+ fractions (**Supplementary Figure 5B**). This is consistent with our previous studies where we found multipotency within both CD11a- and CD11a+ fractions at e12.5 (Inlay et al., 2014), and found both CD11a- and CD11a+ fetal HSCs at e17.5 (Fathman et al., 2014). This suggests that pre-HSCs/HSCs transiently upregulate CD11a during their maturation from pre-HSCs to HSCs.

All Pre-HSCs Are Sca1+ at e11.5 and Efficiently Identified by Anti-Sca1 Staining

Some groups have reported low/undetectable Sca1 protein expression on early hematopoietic progenitors (De Bruijn et al., 2002), and require a Sca1-GFP transgenic

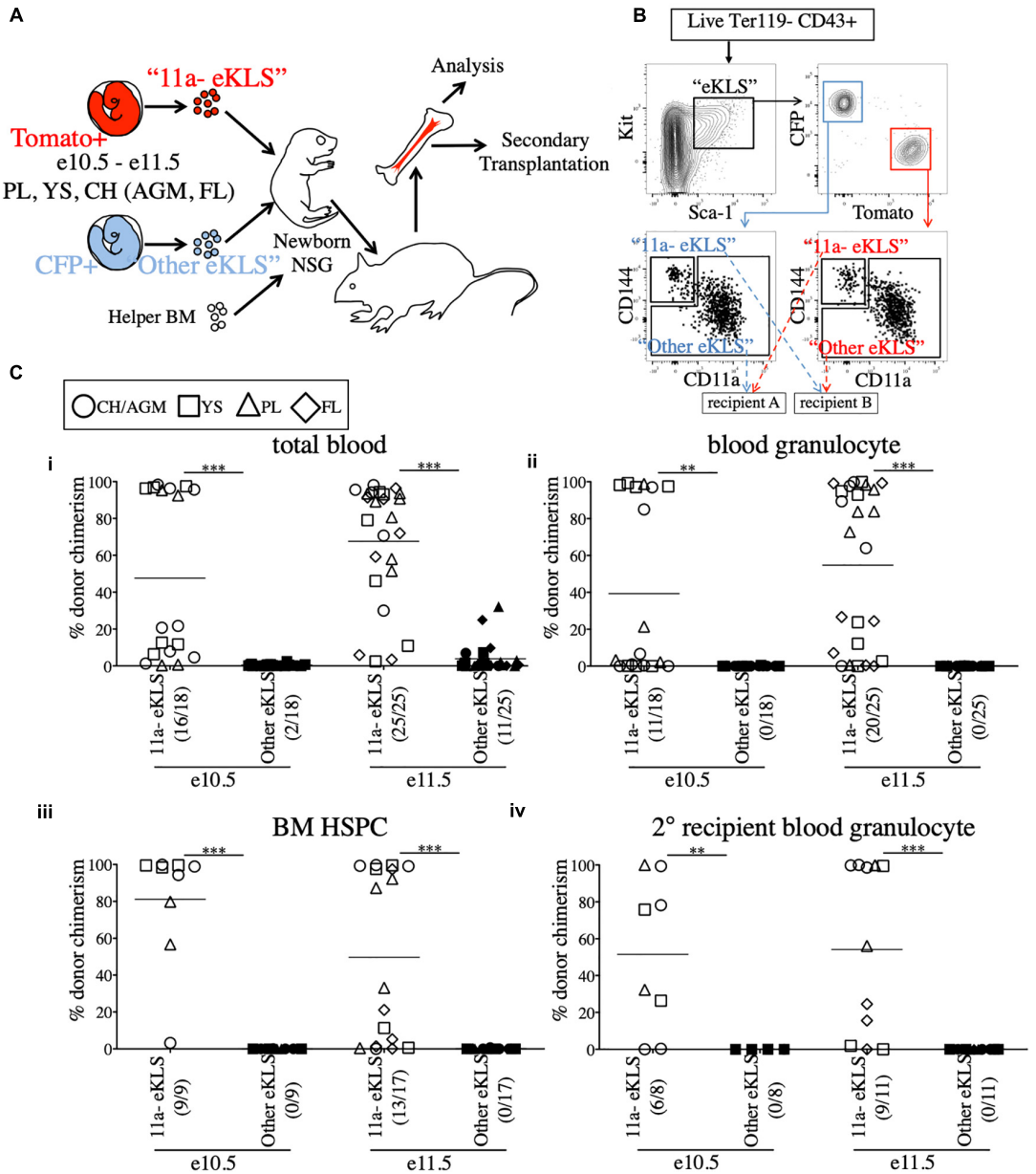

FIGURE 2 | All functional pre-HSCs are contained within the CD11a- fraction of e10.5 and e11.5 embryonic progenitors. **(A)** Schematic representation of the competitive transplant system. Sorted Tomato-expressing "11a-eKLS" and CFP-expressing "Other eKLS" cells (and vice versa) are combined and mixed with non-fluorescent CD45.2+ adult helper BM for transplantation into newborn NSG recipients. **(B)** Representative sorting strategy for the competitive transplantation of 11a- eKLS and Other eKLS populations. Embryonic progenitors are defined as live, Ter119- CD43+ Kit+ Sca1+ cells. Tomato+ and CFP+ progenitors are then gated, and CD11a- CD144+ ("11a- eKLS") and everything else ("Other eKLS") are sorted. Opposing populations of different colors are mixed post-sort and transplanted into the same recipient. Representative plots and gates for each tissue and timepoint can be found in **Supplementary Figure 3**. **(C)** Donor chimerism from 11a- eKLS and Other eKLS populations in primary and secondary recipients. Percent donor chimerism of total blood **(i)**, blood granulocyte **(ii)**, BM HSPC **(iii)** in primary recipients and blood granulocyte chimerism in secondary recipients **(iv)** from 11a- eKLS (white symbols) and Other eKLS (black symbols). Numbers in parenthesis indicate successful chimerism/total recipients engrafted with embryonic cells of any source. Blood analysis was done after at least 12 weeks post primary transplant and after at least 6 weeks post secondary transplant. 1% is set as a threshold to define successful chimerism. CH/AGM (circle), YS (squares), PL (triangles), and FL (diamond) are shown. For a tissue-specific analysis of both timepoints, refer to **Supplementary Figure 4**.

reporter (Ly-6A-GFP) in order to identify Sca1+ cells in the embryo. To rule out whether any pre-HSC activity was present in the Sca1- fraction, e11.5 CFP/Tomato embryos were separated into individual tissues (YS, FL, PL, and AGM) and stained (**Figure 3**). CD43+ Ter119- Kit+ cells were separated into Sca1+ and Sca1- fractions (from different reporters) and co-transplanted into neonatal NSG recipients (**Figure 3A**). 12 weeks after transplantation, we found that only

the Sca1+ fraction consistently produced donor chimerism (blood granulocytes and BM HSPCs) in the recipient mice, including in secondary recipients, indicating that few, if any, pre-HSCs are contained in the Sca1- population in e11.5 tissues (**Figure 3B**). It should be noted that in this set of experiments, not all tissues engrafted equally, and the PL and AGM eKLS populations had higher overall chimerism than that from the YS and FL.

CD11a- Embryonic Progenitors Are More Quiescent Compared to Their CD11a+ Counterparts

Next, we examined the absolute numbers of CD11a- and CD11a+ eKLS progenitors at different embryonic stages and in different tissues. At e10.5, both populations were most abundant in the YS, followed by the PL and AGM, with the fewest found in the FL. However, by e11.5, both populations were most abundant in the FL, and reduced in the other tissues (**Figures 4Ai,ii**). These data support the previously described migration of hematopoietic progenitors from the AGM, YS, and PL to the FL over time and confirm the FL as the primary site of hematopoiesis in mid-gestation (Kumaravelu et al., 2002). Furthermore, a much higher frequency of CD11a+ eKLS cells in e14.5 FL suggested the higher expansion rate of CD11a+ progenitors and/or less frequent division of the CD11a- progenitors.

We next examined the cell cycle status of early (e10.5) and late (e14.5) embryonic progenitor (eKLS) fractions (**Figure 4B**), using staining for the proliferation marker Ki-67 and the nuclear dye DAPI, which collectively can distinguish cells in G0, G1, and S/G2/M phases (Kim and Sederstrom, 2015). In e10.5 tissues, we observed a shift in the fraction of cells in G0/G1 phase vs. S/G2/M phase between CD11a- and CD11a+ eKLS cells respectively, suggesting a higher rate of division among the CD11a+ fraction (**Figure 4Ci**). This difference was more pronounced in e14.5 FL tissues, as many CD11a- eKLS cells were in G0 phase while the CD11a+ fraction had increased S/G2/M phase cells (**Figure 4Cii**). These observations support the notion that the CD11a- and CD11a+ embryonic progenitors begin to resemble quiescent adult HSCs and downstream transit-amplifying cells, respectively.

The Neonatal Liver Harbors Transplanted Embryonic Progenitors Shortly After Transplant

Why do pre-HSCs engraft in neonates, but not adult recipients? Previous studies have suggested a role for the neonatal liver in providing a niche for the maturation of pre-HSCs prior to BM seeding (Arora et al., 2014). To determine whether embryonic progenitors seeded the FL directly, we transplanted e10.5 and e11.5 sorted hematopoietic progenitors (Ter119- CD43+ Kit+) along with adult BM into NSG neonates and analyzed recipient tissues 15 h post-transplant for the presence of transplanted cells (**Figure 5A** and **Supplementary Figure 6**). Amongst the different tissues examined, the liver of the recipients contained by far the highest number of transplanted progenitors originating from both e10.5 and e11.5 embryonic sources as well as the adult donor source (**Figure 5B**). Similar results were found when we investigated the presence of embryo-derived donor leukocytes (Ter119- CD43+) and donor eKLS (**Supplementary Figure 6**). These results suggest that pre-HSCs and other Kit+ progenitors may be unable to migrate directly to the BM upon transplantation, but instead first seed the FL.

To that end, we also investigated the expression of CXCR4, a receptor on HSCs known to be involved in homing to the BM on adult HSCs and embryonic pre-HSCs (Wright et al., 2002). CXCR4 was expressed on a very low percentage of e10.5 11a-eKLS cells regardless of tissue, whereas it was expressed on nearly all adult HSCs (**Figures 5Ci,ii**). At e14.5, the FL contains adult-engraftable phenotypic HSCs (defined as CD150+ CD48- KLS). These HSCs also expressed CXCR4 on their surface to a similar degree as adult HSCs (**Figure 5Ciii**). This suggests that pre-HSCs are unable to directly home to the BM in part because they lack CXCR4 expression. Together, these results suggest that the neonatal liver may serve as the initial site of engraftment of transplanted embryonic cells until their eventual maturation and seeding of the BM.

DISCUSSION

The precise surface marker identity of pre-HSCs in the embryo has remained elusive, hampering efforts to understand how HSCs arise during embryonic development. Our previous results identified a candidate pre-HSC population using an *in vitro* multipotency assay (Inlay et al., 2014). Here, using an *in vivo* neonatal transplantation assay, we demonstrate that this population, which we call "11a- eKLS" (Ter119- CD43+ Kit+ Sca1+ CD144+ CD11a-), contains all *in vivo* pre-HSC activity at gestational days e10.5 and e11.5 in the mouse embryo. As we compared 11a- eKLS cells to all other KLS cells in the embryo (**Figure 2**), as well as all Kit+ cells (**Figure 3**), we are confident 11a- eKLS cells are the *only* source of pre-HSCs at these timepoints. Additional markers may subdivide this population further, but 11a- eKLS cells also express CD41, CD105, and Tie2, and lack expression of Fcγr, CD11b, and Flk2 (Inlay et al., 2014). Importantly, the lack of CD11a expression on these cells was critical for distinguishing them from downstream progenitors, and could not be replaced with other pre-HSC markers such as VE-Cadherin (CD144), CD41, or CD45. While CD27 has been found to be expressed on Type II pre-HSCs in the e11.5 AGM (Li et al., 2017), we have not found CD27 to be expressed on CD11a- eKLS cells (previous unpublished observations). CD27 expression is rare in the embryo during these stages, and may upregulate later in development to mark more mature pre-HSCs. Additionally, our analysis of the cell cycle status of these populations (**Figure 4**) supports the notion that CD11a-eKLS cells contain pre-HSCs that slowly transition to quiescent HSCs, while the CD11a+ fraction represents downstream transit-amplifying cells.

Many groups studying embryonic origins of HSCs have found success in identifying embryonic cells with HSC potential by first culturing them *ex vivo* in cytokine combinations that drive hematopoietic maturation (Rybtsov et al., 2014). We chose an

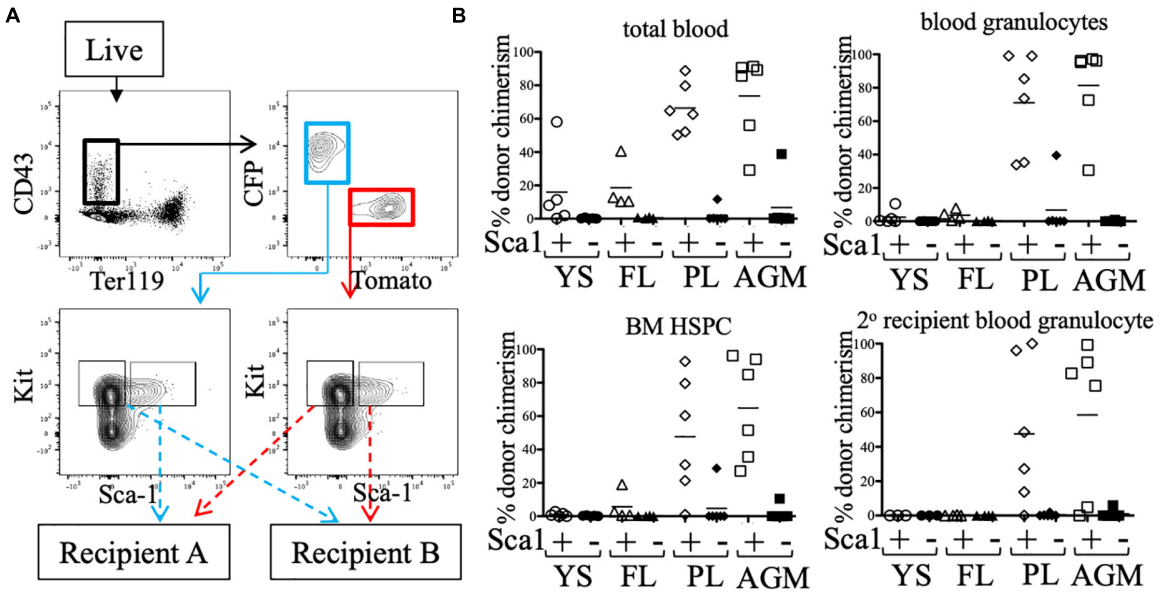

FIGURE 3 | Sca1 "plus/minus" sort and neonatal transplant. **(A)** Representative FACS plot of sorted populations for transplantation (AGM shown). Live cells from e11.5 embryonic tissues were first gated on CD43+ Ter119-, then separated into CFP+ and Tomato+ fractions. Kit+ cells within these gates were sorted into Sca1+ and Sca1- fractions. Prior to transplantation into neonatal NSG recipients, cells were mixed such that Sca1+ fraction of one color (e.g., CFP) was co-transplanted with the Sca1- fraction of the other color (e.g., Tomato). **(B)** Total blood (CD45+ cells), blood granulocyte, and BM HSPC chimerism of the Sca1+ (white symbols) and Sca1- (black symbols) fractions of e11.5 embryos are shown at week 12. Week 12 bone marrow was harvested and transplanted into lethally-irradiated B6 adult recipients and blood granulocyte chimerism was analyzed 6 weeks post-secondary transplant.

in vivo approach to identify cells with neonatal engraftability as an alternative, independent method of identifying HSC precursors. While primitive hematopoiesis is known to begin at e7.0–e7.5, and definitive hematopoiesis at 8.5, we did not identify neonatal engraftable cells until e9.5. Furthermore, we only identified this from unsorted caudal half tissue, and could not consistently achieve neonatal engraftment from sorted cells at e9.5. While we could identify 11a- eKLS cells at e9.5 (Inlay et al., 2014), we cannot claim this population is neonatal engraftable until e10.5.

We found 11a- eKLS cells (and its pre-HSC activity) in all tissues we examined, and thus this study is agnostic as to which embryonic tissue(s) produce pre-HSCs. Due to the challenges and highly variable engraftment rates in the neonatal transplantation system, we did not attempt to compare engraftment levels of sorted pre-HSCs between each tissue to determine which tissue contained more pre-HSCs. Unfortunately, we were unable to consistently sort enough 11a- eKLS cells from the vitelline vessels to transplant them, though they are likely an important source of pre-HSCs (de Bruijn, 2000). Vitelline vessels were carefully excluded from the YS dissections to avoid any vitelline-derived pre-HSCs from being included in the YS analyses. It should also be noted that at e9.5, only the unsorted cells from the caudal half (CH) engrafted long-term (**Figure 1C**). In the sorted experiments, we more often observed higher chimerism from AGM than from the YS (**Figure 2C**). Lastly, in the Sca1 plus/minus transplants (**Figure 3B**), we observed robust engraftment only from the Sca1+ (CD43+ Ter119- Kit+) cells sorted from the AGM and placenta, but not the YS or FL. Thus, while we observed engraftment from 11a- eKLS cells regardless of which timepoint or tissue we sorted them from, those sorted from the AGM tended to lead to higher engraftment. It is possible that 11a- eKLS cells are distinct from one another depending on which tissue they originated in. There appeared to be some differences in lineage distribution amongst the 11a- eKLS derived cells in the recipients (**Supplementary Figure 4**), most notably an increase in T cells in several recipients. However, given that the recipients are immunodeficient and devoid of their own lymphocytes, the expansion of T cells in these recipients after transplantation may be due to variability in their reconstitution kinetics and not due to intrinsic lineage biases *per se*. We had hypothesized that extra-embryonic sources of pre-HSCs (YS, PL) may contain a myeloid bias compared to embryonic sources (AGM, FL), but our results do not support that. Given the variability in lineage output in the recipients, it is possible that lineage biases exist between pre-HSCs derived from different tissues, but our assay was not sensitive enough to detect it. Alternatively, the pre-HSCs emerging from different tissues may have initial differences that disappear as these cells migrate to secondary sites such as the fetal liver and BM and mature there.

Whether fully-functional HSCs emerge *de novo* from hemogenic endothelium (HE) is unclear. Our results support the notion that a precursor emerges first from HE and then later matures into HSCs. This may require migration to a different site in order to complete development. As part of the LFA-1 complex, CD11a is involved in the extravasation of circulating immune cells. Thus, the differentiation of a pre-HSC (CD11a-) to a downstream transit amplifying progenitor (CD11a+)

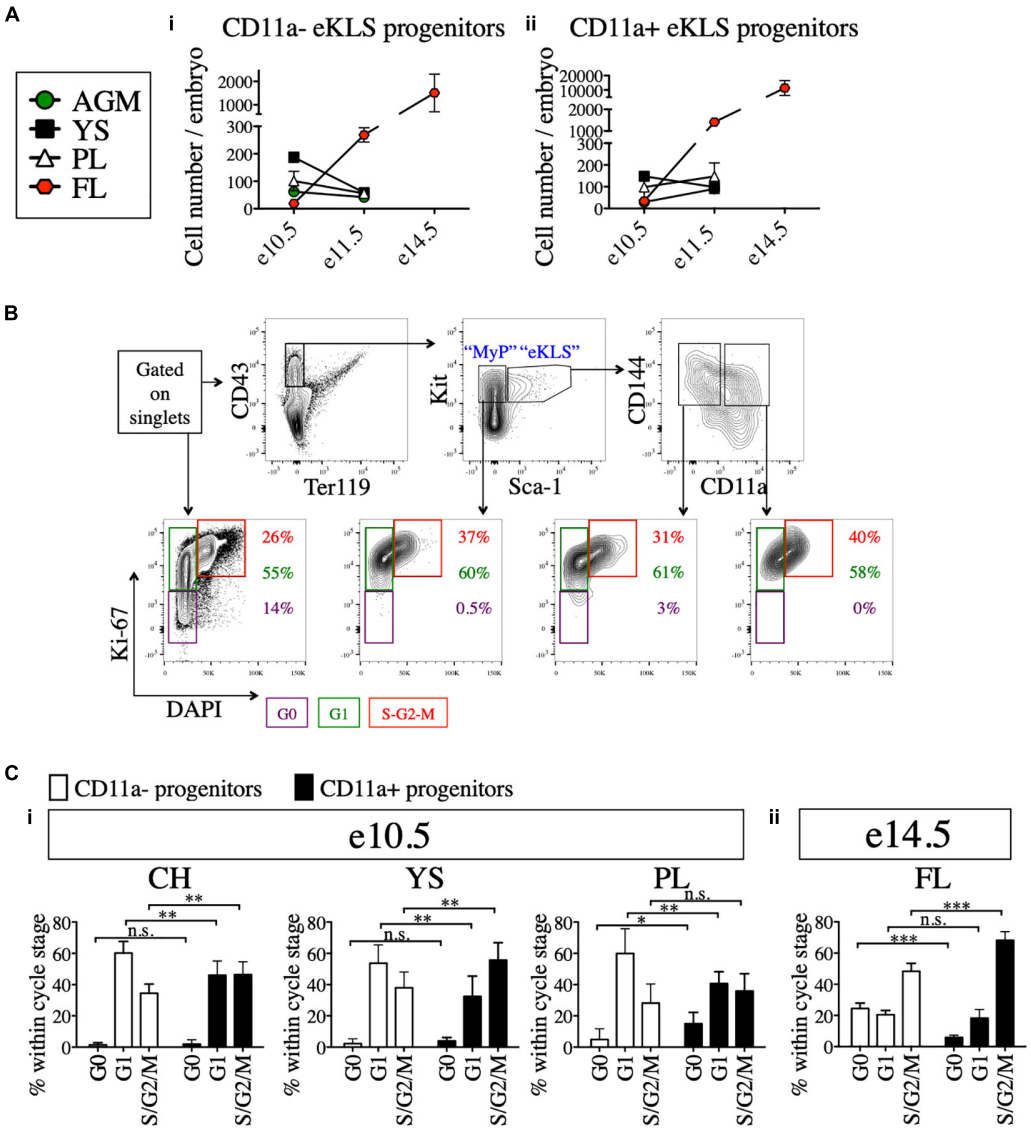

FIGURE 4 | Cell cycle analysis of 11a- eKLS cells and CD11a+ progenitors. **(A)** Numbers of CD11a- and CD11a+ progenitors in embryos over time. Estimated number of CD11a- progenitors **(i)** and CD11a+ progenitors **(ii)** per embryo is depicted in embryonic tissues at e10.5, e11.5, and e14.5. "eKLS progenitors" are defined as Ter119- CD43+ Sca1+ Kit+ CD144+ at e10.5 and e11.5, and as Ter119- CD43+ Sca1+ Kit+ EPCR+ at e14.5. e10.5, $n = 4$ (two independent experiments); e11.5, $n = 5$ (three independent experiments; e14.5, $n = 10$ (two independent experiments). **(B)** Representative analysis of the cell cycle status in embryonic population. Bottom plots show DAPI (x-axis) and Ki-67 (y-axis) within total single cells, myeloid progenitors (MyP), 11a- eKLS, and 11a+ eKLS from left to right. The color of percentage values inside the gates correlate with the color of each gate/cell cycle phase. e10.5 CH is shown as a representation. **(C)** Cell cycle analysis of CD11a- and CD11a+ progenitors at e10.5 and e14.5. Cell cycle status of each population is depicted for e10.5 tissues **(i)** and e14.5 FL **(ii)**. "Progenitors" are defined as Ter119- CD43+ Sca1+ Kit+ CD144+ at e10.5, and as Ter119- CD43+ Sca1+ Kit+ CD150+ at e14.5. *$p \leq 0.05$, **$p \leq 0.01$, and ***$p \leq 0.001$ (Student's unpaired t test) e10.5, $n = 8$ (two independent experiments); e14.5 = 5 (two independent experiments).

could be associated with a transition to a more migratory state. Interestingly, CD11a upregulation correlates with the downregulation of VE-Cadherin (CD144), a molecule necessary for forming junctions between endothelial cells. Downregulation of VE-Cadherin could allow pre-HSCs to detach from the endothelium and enter circulation while CD11a upregulation signals their extravasation to other tissues. In support of this concept, we have observed CD11a+ pre-HSC at e14.5 (**Supplementary Figure 5**), and CD11a+ fetal HSCs at e17.5 (Fathman et al., 2014). CD11a upregulation could be coupled to the migration of pre-HSCs into the fetal liver, and HSCs into the newly-formed BM cavity. However, it should be noted that chimerism was always lower from the CD11a+ fraction than CD11a-, suggesting CD11a+ pre-HSCs are a rare and transient population.

Why can pre-HSCs engraft in neonatal recipients, but not adult? The liver persists as an active site of hematopoiesis until shortly after birth (up to 3 weeks) (Bowie et al., 2007). As

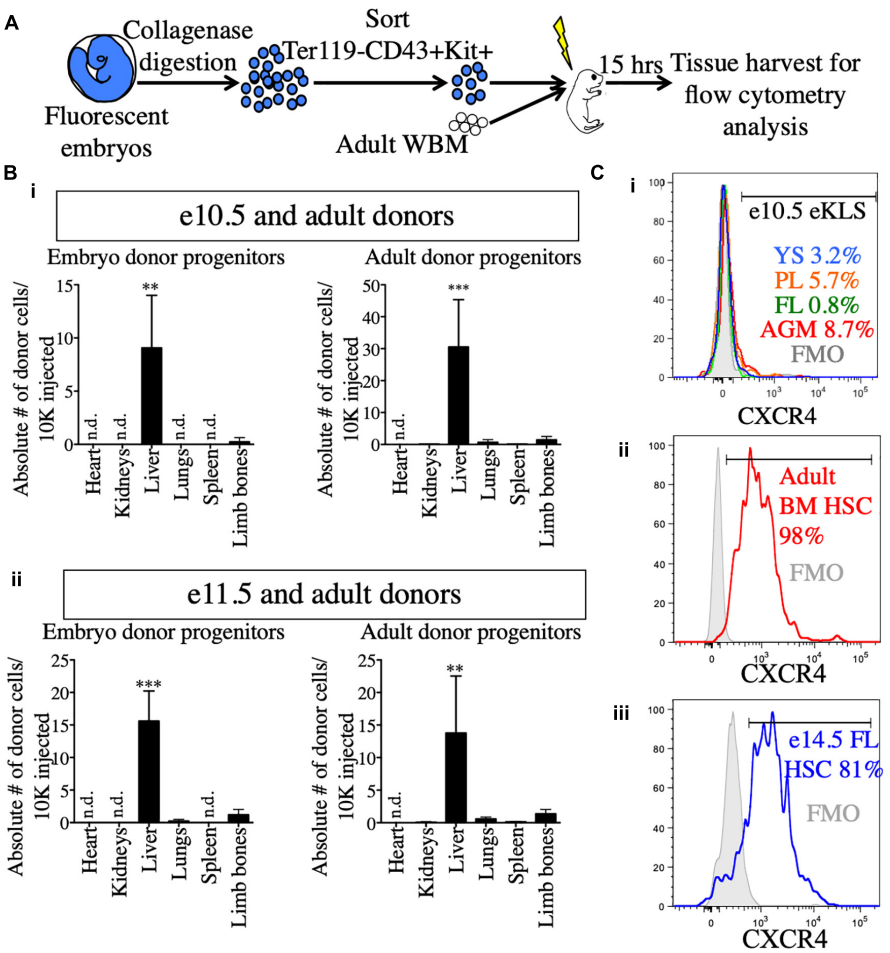

FIGURE 5 | Neonatal liver harbors transplanted embryonic and adult donors in the short-term post-transplant. **(A)** Schematic representation of short-term homing assay. Ter119- CD43+ Kit+ progenitors were sorted from whole embryos, mixed with 100,000 adult WBM and transplanted into irradiated P1-P4 neonatal recipients. 15 h post-transplant, organs were harvested for FACS analysis. **(B)** Detection of donor progenitors shortly after transplant. Absolute number of Ter119- CD43+ Kit+ progenitors originating from e10.5 **(i)** and e11.5 **(ii)** embryos and the accompanying adult source normalized to 10,000 injected cells are shown in the heart, kidneys, liver, spleen, and limb bones of the neonatal recipients. Tissues were harvested and processed in their entirety. "Limb bones" includes femurs and tibias from the hind limbs and humeri from the forelimbs. $^{**}p \leq 0.01$ and $^{***}p \leq 0.001$ (Student's unpaired *t* test). e10.5, $n = 3$ (two independent experiments); e11.5, $n = 4$. **(C)** Surface expression of CXCR4 in e10.5 pre-HSCs **(i)**, adult BM HSCs **(ii),** and e14.5 FL HSCs **(iii)**. Percentages of CXCR4+ cells are shown in histograms. FMOs were used to set the positive gate. Adult BM and e14.5 FL HSCs were stained and analyzed in the same experiment. e10.5 pre-HSCs were analyzed in a separate experiment alongside appropriate positive staining controls (adult BM HSCs, data not shown). FMO, fluorescence minus one; n.d., not detected.

such, the neonatal liver might provide a temporary and readily accessible niche for transplanted pre-HSCs. Indeed, we found that almost all transplanted embryonic progenitors homed to the liver of neonatal recipients shortly after transplantation (**Figure 5**). We also observed that adult HSCs also preferentially seeded the neonatal liver over the BM, suggesting a more passive mechanism for liver seeding rather than direct homing (**Figure 5B**). Regardless, this suggests that the developing liver microenvironment provides pre-HSCs with maturation signals required for eventual BM homing/engraftment, such as the upregulation of the BM homing receptor CXCR4. Indeed, the upregulation of CXCR4 in the FL from e10.5 to e14.5 suggests the ability to respond to BM homing signals (CXCL12) correlates with the maturation of pre-HSCs into BM-engraftable HSCs. In this regard, many previous studies have highlighted the supportive effects of the FL niche stroma on HSC maintenance/expansion (Moore et al., 1997; Martin and Bhatia, 2005; Chou and Lodish, 2010; Khan et al., 2016).

In summary, we report a highly-enriched population "11a-eKLS" that contains *all* pre-HSC activity in the embryo. Upon transplantation into neonatal recipients, these cells appear to seed the liver first, and therein mature into BM-engraftable HSCs. As such, our data implicate this population as the immediate precursor population to HSCs. CD11a negativity was critical for identifying these cells up to e11.5, and can allow for improved isolation and characterization of developing pre-HSCs. This in turn can lay the groundwork to determine the molecular cues required for maturation into HSCs. Efforts aimed to generate HSCs from pluripotent sources, although promising and improving, have failed to display robust BM engraftment

of the differentiated HSCs (Riddell et al., 2014; Lee et al., 2017; Sugimura et al., 2017). Given the similarities between pluripotent source-derived HSCs and pre-HSCs (e.g., HSC-like phenotype without BM homing/engraftment potential), identification of environmental stimuli involved in pre-HSC maturation could reveal how to generate engraftable HSCs from pluripotent stem cells.

DATA AVAILABILITY STATEMENT

The original contributions presented in the study are included in the article/**Supplementary Material**, further inquiries can be directed to the corresponding author/s.

ETHICS STATEMENT

The animal study was reviewed and approved by International Animal Care and Use Committee (IACUC), and University Laboratory Animal Resources (ULAR), of the University of California, Irvine.

AUTHOR CONTRIBUTIONS

AK, EV, and MI designed the study and all experiments. AK and EV performed all experiments, with contributions from VS, CC, KG, PN, and YG. IW and TS contributed intellectual support, experimental strategy, and unpublished data. AK wrote the first draft of the manuscript. EV provided additional writing. MI edited the manuscript. All experiments were performed in the laboratory of MI. All authors contributed to the article and approved the submitted version.

FUNDING

This study was supported by National Institutes of Health (NIH) grants R56HL133656 and R21CA224022 (to MI), R35CA220434 and R01DK115600 (to IW), American Cancer Society ACS/IRG Seed Grant IRG 98-27-10 (to MI), and California Institute for Regenerative Medicine grant CL1-00520-1.2 (to VS and the UC Irvine Stem Cell FACS Core). AK was supported in part from NIH grant R01AG055524, and EV was supported by NIH T32AI060573 through the Institute for Immunology at UC Irvine, and a gift from the Oxnard Foundation.

ACKNOWLEDGMENTS

The authors would like to thank Martina Sassone-Corsi, Craig Walsh, Melissa Lodoen, Matthew Blurton-Jones, and David Fruman for helpful input, and Tannaz Faal and Ankita Shukla of the Inlay lab for constructive comments.

SUPPLEMENTARY MATERIAL

The Supplementary Material for this article can be found online at: https://www.frontiersin.org/articles/10.3389/fcell.2021.734176/full#supplementary-material

REFERENCES

Akashi, K., and Weissman, I. L. (2001). "Stem cells and hematolymphoid development," in *Hematopoiesis A Developmental Approach*, ed. L. I. Zon (Oxford: Oxford University Press), 15–34.

Alvarez-Silva, M., Belo-Diabangouaya, P., Salaün, J., and Dieterlen-Lièvre, F. (2003). Mouse placenta is a major hematopoietic organ. *Development* 130, 5437–5444. doi: 10.1242/dev.00755

Arora, N., Wenzel, P. L., McKinney-Freeman, S. L., Ross, S. J., Kim, P. G., Chou, S. S., et al. (2014). Effect of developmental stage of HSC and recipient on transplant outcomes. *Dev. Cell* 29, 621–628. doi: 10.1016/j.devcel.2014.04.013

Balazs, A. B., Fabian, A. J., Esmon, C. T., and Mulligan, R. C. (2006). Endothelial protein C receptor (CD201) explicitly identifies hematopoietic stem cells in murine bone marrow. *Blood* 107, 2317–2321. doi: 10.1182/blood-2005-06-2249

Beaudin, A. E., Boyer, S. W., Perez-Cunningham, J., Hernandez, G. E., Derderian, S. C., Jujjavarapu, C., et al. (2016). A transient developmental hematopoietic stem cell gives rise to innate-like B and T cells. *Cell Stem Cell* 19, 768–783. doi: 10.1016/j.stem.2016.08.013

Boisset, J. C., Van Cappellen, W., Andrieu-Soler, C., Galjart, N., Dzierzak, E., and Robin, C. (2010). In vivo imaging of haematopoietic cells emerging from the mouse aortic endothelium. *Nature* 464, 116–120. doi: 10.1038/nature08764

Bowie, M. B., Kent, D. G., Dykstra, B., McKnight, K. D., McCaffrey, L., Hoodless, P. A., et al. (2007). Identification of a new intrinsically timed developmental checkpoint that reprograms key hematopoietic stem cell properties. *Proc. Natl. Acad. Sci. U.S.A.* 104, 5878–5882. doi: 10.1073/pnas.0700460104

Chou, S., and Lodish, H. F. (2010). Fetal liver hepatic progenitors are supportive stromal cells for hematopoietic stem cells. *Proc. Natl. Acad. Sci. U.S.A.* 107, 7799–7804. doi: 10.1073/pnas.1003586107

Cumano, A., and Godin, I. (2007). Ontogeny of the hematopoietic system. *Annu. Rev. Immunol.* 25, 745–785. doi: 10.1146/annurev.immunol.25.022106.141538

Dai, H., Friday, A. J., Abou-Daya, K. I., Williams, A. L., Mortin-Toth, S., Nicotra, M. L., et al. (2017). Donor SIRP polymorphism modulates the innate immune response to allogeneic grafts. *Sci. Immunol.* 2:eaam6202. doi: 10.1126/sciimmunol.aam6202

de Bruijn, M. F. T. R. (2000). Definitive hematopoietic stem cells first develop within the major arterial regions of the mouse embryo. *EMBO J.* 19, 2465–2474. doi: 10.1093/emboj/19.11.2465

De Bruijn, M. F. T. R., Ma, X., Robin, C., Ottersbach, K., Sanchez, M. J., and Dzierzak, E. (2002). Hematopoietic stem cells localize to the endothelial cell layer in the midgestation mouse aorta. *Immunity* 16, 673–683. doi: 10.1016/S1074-7613(02)00313-8

Fathman, J. W., Fernhoff, N. B., Seita, J., Chao, C., Scarfone, V. M., Weissman, I. L., et al. (2014). Upregulation of CD11A on hematopoietic stem cells denotes the loss of long-term reconstitution potential. *Stem Cell Rep.* 3, 707–715. doi: 10.1016/j.stemcr.2014.09.007

Gekas, C., Dieterlen-Lièvre, F., Orkin, S. H., and Mikkola, H. K. A. (2005). The placenta is a niche for hematopoietic stem cells. *Dev. Cell* 8, 365–375. doi: 10.1016/j.devcel.2004.12.016

Hadland, B. K., Varnum-Finney, B., Mandal, P. K., Rossi, D. J., Poulos, M. G., Butler, J. M., et al. (2017). A common origin for B-1a and B-2 lymphocytes in clonal pre- hematopoietic stem cells. *Stem Cell Rep.* 8, 1563–1572. doi: 10.1016/j.stemcr.2017.04.007

Hagedorn, E. J., Durand, E. M., Fast, E. M., and Zon, L. I. (2014). Getting more for your marrow: boosting hematopoietic stem cell numbers with PGE2. *Exp. Cell Res.* 329, 220–226. doi: 10.1016/j.yexcr.2014.07.030

Inlay, M. A., Serwold, T., Mosley, A., Fathman, J. W., Dimov, I. K., Seita, J., et al. (2014). Identification of multipotent progenitors that emerge prior to

hematopoietic stem cells in embryonic development. *Stem Cell Rep.* 2, 457–472. doi: 10.1016/j.stemcr.2014.02.001

Ishikawa, F. (2013). Modeling normal and malignant human hematopoiesis in vivo through newborn NSG xenotransplantation. *Int. J. Hematol.* 98, 634–640. doi: 10.1007/s12185-013-1467-9

Karimzadeh, A., Scarfone, V. M., Varady, E., Chao, C., Grathwohl, K., Fathman, J. W., et al. (2018). The CD11a and endothelial protein C receptor marker combination simplifies and improves the purification of mouse hematopoietic stem cells. *Stem Cells Transl. Med.* 7. doi: 10.1002/sctm.17-0189

Karlsson, G., Rörby, E., Pina, C., Soneji, S., Reckzeh, K., Miharada, K., et al. (2013). The tetraspanin CD9 affords high-purity capture of all murine hematopoietic stem cells. *Cell Rep.* 4, 642–648. doi: 10.1016/j.celrep.2013.07.020

Khan, J. A., Mendelson, A., Kunisaki, Y., Birbrair, A., Kou, Y., Arnal-Estapé, A., et al. (2016). Fetal liver hematopoietic stem cell niches associate with portal vessels. *Science* 351, 176–180. doi: 10.1126/science.aad0084

Kiel, M. J., Yilmaz, ÖH., Iwashita, T., Yilmaz, O. H., Terhorst, C., and Morrison, S. J. (2005). SLAM family receptors distinguish hematopoietic stem and progenitor cells and reveal endothelial niches for stem cells. *Cell* 121, 1109–1121. doi: 10.1016/j.cell.2005.05.026

Kim, K. H., and Sederstrom, J. M. (2015). Assaying cell cycle status using flow cytometry. *Curr. Protoc. Mol. Biol.* 111, 28.6.1–28.6.11. doi: 10.1002/0471142727.mb2806s111

Kinashi, T. (2005). Intracellular signalling controlling integrin activation in lymphocytes. *Nat. Rev. Immunol.* 5, 546–559. doi: 10.1038/nri1646

Kumaravelu, P., Hook, L., Morrison, A. M., Ure, J., Zhao, S., Zuyev, S., et al. (2002). Quantitative developmental anatomy of definite haematopoietic stem cells/long-term repopulating units (HSC/RUs): role of the aorta-gonad-mesonephros (AGM) region and the yolk sac in colonisation of the mouse embryonic liver. *Development* 129, 4891–4899. doi: 10.1242/dev.129.21.4891

Lancrin, C., Sroczynska, P., Stephenson, C., Allen, T., Kouskoff, V., and Lacaud, G. (2009). The haemangioblast generates haematopoietic cells through a haemogenic endothelium stage. *Nature* 457, 892–895. doi: 10.1038/nature07679

Lee, J., Dykstra, B., Spencer, J. A., Kenney, L. L., Greiner, D. L., Shultz, L. D., et al. (2017). MRNA-mediated glycoengineering ameliorates deficient homing of human stem cell-derived hematopoietic progenitors. *J. Clin. Invest.* 127, 2433–2437. doi: 10.1172/JCI92030

Li, Y., Gao, L., Hadland, B., Tan, K., and Speck, N. A. (2017). CD27 marks murine embryonic hematopoietic stem cells and type II prehematopoietic stem cells. *Blood* 130, 372–376. doi: 10.1182/blood-2017-03-776849

Martin, M. A., and Bhatia, M. (2005). Analysis of the human fetal liver hematopoietic microenvironment. *Stem Cells Dev.* 14, 493–504. doi: 10.1089/scd.2005.14.493

Moore, K. A., Ema, H., and Lemischka, I. R. (1997). In vitro maintenance of highly purified, transplantable hematopoietic stem cells. *Blood* 89, 4337–4347. doi: 10.1182/blood.v89.12.4337

Moore, M. A., and Metcalf, D. (1970). Ontogeny of the haemopoietic system: yolk sac origin of in vivo and in vitro colony forming cells in the developing mouse embryo. *Br. J. Haematol.* 18, 279–296. doi: 10.1111/j.1365-2141.1970.tb01443.x

Muller, A. M., Medvinsky, A., Strouboulis, J., Grosveld, F., and Dzierzak, E. (1994). Development of hematopoietic stem cell activity in the mouse embryo. *Immunity* 1, 291–301. doi: 10.1016/1074-7613(94)90081-7

Palis, J. (2016). Hematopoietic stem cell-independent hematopoiesis: emergence of erythroid, megakaryocyte, and myeloid potential in the mammalian embryo. *FEBS Lett.* 590, 3965–3974. doi: 10.1002/1873-3468.12459

Palis, J., Robertson, S., Kennedy, M., Wall, C., and Keller, G. (1999). Development of erythroid and myeloid progenitors in the yolk sac and embryo proper of the mouse. *Development* 126, 5073–5084. doi: 10.1242/dev.126.22.5073

Riddell, J., Gazit, R., Garrison, B. S., Guo, G., Saadatpour, A., Mandal, P. K., et al. (2014). Reprogramming committed murine blood cells to induced hematopoietic stem cells with defined factors. *Cell* 157, 549–564. doi: 10.1016/j.cell.2014.04.006

Rybtsov, S., Batsivari, A., Bilotkach, K., Paruzina, D., Senserrich, J., Nerushev, O., et al. (2014). Tracing the origin of the HSC hierarchy reveals an SCF-dependent, IL-3-independent CD43- embryonic precursor. *Stem Cell Rep.* 3, 489–501. doi: 10.1016/j.stemcr.2014.07.009

Rybtsov, S., Ivanovs, A., Zhao, S., and Medvinsky, A. (2016). Concealed expansion of immature precursors underpins acute burst of adult HSC activity in foetal liver. *Development* 143, 1284–1289. doi: 10.1242/dev.131193

Rybtsov, S., Sobiesiak, M., Taoudi, S., Souilhol, C., Senserrich, J., Liakhovitskaia, A., et al. (2011). Hierarchical organization and early hematopoietic specification of the developing HSC lineage in the AGM region. *J. Exp. Med.* 208, 1305–1315. doi: 10.1084/jem.20102419

Shamri, R., Grabovsky, V., Gauguet, J. M., Feigelson, S., Manevich, E., Kolanus, W., et al. (2005). Lymphocyte arrest requires instantaneous induction of an extended LFA-1 conformation mediated by endothelium-bound chemokines. *Nat. Immunol.* 6, 497–506. doi: 10.1038/ni1194

Sugimura, R., Jha, D. K., Han, A., Soria-Valles, C., da Rocha, E. L., Lu, Y.-F., et al. (2017). Haematopoietic stem and progenitor cells from human pluripotent stem cells. *Nature* 545, 432–438. doi: 10.1038/nature22370

Taoudi, S., Gonneau, C., Moore, K., Sheridan, J. M., Blackburn, C. C., Taylor, E., et al. (2008). Extensive hematopoietic stem cell generation in the AGM region via maturation of VE-Cadherin +CD45 + pre-definitive HSCs. *Cell Stem Cell* 3, 99–108. doi: 10.1016/j.stem.2008.06.004

Verbiest, T., Finnon, R., Brown, N., Finnon, P., Bouffler, S., and Badie, C. (2016). NOD scid gamma mice are permissive to allogeneic HSC transplantation without prior conditioning. *Int. J. Mol. Sci.* 17, 1850. doi: 10.3390/ijms17111850

Weissman, I. L., Papaioannou, V., and Gardner, R. (1978). "Fetal hematopoietic origin of the adult hematolymphoid system," in *Differentiation of Normal and Neoplastic Hematopoietic Cells*, eds B. Clarkson, P. A. Marks, and J. E. Till (Cold Spring Harbor, NY: Cold Spring Harbor Laboratory Press), 33–47.

Wiesmann, A., Phillips, R. L., Mojica, M., Pierce, L. J., Searles, A. E., Spangrude, G. J., et al. (2000). Expression of CD27 on murine hematopoietic stem and progenitor cells. *Immunity* 12, 193–199. doi: 10.1016/S1074-7613(00)80172-7

Wright, D. E., Bowman, E. P., Wagers, A. J., Butcher, E. C., and Weissman, I. L. (2002). Hematopoietic stem cells are uniquely selective in their migratory response to chemokines. *J. Exp. Med.* 195, 1145–1154. doi: 10.1084/jem.20011284

Yoder, M. C., and Hiatt, K. (1997). Engraftment of embryonic hematopoietic cells in conditioned newborn recipients. *Blood* 89, 2176–2183. doi: 10.1182/blood.v89.6.2176

Yoder, M. C., Hiatt, K., Dutt, P., Mukherjee, P., Bodine, D. M., and Orlic, D. (1997a). Characterization of definitive lymphohematopoietic stem cells in the day 9 murine yolk sac. *Immunity* 7, 335–344. doi: 10.1016/S1074-7613(00)80355-6

Yoder, M. C., Hiatt, K., and Mukherjee, P. (1997b). In vivo repopulating hematopoietic stem cells are present in the murine yolk sac at day 9.0 postcoitus. *Proc. Natl. Acad. Sci. U.S.A.* 94, 6776–6780. doi: 10.1073/pnas.94.13.6776

Zhang, Y., and Wang, H. (2012). Integrin signalling and function in immune cells. *Immunology* 135, 268–275. doi: 10.1111/j.1365-2567.2011.03549.x

Zhou, F., Li, X., Wang, W., Zhu, P., Zhou, J., He, W., et al. (2016). Tracing haematopoietic stem cell formation at single-cell resolution. *Nature* 533, 487–492. doi: 10.1038/nature17997

Zovein, A. C., Hofmann, J. J., Lynch, M., French, W. J., Turlo, K. A., Yang, Y., et al. (2008). Fate tracing reveals the endothelial origin of hematopoietic stem cells. *Cell Stem Cell* 3, 625–636. doi: 10.1016/j.stem.2008.09.018

Conflict of Interest: The authors declare that the research was conducted in the absence of any commercial or financial relationships that could be construed as a potential conflict of interest.

Publisher's Note: All claims expressed in this article are solely those of the authors and do not necessarily represent those of their affiliated organizations, or those of the publisher, the editors and the reviewers. Any product that may be evaluated in this article, or claim that may be made by its manufacturer, is not guaranteed or endorsed by the publisher.

frontiers in Cell and Developmental Biology

ORIGINAL RESEARCH
published: 13 September 2021
doi: 10.3389/fcell.2021.728057

Hlf Expression Marks Early Emergence of Hematopoietic Stem Cell Precursors With Adult Repopulating Potential and Fate

Wanbo Tang[1], Jian He[1], Tao Huang[1], Zhijie Bai[1], Chaojie Wang[2], Haizhen Wang[2], Ruichuang Yang[3], Yanli Ni[4], Jun Hou[3], Junliang Wang[5], Jie Zhou[4], Yingpeng Yao[2], Yandong Gong[4], Siyuan Hou[2], Bing Liu[1,2,4] and Yu Lan[2]**

[1] State Key Laboratory of Proteomics, Academy of Military Medical Sciences, Academy of Military Sciences, Beijing, China, [2] Key Laboratory for Regenerative Medicine of Ministry of Education, School of Medicine, Institute of Hematology, Jinan University, Guangzhou, China, [3] National Clinical Research Center for Infectious Diseases, Fifth Medical Center of Chinese PLA General Hospital, Beijing, China, [4] State Key Laboratory of Experimental Hematology, Fifth Medical Center of Chinese PLA General Hospital, Beijing, China, [5] Department of Radiotherapy, Fifth Medical Center of Chinese PLA General Hospital, Beijing, China

OPEN ACCESS

Edited by:
Yiyue Zhang,
South China University of Technology, China

Reviewed by:
Zilong Wen,
Hong Kong University of Science and Technology, SAR China
Yan Li,
Zhejiang University, China
Mihaela Crisan,
University of Edinburgh, United Kingdom

***Correspondence:**
Bing Liu
bingliu17@126.com
Yu Lan
rainyblue_1999@126.com

Specialty section:
This article was submitted to Stem Cell Research, a section of the journal Frontiers in Cell and Developmental Biology

Received: *20 June 2021*
Accepted: *17 August 2021*
Published: *13 September 2021*

Citation:
Tang W, He J, Huang T, Bai Z, Wang C, Wang H, Yang R, Ni Y, Hou J, Wang J, Zhou J, Yao Y, Gong Y, Hou S, Liu B and Lan Y (2021) Hlf Expression Marks Early Emergence of Hematopoietic Stem Cell Precursors With Adult Repopulating Potential and Fate. Front. Cell Dev. Biol. 9:728057. doi: 10.3389/fcell.2021.728057

In the aorta-gonad-mesonephros (AGM) region of mouse embryos, pre-hematopoietic stem cells (pre-HSCs) are generated from rare and specialized hemogenic endothelial cells (HECs) *via* endothelial-to-hematopoietic transition, followed by maturation into bona fide hematopoietic stem cells (HSCs). As HECs also generate a lot of hematopoietic progenitors not fated to HSCs, powerful tools that are pre-HSC/HSC-specific become urgently critical. Here, using the gene knockin strategy, we firstly developed an *Hlf-tdTomato* reporter mouse model and detected Hlf-tdTomato expression exclusively in the hematopoietic cells including part of the immunophenotypic $CD45^{-}$ and $CD45^{+}$ pre-HSCs in the embryonic day (E) 10.5 AGM region. By *in vitro* co-culture together with long-term transplantation assay stringent for HSC precursor identification, we further revealed that unlike the $CD45^{-}$ counterpart in which both Hlf-tdTomato-positive and negative sub-populations harbored HSC competence, the $CD45^{+}$ E10.5 pre-HSCs existed exclusively in Hlf-tdTomato-positive cells. The result indicates that the cells should gain the expression of Hlf prior to or together with CD45 to give rise to functional HSCs. Furthermore, we constructed a novel *Hlf-CreER* mouse model and performed time-restricted genetic lineage tracing by a single dose induction at E9.5. We observed the labeling in E11.5 AGM precursors and their contribution to the immunophenotypic HSCs in fetal liver (FL). Importantly, these Hlf-labeled early cells contributed to and retained the size of the HSC pool in the bone marrow (BM), which continuously differentiated to maintain a balanced and long-term multi-lineage hematopoiesis in the adult. Therefore, we provided another valuable mouse model to specifically trace the fate of emerging HSCs during development.

Keywords: pre-hematopoietic stem cells, hematopoietic stem cells, Hlf, aorta-gonad-mesonephros, genetic lineage tracing, hematopoietic development

INTRODUCTION

Hematopoietic stem cells (HSCs) are a unique cell population which can differentiate into nearly all kinds of blood lineage and maintain its quantity by self-renewal throughout the lifetime (Dzierzak and Bigas, 2018). At embryonic day (E) 10.5, the first functional HSCs are detected in the aorta-gonad-mesonephros (AGM) region (Muller et al., 1994; Medvinsky and Dzierzak, 1996; de Bruijn et al., 2000, 2002; North et al., 2002). At around E11.5, AGM HSCs start to migrate and colonize the fetal liver (FL) where they rapidly expand (Sánchez et al., 1996). During the perinatal period, HSCs begin to migrate to the bone marrow (BM) where they permanently reside throughout adult life (Morrison et al., 1995; Christensen et al., 2004).

It is generally accepted that HSCs are derived from specialized endothelial cells termed hemogenic endothelial cells (HECs) through endothelial-to-hematopoietic transition in mid-gestational embryos (Zovein et al., 2008; Chen et al., 2009; Dzierzak and Bigas, 2018; Neo et al., 2021). During this process, HECs bud from the dorsal aorta and then aggregate to form intra-aortic hematopoietic clusters (IAHCs) (Boisset et al., 2010). The earliest IAHCs appear at E9.5, and their number peaks to about 600 at E10.5 (Yokomizo and Dzierzak, 2010). IAHCs comprise progenitors that simultaneously express endothelial surface markers, such as CD31 and VE-Cadherin and hematopoietic marker Runx1 (Taoudi et al., 2008; Yamamoto et al., 2013; Solaimani Kartalaei et al., 2015). Pre-hematopoietic stem cells (pre-HSCs) are an intermediate population between HECs and HSCs (Hou et al., 2020), which do not have the capacity to repopulate irradiated recipients directly but can obtain this capacity after being co-cultured with stromal cells. Pre-HSCs are considered to be localized mainly within the IAHCs and reach approximately 50 at around E11 (Taoudi et al., 2008; Rybtsov et al., 2011, 2016; Boisset et al., 2015; Baron et al., 2018). These cells experience two stages including type I pre-HSCs ($CD45^-$, known as T1 pre-HSCs) and type II pre-HSCs ($CD45^+$, known as T2 pre-HSCs), which can both be detected in the E11.0 AGM region (Taoudi et al., 2008; Rybtsov et al., 2011; Zhou et al., 2016).

To isolate and decipher the embryonic hematopoietic populations, several researches have made great efforts in developing novel enrichment strategies or mouse models over the past few decades. With the help of the genetic lineage tracing mouse model *VE-Cadherin-Cre*, HSCs are proven to be derived from endothelial cells (Zovein et al., 2008; Chen et al., 2009). The progenies of endothelial cells contribute to a fraction of hematopoietic cells in adult BM, thymus, and spleen when labeled at E9.5 (Zovein et al., 2008; Chen et al., 2009). Additionally, time-lapse confocal imaging of *Ly6A-GFP* embryo slices confirms that aortic endothelial cells expressing GFP can generate Ly6A-$GFP^+Kit^+CD41^+$ hematopoietic stem progenitor cells (HSPCs) at E10.5 (Boisset et al., 2010). The iterations of index-sorting analyses on *Gata2IRESVenus* reporter mice suggest that the functional HSCs emerge in the E11 IAHCs with a quantity of one to two cells (Vink et al., 2020). Recently, HECs are proven to be highly enriched by a cocktail of surface markers named PK44 ($CD41^-CD43^-CD45^-CD31^+CD201^+Kit^+CD44^+$) or the newly established reporter *Neurl3-EGFP* (Hou et al., 2020). Previous studies verified T1 and T2 pre-HSCs exhibit phenotypes as VE-$Cadherin^+CD45^-CD41^{lo}$ and VE-$Cadherin^+CD45^+$ in the E11.5 AGM region, respectively (Taoudi et al., 2008; Rybtsov et al., 2011). Notably, functional T1 and T2 pre-HSCs are identified to be highly enriched by CD201 and, thus, are further precisely characterized as $CD31^+CD45^-CD41^{lo}Kit^+CD201^{hi}$ and $CD31^+CD45^+Kit^+CD201^{hi}$ at E11.0, respectively (Zhou et al., 2016).

Hlf is a transcription factor that belongs to the proline and acidic amino acid-rich (PAR) basic leucine zipper (bZip) family. Hlf is initially recognized in leukemia, and recent studies have identified its high expression in BM HSCs and essential role in maintaining hematopoiesis in a quiescent state (Gazit et al., 2013; Komorowska et al., 2017; Wahlestedt et al., 2017). In embryos, Hlf is specially expressed in IAHCs and FL HSCs without marking yolk sac erythro-myeloid progenitors, and its expression level is up-regulated along the maturation of HSCs during development (Yokomizo et al., 2019).

Recently, we identified *Hlf* as a signature gene for pre-HSCs in addition to HSCs (Zhou et al., 2016), suggesting that Hlf is a suitable molecule for studying the emergence of early pre-HSCs and their contribution to adult hematopoiesis. Therefore, we newly constructed *Hlf-tdTomato* and *Hlf-CreER* mouse models to investigate the dynamic marker changes of pre-HSCs and the adult fate of pre-HSCs labeled by *Hlf-CreER*.

MATERIALS AND METHODS

Mice

Mice were fed at the Laboratory Animal Center of Academy of Military Medical Sciences in accordance with institutional guidelines. Mouse operations were approved by the Animal Care and Use Committee of the institute. The $Hlf^{tdTomato/+}$ reporter mouse line and the $Hlf^{CreER/+}$ lineage tracing mouse line were generated with the CRISPR/Cas9-mediated gene knockin technique by Beijing Biocytogen and Shanghai Model Organisms Center, respectively. The $ROSA^{ZsGreen/ZsGreen}$ reporter mice were described previously (Madisen et al., 2010). CD45.1/1 mice were purchased from Jackson Laboratory. CD45.2/2 mice were purchased from SPF (Beijing) Biotechnology Co., Ltd. All mice were maintained on C57BL/6 background. Embryos were staged by the number of somite pair (sp): E10.5, 36–40 sp; E11.0, 41–45 sp; and E11.5, 46–50 sp. The AGM region was dissected as previously described (Li et al., 2012).

Flow Cytometry

Cells were analyzed and sorted by flow cytometers FACSymphony and FACS Aria 2 (BD Biosciences), respectively. Data were analyzed by FlowJo software (Tree Star). The antibodies with their supplier, clone number, dilution ratio, and catalog number are listed as follows: BD Biosciences: Rat anti-mouse Ly6A/E-BV605 (D7, 1:100, Cat#563288), Rat anti-mouse CD45-BV421 (30-F11, 1:40, Cat#563890), Rat monoclonal anti-mouse CD41-APC (MWReg30, 1:40, Cat#740903), Rat anti-mouse CD43-PE-Cy7 (S7, 1:50, Cat#562866), Rat anti-mouse CD31-BV786 (MEC13.3, 1:200, Cat#740870), and Rat

anti-mouse TER-119-BV421 (TER-119, 1:40, Cat#566248); Biolegend: Rat monoclonal anti-mouse CD117 (c-kit)-BV650 (ACK2, 1:100, Cat#135125), Rat monoclonal anti-mouse CD150-BV785 (TC15-12F12.2, 1:100, Cat#115937), Rat monoclonal anti-mouse CD48-BV711 (HM48-1, 1:50, Cat#103439), Rat monoclonal anti-mouse CD16/32-BV510 (93, 1:50, Cat#101333), Rat monoclonal anti-mouse/human CD44-BV510 (IM7, 1:20, Cat#103044), Rat monoclonal anti-mouse CD144-BV421 (BV13, 1:50, Cat#138013), Rat monoclonal anti-mouse Ly6G-PE-Cy7 (1A8, 1:100, Cat#127618), and Mouse monoclonal anti-mouse CD45.2-PerCP5.5 (104, 1:100, Cat#109828); eBioscience: Rat monoclonal anti-mouse CD117 (c-kit)-APC-Cy7 (2B8, 1:200, Cat#47-1171-82), Rat monoclonal anti-mouse CD48-APC-Cy7 (HM48-1, 1:100, Cat#47-0481-82), Rat monoclonal anti-mouse CD34-eFluor 660 (RAM34, 1:20, Cat#50-0314-82), Rat monoclonal anti-mouse CD34-eFluor 450 (RAM34, 1:20, Cat#48-0341-82), Rat monoclonal anti-mouse CD11b-PE-Cy7 (M1/70, 1:200, Cat#25-0112-82), Rat monoclonal anti-mouse CD11b-FITC (M1/70, 1:400, Cat#11-0112-85), Rat monoclonal anti-mouse CD201-PE (eBio1560, 1:200, Cat#12-2012-80), Rat monoclonal anti-mouse CD201-APC (eBio1560, 1:100, Cat#17-2012-82), Rat monoclonal anti-mouse CD45-PE-Cy7 (30-F11, 1:200, Cat#25-0451-82), Rat monoclonal anti-mouse CD41-APC (eBioMWReg30, 1:100, Cat#17-0411-80), Rat monoclonal anti-mouse CD135-APC (A2F10, 1:20, Cat#17-1351-82), Rat monoclonal anti-mouse TER-119-PE-Cy7 (TER-119, 1:200, Cat#25-5921-82), Rat monoclonal anti-mouse Ly6G/Ly-6C-FITC (RB6-8C5, 1:200, Cat#11-5931-86), Rat monoclonal anti-mouse B220-BV421 (RA3-6B2, 1:40, Cat#48-0452-80), Rat monoclonal anti-mouse CD4-APC-Cy7 (GK1.5, 1:200, Cat#47-0041-82), Rat monoclonal anti-mouse CD8-PE-Cy7 (53-6.7, 1:40, Cat#25-0081-82), Rat monoclonal anti-mouse CD42d-APC (1C2, 1:40, Cat#17-0421-80), Rat monoclonal anti-mouse CD3e-APC (145-2C11, 1:200, Cat#17-0031-83), Mouse monoclonal anti-mouse CD45.1-APC (A20, 1:100, Cat#17-0453-82), Rat monoclonal anti-mouse Ly6G/Ly-6C-Biotin (RB6-8C5, 1:100, Cat#13-5931-82), Rat monoclonal anti-mouse TER-119-Biotin (TER-119, 1:100, Cat#13-5921-82), Rat monoclonal anti-mouse B220-Biotin (RA3-6B2, 1:400, Cat#13-0452-82), Rat monoclonal anti-mouse CD4-Biotin (RM4-5, 1:400, Cat#13-0042-82), Rat monoclonal anti-mouse CD8a-Biotin (53-6.7, 1:100, Cat#13-0081-81), Rat monoclonal anti-mouse CD11b-Biotin (M1/70, 1:400, Cat#13-0112-82), Rat monoclonal anti-mouse CD127-Biotin (A7R34, 1:100, Cat#13-1271-81), Streptavidin APC-eFluor 780 (1:50, Cat#47-4317-82), and Streptavidin eFluor 450 (1:50, Cat#48-4317-82).

OP9-DL1 Co-culture and Transplantation Assay

The OP9-DL1 stromal cells were thawed 4 days before co-culture, and 3×10^4 OP9-DL1 stromal cells (passage 3–7) were seeded into a 24-well plate the day before co-culture without irradiation. A total of 15 AGM regions were dissected and digested into single-cell suspension. The cells from AGM regions were stained with antibodies and sorted by flow cytometry with the gating strategies for indicated populations. Then, the sorted cells were seeded into a 24-well plate containing OP9-DL1 feeder cells with 3 ee (embryo equivalents) per well and incubated in α-MEM (Gibco) with 10% fetal bovine serum (Hyclone) and cytokines (100 ng/ml SCF, 100 ng/ml IL-3, and 100 ng/ml Flt3 ligand, PeproTech) for 6 days. On the fourth day, a half amount of cell culture medium mentioned above was added to the wells. Six days later, the co-cultured cells in each well were detached by 0.25% trypsin (Beyotime Biotechnology, C0203) and harvested independently for flow cytometry analysis or transplantation assay. For transplantation, male CD45.1/1 were mated with female $Hlf^{tdTomato/+}$ (CD45.2/2) to obtain CD45.1/2 embryos. Cell suspension harvested after 6 days of co-culture were mixed with 2×10^4 nucleated BM helper cells (CD45.2/2). The mixture was injected *via* the tail vein into 8–12-week-old female recipients (CD45.2/2) which had been exposed to a split dose of 9 Gy γ-irradiation (^{60}Co). The recipients demonstrating ≥5% donor-derived chimerism in peripheral blood were considered as successfully reconstituted. Donor contribution to each blood lineage is calculated as: (percentage of donor cells of a given lineage in $CD45^+$ cells/total percentage of a given lineage in $CD45^+$ cells) × 100%; Donor contribution to LSK ($Lin^-Sca1^+Kit^+$) cells is calculated as: percentage of donor cells in LSK cells × 100% (Benz et al., 2012; Li et al., 2012; Ye et al., 2017).

Immunofluorescence

Embryos were isolated and fixed with 4% paraformaldehyde for 2–4 h at 4°C, embedded in paraffin and sectioned into 5-μm slices using Leica RM2235. Sections were placed in an oven at 60°C for 15 min, deparaffinized with ethanol of gradient concentration, and subsequently placed in a microwave for 20 min at 95°C within citrate buffer (pH 6.0). The sections were cooled to room temperature and then placed in 3% H_2O_2 for 20 min to remove endogenous peroxidase. Sections were blocked in blocking solution (1:1, Cat#ZLI-9056, Zhongshan golden bridge) for 30 min at room temperature, and then incubated with primary antibodies overnight at 4°C. After being washed with PBS three times, sections were incubated with corresponding secondary antibodies (Zhongshan golden bridge) for 30 min at room temperature. After being washed with PBS, sections were stained with DendronFluor TSA (Histova, NEON 4-color IHC Kit for FFPE, NEFP450, 1:100, 20–60 s). After the staining of the first antigen was completed, we thoroughly eluted the primary and secondary antibodies by re-heating the slides in a microwave with citrate buffer (pH 6.0) for 20 min at 95°C, and repeated the above steps from the microwave repair step to the DendronFluor TSA staining step, so that each antigen was labeled by distinct fluorophores finally. After all the antibodies were stained, the slices were stained with DAPI (4',6-diamidino-2-phenylindole). Images were collected by confocal microscope (Nikon Ti-E A1/ZEISS LSM 880). The primary antibodies and their clone number, dilution ratio, catalog number, and company are listed as follows: Rabbit polyclonal anti-RFP (1:1,500, Cat#600-401-379, Rockland); Rabbit monoclonal anti-Estrogen Receptor alpha (SP1, 1:200, Cat#ab16660, Abcam),

Rabbit monoclonal anti-RUNX1/AML1 + RUNX3 + RUNX2 (EPR3099, 1:150, Cat#ab92336, Abcam), and Rabbit monoclonal anti-CD31 (EPR17259, 1:1,000, Cat#ab182981, Abcam). The second antibody was HRP-labeled Goat anti-Rabbit IgG polymer (1:1, Cat#PV6001, Zhongshan golden bridge).

Inducible Genetic Lineage Tracing

Tamoxifen free base (T5648-5G, Sigma) 200 mg was dissolved in 10 ml sunflower-seed oil (S5007; Sigma) and shaken overnight at the room temperature. For lineage tracing, $Hlf^{CreER/+}$ mice were firstly bred with $ROSA^{ZsGreen/ZsGreen}$ mice to generate $Hlf^{CreER/+}$; $ROSA^{ZsGreen/+}$ (referred as *Hlf-CreER;ZsGreen*), then male *Hlf-CreER;ZsGreen* mice were crossed with female C57BL/6 mice. The pregnant C57BL/6 mice were administered with a single dose of tamoxifen by gavage (3 mg per 30 g body weight) at E9.5. At indicated embryonic stages, the pregnant C57BL/6 mice were sacrificed, the embryos were isolated with subsequent genotyping, and the *Hlf-CreER;ZsGreen* embryos were used for further flow cytometry analysis, with the $ROSA^{ZsGreen/+}$ embryos from the same litter serving as controls. For adult mice analysis, *Hlf-CreER;ZsGreen* offspring with a single dose of tamoxifen induction at E9.5 as described above were used for flow cytometry analysis.

Single Cell RNA-Seq Dataset Source

The scRNA-seq data are from our previous study (Zhou et al., 2016) and downloaded from the GEO database (GSE67120).

RESULTS

Establishment of an *Hlf-tdTomato* Reporter Mouse Model

By analyzing the transcriptomic dataset we previously constructed (Zhou et al., 2016), we found that *Hlf* was expressed in almost all of the HSC-competent cells from embryo to adult but not in endothelial cells of the mid-gestational AGM region, with a gradual up-regulation from pre-HSCs to adult HSCs (**Figure 1A**). Therefore, for a better understanding about the stepwise specification of nascent HSCs, we generated an *Hlf-tdTomato* reporter mouse model using the gene knockin strategy to insert a P2A-tdTomato cassette between exon 4 and stop codon of *Hlf* gene locus without disrupting its expression (**Figure 1B**).

We firstly evaluated the expression pattern of Hlf-tdTomato in hematopoietic populations of the E11.0 AGM region, E15.5 FL, and adult BM and peripheral blood by fluorescence activated cell sorting (FACS) analyses. With the use of the highly functionally enriched markers of pre-HSCs (Zhou et al., 2016), we showed that about half of the immunophenotypic T1 pre-HSCs and most if not all of T2 pre-HSCs at E11.0 were positive for Hlf-tdTomato (**Figures 1C,D**). Furthermore, Hlf-tdTomato was expressed in more than 80% of immunophenotypic HSCs and multi-potent progenitors, much higher than in common myeloid progenitors, but was seldom expressed in other committed progenitors and mature blood cells in E15.5 FL (**Figure 1C** and **Supplementary Figure 1A**). In adult BM, Hlf-tdTomato was expressed in almost all the immunophenotypic long-term HSCs and short-term HSCs, irrespective of the marker combinations used, and also in a predominant portion of multi-potent progenitors and in about half of common myeloid progenitors, but hardly in other progenitors and mature blood cells (**Figure 1C** and **Supplementary Figures 1B,C**). Analysis of peripheral blood showed that mature blood lineages, including granulocytes/monocytes, B cells, and T cells, lacked Hlf-tdTomato expression (**Figure 1C** and **Supplementary Figure 1D**). The expression pattern of Hlf-tdTomato in various hematopoietic populations at different developmental stages was not only basically in accordance with our transcriptomic data (**Figure 1A**) but also principally in line with a previous report (Yokomizo et al., 2019) validating the successful construction of the *Hlf-tdTomato* reporter mouse model.

We next investigated the expression of Hlf-tdTomato at E10.5 by immunostaining and flow cytometry. Immunostaining on sections of the E10.5 AGM region showed that Hlf-tdTomato was expressed in the IAHC cells, co-expressing hematopoietic transcription factor Runx1 and endothelial marker CD31, in line with a previous report (Yokomizo et al., 2019). On the other hand, Hlf-tdTomato expression was not detected in the endothelial layer of the dorsal aorta (**Figure 1E**). Consistently, FACS analyses indicated that Hlf-tdTomato expression was not detected in the immunophenotypic non-hematopoietic cells ($CD41^-CD43^-CD45^-$) from multiple intra-embryonic sites, including the AGM region, head, trunk, and limb. In contrast, its expression was confined to the immunophenotypic hematopoietic cells ($CD41^+/CD43^+/CD45^+$) (**Figure 1F** and **Supplementary Figures 2A,B**). We also noticed that only $0.069 \pm 0.013\%$ cells in the E10.5 AGM region expressed Hlf-tdTomato, in which $17.0 \pm 3.4\%$ cells were CD45-negative (**Figures 1G,H**). This expression pattern suggested that Hlf-tdTomato expression may initiate from $CD45^-$ pre-HSCs along HSC specification.

Hlf-tdTomato Expression in Functional $CD45^-$ Pre-HSCs in the E10.5 AGM Region

Previous studies showed that precursors of HSCs in E10.5 AGM are enriched in VE-cad^+CD45^- population and $CD201^{hi}$ population (Rybtsov et al., 2011; Hadland et al., 2017). We examined the E10.5 AGM region by FACS and found that Hlf-tdTomato expression was observed in $68.9 \pm 3.6\%$ of the $CD31^+CD45^-Kit^+CD201^{hi}$ population that has been proven to enrich functional T1 pre-HSCs (**Figure 2A**). Subsequently, we sorted Hlf-tdTomato$^+$ and Hlf-tdTomato$^-$ cells within the $CD31^+CD45^-Kit^+CD201^{hi}$ population from the E10.5 AGM region, respectively, and co-cultured them with OP9-DL1 *in vitro*. After 6 days of co-culture, both Hlf-tdTomato$^+$ and Hlf-tdTomato$^-$ groups generated typical hematopoietic clusters (**Figure 2B**). Progenies of both groups contained HSC-like cells with a $Lin^-CD45^+Sca\text{-}1^+CD201^+$ immunophenotype by FACS analysis (Hadland et al., 2017; **Figure 2C**). Moreover, most of

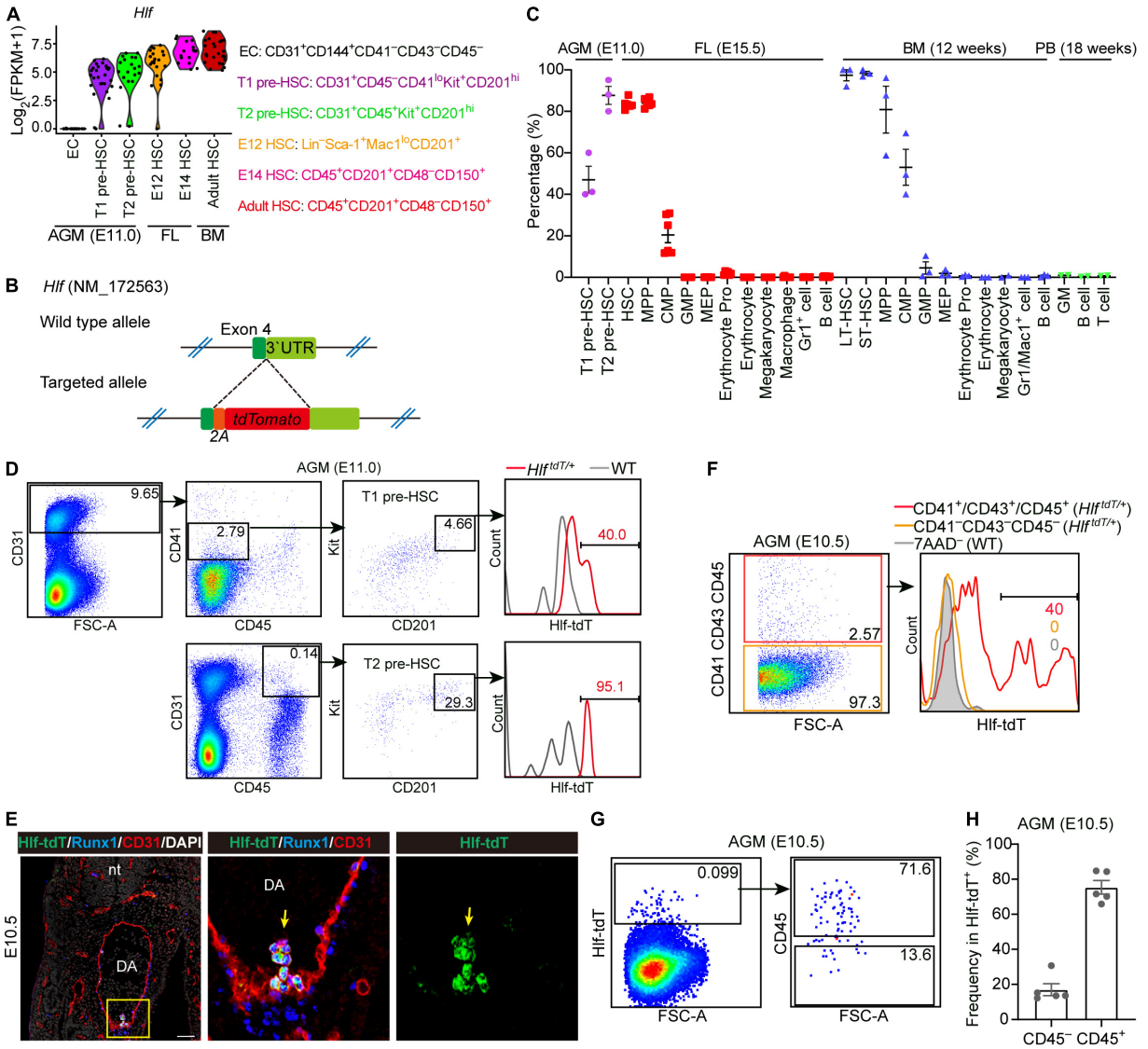

FIGURE 1 | Establishment of an *Hlf-tdTomato* reporter mouse model. **(A)** Violin plots showing the transcription level of *Hlf* in six populations as indicated. Data are from GSE67120. **(B)** Schematic model of the gene-targeting strategy for constructing *Hlf-tdTomato* reporter mouse line *via* CRISPR/Cas9 system. **(C)** Graph showing the percentage of Hlf-tdTomato expression in each hematopoietic population of the E11.0 AGM region, E15.5 fetal liver (FL), adult bone marrow (BM), and peripheral blood (PB). Data are shown as means ± SEM from at least two independent experiments. MPP, multipotent progenitor; CMP, common myeloid progenitor; GMP, granulocyte-monocyte progenitor; MEP, megakaryocyte-erythroid progenitor; erythrocyte pro, erythrocyte progenitor; LT-HSC, long-term hematopoietic stem cell; ST-HSC, short-term hematopoietic stem cell. **(D)** Representative FACS plots showing the Hlf-tdTomato expression in T1 and T2 pre-HSCs in the AGM region of E11.0 *Hlf-tdTomato* embryos. Data are representative of three independent experiments. $Hlf^{tdT/+}$, $Hlf^{tdTomato/+}$; WT, wild type. **(E)** Representative immunostaining on sections from the AGM region of E10.5 *Hlf-tdTomato* embryos. Arrows indicate Hlf-tdTomato$^+$ IAHCs. The two images to the right present the high magnification view of yellow box. nt, neural tube; DA, dorsal aorta. Scale bar, 50 μm. **(F)** Representative FACS plots showing the proportion of Hlf-tdTomato positive cells in CD41$^-$CD43$^-$CD45$^-$ and CD41$^+$/CD43$^+$/CD45$^+$ populations in the AGM region of E10.5 *Hlf-tdTomato* embryos. Data are representative of two independent experiments. Genotypes are indicated in the brackets. $Hlf^{tdT/+}$, $Hlf^{tdTomato/+}$; WT, wild type. **(G)** Representative FACS plots showing the CD45 expression in Hlf-tdTomato$^+$ cells in the AGM region of E10.5 *Hlf-tdTomato* embryos. **(H)** Graph showing the frequencies of CD45$^-$ or CD45$^+$ cells in Hlf-tdTomato$^+$ cells of the E10.5 AGM region. Data are shown as means ± SEM from five independent experiments.

these HSC-like cells expressed Hlf-tdTomato as well as Kit, further suggesting their HSC-like identity (**Figure 2D**).

For *in vivo* functional validation, Hlf-tdTomato$^+$ and Hlf-tdTomato$^-$ cells within CD31$^+$Kit$^+$CD45$^-$ population from the E10.5 AGM region were, respectively, co-cultured with OP9-DL1 for 6 days, then the culture products were transplanted into lethally irradiated adult mice. At 16 weeks post-transplantation, multi-lineage repopulation was observed in peripheral blood and multiple organs (BM, spleen, and thymus) of the recipients of both Hlf-tdTomato$^+$ (2/4) and Hlf-tdTomato$^-$ (2/5) groups. Moreover, the contribution of the donor cells to the immunophenotypic HSCs and hematopoietic

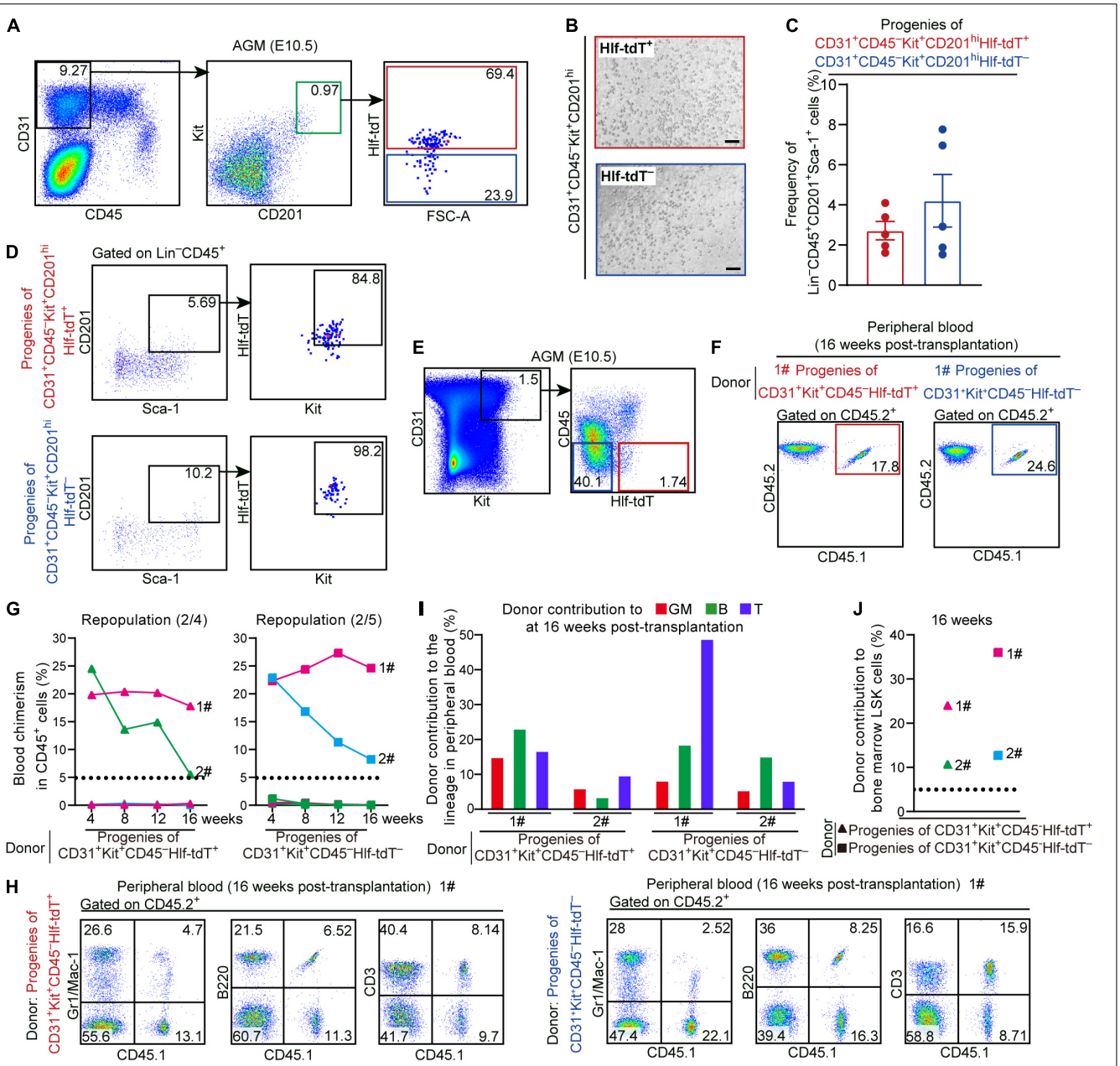

FIGURE 2 | Hlf-tdTomato expression in functional CD45$^-$ pre-HSCs in the E10.5 AGM region. **(A)** Representative FACS plots showing the proportions of Hlf-tdTomato$^+$ and Hlf-tdTomato$^-$ cells in CD31$^+$CD45$^-$Kit$^+$CD201^{hi} population in the AGM region of E10.5 *Hlf-tdTomato* embryos. Data are representative of five independent experiments. **(B)** Representative morphology of hematopoietic cells generated from Hlf-tdTomato$^+$ cells (red) and Hlf-tdTomato$^-$ cells (blue) within CD31$^+$CD45$^-$Kit$^+$CD201^{hi} population. Scale bar, 100 μm. **(C)** Graph showing the frequency of Lin$^-$CD45$^+$CD201$^+$Sca-1$^+$ cells generated from the indicated populations from the E10.5 AGM region after co-culture analyzed by FACS. Data are shown as means ± SEM from five independent experiments. **(D)** Representative FACS plots showing the expression of Hlf-tdTomato and Kit in Lin$^-$CD45$^+$CD201$^+$Sca-1$^+$ cells that are generated from the indicated populations of the E10.5 AGM region after co-culture. Data are representative of five independent experiments. **(E)** Sorting strategy for the populations from the AGM region of E10.5 *Hlf-tdTomato* embryos for co-culture/transplantation assay. The cell populations sorted for functional assay are denoted as colored boxes. **(F)** Representative FACS plots of blood chimerism of donor-derived (CD45.1$^+$CD45.2$^+$) cells in CD45$^+$ cells at 16 weeks post-transplantation. **(G)** Graphs showing the blood chimerism in CD45$^+$ cells of each of all the recipients from 4 to 16 weeks post-transplantation. The recipients were transplanted with the culture products of CD31$^+$Kit$^+$CD45$^-$Hlf-tdTomato$^+$ (triangle, left) or CD31$^+$Kit$^+$CD45$^-$Hlf-tdTomato$^-$ (square, right) cells from the AGM region of E10.5 *Hlf-tdTomato* embryos. Numbers of repopulated/total recipients are shown in the brackets. For each transplantation assay, cells from a total of 15 Hlf-tdTomato positive embryos belonging to three independent litters (biological repeats) were sampled and cultured as donor cells, and five recipients were used. Each line represents a recipient and each color represents an independent litter (biological repeat). **(H)** Representative FACS plots showing proportions of donor cells and each hematopoietic lineage at 16 weeks post-transplantation. Myeloid cells (Gr1/Mac-1$^+$), B cells (B220$^+$), and T cells (CD3$^+$) in peripheral blood are shown. **(I)** Bar plot representing the percentages of donor contribution to granulocytes/monocytes (GM, red), B cells (green), and T cells (blue) in the peripheral blood at 16 weeks post-transplantation. **(J)** Graph showing donor contribution to the bone marrow hematopoietic stem progenitor cells (Lin$^-$Sca-1$^+$Kit$^+$, LSK) of the successfully repopulated recipients at 16 weeks post-transplantation.

progenitors in BM was also observed, validating the bona fide HSC competence (**Figures 2E–J** and **Supplementary Figures 3A,B**). These data indicated that precursors of HSCs were distributed in both Hlf-tdTomato$^+$ and Hlf-tdTomato$^-$ subpopulations of CD45$^-$ cells in the E10.5 AGM region. Considering the restricted expression of Hlf-tdTomato in the hematopoietic cells (**Figure 1F**), the CD45$^-$Hlf-tdTomato$^+$ population with the HSC-competence should belong to T1 pre-HSCs. On the other hand, as HSC-competent HECs in the AGM region represented by PK44 did not express Hlf-tdTomato (**Supplementary Figure 2B**), the repopulating capacity of the progenies of CD31$^+$Kit$^+$CD45$^-$Hlf-tdTomato$^-$ population should be partially due to the existence of HSC-primed HECs therein, although the existence of Hlf-tdTomato$^-$ pre-HSCs could not be completely excluded.

Hlf-tdTomato Enriches Functional CD45$^+$ Pre-HSCs in the E10.5 AGM Region

We noticed that the proportion of Hlf-tdTomato-expressing cells in the immunophenotypic T2 pre-HSCs (CD31$^+$CD45$^+$Kit$^+$CD201^{hi}) in the E10.5 AGM region was lower than that in the E11.0 AGM region (**Figures 1D**, **3A**). Furthermore, the mean fluorescence intensity (MFI) of tdTomato in Hlf-tdTomato$^+$ cells was higher in the CD45$^+$ sub-population than in the CD45$^-$ counterpart within CD31$^+$Kit$^+$CD201^{hi} cells (**Figure 3B**). As a previous report revealed that the expression intensity of Hlf gradually increases along with the maturation of embryonic HSCs (Yokomizo et al., 2019), we wondered whether *Hlf* expression marks the HSC-competence in the CD45$^+$ cells as early as E10.5. Therefore, we sorted Hlf-tdTomato$^+$ and Hlf-tdTomato$^-$ within the CD31$^+$CD45$^+$Kit$^+$CD201^{hi} population from the E10.5 AGM region (**Figure 3A**), and co-cultured them with OP9-DL1 *in vitro*, respectively. Six days later, both Hlf-tdTomato$^+$ and Hlf-tdTomato$^-$ groups generated hematopoietic clusters (**Figure 3C**), but the former yielded much more HSC-like cells (Lin$^-$CD45$^+$Sca-1$^+$CD201$^+$) than the latter by FACS analyses (**Figures 3D,E**).

Next, Hlf-tdTomato$^+$ and Hlf-tdTomato$^-$ cells within the CD31$^+$Kit$^+$CD45$^+$ population from the E10.5 AGM region were, respectively, isolated and co-cultured with OP9-DL1 for 6 days, then transplantation assay was performed with the culture products. Of note, multi-lineage repopulation in peripheral blood and multiple organs (BM, spleen, and thymus) at 16 weeks post-transplantation was only detected in the recipients of Hlf-tdTomato$^+$ group, consistent with the detection of the chimerism in the immunophenotypic HSCs and hematopoietic progenitors in BM (**Figures 3F–K** and **Supplementary Figures 3C,D**). Therefore, Hlf-tdTomato expression further enriched the HSC-competence in E10.5 CD45$^+$ population. The finding also indicated that if a cell expresses CD45 prior to Hlf at this early stage, it has lost the possibility of specification toward HSCs.

Generation of an Inducible *Hlf-CreER* Mouse Model

To determine the physiological contribution of the Hlf-expressing early cells, including pre-HSCs and nascent HSCs, to FL and adult hematopoiesis, we newly generated an *Hlf-CreER* mouse model by CRISPR/Cas9-mediated gene knockin strategy, with an inducible *CreERT2* cassette inserted between exon 4 and 3′UTR of the *Hlf* gene locus (**Figure 4A**). Immunostaining of ER in the AGM region showed the expression of the inducible Cre recombinase specifically in the IAHC cells from E9.5 to E10.5 (**Figure 4B**), consistent with the expression pattern of Hlf-tdTomato (**Figure 1E**).

Next, *Hlf-CreER;ROSA-LSL-ZsGreen* (referred to as *Hlf-CreER;ZsGreen*) mice were generated for lineage tracing. We performed the single-dose tamoxifen induction at E9.5, 24 h before the first HSCs appear at E10.5 (**Figure 4C**), and the labeling would involve the pre-HSCs and emerging HSCs marked by Hlf expression mainly within the next 48 h from injection (Zovein et al., 2008). We first assessed the labeling proportions of several populations related to HSC ontogeny by FACS analyses, including endothelial cells, IAHC cells, as well as T1 and T2 pre-HSCs in the E11.5 AGM region. Endothelial cells were not labeled as expected (**Figure 4D** and **Supplementary Figure 4A**). In contrast, the labeling was found in 3.9 ± 0.7% of the immunophenotypic IAHC cells (CD31$^+$Kit^{hi}) (**Figure 4D** and **Supplementary Figure 4A**). Compared with that in T1 pre-HSCs (CD31$^+$CD45$^-$CD41^{lo}Kit$^+$CD201^{hi}, 1.2 ± 0.8%), the average constitution of labeled cells in T2 pre-HSCs (CD31$^+$CD45$^+$Kit$^+$CD201^{hi}) was higher (5.1 ± 2.5%) (**Figure 4D** and **Supplementary Figure 4A**), in line with the higher expression of Hlf-tdTomato in T2 pre-HSCs than in T1 pre-HSCs (**Figure 1D**). Interestingly, the labeling of pre-HSCs in individual AGM regions was concentrated in either T1 or T2 pre-HSCs (**Supplementary Figure 4B**), suggesting the transient dynamics of pre-HSC maturation.

We then evaluated the contribution of these Hlf-labeled early cells to the immunophenotypic HSCs in FL. Of note, the average constitution of lineage-labeled cells in FL HSCs (Lin$^-$Sca-1$^+$Mac-1^{lo}CD201$^+$) (Zhou et al., 2016) was 13.6 ± 1.8% at E13.5 and 9.4 ± 1.6% at E15.5, higher than that in pre-HSCs in the E11.5 AGM region (**Figures 4D,E**). When using another surface marker combination ESLAM (CD45$^+$CD201$^+$CD150$^+$CD48$^-$) (Benz et al., 2012) to check E15.5 FL HSCs, we came to a similar conclusion (**Supplementary Figure 4C**). These results indicated that *Hlf-CreER;ZsGreen* was able to trace part of AGM pre-HSCs and/or nascent HSCs without labeling endothelial cells when induced at E9.5, and the progenies of the labeled cells could migrate and colonize FL, possibly with an expansion to some extent.

Hlf-Labeled Early Cells Contribute to Long-Term and Multi-Lineage Adult Hematopoiesis

To evaluate the contribution of Hlf-labeled early cells to adult hematopoiesis, we administrated a single dose of tamoxifen at E9.5, and the contribution to multiple hematopoietic lineages in peripheral blood was chased up to 32 weeks after birth (**Figure 4C**). The labeling in total CD45$^+$ leukocytes was ranged from 5.2 to 7.7%, with little fluctuation from 4 to 32 weeks (**Figures 5A,B**). The constitutions of traced cells in different

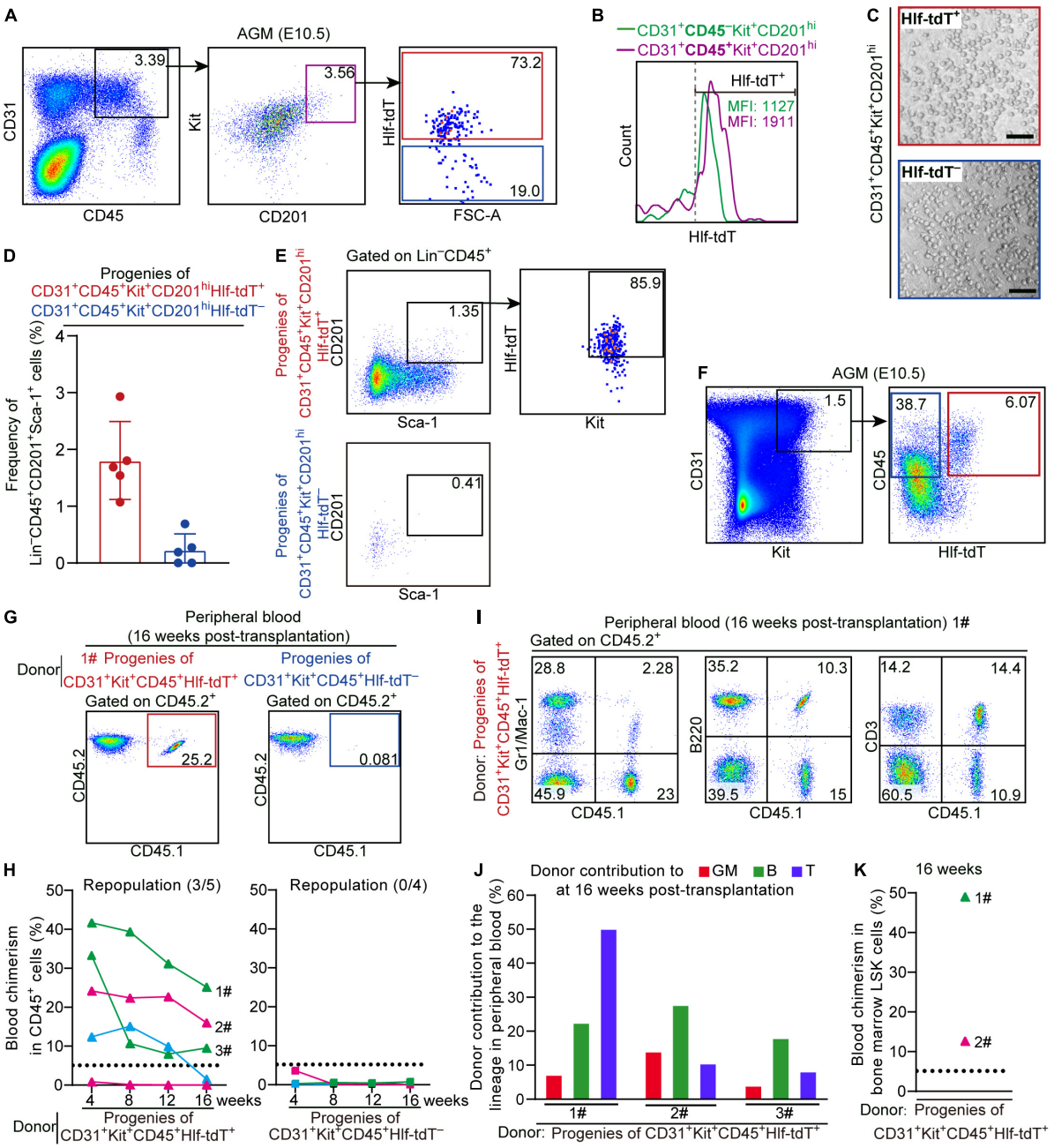

FIGURE 3 | Hlf-tdTomato enriches functional CD45$^+$ pre-HSCs in the E10.5 AGM region. **(A)** Representative FACS plots showing the proportion of Hlf-tdTomato$^+$ and Hlf-tdTomato$^-$ cells in the CD31$^+$CD45$^+$Kit$^+$CD201^{hi} population in the AGM region of E10.5 *Hlf-tdTomato* embryos. Data are representative of five independent experiments. **(B)** Representative FACS histogram showing the fluorescence intensity of tdTomato in the CD31$^+$CD45$^-$Kit$^+$CD201^{hi} and CD31$^+$CD45$^+$Kit$^+$CD201^{hi} populations in the AGM region of E10.5 *Hlf-tdTomato* embryos. Values of mean fluorescence intensity of tdTomato in the Hlf-tdTomato$^+$ cells are indicated. Data are representative of five independent experiments. **(C)** Representative morphology of hematopoietic cells generated from Hlf-tdTomato$^+$ cells and Hlf-tdTomato$^-$ cells within the CD31$^+$CD45$^+$Kit$^+$CD201^{hi} population. Scale bar, 100 μm. **(D)** Graph showing the frequency of Lin$^-$CD45$^+$CD201$^+$Sca-1$^+$ cells generated from the indicated populations from the E10.5 AGM region after co-culture measured by FACS analysis. Data are shown as means ± SEM from five independent experiments. **(E)** Representative FACS plots showing the expression of Hlf-tdTomato and Kit in Lin$^-$CD45$^+$CD201$^+$Sca-1$^+$ cells that are generated from the indicated populations of the E10.5 AGM region after co-culture. Data are representative of five independent experiments. **(F)** Cell sorting strategy for the populations from the AGM region of E10.5 *Hlf-tdTomato* embryos for co-culture/transplantation assay. The cell populations sorted for functional assay are denoted by colored boxes. **(G)** Representative FACS plots of blood chimerism of donor-derived (CD45.1$^+$CD45.2$^+$) cells in CD45$^+$ cells at 16 weeks post-transplantation. **(H)** Graphs showing the blood chimerism in CD45$^+$ cells of each of all the recipients from 4 to 16 weeks post-transplantation. The recipients were transplanted with the culture products of CD31$^+$Kit$^+$CD45$^+$Hlf-tdTomato$^+$ (triangle, left) or CD31$^+$Kit$^+$CD45$^+$Hlf-tdTomato$^-$ (square, right) cells from the AGM region of E10.5 *Hlf-tdTomato* embryos. Numbers of repopulated/total recipients are shown in the brackets. For each transplantation assay, cells from

(Continued)

FIGURE 3 | (Continued)
a total of 15 Hlf-tdTomato positive embryos belonging to three independent litters (biological repeats) were sampled and cultured as donor cells, and five recipients were used. Each line represents a recipient and each color represents an independent litter (biological repeat). **(I)** Representative FACS plots showing proportions of donor cells and each hematopoietic lineage at 16 weeks post-transplantation. Myeloid cells (Gr1/Mac-1$^+$), B cells (B220$^+$), and T cells (CD3$^+$) in peripheral blood are shown. **(J)** Bar plot showing the percentages of donor contribution to granulocytes/monocytes (GM, red), B cells (green), and T cells (blue) in the peripheral blood at 16 weeks post-transplantation. **(K)** Graph showing donor contribution to the bone marrow hematopoietic stem progenitor cells (Lin$^-$Sca-1$^+$Kit$^+$, LSK) of two successfully repopulated recipients at 16 weeks post-transplantation.

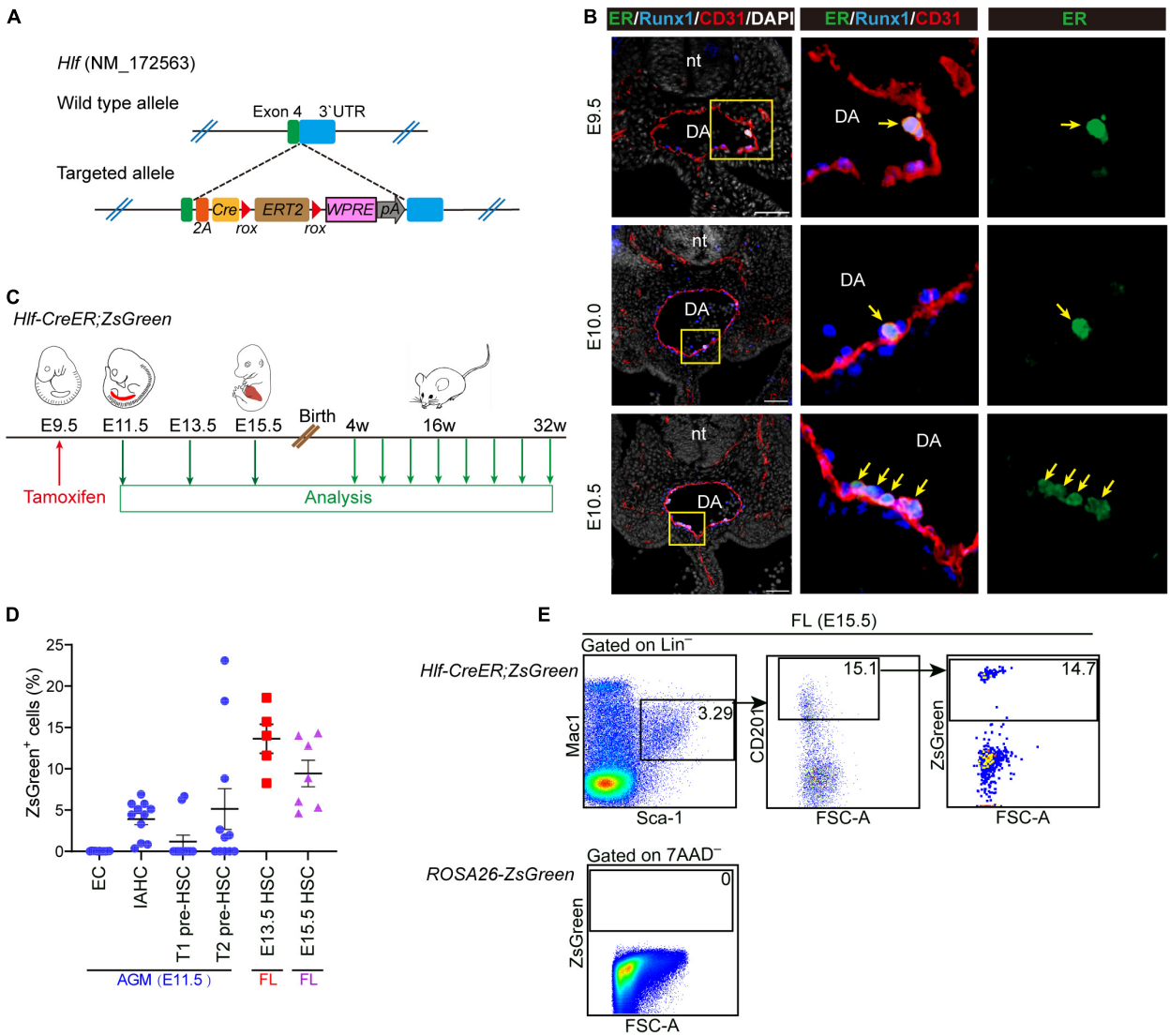

FIGURE 4 | Generation of an inducible *Hlf-CreER* mouse model. **(A)** Schematic model of the gene-targeting strategy for constructing *Hlf-CreER* lineage tracing mouse line *via* CRISPR/Cas9 system. **(B)** Representative immunostaining on sections at the E9.5, E10.0, and E10.5 AGM region of *Hlf-CreER* embryos. Arrows indicate ER$^+$ IAHCs. The images to the right present the magnification view of yellow boxes. Scale bar, 50 μm. **(C)** Schematic of the experimental design for the genetic lineage tracing with *Hlf-CreER;ZsGreen* mice. Single dose of induction by tamoxifen injection was performed at E9.5 (red arrow). Green arrows indicate the time points for analyses. The contribution of labeled cells in peripheral blood was chased every 4 weeks for up to 32 weeks after birth. **(D)** Graph showing the labeled proportions in the indicated populations. EC, endothelial cell. Data are shown as means ± SEM from three independent experiments. **(E)** Representative FACS plots showing the proportion of labeled cells in the immunophenotypic HSCs (Lin$^-$Sca-1$^+$Mac-1^{lo}CD201$^+$) in E15.5 fetal liver (FL). Data are representative of four independent experiments.

lineages were similar, including granulocytes/monocytes (CD45$^+$Gr1/Mac-1$^+$), B lymphocytes (CD45$^+$B220$^+$), T lymphocytes (CD45$^+$CD3$^+$), erythrocytes (CD45$^-$Ter119$^+$), and megakaryocytes (CD45$^-$CD41$^+$), with on average of 5.2–8.1% for all the lineages and all the time points detected (**Figures 5A,B**).

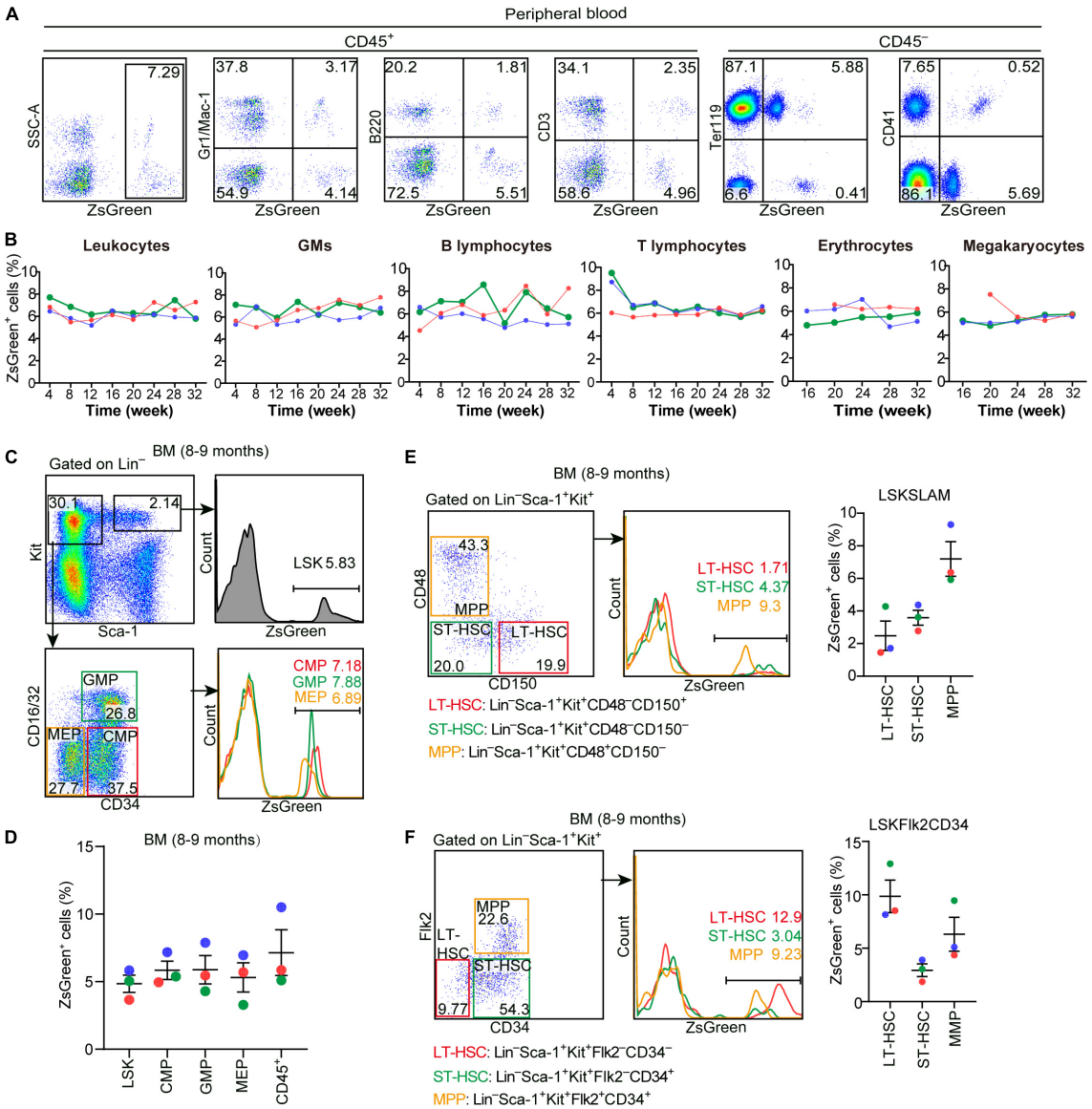

FIGURE 5 | Hlf-labeled early cells contribute to long-term and multi-lineage adult hematopoiesis. **(A)** Representative FACS plots showing the proportions of Hlf-labeled cells in CD45$^+$ cells and in each hematopoietic lineage in the peripheral blood from a 32-week old *Hlf-CreER;ZsGreen* mouse with tamoxifen administration at E9.5. **(B)** Graphs showing the dynamics of the labeling proportions in CD45$^+$ leukocytes, granulocytes/monocytes (GMs), B lymphocytes, T lymphocytes, erythrocytes, and megakaryocytes, respectively, in the peripheral blood of *Hlf-CreER;ZsGreen* mice at 4–32 weeks old with tamoxifen administration at E9.5. Data are from three individuals represented by different colors. **(C)** Representative FACS plots showing the proportions of Hlf-labeled cells in LSK (Lin$^-$Sca-1$^+$Kit$^+$) cells, CMPs, GMPs, and MEPs in the bone marrow (BM) of 8–9 month-old *Hlf-CreER;ZsGreen* mice with tamoxifen administration at E9.5. **(D)** Graph showing the proportions of Hlf-labeled cells in LSK cells, CMPs, GMPs, MEPs, and CD45$^+$ cells in the bone marrow (BM) of 8–9 month-old *Hlf-CreER;ZsGreen* mice with tamoxifen administration at E9.5. Data are shown as means ± SEM from three independent experiments represented by different colors. CMP, common myeloid progenitor; GMP, granulocyte-monocyte progenitor; MEP, megakaryocyte-erythroid progenitor. **(E)** Representative FACS plots (left) and graph (right) showing the proportions of Hlf-labeled cells in LT-HSCs, ST-HSCs, and MPPs in the bone marrow (BM) of adult *Hlf-CreER;ZsGreen* mice with tamoxifen administration at E9.5. LSKSLAM marker combination was used. Data are from three independent experiments represented by different colors. **(F)** Representative FACS plots (left) and graph (right) showing the proportions of Hlf-labeled cells in LT-HSCs, ST-HSCs, and MPPs in the bone marrow (BM) of adult *Hlf-CreER;ZsGreen* mice with tamoxifen administration at E9.5. LSKFlk2CD34 marker combination was used. Data are from three independent experiments represented by different colors. LT-HSC, long-term hematopoietic stem cell; ST-HSC, short-term hematopoietic stem cell; MPP, multipotent progenitor.

To further determine whether and to what extent the Hlf-labeled early cells contributed to BM hematopoiesis in adult, we analyzed BM samples from three 8–9-month-old mice by flow cytometry. The constitutions of lineage-labeled cells in the immunophenotypically defined committed hematopoietic progenitors, including common myeloid progenitors, granulocyte-monocyte progenitors, and megakaryocyte-erythroid progenitors, were similar to each other, and also to

that in the upstream HSC-enriched LSK ($Lin^-Sca1^+Kit^+$) cells as well as to those in the mature blood lineages in the peripheral blood (**Figures 5C,D**). Interestingly, when using different marker combinations to define the enriched long-term HSCs, short-term HSCs, and multi-potent progenitors, the results varied regarding the contribution of lineage-traced cells to each of these HSPC populations (**Figures 5E,F**), suggestive of the heterogeneity within these immunophenotypically defined HSPC populations.

Taken together, these data unambiguously indicated that the early Hlf-expressing cells in the embryo contribute to and retain the size of the HSC pool in the BM, which continuously differentiate to maintain a balanced and long-term multi-lineage hematopoiesis in the adult. Therefore, here we provided a valuable mouse model to specifically trace the fate of emerging HSCs in the embryo.

DISCUSSION

Considering that *Hlf* is an HSC-related gene that is specifically expressed in both embryonic and adult HSCs but neither in primitive blood cells nor erythro-myeloid progenitors, which is conserved in both mouse and human (Shojaei et al., 2005; Magnusson et al., 2007; Yokomizo et al., 2019; Zeng et al., 2019), here we specifically chose it and successfully constructed two mouse models, *Hlf-tdTomato* reporter mice and *Hlf-CreER* lineage tracing mice, which would without doubt serve as valuable mouse models for studying HSC biology.

In addition to validating the expression pattern of Hlf-tdTomato in FL and BM, which was principally consistent with the findings in a recent study (Yokomizo et al., 2019), we made an effort in the present study to explore the expression pattern of Hlf-tdTomato in early pre-HSCs with functional evaluation. Previous study has reported the presence of $CD45^-$ pre-HSCs in the E10.5 AGM region (Rybtsov et al., 2011); however, whether there exist $CD45^+$ pre-HSCs at E10.5 has been controversial (Boisset et al., 2015). Based on the *in vitro* co-culture system we used, the progenies of $CD45^+$Hlf-tdTomato$^+$ but not $CD45^+$Hlf-tdTomato$^-$ cells in the E10.5 AGM region were capable of repopulating irradiated adult recipients. Thus, we demonstrated the existence of $CD45^+$ pre-HSCs in E10.5 AGM, which express Hlf. Moreover, our finding suggested that Hlf expression prior to CD45 expression is a prerequisite for the cells to keep the HSC competence. Unlike the $CD45^+$ cells, $CD45^-$ cells showed repopulating activity in both Hlf-tdTomato$^+$ and Hlf-tdTomato$^-$ counterparts. However, presently, we could not figure out to what extent the HSC-primed HEC population contributed to the repopulating capacity of the Hlf-tdTomato$^-$ sub-population in the E10.5 AGM region. Further precise study designs are needed to address this question. It is conceivable that Hlf-tdTomato reporter can be used as an indicator of HSC emergence when carrying out reprogramming experiment or inducing ES cell differentiation *in vitro*.

Although a variety of mouse models have been used to trace the fate of HSCs, there is still room for improvement. Some mouse models have been used to mark adult HSCs, such as *Pdzk1ip1-CreERT2*, *Fgd5-CreERT2*, *Vwf-CreERT2*, *Krt18-CreERT2*, and *Tie2-MerCreMer*, with varied efficiencies to label adult HSCs when induced at adult stage (Busch et al., 2015; Sawai et al., 2016; Carrelha et al., 2018; Chapple et al., 2018; Sawen et al., 2018). However, the expression of most of these molecules is not specific to HSCs during development. Some mouse models, including *Cdh5-CreERT2*, *Tie2-MerCreMer*, and *Runx1-MerCreMer*, have been used to label embryonic HSCs when induced at mid-gestation (Zovein et al., 2008; Gomez Perdiguero et al., 2015; Hoeffel et al., 2015). Since these molecules are also expressed in the cells of other waves of hematopoiesis in addition to HSC generation during embryogenesis, and the occurring period for different waves of hematopoiesis overlaps to a certain extent, lineage tracing models using HSC-specific markers are urgently needed to more specifically and clearly delineate the fate of embryonic HSCs exclusively. Together with a previous study showing that Hlf is not expressed in erythro-myeloid progenitors, a population belonging to HSC-independent hematopoiesis (Yokomizo et al., 2019), our present findings suggested *Hlf-CreER* mice as an unprecedented model for studying embryonic HSC-derived hematopoiesis.

Our previous studies have reported the expression of CD201 (known as EPCR, encoded by *Procr*) in HSC-primed HECs and pre-HSCs, which is a stemness molecule and also expressed in aortic endothelial cells, as well as the contribution of CD201-labeled embryonic cells to fetal and adult blood lineages revealed by *Procr-CreER*-mediated lineage tracing when induced at E9.5 (Zhou et al., 2016; Lan, 2017; Zheng et al., 2019; Hou et al., 2020). Moreover, we have identified Neurl3 as a signature gene of HSC-primed HECs and pre-HSCs and achieved the enrichment of HSC-competent HECs by the *Neurl3-EGFP* reporter (Hou et al., 2020). In the future, by combining these mouse models, we will more precisely delineate the comprehensive roadmap for the diversified fate choice of different hematopoietic lineages from embryonic HSCs.

DATA AVAILABILITY STATEMENT

The original contributions presented in the study are included in the article/**Supplementary Material**, further inquiries can be directed to the corresponding author/s.

ETHICS STATEMENT

The animal study was reviewed and approved by the Academy of Military Medical Sciences (Fifth Medical Center of Chinese PLA General Hospital).

AUTHOR CONTRIBUTIONS

YL and BL designed the study. WT performed the cell sorting, culture, immunostaining, and transplantation assays with help from JHe, TH, ZB, CW, HW, RY, YN, YY, YG, SH, JHo, JW, and JZ. WT, YL, and BL wrote the manuscript and revision. All authors reviewed the manuscript.

FUNDING

This work was supported by the National Key R&D Program of China (2020YFA0112402 and 2017YFA0103401), the National Natural Science Foundation of China (81890991, 31871173, 31930054, and 81900115), the Program for Guangdong Introducing Innovative and Entrepreneurial Teams (2017ZT07S347), and the Key Research and Development Program of Guangdong Province (2019B020234002).

ACKNOWLEDGMENTS

We thank Bo Zhou for providing *ROSA-LSL-ZsGreen* reporter mice.

SUPPLEMENTARY MATERIAL

The Supplementary Material for this article can be found online at: https://www.frontiersin.org/articles/10.3389/fcell.2021.728057/full#supplementary-material

Supplementary Figure 1 | Gating strategies for FACS analyses of Hlf-tdTomato expression in different hematopoietic populations from *Hlf-tdTomato* mice. **(A)** Representative FACS plots showing the expression of Hlf-tdTomato in Gr1$^+$ cells and F4/80$^+$ macrophages in E15.5 fetal liver (FL). Data are representative of two independent experiments. **(B)** Representative FACS plots showing Hlf-tdTomato expression in the indicated hematopoietic populations in the adult bone marrow (BM). LT-HSC, long-term hematopoietic stem cell; ST-HSC, short-term hematopoietic stem cell; MPP, multipotent progenitor; CMP, common myeloid progenitor; GMP, granulocyte-monocyte progenitor; MEP, megakaryocyte-erythroid progenitor. Data are representative of three independent experiments. **(C)** Representative FACS plots (left) and graph (right) showing the Hlf-tdTomato expression in LT-HSCs, ST-HSCs and MPPs in the bone marrow (BM) of adult *Hlf-tdTomato* mice. LSKFlk2CD34 marker combination was used. Data are from three independent experiments. **(D)** Representative FACS plots showing the Hlf-tdTomato expression in granulocytes/monocytes (GMs), B cells, and T cells in the peripheral blood of adult *Hlf-tdTomato* mice. Data are representative of two independent experiments.

Supplementary Figure 2 | Representative FACS analyses of Hlf-tdTomato expression in embryos. **(A)** Representative FACS plots showing the proportions of Hlf-tdTomato$^+$ cells in hematopoietic cells (CD41$^+$/CD43$^+$/CD45$^+$) and non-hematopoietic cells (CD41$^-$CD43$^-$CD45$^-$) of the limb, head, and trunk from E10.5 *Hlf-tdTomato* embryos. Data are representative of two independent experiments. **(B)** Representative FACS plots showing no Hlf-tdTomato expression in PK44 (CD41$^-$CD43$^-$CD45$^-$CD31$^+$CD44$^+$Kit$^+$CD201$^+$) population of the E10.5 *Hlf-tdTomato* AGM region.

Supplementary Figure 3 | Representative FACS analyses of multi-lineage repopulation in multiple organs. **(A)** Representative FACS plots showing multi-organ and multi-lineage repopulation in the recipients 16 weeks post-transplantation transplanted with the culture products of the indicated cell populations from the E10.5 AGM region. The myeloid cells (Gr1/Mac-1$^+$), B cells (B220$^+$), and T cells (CD3$^+$ or CD4/CD8$^+$) in multiple hematopoietic organs are shown. **(B)** Representative FACS plots showing the proportions of donor-derived cells (represented by CD45.1$^+$) in hematopoietic stem progenitor populations in the bone marrow of the reconstituted recipients 16 weeks post-transplantation transplanted with the progenies of the indicated cell populations from the E10.5 AGM region. LSKSLAM marker combination was used. **(C)** Representative FACS plots showing multi-organ and multi-lineage repopulation in the recipient 16 weeks post-transplantation transplanted with the progenies of the indicated cell populations from the E10.5 AGM region. The myeloid cells (Gr1/Mac-1$^+$), B cells (B220$^+$), and T cells (CD3$^+$ or CD4/CD8$^+$) in multiple hematopoietic organs are shown. **(D)** Representative FACS plots showing the proportions of donor-derived cells (represented by CD45.1$^+$) in hematopoietic stem progenitor populations in the bone marrow of the reconstituted recipient 16 weeks post-transplantation transplanted with the progenies of the indicated cell populations from the E10.5 AGM region. LSKSLAM marker combination was used. LT-HSC, long-term hematopoietic stem cell; ST-HSC, short-term hematopoietic stem cell; MPP, multipotent progenitor; CMP, common myeloid progenitor; GMP, granulocyte-monocyte progenitor; MEP, megakaryocyte-erythroid progenitor.

Supplementary Figure 4 | Representative FACS analyses of lineage-traced cells in *Hlf-CreER;ZsGreen* mice. **(A)** Representative FACS plots showing the Hlf-labeled cells in endothelial cells (ECs), IAHCs, and T1 and T2 pre-HSCs in the AGM region of E11.5 *Hlf-CreER;ZsGreen* embryos with tamoxifen administrated at E9.5. Data are representative of six independent experiments. **(B)** Graph showing the dynamics of labeling in endothelial cells (ECs), IAHCs, and T1 and T2 pre-HSCs in the AGM region of E11.5 *Hlf-CreER;ZsGreen* embryos with tamoxifen administration at E9.5. Each line represents an individual embryo. **(C)** Representative FACS plots (left) and graph (right) showing the proportions of Hlf-labeled cells in the immunophenotypic HSCs (ESLAM) in the fetal liver (FL) of E15.5 *Hlf-CreER;ZsGreen* embryos with tamoxifen administration at E9.5. Data are representative of four independent experiments.

REFERENCES

Baron, C. S., Kester, L., Klaus, A., Boisset, J. C., Thambyrajah, R., Yvernogeau, L., et al. (2018). Single-cell transcriptomics reveal the dynamic of haematopoietic stem cell production in the aorta. *Nat. Commun.* 9:2517. doi: 10.1038/s41467-018-04893-3

Benz, C., Copley, M. R., Kent, D. G., Wohrer, S., Cortes, A., Aghaeepour, N., et al. (2012). Hematopoietic stem cell subtypes expand differentially during development and display distinct lymphopoietic programs. *Cell Stem Cell* 10, 273–283. doi: 10.1016/j.stem.2012.02.007

Boisset, J. C., Clapes, T., Klaus, A., Papazian, N., Onderwater, J., Mommaas-Kienhuis, M., et al. (2015). Progressive maturation toward hematopoietic stem cells in the mouse embryo aorta. *Blood* 125, 465–469. doi: 10.1182/blood-2014-07-588954

Boisset, J. C., van Cappellen, W., Andrieu-Soler, C., Galjart, N., Dzierzak, E., and Robin, C. (2010). In vivo imaging of haematopoietic cells emerging from the mouse aortic endothelium. *Nature* 464, 116–120. doi: 10.1038/nature08764

Busch, K., Klapproth, K., Barile, M., Flossdorf, M., Holland-Letz, T., Schlenner, S. M., et al. (2015). Fundamental properties of unperturbed haematopoiesis from stem cells in vivo. *Nature* 518, 542–546. doi: 10.1038/nature14242

Carrelha, J., Meng, Y., Kettyle, L. M., Luis, T. C., Norfo, R., Alcolea, V., et al. (2018). Hierarchically related lineage-restricted fates of multipotent haematopoietic stem cells. *Nature* 554, 106–111. doi: 10.1038/nature25455

Chapple, R. H., Tseng, Y. J., Hu, T., Kitano, A., Takeichi, M., Hoegenauer, K. A., et al. (2018). Lineage tracing of murine adult hematopoietic stem cells reveals active contribution to steady-state hematopoiesis. *Blood Adv.* 2, 1220–1228. doi: 10.1182/bloodadvances.2018016295

Chen, M. J., Yokomizo, T., Zeigler, B. M., Dzierzak, E., and Speck, N. A. (2009). Runx1 is required for the endothelial to haematopoietic cell transition but not thereafter. *Nature* 457, 887–891. doi: 10.1038/nature07619

Christensen, J. L., Wright, D. E., Wagers, A. J., and Weissman, I. L. (2004). Circulation and chemotaxis of fetal hematopoietic stem cells. *PLoS Biol.* 2:E75. doi: 10.1371/journal.pbio.0020075

de Bruijn, M. F., Ma, X., Robin, C., Ottersbach, K., Sanchez, M. J., and Dzierzak, E. (2002). Hematopoietic stem cells localize to the endothelial cell layer in the midgestation mouse aorta. *Immunity* 16, 673–683. doi: 10.1016/s1074-7613(02)00313-8

de Bruijn, M. F., Speck, N. A., Peeters, M. C., and Dzierzak, E. (2000). Definitive hematopoietic stem cells first develop within the major arterial regions of the mouse embryo. *EMBO J.* 19, 2465–2474. doi: 10.1093/emboj/19.11.2465

Dzierzak, E., and Bigas, A. (2018). Blood development: hematopoietic stem cell dependence and independence. *Cell Stem Cell* 22, 639–651. doi: 10.1016/j.stem.2018.04.015

Gazit, R., Garrison, B. S., Rao, T. N., Shay, T., Costello, J., Ericson, J., et al. (2013). Transcriptome analysis identifies regulators of hematopoietic stem and progenitor cells. *Stem Cell Rep.* 1, 266–280. doi: 10.1016/j.stemcr.2013.07.004

Gomez Perdiguero, E., Klapproth, K., Schulz, C., Busch, K., Azzoni, E., Crozet, L., et al. (2015). Tissue-resident macrophages originate from yolk-sac-derived erythro-myeloid progenitors. *Nature* 518, 547–551. doi: 10.1038/nature13989

Hadland, B. K., Varnum-Finney, B., Mandal, P. K., Rossi, D. J., Poulos, M. G., Butler, J. M., et al. (2017). A common origin for B-1a and B-2 lymphocytes in Clonal Pre- hematopoietic stem cells. *Stem Cell Rep*. 8, 1563–1572. doi: 10.1016/j.stemcr.2017.04.007

Hoeffel, G., Chen, J., Lavin, Y., Low, D., Almeida, F. F., See, P., et al. (2015). C-Myb(+) erythro-myeloid progenitor-derived fetal monocytes give rise to adult tissue-resident macrophages. *Immunity* 42, 665–678. doi: 10.1016/j.immuni.2015.03.011

Hou, S., Li, Z., Zheng, X., Gao, Y., Dong, J., Ni, Y., et al. (2020). Embryonic endothelial evolution towards first hematopoietic stem cells revealed by single-cell transcriptomic and functional analyses. *Cell Res.* 30, 376–392. doi: 10.1038/s41422-020-0300-2

Komorowska, K., Doyle, A., Wahlestedt, M., Subramaniam, A., Debnath, S., Chen, J., et al. (2017). Hepatic leukemia factor maintains quiescence of hematopoietic stem cells and protects the stem cell pool during regeneration. *Cell Rep.* 21, 3514–3523. doi: 10.1016/j.celrep.2017.11.084

Lan, Y. (2017). Procr+ stem cells: from vessel to blood. *Nat. Sci. Rev.* 4, 523–524. doi: 10.1093/nsr/nwx104

Li, Z., Lan, Y., He, W., Chen, D., Wang, J., Zhou, F., et al. (2012). Mouse embryonic head as a site for hematopoietic stem cell development. *Cell Stem Cell* 11, 663–675. doi: 10.1016/j.stem.2012.07.004

Madisen, L., Zwingman, T. A., Sunkin, S. M., Oh, S. W., Zariwala, H. A., Gu, H., et al. (2010). A robust and high-throughput Cre reporting and characterization system for the whole mouse brain. *Nat. Neurosci.* 13, 133–140. doi: 10.1038/nn.2467

Magnusson, M., Brun, A. C., Miyake, N., Larsson, J., Ehinger, M., Bjornsson, J. M., et al. (2007). HOXA10 is a critical regulator for hematopoietic stem cells and erythroid/megakaryocyte development. *Blood* 109, 3687–3696. doi: 10.1182/blood-2006-10-054676

Medvinsky, A., and Dzierzak, E. (1996). Definitive hematopoiesis is autonomously initiated by the AGM region. *Cell* 86, 897–906. doi: 10.1016/s0092-8674(00)80165-8

Morrison, S. J., Hemmati, H. D., Wandycz, A. M., and Weissman, I. L. (1995). The purification and characterization of fetal liver hematopoietic stem cells. *Proc. Natl. Acad. Sci. U.S.A.* 92, 10302–10306. doi: 10.1073/pnas.92.22.10302

Muller, A. M., Medvinsky, A., Strouboulis, J., Grosveld, F., and Dzierzak, E. (1994). Development of hematopoietic stem cell activity in the mouse embryo. *Immunity* 1, 291–301. doi: 10.1016/1074-7613(94)90081-7

Neo, W. H., Lie, A. L. M., Fadlullah, M. Z. H., and Lacaud, G. (2021). Contributions of embryonic HSC-Independent hematopoiesis to organogenesis and the adult hematopoietic system. *Front. Cell Dev. Biol.* 9:631699. doi: 10.3389/fcell.2021.631699

North, T. E., de Bruijn, M. F., Stacy, T., Talebian, L., Lind, E., Robin, C., et al. (2002). Runx1 expression marks long-term repopulating hematopoietic stem cells in the midgestation mouse embryo. *Immunity* 16, 661–672. doi: 10.1016/s1074-7613(02)00296-0

Rybtsov, S., Ivanovs, A., Zhao, S., and Medvinsky, A. (2016). Concealed expansion of immature precursors underpins acute burst of adult HSC activity in foetal liver. *Development* 143, 1284–1289. doi: 10.1242/dev.131193

Rybtsov, S., Sobiesiak, M., Taoudi, S., Souilhol, C., Senserrich, J., Liakhovitskaia, A., et al. (2011). Hierarchical organization and early hematopoietic specification of the developing HSC lineage in the AGM region. *J. Exp. Med.* 208, 1305–1315. doi: 10.1084/jem.20102419

Sánchez, M. J., Holmes, A., Miles, C., and Dzierzak, E. (1996). Characterization of the first definitive hematopoietic stem cells in the AGM and liver of the mouse embryo. *Immunity* 5, 513–525. doi: 10.1016/s1074-7613(00)80267-8

Sawai, C. M., Babovic, S., Upadhaya, S., Knapp, D., Lavin, Y., Lau, C. M., et al. (2016). Hematopoietic stem cells are the major source of Multilineage Hematopoiesis in adult animals. *Immunity* 45, 597–609. doi: 10.1016/j.immuni.2016.08.007

Sawen, P., Eldeeb, M., Erlandsson, E., Kristiansen, T. A., Laterza, C., Kokaia, Z., et al. (2018). Murine HSCs contribute actively to native hematopoiesis but with reduced differentiation capacity upon aging. *eLife* 7:e41258. doi: 10.7554/eLife.41258

Shojaei, F., Trowbridge, J., Gallacher, L., Yuefei, L., Goodale, D., Karanu, F., et al. (2005). Hierarchical and ontogenic positions serve to define the molecular basis of human hematopoietic stem cell behavior. *Dev. Cell* 8, 651–663. doi: 10.1016/j.devcel.2005.03.004

Solaimani Kartalaei, P., Yamada-Inagawa, T., Vink, C. S., de Pater, E., van der Linden, R., Marks-Bluth, J., et al. (2015). Whole-transcriptome analysis of endothelial to hematopoietic stem cell transition reveals a requirement for Gpr56 in HSC generation. *J. Exp. Med.* 212, 93–106. doi: 10.1084/jem.20140767

Taoudi, S., Gonneau, C., Moore, K., Sheridan, J. M., Blackburn, C. C., Taylor, E., et al. (2008). Extensive hematopoietic stem cell generation in the AGM region via maturation of VE-cadherin+CD45+ pre-definitive HSCs. *Cell Stem Cell* 3, 99–108. doi: 10.1016/j.stem.2008.06.004

Vink, C. S., Calero-Nieto, F. J., Wang, X., Maglitto, A., Mariani, S. A., Jawaid, W., et al. (2020). Iterative single-cell analyses define the transcriptome of the first functional hematopoietic stem cells. *Cell Rep.* 31:107627. doi: 10.1016/j.celrep.2020.107627

Wahlestedt, M., Ladopoulos, V., Hidalgo, I., Sanchez Castillo, M., Hannah, R., Sawen, P., et al. (2017). Critical modulation of hematopoietic lineage fate by hepatic leukemia factor. *Cell Rep.* 21, 2251–2263. doi: 10.1016/j.celrep.2017.10.112

Yamamoto, R., Morita, Y., Ooehara, J., Hamanaka, S., Onodera, M., Rudolph, K. L., et al. (2013). Clonal analysis unveils self-renewing lineage-restricted progenitors generated directly from hematopoietic stem cells. *Cell* 154, 1112–1126. doi: 10.1016/j.cell.2013.08.007

Ye, H., Wang, X., Li, Z., Zhou, F., Li, X., Ni, Y., et al. (2017). Clonal analysis reveals remarkable functional heterogeneity during hematopoietic stem cell emergence. *Cell Res.* 27, 1065–1068. doi: 10.1038/cr.2017.64

Yokomizo, T., and Dzierzak, E. (2010). Three-dimensional cartography of hematopoietic clusters in the vasculature of whole mouse embryos. *Development* 137, 3651–3661. doi: 10.1242/dev.051094

Yokomizo, T., Watanabe, N., Umemoto, T., Matsuo, J., Harai, R., Kihara, Y., et al. (2019). Hlf marks the developmental pathway for hematopoietic stem cells but not for erythro-myeloid progenitors. *J. Exp. Med.* 216, 1599–1614. doi: 10.1084/jem.20181399

Zeng, Y., He, J., Bai, Z., Li, Z., Gong, Y., Liu, C., et al. (2019). Tracing the first hematopoietic stem cell generation in human embryo by single-cell RNA sequencing. *Cell Res.* 29, 881–894. doi: 10.1038/s41422-019-0228-6

Zheng, X., Zhang, G., Gong, Y., Ning, X., Bai, Z., He, J., et al. (2019). Embryonic lineage tracing with Procr-CreER marks balanced hematopoietic stem cell fate during entire mouse lifespan. *J. Genet. Genom.* 46, 489–498. doi: 10.1016/j.jgg.2019.10.005

Zhou, F., Li, X., Wang, W., Zhu, P., Zhou, J., He, W., et al. (2016). Tracing haematopoietic stem cell formation at single-cell resolution. *Nature* 533, 487–492. doi: 10.1038/nature17997

Zovein, A. C., Hofmann, J. J., Lynch, M., French, W. J., Turlo, K. A., Yang, Y., et al. (2008). Fate tracing reveals the endothelial origin of hematopoietic stem cells. *Cell Stem Cell* 3, 625–636. doi: 10.1016/j.stem.2008.09.018

Conflict of Interest: The authors declare that the research was conducted in the absence of any commercial or financial relationships that could be construed as a potential conflict of interest.

Publisher's Note: All claims expressed in this article are solely those of the authors and do not necessarily represent those of their affiliated organizations, or those of the publisher, the editors and the reviewers. Any product that may be evaluated in this article, or claim that may be made by its manufacturer, is not guaranteed or endorsed by the publisher.

frontiers in Cell and Developmental Biology

BRIEF RESEARCH REPORT
published: 17 September 2021
doi: 10.3389/fcell.2021.732527

Wild-Type p53-Induced Phosphatase 1 Plays a Positive Role in Hematopoiesis in the Mouse Embryonic Head

Wenyan He[1†‡], Ying Zhang[2†], Zhan Cao[2], Zehua Ye[2], Xun Lu[2], Junwan Fan[1], Wei Peng[3] and Zhuan Li[2*‡]*

[1] China National Clinical Research Center for Neurological Diseases, Beijing Tiantan Hospital, Capital Medical University, Beijing, China, [2] Department of Developmental Biology, School of Basic Medical Sciences, Southern Medical University, Guangzhou, China, [3] Department of Stomatology, The First Affiliated Hospital, Sun Yat-sen University, Guangzhou, China

OPEN ACCESS

Edited by:
Jianwei Wang,
Tsinghua University, China

Reviewed by:
Yanni Ma,
Peking Union Medical College, China
Jin Xu,
South China University of Technology, China

***Correspondence:**
Wenyan He
hewenyan77@163.com
Zhuan Li
zhuanli2018@smu.edu.cn

[†] These authors have contributed equally to this work and share first authorship

[‡] These authors have contributed equally to this work

Specialty section:
This article was submitted to Stem Cell Research, a section of the journal Frontiers in Cell and Developmental Biology

Received: *29 June 2021*
Accepted: *18 August 2021*
Published: *17 September 2021*

Citation:
He W, Zhang Y, Cao Z, Ye Z, Lu X, Fan J, Peng W and Li Z (2021) Wild-Type p53-Induced Phosphatase 1 Plays a Positive Role in Hematopoiesis in the Mouse Embryonic Head. Front. Cell Dev. Biol. 9:732527. doi: 10.3389/fcell.2021.732527

The first adult repopulating hematopoietic stem cells (HSCs) are found in the aorta-gonad-mesonephros (AGM) region, which are produced from hemogenic endothelial cells. Embryonic head is the other site for HSC development. Wild-type p53-induced phosphatase 1 (Wip1) is a type-2Cδ family serine/threonine phosphatase involved in various cellular processes such as lymphoid development and differentiation of adult HSCs. Most recently, we have shown that Wip1 modulates the pre-HSC maturation in the AGM region. However, it is not clear whether Wip1 regulates hematopoiesis in the embryonic head. Here we reported that disruption of Wip1 resulted in a decrease of hematopoietic progenitor cell number in the embryonic head. *In vivo* transplantation assays showed a reduction of HSC function after Wip1 ablation. We established that Wip1 deletion reduced the frequency and cell number of microglia in the embryonic head. Further observations revealed that Wip1 absence enhanced the gene expression of microglia-derived pro-inflammatory factors. Thus, it is likely that Wip1 functions as a positive regulator in HSC development by regulating the function of microglia in the embryonic head.

Keywords: embryonic head, hematopoietic stem cell, Wip1, microglia, pro-inflammatory factor

INTRODUCTION

Hematopoietic stem cells (HSCs) provide hematopoietic progenitor cells (HPCs) and mature blood cells depending on the capacity of self-renewing and differentiation. The aorta-gonad-mesonephros (AGM) region is the site for the generation of the first HSC with long-term repopulating potential in the embryo (Muller et al., 1994). It is well known that HSCs are derived from hemogenic endothelial cells (ECs), which are produced by early arterial EC precursors (Chen et al., 2009; Kim et al., 2010; Hou et al., 2020; Howell and Speck, 2020). Previous studies have identified the regulatory molecules of AGM HSC productions, such as pro-inflammatory factors, adrenomedullin (ADM)/receptor activity-modifying protein 2 (RAMP2), and G protein-coupled receptor 56 (Gpr56) (Li et al., 2014, 2019; Solaimani Kartalaei et al., 2015; Dzierzak and Bigas, 2018; Mariani et al., 2019; Yvernogeau et al., 2020). Moreover, definitive erythro-myeloid progenitors (EMPs) are emerged from ECs in the yolk sac beginning at embryonic day (E) 8/8.5. EMPs are phenotypically defined by a cocktail

of markers CD41, cKit, and CD16/32, positively distinguishing EMPs from embryonic HPCs in the yolk sac (McGrath et al., 2015; Frame et al., 2016). Recent fate-mapping studies have evidently demonstrated that EMPs from yolk sac contribute macrophages in the embryonic head (microglia) during conditions of hemostasis (Gomez Perdiguero et al., 2015).

Embryonic head is the other site for hematopoietic stem and progenitor cell (HSPC) emergence from our previous study. Functional transplantation and lineage tracing data have demonstrated that HSPCs are produced from the vascular of head (Li et al., 2012). These HSPCs in the embryonic head display a single cell phenotype, not forming "hematopoietic clusters," which appeared in the AGM region (Iizuka et al., 2016; Li et al., 2016), suggesting differences in the regulation of head hematopoiesis. Recently, we found that head $CD45^+F4/80^+CD11b^+$ macrophages (microglia) acted as microenvironmental cellular regulators, promoting the process of endothelial to hematopoietic transition in the embryonic head by secreting the pro-inflammatory factor tumor necrosis factor-α (*TNF-α*) (Li et al., 2019). However, the regulatory mechanisms of hematopoiesis in the embryonic head remain to be investigated.

Wild-type p53-induced phosphatase 1 (Wip1) is encoded by protein phosphatase magnesium-dependent 1 delta (*PPM1D*), which is a critical regulator involved in various cellular processes (Uyanik et al., 2017), including neurogenesis (Zhu et al., 2009), tumorigenesis (Belova et al., 2005; Demidov et al., 2007), cell aging, neutrophil maturation (Liu et al., 2013; Sun et al., 2014), and lymphoid development (Yi et al., 2015). Specially, Chen et al. (2015) showed that Wip1 affects the function of HSCs *via* p53 and mammalian target of rapamycin complex 1 (mTORC1) pathways. Wip1-deficient embryos were viable; however, the defects in growth, organ structure, and fertility were observed in postnatal mice (Choi et al., 2002). Most recently, we reported that Wip1 affects the pre-HSC maturation and HPC development by altering cell cycle in the embryonic AGM region (He et al., 2021). However, the effects of Wip1 on mediating embryonic head hematopoiesis have yet to be established.

In this study, we find that Wip1 is required for the development of definitive HSPCs in the embryonic head. Moreover, Wip1 affects the development/function of microglia by enhancing pro-inflammatory factor gene expression. Our findings suggest that Wip1 regulates hematopoiesis in the embryonic head region by altering the pro-inflammatory factor status.

RESULTS

Wild-Type p53-Induced Phosphatase 1 Deficiency Results in the Reduction of Hematopoietic Progenitor Cells in the Embryonic Head

Recently, we have reported that Wip1 is involved in the regulation of HSPC development in the AGM region. To test whether Wip1 plays a role in hematopoiesis of the embryonic head, *Wip1* homozygous deficient embryos ($Wip1^{-/-}$, KO) were obtained by crossing *Wip1* heterozygous deficient ($Wip1^{+/-}$, HT) mice. A reduced head size was observed under microscope from E9.5 to E12.5 (data not shown). But the total cell numbers were decreased only in E9.5 and E10.5 Wip1-deficient head compared with wild-type (WT) controls and not in E11.5 (**Figure 1A**). However, the head cell viabilities in all stages we detected by flow cytometry were comparable (**Supplementary Figure 1A**). Flow cytometry analysis showed that the percentage of $CD45^+$ cells was significantly increased at E9.5 ($0.23 \pm 0.05\%$ vs. $0.09 \pm 0.03\%$) but decreased at E11.5 $Wip1^{-/-}$ head ($0.84 \pm 0.05\%$ vs. $0.98 \pm 0.04\%$); however, it was not changed in E10.5 head ($0.70 \pm 0.08\%$ vs. $0.80 \pm 0.08\%$) (**Figures 1B–D** and **Supplementary Figure 1B**). The absolute numbers of $CD45^+$ cells were reduced dramatically in the E10.5 ($4.78 \pm 0.80 \times 10^3$ vs. $8.03 \pm 1.46 \times 10^3$) and E11.5 ($1.76 \pm 0.28 \times 10^4$ vs. $3.10 \pm 0.45 \times 10^4$) $Wip1^{-/-}$ head but not in E9.5 (**Figures 1C,D** and **Supplementary Figure 1C**). Moreover, Wip1 deletion decreased the percentage ($0.39 \pm 0.02\%$ vs. $0.47 \pm 0.02\%$) and the cell number (33% reduction, $1.32 \pm 0.08 \times 10^4$ vs. $1.98 \pm 0.08 \times 10^4$) of $CD41^{low}CD45^-$ cells (including HPCs) in the E11.5 head (**Figure 1E**), indicating impaired hematopoietic development in the embryonic head. Furthermore, to test the hematopoietic progenitor function, colony-forming unit-culture (CFU-C) assays confirmed a dramatic decrease in HPC function from E9.5 to E11.5 $Wip1^{-/-}$ head compared to WT head, including the reductions of burst forming unit-erythroid (BFU-E) of E11.5 (5 ± 5 vs. 80 ± 42), CFU-granulocyte-macrophage (CFU-GM) in E9.5–E11.5 (E9.5, 0 ± 0 vs. 7 ± 2; E10.5, 238 ± 81 vs. 486 ± 80; E11.5, 365 ± 50 vs. 993 ± 165), and CFU-granulocyte-erythroid-macrophage-megakaryocyte [CFU-GEMM(Mix)] in E9.5 (0 ± 0 vs. 1 ± 1) and E11.5 (10 ± 10 vs. 120 ± 61) (**Figure 1F**), which is similar to the trend of CD41-enriched HPCs in the embryonic head (**Figure 1E**) and AGM region (He et al., 2021). Meanwhile, the reduced morphologic size of CFU-Cs was seen in all stages, and the CFU-Cs per input cell number were decreased dramatically in E9.5 and E11.5 (**Supplementary Figures 1D,E**). These results suggest that Wip1 is involved in HPC development of the embryonic head.

Loss of Wild-Type p53-Induced Phosphatase 1 Results in Impaired Hematopoietic Stem Cell Function in the Mid-Gestation Head

To see whether Wip1 deletion affects HSC function, *in vivo* transplantation assays were performed. E11.5–E12.5 head cells were injected intravenously into irradiated adult recipients, and the chimerism was detected in the peripheral blood of recipients at 4 and 16 weeks posttransplantation. None of recipients received E11.5 $Wip1^{-/-}$ head cells were repopulated at 4 and 16 weeks, although four out of five recipients (chimerism $57.6 \pm 18.0\%$) by injecting with WT head showed long-term, high-level, multilineage repopulation at E11.5 (**Figure 2A**). Unexpectedly, the repopulated ratios

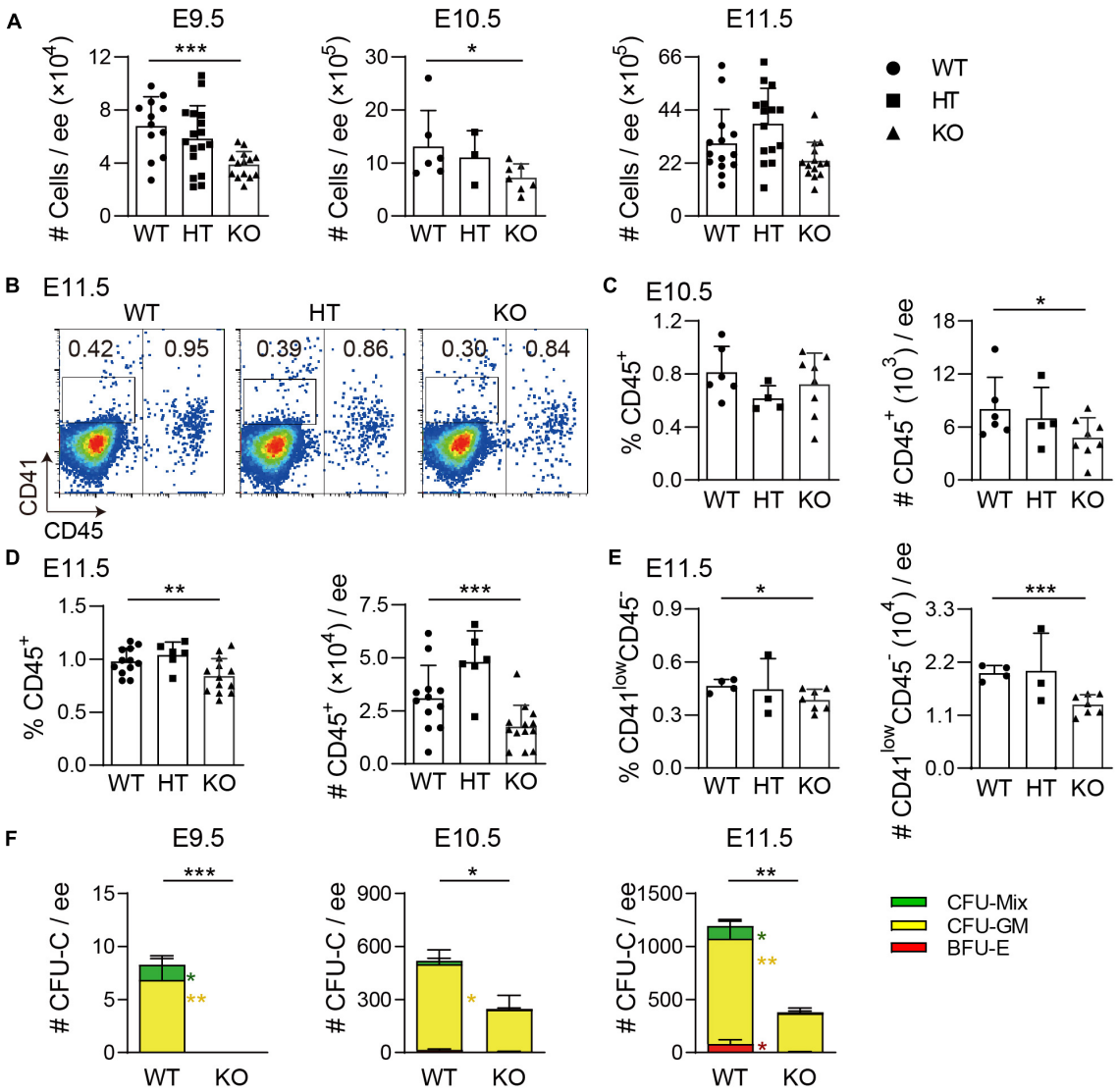

FIGURE 1 | Wip1 deficiency results in the reduction of hematopoietic progenitor cell number in the embryonic head. **(A)** The reduction of the total numbers in the E9.5–E11.5 embryonic head. E9.5, $n = 5$; E10.5, $n = 3$; E11.5, $n = 8$; $^{*}p < 0.05$, $^{***}p < 0.001$. **(B)** Representative flow cytometry analysis of $CD41^{low}CD45^{-}$ and $CD45^{+}$ cells in the E11.5 embryonic head. **(C,D)** The percentages and absolute numbers of $CD45^{+}$ cells in the E10.5–E11.5 embryonic head. E10.5, $n = 3$; E11.5, $n = 6$; $^{*}p < 0.05$, $^{**}p < 0.01$, $^{***}p < 0.001$. **(E)** The percentage and absolute number of $CD41^{low}CD45^{-}$ cells in the E11.5 embryonic head. $n = 3$; $^{*}p < 0.05$, $^{***}p < 0.001$. **(F)** Colony-forming unit-culture (CFU-C) assays showed the number of CFU-Cs in the E9.5–E11.5 embryonic head. Numbers of colony type are indicated by bar color. E9.5, $n = 3$; E10.5, $n = 2$; E11.5, $n = 4$; $^{*}p < 0.05$, $^{**}p < 0.01$, $^{***}p < 0.001$.

from the E12.5 $Wip1^{-/-}$ head cell with lower chimerism (28.9 ± 15.0% vs. 70.9 ± 11.6%) were reduced significantly at 16 weeks posttransplantation compared to those in the control group (2/3 vs. 7/8) (**Figure 2B**). The profile of multilineage output was similar to our previous data, with an increased trend of myeloid and T lymphoid lineage output, at the expense of B lymphoid output in the peripheral blood of $Wip1^{-/-}$ head-derived recipients (**Figure 2C**). Moreover, the $Wip1^{-/-}$ head-derived HSC attributed to hematopoietic cells in the various hematopoietic organs (spleen, bone marrow, and thymus) (**Figures 2D–F**) demonstrated the capacity for multilineage engraftment. In conclusion, these findings indicate that Wip1 affects HSC activity definitively in the E11.5–E12.5 head.

Deletion of Wild-Type p53-Induced Phosphatase 1 Affects Macrophage Development in the Embryonic Head but Not in the Yolk Sac

Our recent studies have shown that head microglia cells are pivotal as positive hematopoietic regulators. As we mentioned, $CD45^{+}$ cells were decreased after Wip1 deletion. To uncover whether Wip1 regulates the number and function of embryonic

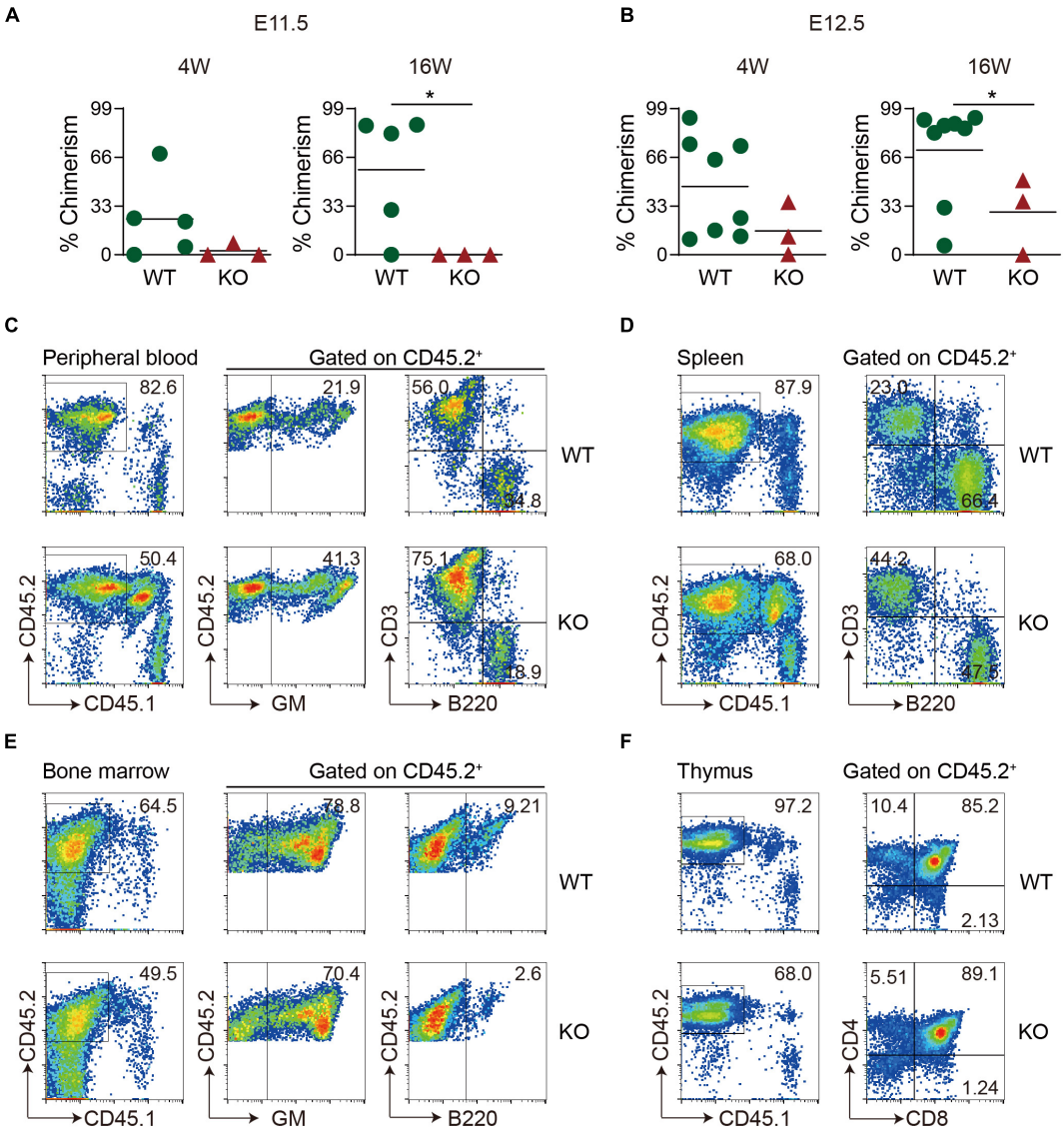

FIGURE 2 | Hematopoietic stem cell activity is decreased in Wip1 knockout head of the E11.5–E12.5 embryo. **(A,B)** Direct transplantation assay showing the repopulating ability of E11.5 and E12.5 wild-type (WT) and *Wip1*$^{-/-}$ embryonic head. Symbols represent the donor chimerism of CD45.2^{+} cells in peripheral blood of individual recipients in 4 weeks (left) and 16 weeks (right) posttransplantation. *$p < 0.05$. **(C–F)** Representative analysis of multilineage output of repopulated recipients receiving E12.5 head cells. The donor contribution is revealed by the presence of the donor of CD45.2^{+} cells in the myeloid (Gr-1/Mac1), B lymphoid (B220), and T lymphoid (CD3, CD4, and CD8) cells of the peripheral blood **(C)**, spleen **(D)**, bone marrow **(E)**, and thymus **(F)** in two representative recipients at 6 months posttransplantation. The recipients were injected with 1 embryo equivalent (ee) of E11.5 and E12.5 head cells.

head microglial cells, F4/80 as a microglia marker was used for flow cytometry analysis. Compared to WT head, the deletion of Wip1 resulted in a reduction of microglia proportions (CD45^{+}F4/80^{+}%) in E10.5 (0.46 ± 0.06% vs. 0.65 ± 0.06%) and E11.5 (0.65 ± 0.04% vs. 0.76 ± 0.04%) but not in E9.5 (0.024 ± 0.009% vs. 0.003 ± 0.003%). In contrast, the percentages of CD45^{+} F4/80^{-} were increased in E10.5 (**Figures 3A,B** and **Supplementary Figure 2A**), in line with the impaired hematopoietic activity. Similarly, the cell number of microglia was radically reduced in E10.5 (51% reduction, $3.16 \pm 0.55 \times 10^3$ vs. $6.50 \pm 1.09 \times 10^3$) to E11.5 (37% reduction, $1.59 \pm 0.19 \times 10^4$ vs. $2.52 \pm 0.33 \times 10^4$) but not in E9.5. Furthermore, the numbers of CD45^{+} F4/80^{-} were comparable (**Figure 3C** and **Supplementary Figure 2B**). The above results indicated that Wip1 loss reduced the microglia cell number in the embryonic head, suggesting impaired physiologic hematopoietic support.

In contrast, the percentages and absolute numbers of macrophage (CD45^{+}F480^{+}CD11b^{+}) were comparable in the E11.5 Wip1$^{-/-}$ yolk sac, as well as the same trend of CD45^{+} cells (**Supplementary Figures 3A–D**). As is known, microglia are derived from the EMPs of the yolk sac (Gomez Perdiguero et al., 2015), so we used flow cytometry analysis to define

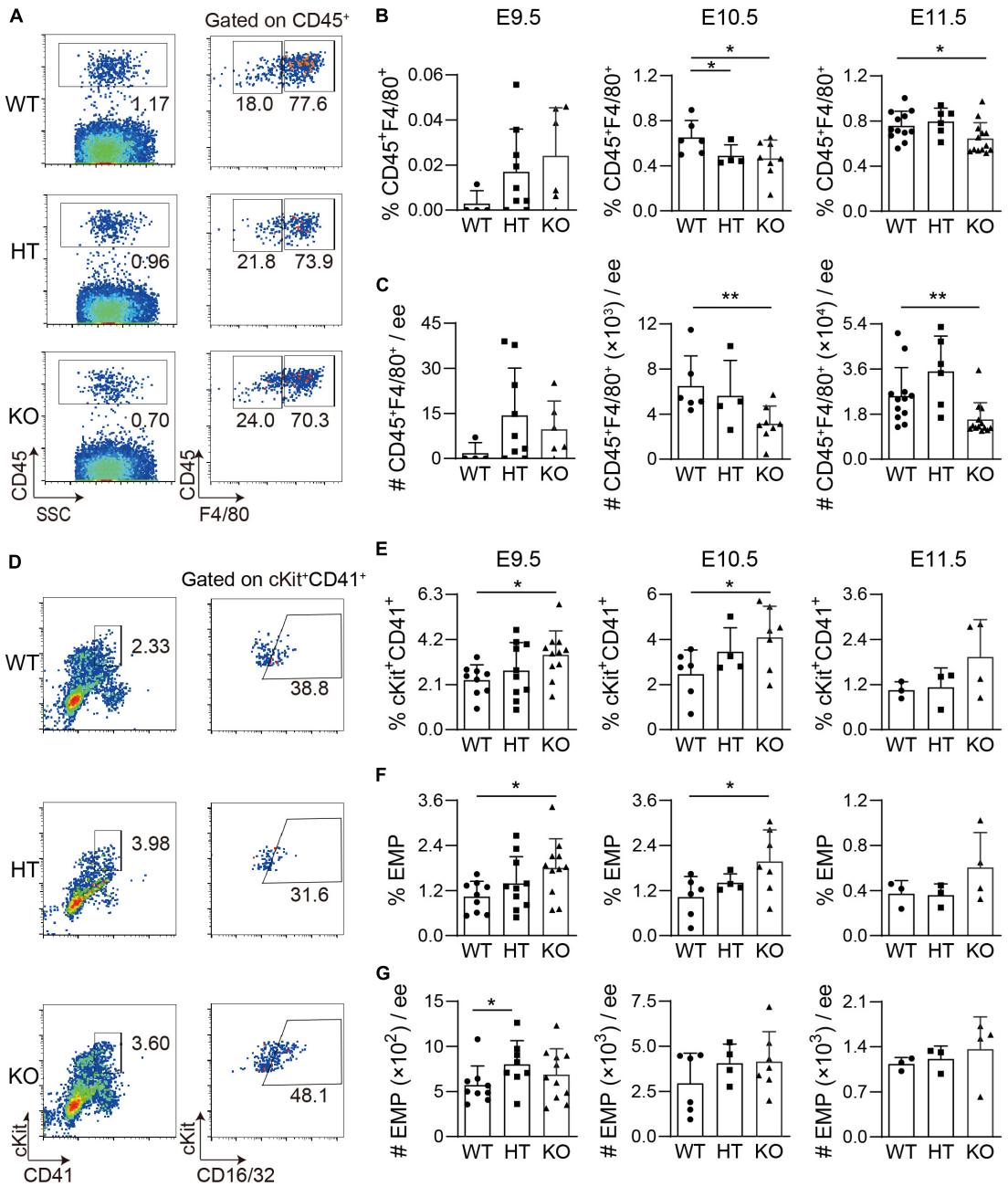

FIGURE 3 | The development of microglia and related cell population in the Wip1 ablation embryonic head/yolk sac. **(A)** Representative flow cytometry analysis of $CD45^+$ cells and $F4/80^+$ microglia of the E11.5 embryonic head. **(B)** The percentages of $CD45^+F4/80^+$ E9.5–E11.5 embryonic head. $^*p < 0.05$. **(C)** The absolute numbers of $F480^+CD45^+$ cells in E9.5–E11.5 embryonic head. E9.5, $n = 4$; E10.5, $n = 3$; E11.5, $n = 6$; $^{**}p < 0.01$. **(D)** Representative flow cytometry analysis of $ckit^+CD41^+$ cells and erythro-myeloid progenitors (EMPs) in the E9.5 yolk sac. **(E)** The percentages of $ckit^+CD41^+$ cells in the E9.5-E11.5 yolk sac. E9.5, $n = 5$; E10.5, $n = 3$; E11.5, $n = 3$; $^*p < 0.05$. **(F,G)** The percentages and absolute numbers of EMPs ($ckit^+CD41^+CD16/32^+$) in the E9.5–E11.5 yolk sac. E9.5, $n = 5$; E10.5, $n = 3$; E11.5, $n = 3$; $^*p < 0.05$.

the effects on EMPs in the yolk sac of Wip1 deletion by using the cocktail of cKit, CD41, and CD16/32. We found that Wip1 ablation increased the percentages of $cKit^+CD41^+$ cells (including HPCs) in the E9.5 (3.49 ± 0.33% vs. 2.31 ± 0.24%) and E10.5 (4.10 ± 0.52% vs. 2.47 ± 0.44%) but not in the E11.5 yolk sac (1.94 ± 0.49% vs. 1.05 ± 0.13%) (**Figures 3D,E**). Furthermore, the percentage of EMP ($cKit^+CD41^+CD16/32^+$) was enhanced at the same stage of yolk sac (E9.5: 1.80 ± 0.23% vs. 1.04 ± 0.14%, E10.5: 1.97 ± 0.32% vs. 1.03 ± 0.22%). However, the numbers of $c\text{-}Kit^+CD41^+$ cells and EMPs were

unchanged in the E9.5–E11.5 Wip1$^{-/-}$ yolk sac compared to WT (**Figures 3F,G** and **Supplementary Figure 3E**), possibly due to the reduction of total number. These data indicate that Wip1 is indeed involved in the EMP development of the yolk sac that might affect the migration of EMP in the yolk sac to the head, leading to the reduction of microglia.

Deletion of Wild-Type p53-Induced Phosphatase 1 Affects Pro-inflammatory Factor Expression in Microglia

To observe the morphology of microglia, immunostaining assays of cryosections were performed. There were fewer F4/80^{+} cells in Wip1$^{-/-}$ head sections, including round and non-round microglia cells, in line with flow cytometry analysis data (**Figures 3B,C**). Wip1 deletion appeared to change the morphology of microglia, which might be related to the immune function (**Figures 4A,B**). It is known that microglial cells positively regulate the hemogenic potential of ECs through pro-inflammatory factors in the embryo (Li et al., 2019). qRT-PCR was performed to check the expression of pro-inflammatory factors, such as interleukin-1α (*IL-1*α), *IL-1*β, *TNF*-α, and *IL-6*, of microglia (CD45^{+}F4/80^{+}CD11b^{+}, Mac)/mesenchymal cells (CD31^{-}CD45^{-}CD41^{-}, MCs) and their receptors of ECs (CD31^{+}CD41^{-}CD45^{-}, EC)/MC. The percentages of EC were comparable after Wip1 deficiency (**Figure 4C**). We found that the expression of pro-inflammatory factors (*IL-1*α, *IL-1*β, and *TNF*-α) appeared to be higher in the microglia of head compared to MC in the Wip$^{-/-}$ head, which is similar to the expression of most cognate receptors (**Figures 4D,E**). The expressions of *IL-1*β and *TNF*-α were significantly increased by >30% in Wip1$^{-/-}$ head compared with those in control (**Figure 4D**), although the mRNA levels of *IL-1*α and *IL-6* were unaltered in the Wip1$^{-/-}$ microglial cells. Interestingly, the receptors relevant to the *IL-1* and *TNF*-α pathways were not changed in the endothelial when Wip1 was ablated (**Figure 4E**). Unexpectedly, the expressions of pro-inflammatory factors (*IL-1*α, *IL-1*β, and *TNF*-α) were decreased in the macrophage of Wip1$^{-/-}$ yolk sac compared to WT but not in the MC fractions. The cognate receptors such as *IL1R2*, *IL1Rap*, and *TNFR2* were expressed less in the EC fraction; however, the expressions of *TNF1R1* and *TNFR2* were increased in the MC fractions of yolk sac (**Supplementary Figures 4A,B**). These different regulating effects of Wip1 on pro-inflammatory factor pathways between the head and the yolk sac indicate the specific regulatory mechanisms in distinct hematopoietic tissues. These results imply that Wip1 probably influences the secretion of pro-inflammatory factors from microglia, thereby affecting hematopoietic function.

DISCUSSION AND CONCLUSION

Here, we have identified a novel role for Wip1 in hematopoietic development in the embryonic head, expanding its known role in HSC development and differentiation (Liu et al., 2013; Chen et al., 2015; Yi et al., 2015). Wip1 influences the definitive HSPC function in the embryonic head, regulates the microglia numbers, and probably alters the secretion of the pro-inflammatory factor. Intriguingly, Wip1 is essential for EMPs but not for macrophage development (cell number) in the embryonic yolk sac. Although we do not precisely demonstrate Wip1 function in the specific cells because of mouse model limitation, we have found that Wip1 plays an important role in the embryonic head hematopoiesis. And, this is the first demonstration that Wip1 is a positive regulator of definitive HSPCs in the embryonic head.

Wild-Type p53-Induced Phosphatase 1 Regulates Hematopoietic Development in the Embryonic Head

As *Wip1* is expressed in the key cell types of hematopoietic development from a previous report (Zhou et al., 2016). Chen et al. (2015) have displayed that *Wip1* is highly expressed in adult bone marrow HSCs but decreased with age, exhibiting multifaceted HSC aging phenotype and impaired HSC activity. HSCs in E11.5–E12.5 embryonic head have a lower capacity of engraftment after Wip1 deletion, with increase of T/myeloid lineage output at the expense of B lymphoid cells, consistent with previous reports that Wip1 ablation impaired B-cell differentiation. Moreover, no transplantable HSCs were found in the E11.5 head region. Noticeably, less HSCs with lower engraftment ability were observed in the E12.5 head, which may be from or delayed functional HSC or other hematopoietic tissues *via* circulation. Wip1 knockout mice showed much less numbers of HPCs and hematopoietic cells by immune phenotype (CD41^{low}CD45^{-} and CD45^{+}, respectively) and functional assay (CFU-Cs) in the head of embryo at different time points as well as that in the yolk sac, AGM region, and fetal liver, respectively (He et al., 2021), indicating the time effects of Wip1 deletion on the development of distinct hematopoietic populations. Additionally, the reduction of total cell number is not the reason for the decrease in HPCs, since the CFU-Cs per cell number input were reduced dramatically in the E9.5 and E11.5 head at least.

Wild-Type p53-Induced Phosphatase 1 Is Efficient in Regulating Erythro-Myeloid Progenitor Formation

Erythro-myeloid progenitors identified by the specific surface markers are generated from ECs in the yolk sac, which also go through endothelial to hematopoietic cell transition (McGrath et al., 2015; Frame et al., 2016). Specific regulatory mechanisms are involved in the process compared to the AGM endothelial *trans*-differentiation. In our study, the number and percentage of macrophages were not affected by Wip1 deletion in the embryonic yolk sac, although the pro-inflammatory factor pathways were changed. Interestingly, we have found that Wip1 negatively regulated EMP proportions in the yolk sac. As expected, the absolute number of EMPs failed to be altered because of the reduction of total number, which was not in line with definitive HSPC phenotype (He et al., 2021). A possible explanation is that the expressions of hematopoietic transcription factors Runx1 and Gata2 are significantly increased in Wip1$^{-/-}$ yolk sac. Therefore, Wip1 regulates the EMP production from

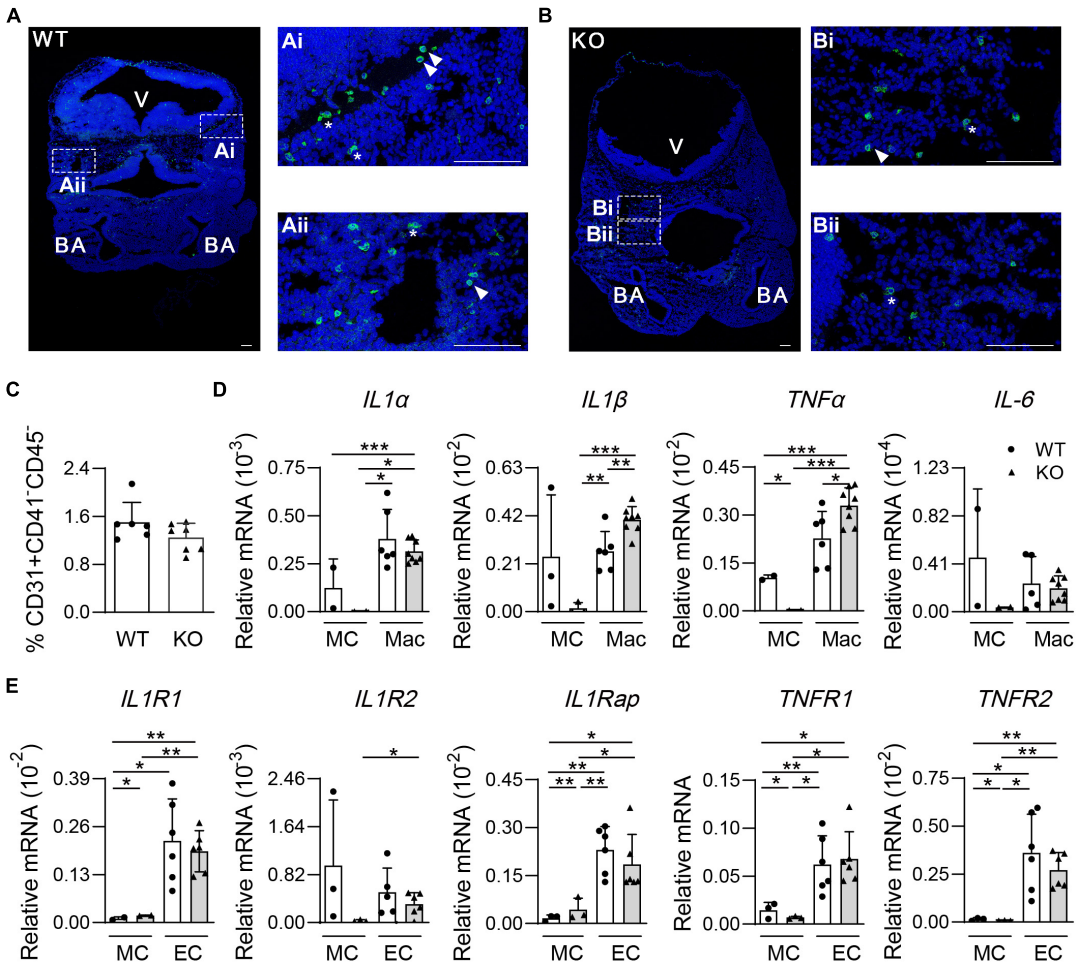

FIGURE 4 | The morphology of microglia and gene expression of pro-inflammatory pathways in the mouse embryonic head. **(A,B)** Representative confocal images of immunostaining by F4/80 (microglia) and Hoechst 33342 in the E11.5 head sections. Wild-type (WT) **(A)** 48 sp., knockout (KO) **(B)** 45 sp. Arrowhead indicated round microglia. Star indicated non-round microglia. V, ventricle; BA, branchial arches. Bar = 100 μm. **(C)** The percentages of endothelial cells ($CD31^+CD41^+CD45^-$, ECs) in the E11.5 embryonic head. $n = 4$. **(D)** Relative mRNA expression of *IL-1α*, *IL-1β*, *TNF-α*, and *IL-6* normalized to β-actin in the microglia ($CD45^+F4/80^+CD11b^+$, Mac) and mesenchymal cells ($CD31^-CD45^-CD41^-$, MCs) of the E11.5 head by qRT-PCR. $n \geq 2$; $^*p < 0.05$, $^{**}p < 0.01$, $^{***}p < 0.001$. **(E)** Relative mRNA expressions of *IL-1* and *TNF* receptor (*IL1R1*, *IL1R2*, *IL1Rap*, *TNFR1*, and *TNFR2*) in ECs ($CD31^+CD41^-CD45^-$) and mesenchymal cells ($CD31^-CD45^-CD41^-$, MCs) of the E11.5 head were determined by qRT-PCR. $n \geq 2$. $^*p < 0.05$, $^{**}p < 0.01$, $^{***}p < 0.001$.

yolk sac ECs in the embryo; however, the specific regulatory mechanisms need to be further investigated in the future.

Wild-Type p53-Induced Phosphatase 1 Influences Microglial Development

Head microglia are the only resident macrophages from yolk sac during hemostasis (Gomez Perdiguero et al., 2015; Li and Barres, 2018). Except microglia, it has been shown that yolk sac-derived EMPs also migrate to the embryonic fetal liver and other tissues (Hoeffel et al., 2015). We also found that Wip1 deletion resulted in a strong decrease of $CD45^+$ cells (mature hematopoietic cells and hematopoietic progenitor/stem cells) along with the dramatic reduction of microglia, contrasting to that in the AGM region and yolk sac (He et al., 2021) (data not shown), indicating that Wip1 is essential for microglial development. Along with the trend of EMP in the yolk sac, Wip1 might change the migration of EMP to influence microglia development. More details concerning their migration are worthy of further study.

Functional HSCs in the embryonic stage are educated *via* several processes including endothelial to hematopoietic cell transition and pro/pre-HSC maturation (Taoudi et al., 2008; Rybtsov et al., 2011, 2014). Wip1 indeed regulates pre-HSC maturation by cell cycle modulation in the AGM region. In the embryonic head, only single hematopoietic cell forms were attached to the vascular without classic "hematopoietic clusters" (Li et al., 2016; Iizuka et al., 2016), indicating the differences of hematopoietic niche. Pro-inflammatory factors derived from macrophages (including microglia) like *TNF-α*, interferon (IFN)-γ, *IL-1α*, and *IL-1β* made influences on hematopoietic cell formation of the aorta and head, partially dependent on the concentration (Li et al., 2014, 2019; Mariani et al., 2019).

In the Wip1 knockout head, the gene expression of pro-inflammatory factors on microglia was enhanced more than 30% compared with WT control; however, the existence of microglial cells failed to rescue the hematopoietic cell production of EC *in vitro* co-culture system (data not shown). There are some possible reasons, as follows: (1) The total number of microglia was reduced by more than 36% in the $Wip1^{-/-}$ head, which compensates for the increase of gene expression; (2) The dependence of concentration is difficult to control in the *in vitro* experiments; (3) Wip1 deletion in germ line cells, including other niche cells, resulted in a more severe phenotype *in vivo*.

In summary, our study provides an additional role for Wip1 in HSC and progenitor cell development in the embryonic head. Moreover, Wip1 indeed modulates microglia development, specially regulating the microglia-derived pro-inflammatory factors. Therefore, we have shown that Wip1 as a hematopoietic regulator, which may provide some theoretical and practical implications to support regenerative medicine.

MATERIALS AND METHODS

Animals

WT C57BL/6-Ly5.2 and $Wip1^{+/-}$ heterogeneous-Ly5.2 mice were used for timed matings, and C57BL/6-Ly5.1 mice (8–12 weeks) were used as transplantable recipients. *Wip1* mutant embryos were generated by crossing $Wip1^{+/-}$ males with $Wip1^{+/-}$ females. Embryos (E9.5–E12.5) were staged by counting somite pairs. Head and yolk sac were dissected, and tails were used for genotyping. Mice were housed in the animal facilities, and experimentation complied with the ethics committee of Southern Medical University.

Antibodies

CD41 (MWReg30), CD117 (2B8), CD45 (30-F11), and CD31 (MEC13.3) antibodies were purchased from BD Pharmingen. CD16/32 (93), 7-AAD, and Hoechst 33342 were purchased from Invitrogen, and F4/80 (BM8) and CD11b (M1/70) were purchased from BioLegend.

Hematopoietic Progenitor and Stem Cell Assays

Single-cell suspensions from head were plated into MethoCult GF M3434 with Cytokines (Stem Cell Technologies) for CFU-C assays. Hematopoietic colonies were counted after 10 days of culture and then calculated according to embryo equivalent (ee). BFU-Es, CFU-GMs, and CFU-Mixes were clarified in the total CFU-C counting. Cells from the embryonic head were injected intravenously into irradiated recipients (9.0 Gy Cobalt-60-irradiation, split dose). Peripheral blood was taken from recipients (at 4 and 16 weeks) for Ly5.1-/Ly5.2-specific flow cytometry analysis. Recipients were considered repopulated when $\geq$10% of cells were donor-derived.

Flow Cytometry Assay

Cells from the embryonic head or yolk sac, cultures, and adult hematopoietic tissues were stained by fluorescence conjugated antibodies for 30 min on ice. Sorted cells were collected for co-culture or in lysis buffer for RNA extraction. 7-AAD or Hoechst 33342 staining was performed for excluding dead cells. Flow cytometry analysis or sorting was performed on CytoFlex (Beckman Coulter), MoFlo XDP (Beckman Coulter), or Aria II (BD Biosciences). FACS data were analyzed with FlowJo software.

Immunostaining Assays

Dissected E11.5 embryos were fixed in 2% paraformaldehyde at 4°C for 30–60 minutes and embedded in OCT. And then embryos were equilibrated in 20% sucrose/phosphate buffered saline (PBS) at 4°C overnight and then embedded in Tissue Tek before freezing. Ten-micrometer cryosections were prepared. Endogenous biotin activity was blocked by Avidin/Biotin blocking kit. The fixed head sections were incubated with primary antibody (F4/80, D2S9R) or secondary antibody [Anti-Rabbit Alexa Fluor 488 IgG (H + L)] into PBS-block [PBS containing 0.05% Tween and 1% bovine serum albumin (BSA)] overnight and washed three times in PBS-T (PBS with 0.05% Tween). Samples were stained with Hoechst 33342 for 10 min at room temperature and then mounted with mounting buffer. Images were acquired with an inverted confocal microscope (Zeiss LSM 880) and processed using Zeiss Zen.

Gene Expression Analysis

RNA from sorted cells was extracted by using TRIzol reagent (Sigma) plus Glycogen (Macklin, China), and cDNA was reversed transcribed with HiScript III RT SuperMix (+gDNA wiper) for qPCR (Vazyme). Real-time PCR was performed by using ChamQ SYBR qPCR Master Mix (Vazyme) and detected on LightCycler 96 system (Roche). Sequences of primers were used according to a previous report (Li et al., 2019).

Statistical Analysis

All data are presented as mean ± SEM. Student's *t*-test was used for comparison of various groups. $p < 0.05$ was considered statistically significant.

DATA AVAILABILITY STATEMENT

The raw data supporting the conclusions of this article will be made available by the authors, without undue reservation.

ETHICS STATEMENT

The animal study was reviewed and approved by the Ethics Committee of Southern Medical University.

AUTHOR CONTRIBUTIONS

WH and YZ carried out the experiments, data collection, and analysis. ZC performed immunostaining. ZY helped in

genotyping. XL helped in the flow cytometry analysis. WP and JF gave material support. ZL and WH contributed to the study design and prepared the manuscript. All authors contributed to the article and approved the submitted version.

FUNDING

This work was supported by grants from the National Key Research and Development Program (2019YFA0801802 and 2019YFA0111100) and National Natural Science Foundation of China (82070105 and 81570095).

ACKNOWLEDGMENTS

We are grateful to L. A. Donehower from the Baylor College of Medicine for the *Wip1* knockout mice. We thank B. Liu and Y. Lan for kind discussion.

SUPPLEMENTARY MATERIAL

The Supplementary Material for this article can be found online at: https://www.frontiersin.org/articles/10.3389/fcell.2021.732527/full#supplementary-material

REFERENCES

Belova, G. I., Demidov, O. N., Fornace, A. J., and Bulavin, D. V. (2005). Chemical inhibition of Wip1 phosphatase contributes to suppression of tumorigenesis. *Cancer Biol. Ther.* 4, 1154–1158. doi: 10.4161/cbt.4.10.2204

Chen, M. J., Yokomizo, T., Zeigler, B. M., Dzierzak, E., and Speck, N. A. (2009). Runx1 is required for the endothelial to haematopoietic cell transition but not thereafter. *Nature* 457, 887–891. doi: 10.1038/nature07619

Chen, Z., Yi, W., Morita, Y., Wang, H., Cong, Y., Liu, J., et al. (2015). Wip1 deficiency impairs haematopoietic stem cell function via p53 and mTORC1 pathways. *Nat. Commun.* 6:6808. doi: 10.1038/ncomms7808

Choi, J., Nannenga, B., Demidov, O. N., Bulavin, D. V., Cooney, A., Brayton, C., et al. (2002). Mice deficient for the wild-type p53-induced phosphatase gene (Wip1) exhibit defects in reproductive organs, immune function, and cell cycle control. *Mol. Cell Biol.* 22, 1094–1105. doi: 10.1128/MCB.22.4.1094-1105.2002

Demidov, O. N., Timofeev, O., Lwin, H. N., Kek, C., Appella, E., and Bulavin, D. V. (2007). Wip1 phosphatase regulates p53-dependent apoptosis of stem cells and tumorigenesis in the mouse intestine. *Cell Stem Cell* 1, 180–190. doi: 10.1016/j.stem.2007.05.020

Dzierzak, E., and Bigas, A. (2018). Blood development: hematopoietic stem cell dependence and independence. *Cell Stem Cell* 22, 639–651. doi: 10.1016/j.stem.2018.04.015

Frame, J. M., Fegan, K. H., Conway, S. J., McGrath, K. E., and Palis, J. (2016). Definitive hematopoiesis in the yolk sac emerges from Wnt-Responsive hemogenic endothelium independently of circulation and arterial identity. *Stem Cells* 34, 431–444. doi: 10.1002/stem.2213

Gomez Perdiguero, E., Klapproth, K., Schulz, C., Busch, K., Azzoni, E., Crozet, L., et al. (2015). Tissue-resident macrophages originate from yolk-sac-derived erythro-myeloid progenitors. *Nature* 518, 547–551.

He, W., Wang, X., Ni, Y., Li, Z., Liu, W., Chang, Z., et al. (2021). Wip1 regulates hematopoietic stem cell development in the mouse embryo. *Haematologica* 106, 580–584. doi: 10.3324/haematol.2019.235481

Hoeffel, G., Chen, J., Lavin, Y., Low, D., Almeida, F. F., See, P., et al. (2015). C-Myb(+) erythro-myeloid progenitor-derived fetal monocytes give rise to adult tissue-resident macrophages. *Immunity* 42, 665–678. doi: 10.1016/j.immuni.2015.03.011

Hou, S., Li, Z., Zheng, X., Gao, Y., Dong, J., Ni, Y., et al. (2020). Embryonic endothelial evolution towards first hematopoietic stem cells revealed by single-cell transcriptomic and functional analyses. *Cell Res.* 30, 376–392. doi: 10.1038/s41422-020-0300-2

Howell, E. D., and Speck, N. A. (2020). Forks in the road to the first hematopoietic stem cells. *Cell Res.* 30, 457–458. doi: 10.1038/s41422-020-0331-8

Iizuka, K., Yokomizo, T., Watanabe, N., Tanaka, Y., Osato, M., Takaku, T., et al. (2016). Lack of phenotypical and morphological evidences of endothelial to hematopoietic transition in the murine embryonic head during hematopoietic stem cell emergence. *PLoS One* 11:e156427. doi: 10.1371/journal.pone.0156427

Kim, J. J., Lee, J. S., Moon, B. H., Lee, M. O., Song, S. H., Li, H., et al. (2010). Wip1-expressing feeder cells retain pluripotency of co-cultured mouse embryonic stem cells under leukemia inhibitory factor-deprivated condition. *Arch. Pharm. Res.* 33, 1253–1260. doi: 10.1007/s12272-010-0816-y

Li, Q., and Barres, B. A. (2018). Microglia and macrophages in brain homeostasis and disease. *Nat. Rev. Immunol.* 18, 225–242. doi: 10.1038/nri.2017.125

Li, Y., Esain, V., Teng, L., Xu, J., Kwan, W., Frost, I. M., et al. (2014). Inflammatory signaling regulates embryonic hematopoietic stem and progenitor cell production. *Genes Dev.* 28, 2597–2612. doi: 10.1101/gad.253302.114

Li, Z., Lan, Y., He, W., Chen, D., Wang, J., Zhou, F., et al. (2012). Mouse embryonic head as a site for hematopoietic stem cell development. *Cell Stem Cell* 11, 663–675. doi: 10.1016/j.stem.2012.07.004

Li, Z., Mariani, S. A., Rodriguez-Seoane, C., He, W., Ning, X., Liu, B., et al. (2019). A role for macrophages in hematopoiesis in the embryonic head. *Blood* 134, 1929–1940. doi: 10.1182/blood.2018881243

Li, Z., Vink, C. S., Mariani, S. A., and Dzierzak, E. (2016). Subregional localization and characterization of Ly6aGFP-expressing hematopoietic cells in the mouse embryonic head. *Dev. Biol.* 416, 34–41. doi: 10.1016/j.ydbio.2016.05.031

Liu, G., Hu, X., Sun, B., Yang, T., Shi, J., Zhang, L., et al. (2013). Phosphatase Wip1 negatively regulates neutrophil development through p38 MAPK-STAT1. *Blood* 121, 519–529. doi: 10.1182/blood-2012-05-432674

Mariani, S. A., Li, Z., Rice, S., Krieg, C., Fragkogianni, S., and Robinson, M., et al. (2019). Pro-inflammatory aorta-associated macrophages are involved in embryonic development of hematopoietic stem cells. *Immunity* 50, 1439–1452. doi: 10.1016/j.immuni.2019.05.003

McGrath, K. E., Frame, J. M., Fegan, K. H., Bowen, J. R., Conway, S. J., Catherman, S. C., et al. (2015). Distinct sources of hematopoietic progenitors emerge before HSCs and provide functional blood cells in the mammalian embryo. *Cell Rep.* 11, 1892–1904. doi: 10.1016/j.celrep.2015.05.036

Muller, A. M., Medvinsky, A., Strouboulis, J., Grosveld, F., and Dzierzak, E. (1994). Development of hematopoietic stem cell activity in the mouse embryo. *Immunity* 1, 291–301.

Rybtsov, S., Batsivari, A., Bilotkach, K., Paruzina, D., Senserrich, J., Nerushev, O., et al. (2014). Tracing the origin of the HSC hierarchy reveals an SCF-dependent, IL-3-independent CD43(-) embryonic precursor. *Stem Cell Rep.* 3, 489–501. doi: 10.1016/j.stemcr.2014.07.009

Rybtsov, S., Sobiesiak, M., Taoudi, S., Souilhol, C., Senserrich, J., Liakhovitskaia, A., et al. (2011). Hierarchical organization and early hematopoietic specification of the developing HSC lineage in the AGM region. *J. Exp. Med.* 208, 1305–1315. doi: 10.1084/jem.20102419

Solaimani Kartalaei, P., Yamada-Inagawa, T., Vink, C. S., de Pater, E., van der Linden, R., Marks-Bluth, J., et al. (2015). Whole-transcriptome analysis of endothelial to hematopoietic stem cell transition reveals a requirement for Gpr56 in HSC generation. *J. Exp. Med.* 212, 93–106.

Sun, B., Hu, X., Liu, G., Ma, B., Xu, Y., Yang, T., et al. (2014). Phosphatase Wip1 negatively regulates neutrophil migration and inflammation. *J. Immunol.* 192, 1184–1195. doi: 10.4049/jimmunol.1300656

Taoudi, S., Gonneau, C., Moore, K., Sheridan, J. M., Blackburn, C. C., Taylor, E., et al. (2008). Extensive hematopoietic stem cell generation in the AGM region

via maturation of VE-cadherin+CD45+ pre-definitive HSCs. *Cell Stem Cell* 3, 99–108.

Uyanik, B., Grigorash, B. B., Goloudina, A. R., and Demidov, O. N. (2017). DNA damage-induced phosphatase Wip1 in regulation of hematopoiesis, immune system and inflammation. *Cell Death Discov.* 3:17018. doi: 10.1038/cddiscovery.2017.18

Yi, W., Hu, X., Chen, Z., Liu, L., Tian, Y., Chen, H., et al. (2015). Phosphatase Wip1 controls antigen-independent B-cell development in a p53-dependent manner. *Blood* 126, 620–628. doi: 10.1182/blood-2015-02-624114

Yvernogeau, L., Klaus, A., Maas, J., Morin-Poulard, I., Weijts, B., Schulte-Merker, S., et al. (2020). Multispecies RNA tomography reveals regulators of hematopoietic stem cell birth in the embryonic aorta. *Blood* 136, 831–844. doi: 10.1371/journal.pone.0156427

Zhou, F., Li, X., Wang, W., Zhu, P., Zhou, J., He, W., et al. (2016). Tracing haematopoietic stem cell formation at single-cell resolution. *Nature* 533, 487–492. doi: 10.1038/nature17997

Zhu, Y. H., Zhang, C. W., Lu, L., Demidov, O. N., Sun, L., Yang, L., et al. (2009). Wip1 regulates the generation of new neural cells in the adult olfactory bulb through p53-dependent cell cycle control. *Stem Cells* 27, 1433–1442. doi: 10.1002/stem.65

Conflict of Interest: The authors declare that the research was conducted in the absence of any commercial or financial relationships that could be construed as a potential conflict of interest.

Publisher's Note: All claims expressed in this article are solely those of the authors and do not necessarily represent those of their affiliated organizations, or those of the publisher, the editors and the reviewers. Any product that may be evaluated in this article, or claim that may be made by its manufacturer, is not guaranteed or endorsed by the publisher.

frontiers in Cell and Developmental Biology

ORIGINAL RESEARCH
published: 13 October 2021
doi: 10.3389/fcell.2021.709923

Tpr Deficiency Disrupts Erythroid Maturation With Impaired Chromatin Condensation in Zebrafish Embryogenesis

Shuang Wu[1†], Kai Chen[1†], Tao Xu[1,2†], Ke Ma[1], Lei Gao[1], Cong Fu[1], Wenjuan Zhang[1], Changbin Jing[1], Chunguang Ren[1], Min Deng[1], Yi Chen[3], Yi Zhou[4], Weijun Pan[1] and Xiaoe Jia[1,5]**

[1] Shanghai Institute of Nutrition and Health, Chinese Academy of Sciences, Shanghai, China, [2] Central Laboratory, Qingdao Agricultural University, Qingdao, China, [3] State Key Laboratory for Medical Genomics, Shanghai Institute of Hematology, Ruijin Hospital, Shanghai Jiao Tong University School of Medicine, Shanghai, China, [4] Stem Cell Program, Hematology/Oncology Program at Children's Hospital Boston, Harvard Medical School, Boston, MA, United States, [5] Inner Mongolia Key Laboratory of Hypoxic Translational Medicine, Baotou Medical College, Baotou, China

OPEN ACCESS

Edited by:
Yiyue Zhang,
South China University of Technology, China

Reviewed by:
Rui Monteiro,
University of Birmingham, United Kingdom
Jing Liu,
Central South University, China
Alvin Ma,
Hong Kong Polytechnic University, Hong Kong, SAR China

***Correspondence:**
Weijun Pan
weijunpan@sibs.ac.cn
Xiaoe Jia
evangeline2004@163.com

† These authors have contributed equally to this work

Specialty section:
This article was submitted to Stem Cell Research, a section of the journal Frontiers in Cell and Developmental Biology

Received: *14 May 2021*
Accepted: *08 September 2021*
Published: *13 October 2021*

Citation:
Wu S, Chen K, Xu T, Ma K, Gao L, Fu C, Zhang W, Jing C, Ren C, Deng M, Chen Y, Zhou Y, Pan W and Jia X (2021) Tpr Deficiency Disrupts Erythroid Maturation With Impaired Chromatin Condensation in Zebrafish Embryogenesis. Front. Cell Dev. Biol. 9:709923. doi: 10.3389/fcell.2021.709923

Vertebrate erythropoiesis involves nuclear and chromatin condensation at the early stages of terminal differentiation, which is a unique process to distinguish mature erythrocytes from erythroblasts. However, the underlying mechanisms of chromatin condensation during erythrocyte maturation remain elusive. Here, we reported a novel zebrafish mutant^{cas7} with erythroid maturation deficiency. Positional cloning showed that a single base mutation in *tprb* gene, which encodes nucleoporin translocated promoter region (Tpr), is responsible for the disrupted erythroid maturation and upregulation of erythroid genes, including *ae1-globin* and *be1-globin*. Further investigation revealed that deficient erythropoiesis in *tprb*^{cas7} mutant was independent on HIF signaling pathway. The proportion of euchromatin was significantly increased, whereas the percentage of heterochromatin was markedly decreased in *tprb*^{cas7} mutant. In addition, *TPR* knockdown in human K562 cells also disrupted erythroid differentiation and dramatically elevated the expression of globin genes, which suggests that the functions of TPR in erythropoiesis are highly conserved in vertebrates. Taken together, this study revealed that Tpr played vital roles in chromatin condensation and gene regulation during erythroid maturation in vertebrates.

Keywords: erythrocytes, erythroid maturation, chromatin condensation, zebrafish, Tpr

INTRODUCTION

The zebrafish (*Danio rerio*) is a well-established model organism to study hematopoietic development due to its unique advantages (Jong and Zon, 2005; Paik and Zon, 2010). Similar to mammalian hematopoiesis, zebrafish hematopoiesis occurs in two distinct waves. The first primitive wave of hematopoiesis occurs in two different regions: the posterior lateral mesoderm that forms the intermediate cell mass later and the anterior lateral mesoderm, which generate primitive erythroid cells and myeloid cells, respectively (Chen and Zon, 2009; Paik and Zon, 2010). With the start of the heartbeat at 24 h post-fertilization (hpf), these primitive blood cells enter circulation throughout the embryo. The second definitive wave of hematopoiesis is characterized by the formation of self-renewing hematopoietic stem cells (HSCs) in the aorta–gonad–mesonephros

region (Bertrand et al., 2010; Kissa and Herbomel, 2010). Then the nascent HSCs migrate to the caudal hematopoietic tissue and colonize in kidney marrow finally (Murayama et al., 2006; Li et al., 2018).

Almost in all vertebrates, erythropoiesis is a stepwise process that involves differentiation of HSCs to committed burst forming unit-erythroid (BFU-E) followed by colony forming unit-erythroid (CFU-E) (Dzierzak and Philipsen, 2013; Palis, 2014). In terminal erythropoiesis, CFU-Es differentiate to mature erythrocytes and can be divided into four morphologically distinguishable cell types: proerythroblasts, basophilic erythroblasts, polychromatophilic erythroblasts, and orthochromatophilic erythroblasts (Schwartz, 2016). Also, many progressive characteristics are involved in terminal erythropoiesis including several cell divisions, decrease in cell size, nuclear and chromatin condensation, and extrusion of mitochondria and even the nucleus (Palis, 2014).

Although nuclear chromatin condensation is a common feature to define morphologically distinctive erythroblasts at different developmental stages, enucleation is unique to mammals, and nuclei are still retained in mature circulating erythrocytes in fish and avian (Ji et al., 2011). Chromatin condensation is also required for terminal erythropoiesis, as defects in this process are associated with anemia and myelodysplastic syndrome (Wickramasinghe and Wood, 2005; Menon and Ghaffari, 2021). Previous studies have identified several architectural factors including linker histone H5 and nuclear serpin MENT that promote avian erythroid chromatin condensation (Verreault and Thomas, 1993; Istomina et al., 2003). At the same time, histone deacetylation and caspase-3 are necessary for mammalian chromatin condensation (Zermati et al., 2001; Popova et al., 2009; Zhao et al., 2016). However, the detailed mechanisms of chromatin condensation are unclear.

Nucleoporin Tpr (translocated promoter region) is an architectural component of nuclear pore complex (NPC), which locates on the nucleoplasmic side of the pore to form a nuclear basket structure (Cordes et al., 1997; Krull et al., 2004). It exists as a homodimer *via* the N-terminal coiled-coil domain to be one of the eight basket filaments, whereas the C-terminal domain appears unfolded and flexible into the nucleus (Hase et al., 2001). Tpr has been implicated in a variety of nuclear functions, including chromatin organization and transcriptional regulation, nuclear transport, and mitosis. Megator (*Drosophila* Tpr) and its binding partner Nup153 have been shown to bind to 25% of the genome in continuous domains that are transcriptionally active (Vaquerizas et al., 2010). Also, Tpr was shown to be required for heterochromatin exclusion zones (HEZs) at nuclear pores after poliovirus infection (Krull et al., 2010) and maintain an open chromatin state favorable for HIV replication (Lelek et al., 2015). Recently, Tpr has been reported to be necessary for formation and maintenance of senescence-associated heterochromatin foci (SAHFs) during oncogenic Ras-induced senescence (Boumendil et al., 2019). However, Tpr-mediated chromatin organization during developmental processes *in vivo* remains uncertain.

In this study, we reported an essential role of Tpr in terminal erythropoiesis by characterizing a zebrafish mutant^{cas7} with a missense mutation in *tprb* gene. The homozygous *tprb* mutant manifested erythroid cell maturation blockage and abnormal erythroid gene expression. Tpr deficiency did not induce the activation of HIF signaling pathway, and *hif-2a* knockdown could not rescue abnormal erythroid phenotypes in *tprb*^{cas7} mutant. The elevated erythroid gene expression including *ae1-globin* and *be1-globin* in *tprb*^{cas7} mutants was due to their enhanced transcriptional activity, rather than the increased number of erythrocytes. Further investigation revealed that nuclear chromatin condensation and organization were strikingly disrupted specifically in erythrocytes in *tprb*^{cas7} mutant, but not in other tissue cells. In addition, in human K562 cells, *TPR* knockdown also caused blocking of erythroid differentiation and a dramatic increase in α globin and β globin gene expression, indicating that the function of TPR in erythropoiesis is highly conserved in mammalian. Our findings not only revealed the critical role of Tpr in chromatin condensation and gene regulation but also highlighted the importance of nuclear pore proteins in erythroid maturation.

RESULTS

Erythroid Maturation Is Disrupted in Zebrafish Mutant^{cas7}

In a large-scale ENU mutagenesis screen for erythroid development mutations, we obtained *cas7*, a novel mutant with erythrocyte development defects and recessive lethality. The mutant^{cas7} embryos were morphologically indistinguishable from wild-type siblings before 3 dpf, with normal blood flow and heart beats, and survived to about 6 dpf (**Figures 1A,B**). Whole-mount *in situ* hybridization (WISH) revealed that the expressions of erythroid markers (*ae1-globin*, *alas2*, and *band3*) were all increased abnormally (**Figures 1C–H**). Consistent with WISH analysis, real-time qPCR also showed the same result (**Figure 1L**). During the time course of α*e1-globin* WISH analysis, we did not detect any difference between sibling and mutant^{cas7} before 3 dpf (**Supplementary Figures 1A–D**). The marginal decrease of α*e1-globin* expression was detectable until 3 dpf (**Supplementary Figures 1E,F**), while the mutant^{cas7} embryos were morphologically distinguishable from wild-type siblings after 4 dpf.

Erythroid maturation is a stepwise process typically including dramatically decrease in cell size, and the N/C (nucleus-to-cytoplasm) ratio is a robust parameter for terminal differentiation, which had been reported previously (Fraser et al., 2007). Therefore, we can use the N/C ratio as a quantitative marker for erythroid maturation. Comparison of circulating erythrocytes from sibling and mutant^{cas7} embryos showed impaired maturation in the latter, for the latter contains more polychromatophilic erythroblasts while the former was abundant in orthochromatophilic erythroblasts at 4 dpf (**Figures 1I,J**; Qian et al., 2007). Also, the N/C ratio was higher in mutant^{cas7}, confirming the impaired erythrocyte maturation (**Figure 1K**).

To examine other hematopoietic lineages, we firstly performed WISH analysis of definitive hematopoietic cells markers including *cmyb* (hematopoietic stem and progenitor cell marker), *mpx* (granulocyte marker), *lyz* (macrophage

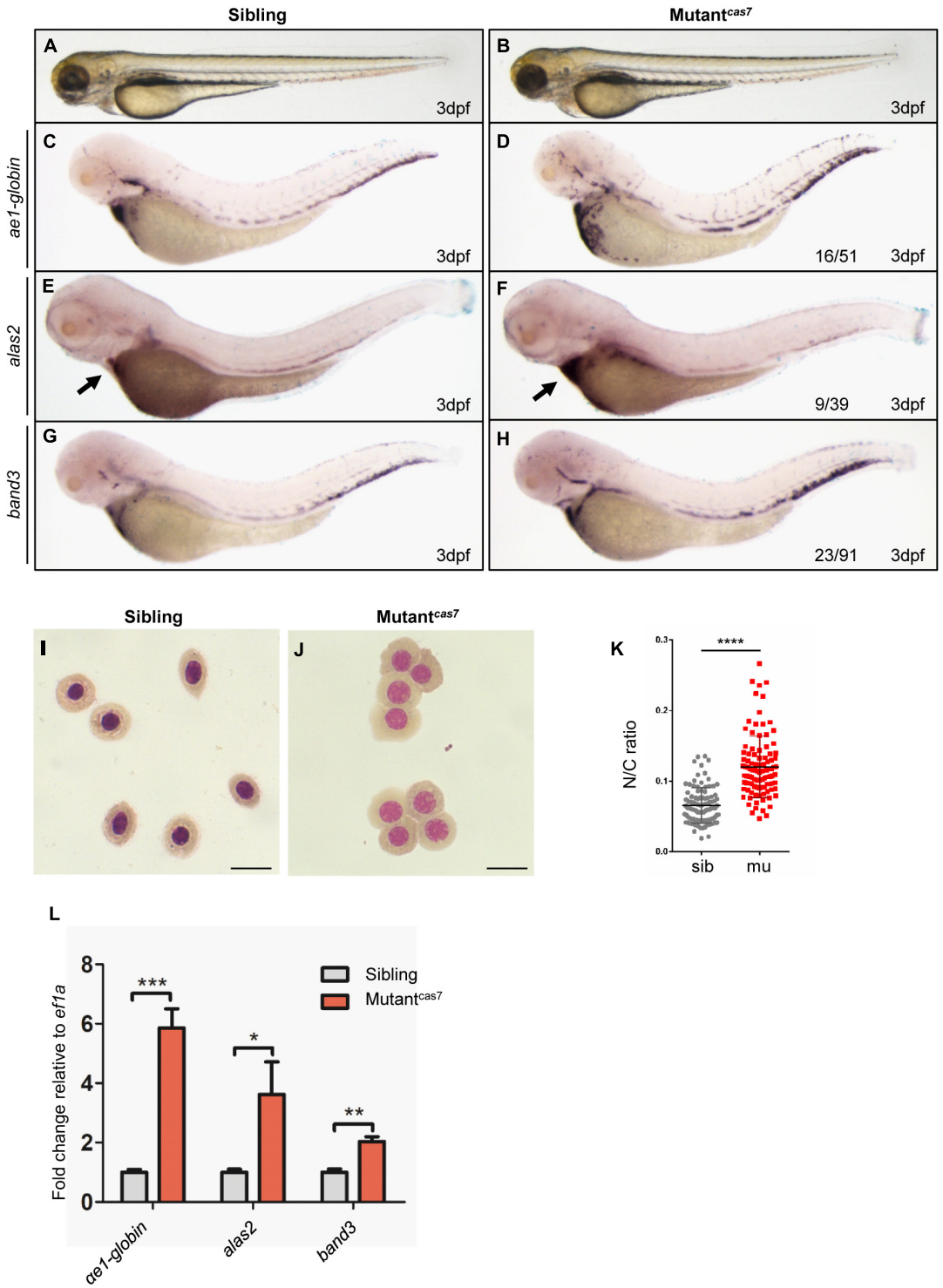

FIGURE 1 | Erythroid maturation is disrupted in zebrafish mutant^{cas7}. **(A,B)** Light microscope images of zebrafish wild-type (WT) sibling and mutant^{cas7} embryos at 3 dpf. **(C–H)** WISH analysis of *ae1-globin* **(C,D)**, *alas2* **(E,F)**, and *band3* **(G,H)** expression in sibling and mutant^{cas7} embryos at 3 dpf. After WISH and photographing, all embryos were extracted for genomic DNA and genotyped by sequencing, then the mutant percentage was evaluated. The number of embryos in a het-het incross clutch with the expression pattern is shown in the mutant^{cas7} column and corresponding percentages are listed inside each panel. Arrow in panel **(E,F)** indicates the *alas2* staining in heart region. **(I,J)** Giemsa staining for erythrocytes at 4 dpf in sibling and mutant^{cas7}. Relative to the number of orthochromatophilic erythroblasts, mutant^{cas7} displayed a marked increase in circulating polychromatophilic erythroblasts compared with sibling. Scale bars represent 10 μm. **(K)** Statistical analysis of the nucleus-to-cytoplasm (N/C) ratio in sibling and mutant^{cas7}. $N = 100$, error bars represent SEM. ****$p \leq 0.0001$. **(L)** The relative expression of *αe1-globin*, *alas2*, *band3* in sibling and mutant^{cas7} embryos at 3 dpf. Error bars represent SEM. *$p \leq 0.05$; **$p \leq 0.01$; *** $p \leq 0.001$.

marker), and *rag-1* (lymphocyte marker). The expression of these markers was identical between sibling and mutant^{cas7} at 3 or 4 dpf, which indicated that the definitive hematopoiesis was normal (**Supplementary Figures 2A–H**). Consistent with WISH results, the real-time qPCR suggested that the expressions of these definitive hematopoietic cell markers (*cmyb, mpo, lyz*, and *rag-1*) were unchanged (**Supplementary Figure 2I**). However, the expression levels of erythroid genes were not all increased, such as *sdhb*, *fth1a* (iron-related protein gene), and *hebp2* (heme binding protein gene) (**Supplementary Figure 2I**). Then, we investigated the primitive hematopoiesis and vascular morphogenesis in mutant^{cas7}. WISH analysis showed that the expression of *scl* (hematopoietic progenitor marker), *gata1* (erythrocyte progenitor marker), *pu.1* (myeloid progenitor marker), *mpx*, and *kdrl* (endothelial cell marker) were also normal in mutant^{cas7} at 22 or 26 hpf (**Supplementary Figure 3**). Taken together, these results suggested that erythroid maturation was specifically disrupted in zebrafish mutant^{cas7}.

Positional Cloning in Zebrafish Mutant^{cas7}

To elucidate the mechanism of erythroid maturation failure in mutant^{cas7}, we carried out positional cloning. The mutant^{cas7} was first mapped on chromosome 20 by bulk segregation analysis (BSA). A high-resolution sequence length polymorphism (SSLP)–based mapping approach established the mutation within a 225-kb region between two markers 294-04 and 297-01 (**Figure 2A**). After sequencing all three candidate genes in this region, we found a C to G missense mutation in *tprb* gene in mutant^{cas7} (**Figure 2B**). Also, genomic sequencing of *tprb* gene also confirmed this result. This mutation yielded the leucine to valine at ninth amino acid (L9V) of Tpr protein and the leucine was highly conserved from human to fruit fly (**Figure 2C**). Among five commonly used laboratory zebrafish strains (Tu, WIK, AB, Shanghai, and Longfin), this point mutation was not found (**Supplementary Figure 4**), excluding the possibility of single-nucleotide polymorphism (SNP). The *tprb* locus on zebrafish chromosome 20 is syntenic to a region of human chromosome 1 that contains the *TPR* gene, based on the conserved location of neighboring orthologous gene pairs (*PRG4*, *PDC*, *PTGS2*, *PLA2G4A*, and *HMCN1*), suggesting that zebrafish *tprb* gene is an ortholog of human *TPR* (**Figure 2D**).

To explore the consequence of the point mutation to *tprb* gene, we customized an anti-Tpr antibody to examine the endogenous Tpr protein level. Western blot results showed that the expression of Tpr protein was markedly decreased over time in mutant^{cas7}, and became undetectable at 5 dpf, suggesting that this point mutation may disrupt the function of *tprb* gene (**Figure 2E**).

Missense Mutation in *tprb* Gene Is Responsible for Mutant^{cas7}

To confirm the point mutation in *tprb* gene is responsible for mutant^{cas7} phenotypes, we injected a validated *tprb* ATG morpholino (MO) into one-cell-stage wild-type embryos to block the translation of endogenous *tprb* mRNA. Also, immunoblotting analysis confirmed the Tpr protein was poorly detectable in *tprb* morphants (**Supplementary Figure 5A**). WISH results showed that erythroid markers including *ae1-globin*, *alas2*, and *band3* were all upregulated (**Figures 3A–F**), while the other hematopoietic lineages were barely unchanged in *tprb* morphants (**Supplementary Figures 5B–I**). Consistent with WISH results, the real-time qPCR suggested the expression levels of *ae1-globin*, *alas2*, and *band3* were all enhanced, while other definitive hematopoietic cell markers (*cmyb, mpo, lyz, rag*, and *kdrl*) were unchanged (**Supplementary Figure 5J**).

To check whether and when the erythroid maturation was impaired, we have performed a different time course of Giemsa staining in circulating erythroid cells in control and *tprb* morphants. The result showed that before 2 dpf, the N/C ratio was not significantly changed between control and *tprb* morphants. Beginning at 3 dpf, the N/C ratio of *tprb* morphants was obviously increased, indicating that erythroid cell differentiation was inhibited from 3 dpf (**Supplementary Figure 6B**). The bigger nuclear area in erythroid cells and immature erythrocytes in *tprb* morphants could be observed at 3 and 4 dpf (**Supplementary Figures 6A,C–J**). Together with these data, Giemsa staining showed more immature erythrocytes in *tprb* morphants by morphological assessment and nucleo-cytoplasmic ratio computation (**Figures 3G–I**), indicating impaired erythroblast maturation in *tprb* morphants.

To further demonstrate our findings, rescue assay was performed by ectopic expression of wild-type *tprb* under the *ubiquitin* promoter in mutant^{cas7} (**Figure 3J**). The result showed that when Tpr protein was rescued in *tprb* mutants, the upregulated erythroid markers could be also largely rescued by wild-type *tprb* overexpression (**Figures 3K–M** and **Supplementary Figure 7**).

Moreover, we generated a second zebrafish *tprb*$^{-3+1}$ mutant by CRISPR-Cas9, which carried a frameshift mutation and premature stop codon in exon 7 and led to a truncated Tpr protein (**Figures 3N,O**). Consistent with phenotype of mutant^{cas7}, the embryonic development of *tprb*$^{-3+1}$ mutant was normal before 3 dpf but died at 5–6 dpf, and WISH analysis of *ae1-globin* level was also significantly increased (**Figures 3P,Q**). Thus, results from MO phenocopy assay, wild-type *tprb* rescue assay, and same phenotype of *tprb*$^{-3+1}$ mutant strongly suggested that the C-to-G mutation led to *tprb* gene loss of function, which was causative for phenotype of mutant^{cas7}. Hence, we rename the mutant as *tprb*^{cas7}.

Given that Tpr is a structural protein that exists in every cell theoretically, we examined the temporal and spatial expression of *tprb* by WISH analysis. The result showed that *tprb* transcript was expressed as maternal mRNA and ubiquitously expressed during zebrafish embryogenesis (**Supplementary Figure 8**). To answer whether the localization of Tpr is in erythroid cells, we performed the Tpr immunofluorescence in *tprb* mutants and morphant erythroid cells at 3 dpf (**Supplementary Figure 9**). In erythroid cells from sibling and control morphant, Tpr protein is indeed located on the nuclear membrane (**Supplementary Figures 9A,B,E,F**). While in *tprb* mutants and morphants there was no fluorescence signal of Tpr protein in erythroid cells (**Supplementary Figures 9C,D,G,H**), indicating the endogenous

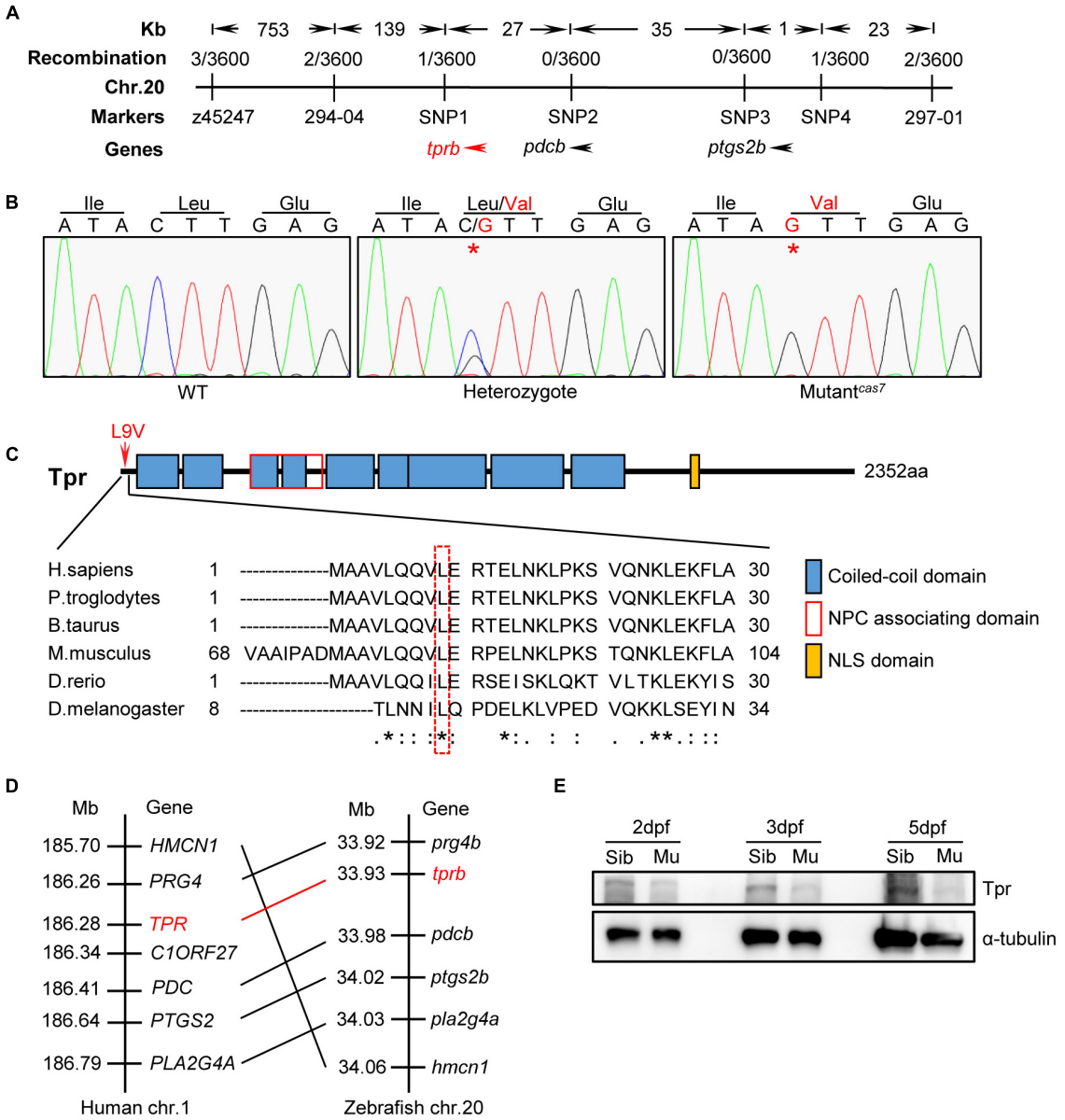

FIGURE 2 | Positional cloning of mutant^{cas7}. **(A)** Genetic mapping of the *cas7* region on chromosome 20. Bulk segregation analysis positioned *cas7* mutation to Chr. 20. Fine mapping using SSLPs narrowed down the region between markers SNP1 and SNP4, including *tprb* and two other genes as indicated. **(B)** There is a C-to-G missense mutation in *tprb* gene in mutant^{cas7}, which leads to leucine to valine (L9V) at ninth amino acid in Tpr protein. **(C)** The ninth amino acid leucine of Tpr is highly conserved from human to fruit fly (* marked). **(D)** Comparison of the gene syntenic relationship between zebrafish *tprb* and human *TPR* loci. Seven genes, including *TPR*, are located within a genomic region on human chromosome 1. (Right) Seven zebrafish homologs of these genes are listed according to their map positions on chromosome 20 (Ensembl website). Mb, mega base. **(E)** Western blotting images of Tpr protein in whole embryo lysates of sibling and mutant^{cas7} embryos at the indicated time. All embryos were extracted for genomic DNA and genotyped by sequencing.

Tpr protein was missing in *tprb* mutant or morphant, consisting with the WB result in **Figure 2E**.

The Phenotype of *tprb*^{cas7} Mutant Is Independent on HIF Signaling Pathway

It has been reported that HIF signaling pathway plays an important role in erythropoiesis, especially in erythrocytosis (Lee and Percy, 2011). Von Hippel-Lindau tumor suppressor (VHL) was the negative regulator of HIFs. The zebrafish *vhl* mutant displayed a hypoxia response, severe polycythemia, and immature erythropoiesis (van Rooijen et al., 2009). Also, results revealed global upregulation of both red and white hematopoietic lineages. Interestingly, we found that the phenotype of upregulation of erythroid genes and immature erythrocytes in *tprb*^{cas7} mutant was similar to reported *vhl*

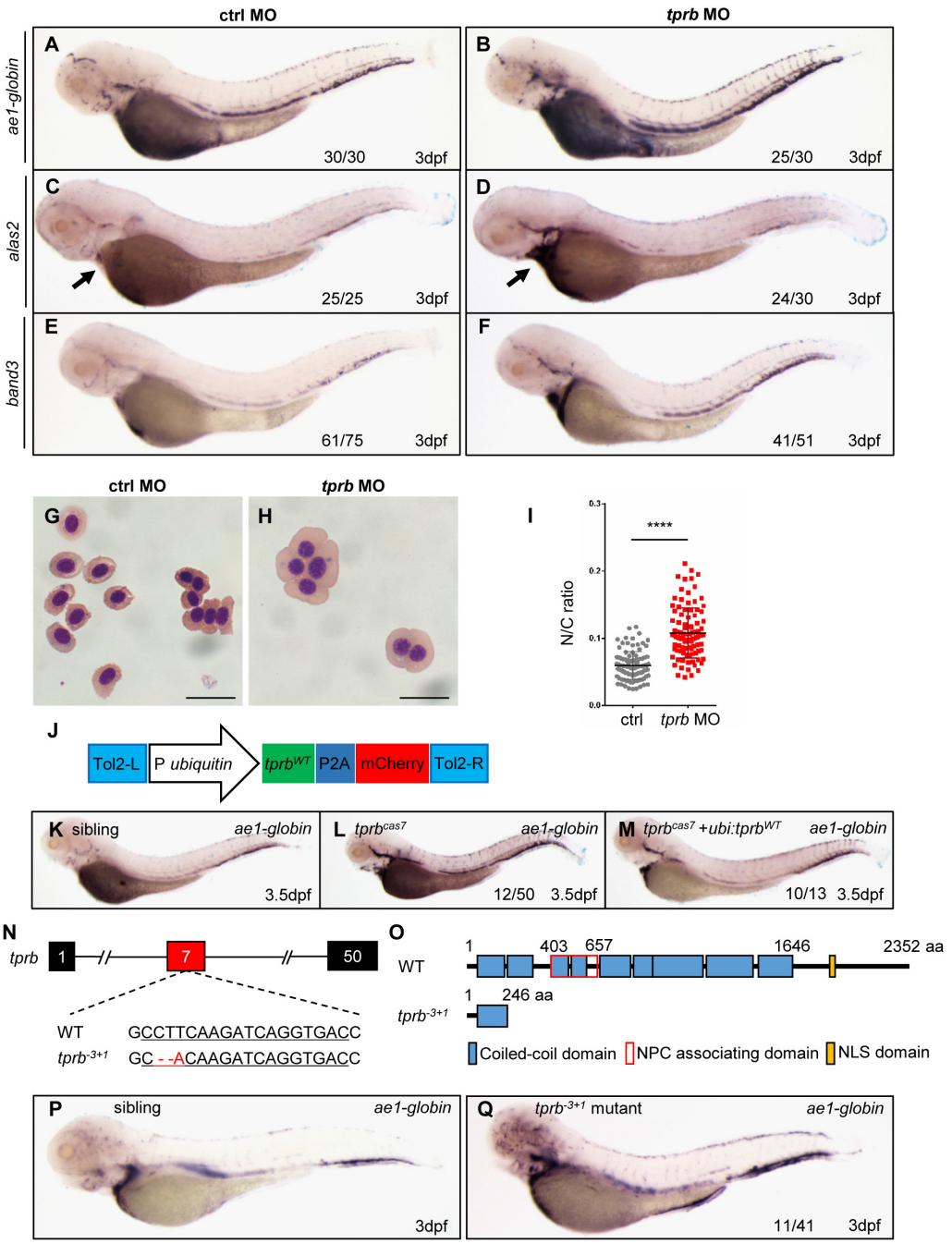

FIGURE 3 | Mutation in *tprb* gene is responsible for mutant^{cas7} phenotypes. **(A–I)** Morpholino knocking down of *tprb* mutant^{cas7} phenocopies. WISH results of *ae1-globin* **(A,B)**, *alas2* **(C,D)**, and *band3* **(E,F)** expression in control and *tprb* morphants at 3 dpf. The percentages of indicated phenotype are listed at the bottom of each panel. Arrow in panel **(E,F)** indicates the *alas2* staining in heart region. **(G,H)** Giemsa staining for erythrocytes at 4 dpf in control and *tprb* morphants. More immature erythrocytes in *tprb* morphants are shown. Scale bars represent 10 μm. **(I)** Statistical analysis of the nucleus-to-cytoplasm (N/C) ratio in control and *tprb* morphants. $N = 100$, error bars represent SEM. ****$p < 0.0001$. **(J)** Construction of the plasmid used in Tol2-transposease-mediated rescue assay. **(K–M)** WISH analysis of *ae1-globin* expression in sibling, *tprb*^{cas7} mutants, and rescued embryos at 3.5 dpf. After WISH and photographing, all embryos were extracted for genomic DNA and genotyped by sequencing, then the rescue percentage was evaluated. The percentage of fully rescued mutant embryos is about 77% (10 out of 13 mutant embryos), while the rest are rescued partially. **(N,O)** Generation of *tprb*$^{-3+1}$ mutant *via* CRISPR-Cas9 technique. The alignment of WT and mutated sequences is listed. The underlined sequence is gRNA target site. The sequencing result of *tprb* genomic DNA shows a 3-bp deletion and 1-bp addition at exon 7 **(N)**, which caused a premature stop codon leading to the production of a truncated 246-amino-acid Tpr protein **(O)**. **(P,Q)** WISH results of *ae1-globin* expression in sibling and *tprb*$^{-3+1}$ mutant at 3 dpf. After WISH and photographing, all embryos were extracted for genomic DNA and genotyped by sequencing, then the mutant percentage was evaluated. The number of embryos in *tprb*$^{-3+1}$ mutant incross clutch with the expression pattern as shown in the *tprb*$^{-3+1}$ column and corresponding percentages are listed inside each panel.

zebrafish mutant. Therefore, to reveal the molecular mechanism of erythroid maturation defect in *tprb*^{cas7} mutant, we explored whether the HIF signaling pathway was activated. First, flow cytometry analysis showed that the number of erythrocytes was not significantly changed in *tprb* morphants compared with control (**Figure 4A** and **Supplementary Figure 10**). Also, mRNA levels of *epo*, a HIF target gene involved in erythropoiesis (Bunn, 2013), and *vegfaa* were not elevated in *tprb* morphants (**Figure 4B**).

Furthermore, to compare the difference of phenotype in *tprb*^{cas7} mutant with embryos activated by HIF signaling, we established a *vhl* mutant by CRISPR-Cas9 as our positive control (**Supplementary Figures 11A,B**). To our surprise, WISH result of *ae1-globin* level was much more increased in *vhl* mutant than *tprb*^{cas7} mutant (**Supplementary Figures 11C,D**). Given that HIF-2a is mainly involved in the regulation of polycythemia (Lee and Percy, 2011; Metelo et al., 2015), we considered rescue experiment to alleviate the degree of polycythemia by using zebrafish *hif-2a* MO. WISH results showed that *hif-2a* MO could partially rescue the increased expression of *ae1-globin* in *vhl* mutant, which indicated the effectiveness of the *hif-2a* MO (**Supplementary Figures 11E,F**), but not in *tprb*^{cas7} mutant (**Figures 4C–F**). These results suggested that loss of *tprb* gene most likely did not cause the activation of HIF signal pathway.

Previous studies have demonstrated that HIF-1a protein is stabilized and enters the nucleus under hypoxic conditions, which is essential for hypoxic response (Koh and Powis, 2012). To further directly confirm whether loss of Tpr protein could result in the activation of HIF signaling, we analyzed the accumulation of HIF-1a protein and the expression of HIF target genes in human cultured cells under hypoxia condition. Western blot analysis in HEK293T cells showed that neither the amount of HIF-1a protein from whole cells nor nucleus was barely changed as *TPR* knock-down (**Figures 4G,H**). At the same time, the expression of several important HIF target genes including *PDK1*, *PGK1*, and *VEGF* also showed no significant change with or without TPR protein (**Figure 4I**). Similarly, we tested in human hepatocyte Hep3B cells and designed *VHL* siRNA as the positive control. Under hypoxic conditions, knocking down *VHL* could upregulate the expression of *EPO* and *VEGF* dramatically, whereas knocking down *TPR* had no significant change (**Figure 4J**). Collectively, the defective erythroid phenotype of *tprb*^{cas7} mutant was indeed independent on the activation of HIF signaling.

Loss of Tpr Protein Enhances the Transcriptional Activity of Erythroid Genes

As described previously, the number of erythrocytes in *tprb*^{cas7} mutant did not alter, leading us to investigate whether the increased staining of erythroid markers by WISH analysis in *tprb*^{cas7} mutant was caused by the upregulation of genes in every erythrocyte. To test this hypothesis, we injected the control and *tprb* MO into one-cell-stage embryos of Tg(gata1: DsRed) transgenic line separately. Then we sorted the same number of erythrocytes through *Tg(gata1: DsRed)* transgenic line and carried out real-time qPCR to analyze the expression levels of erythroid genes. As expected, the *ae1-globin* and *be1-globin* expression levels were dramatically increased in *tprb* morphants, especially for *ae1-globin* (**Figure 5A**).

To determine how Tpr deficiency triggered erythroid genes expression abnormally, we checked the transcriptional activity of these genes by quantitative chromatin immunoprecipitation (qChIP) experiment through RNA polymerase II (Pol II) antibody. ChIP results showed that the relative abundance of Pol II in the promoter region of *ae1-globin* and *be1-globin* in *tprb* morphants was dramatically higher than that of in control morphants (**Figure 5B**).

In yeast, Mlp1 and Mlp2 proteins (ortholog of mammalian Tpr protein) contribute to RNA surveillance by retention of unspliced mRNA in nucleus (Green et al., 2003; Galy et al., 2004) and downregulate gene expression in response to mRNA export defect (Vinciguerra et al., 2005). To analyze whether the mRNA export is blocked in erythrocytes in *tprb*^{cas7} mutant, we tested the cellular localization of *ae1-globin* mRNA. Fluorescent *in situ* hybridization result showed that the *ae1-globin* mRNA was exported out of the nucleus normally and distributed throughout the cytoplasm in both sibling and *tprb*^{cas7} mutant, indicating the mRNA export was normal (**Figure 5C**). These results taken together suggested that loss of Tpr can upregulate erythroid genes expression by enhancing their transcriptional activity, rather than the number of erythrocytes.

Chromatin Condensation Defects Within Erythroid Nuclei in *tprb*^{cas7} Mutant

Chromatin condensation is essential for terminal erythropoiesis and erythroid maturation. To further explore how Tpr regulate the transcriptional activity of erythroid genes, we performed transmission electron microscopy to analyze the ultrastructural changes in the nucleus. It was found that at 4 dpf, there were distinct heterochromatin regions in most of the nuclei of erythrocytes in siblings, and the separation between euchromatin and heterochromatin was obvious (**Figures 6A–C**). Also, in *tprb*^{cas7} mutant, the boundary between them was hard to define precisely, presenting a "homogeneous" chromatin state (**Figures 6D–F**). Relying on the chromatin aggregation degree within the nuclei of erythrocytes, statistical analysis result showed that the proportion of euchromatin was significantly increased, whereas the heterochromatin percentage markedly decreased in *tprb*^{cas7} mutant (**Figure 6G**). Moreover, we also found the disruption of HEZs near NPCs in *tprb*^{cas7} mutant as previously reported (Krull et al., 2010). The aforementioned results indicated that the chromatin condensation in erythroid cells was impaired in *tprb*^{cas7} mutant.

Given Tpr is a structural protein, we analyzed chromatin structures in other tissue cells to test whether chromatin organization abnormality was a common phenomenon. The results showed that such heterochromatin blockage surprisingly only existed in erythrocytes and some hematopoietic cells, not in other tissue cells, such as neural cells, endothelial cells, and

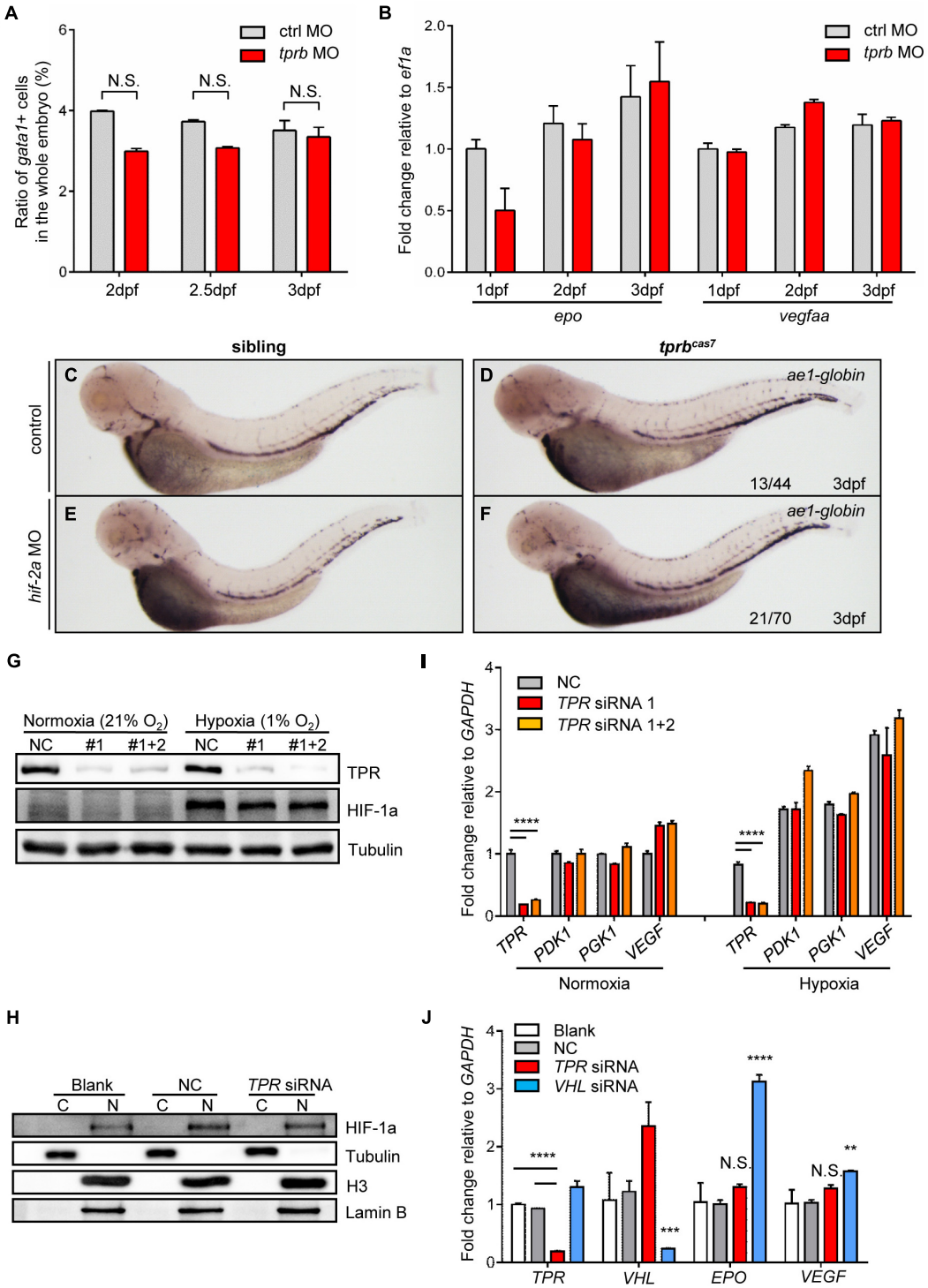

FIGURE 4 | HIF signaling is not activated in *tprb*^{cas7} mutant. **(A)** The statistic results of the ratio of *gata1*$^{+}$ cells sorted by flow cytometer in the whole embryo of control and *tprb* morphants by *Tg(gata1: DsRed; kdrl: EGFP)* transgenic line at different time points. **(B)** Quantitative PCR results of *epo* and *vegfaa* in control and *tprb* morphants at different time points. **(C–F)** WISH analysis of *ae1-globin* expression in sibling and *tprb*^{cas7} mutants at 3 dpf under the control and *hif-2a* morpholino **(E,F)** injection. **(G)** Immunoblotting analysis of TPR and HIF-1a protein level in whole HEK293T cells under normoxia and hypoxia conditions during *TPR* knockdown through siRNA. **(H)** Immunoblotting analysis of HIF-1a protein level in the nuclei of HEK293T cells under hypoxia condition after nuclear and cytoplasmic separation. C, cytoplasma; N, nucleus. **(I)** Quantitative PCR results of HIF target genes including *TPR, PDK1, PGK1*, and *VEGF* in HEK293T cells during *TPR* knockdown through siRNA. **(J)** Quantitative PCR results of HIF target genes including *EPO* and *VEGF* in Hep3B cells during *TPR* or *VHL* knockdown through siRNA under hypoxia condition. NC: negative control. #1: TPR siRNA 1; #1 + 2: TPR siRNA 1 + 2. Error bars represent SEM. N.S.: not significant; $^{**}p \leq 0.01$; $^{***}p \leq 0.001$; $^{****}p \leq 0.0001$.

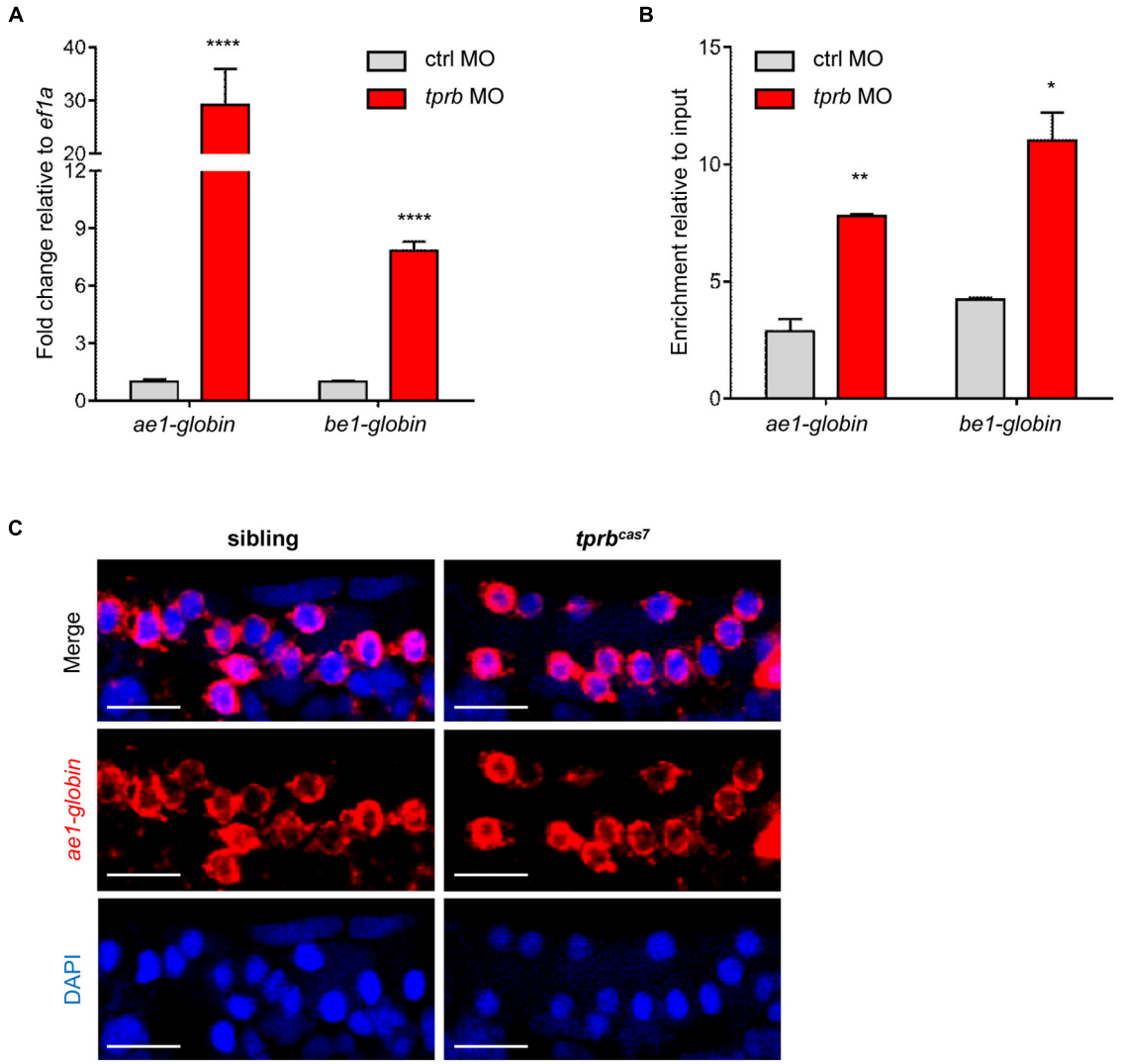

FIGURE 5 | *tprb* inactivation enhances the transcriptional activity of erythroid genes. **(A)** Quantitative PCR results of *ae1-globin*, *be1-globin*, and *alas2* in erythrocytes after sorting an equal number of *gata1*$^{+}$ cells in control and *tprb* morphants at 3 dpf. **(B)** Quantitative qChIP results of the binding enrichment of RNA polymerase II (Pol II) in *ae1-globin*, *be1-globin*, and *alas2* after sorting equal number of *gata1*$^{+}$ cells. **(C)** Fluorescence *in situ* hybridization (FISH) results of *ae1-globin* mRNA localization in sibling and *tprb*^{cas7} mutants at 3 dpf. The nuclei were stained with DAPI (blue). Error bars represent SEM. N.S., not significant; $^{*}p < 0.05$; $^{**}p < 0.01$; $^{****}p < 0.0001$. Scale bars represent 20 μm.

skeletal muscular cells (**Supplementary Figure 12**). Also, there was no significant difference in chromatin morphology in those tissue cells between sibling and *tprb*^{cas7} mutant (**Supplementary Figure 12**). Overall, these results suggested that Tpr deficiency might specifically disrupt the chromatin condensation and later on maturation in erythrocytes.

TPR Is Also Important for Erythroid Differentiation in Humans

To test whether Tpr is also important for mammalian hematopoiesis, we knocked down *TPR* in human K562 cells (**Supplementary Figure 13**). The *TPR* shRNA efficiently knocked down TPR expression (**Supplementary Figures 13A,B**). The K562 line is composed of undifferentiated blast cells that are rich in glycophorin and may be induced to produce fetal and embryonic hemoglobin in the presence of hemin. The K562 cell membrane glycoproteins show many similarities with that of erythrocytes and, in particular, the cells synthesize glycophorin A (CD235a, also named GPA), which is found exclusively in human erythrocytes (Drexler et al., 2004). Therefore, the K562 cell appears to be an excellent tool for the study of human erythroid differentiation and globin gene expression.

We induced K562 erythroid differentiation by treated with hemin, to find TPR functions in erythroid differentiation. Expression of the glycophorin A (CD235a) on the surface of K562 cells was determined by direct immunofluorescence staining and flow cytometer. When treated with hemin for 48 h,

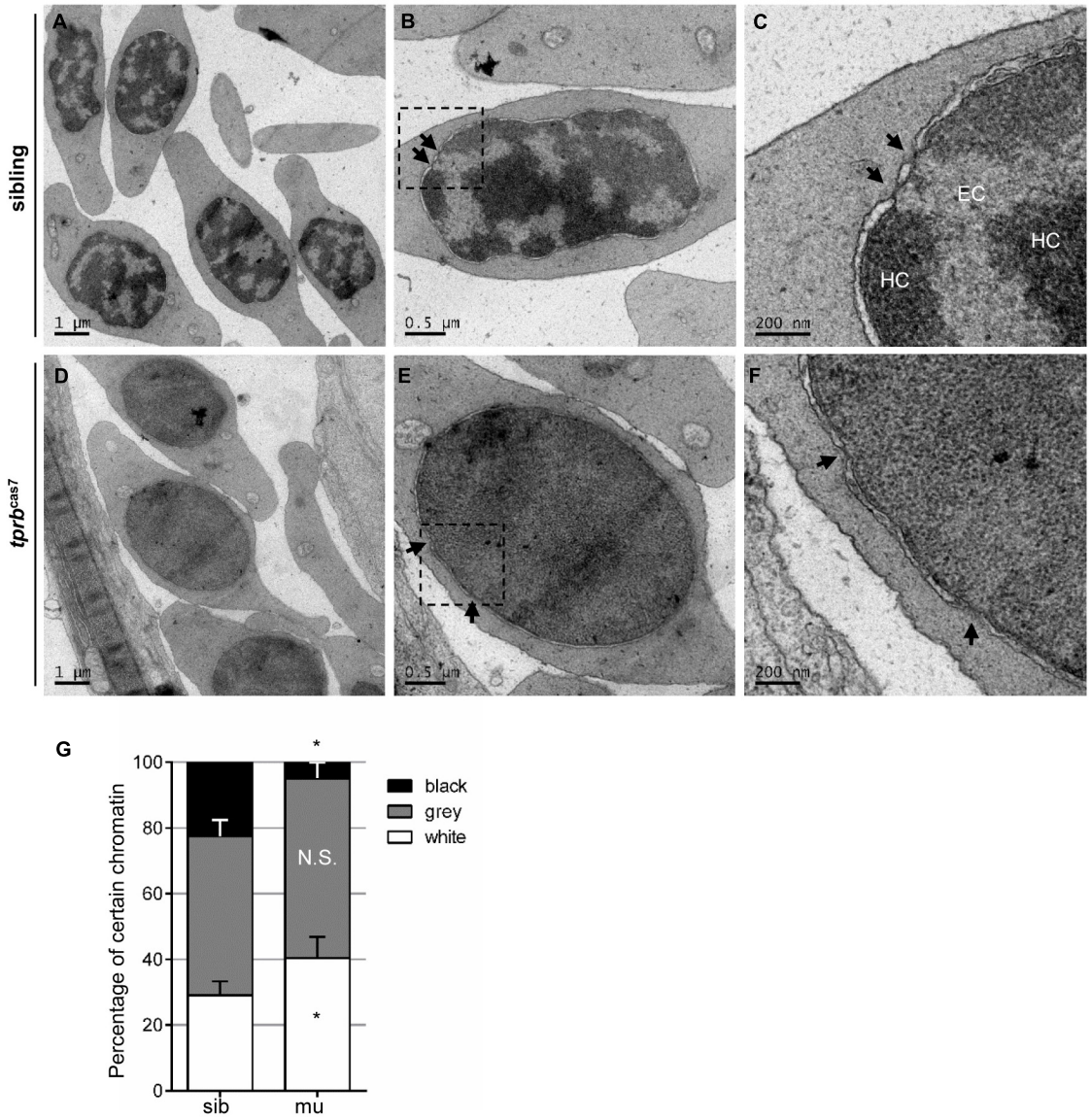

FIGURE 6 | Chromatin condensation is defective in *tprb*^{cas7} mutant erythroid cells. **(A–F)** Representative transmission electron microscopy (TEM) images of erythrocytes from sibling **(A–C)** and *tprb*^{cas7} mutants **(D–F)** at 4 dpf. The images in panels **(C,F)** showed a higher magnification of the corresponding boxes **(B,E)**. Arrows indicate nuclear pores. EC, euchromatin; HC, heterochromatin. Scale bars are shown in each image. **(G)** Quantifications of certain chromatin with classified different color in sibling and *tprb*^{cas7} mutants at 4 dpf. Error bars represent SEM. N.S., not significant; *$p < 0.05$.

the expression of CD235a on the surface showed a significant increase in scramble shRNA K562 cells; however, the expression of CD235a in *TPR* knock-down K562 cells was not obviously enhanced (**Supplementary Figures 13C,D**). We also checked globin expression when *TPR* is knocked down. The α globin and β globin upregulated in *TPR* knock-down cells, while γ globin and δ globin was not obviously changed (**Supplementary Figure 13E**). When treated with hemin, the expressions of α globin, β globin, and γ globin were all increased (**Supplementary Figure 13E**). These data indicated that *TPR* knock-down caused blocking of erythroid differentiation, although the globin expression increased largely in K562 cell line.

DISCUSSION

Here, we reported a novel zebrafish *tprb*^{cas7} mutant with defect in erythroid maturation. Genetic analysis revealed that the missense mutation in *tprb* gene leads to Tpr protein loss of function, which was causative for *tprb*^{cas7} mutant phenotypes. Further studies found that Tpr was essential for the organization and maintenance of chromatin condensation and erythroid gene regulation during terminal erythropoiesis, and the function of TPR in erythropoiesis is highly conserved in mammalian.

In this study, we confirmed that the point mutation in *tprb* gene would lead to Tpr protein loss of function by *tprb*

knockdown, rescue, and knockout experiments. Zebrafish Tpr protein contains 2,352 amino acids. It is interesting to find how the single base mutation results in whole protein inactivation. By detecting the amount of Tpr protein at different stages, we found that the level of Tpr was gradually decreased in *tprb*^{cas7} mutant and almost disappeared from 3 dpf (**Figure 2E**). This result indicates that the missense mutation might affect the stability of Tpr proteins and accelerate their degradation, leading to the loss of function finally. In addition, the erythroid phenotype of *tprb*^{cas7} heterozygotes was checked, and no defect was observed. We propose that the mutation type of Tpr (L9V) has no dominant negative effect.

The increased staining of WISH generally shows the increased expression level of the genes. We found that *tprb* knockdown did not change the number of erythrocytes compared with control, although the expressions of erythroid markers (*ae1-globin*, *alas2*, and *band3*) were all increased by WISH staining. Thus, our results showed that loss of Tpr could upregulate the expression of erythroid genes by enhancing their transcriptional activity.

Also, we confirmed that the phenotype of *tprb*^{cas7} mutant was independent on HIF signaling pathway mainly through four reasons: (1) the number of erythrocytes was not increased; (2) the expression of HIF target genes was not upregulated; (3) *hif-2a* MO could partially rescue the WISH result of *ae1-globin* in *vhl* mutant, rather than in *tprb*^{cas7} mutant; (4) in human cells, there was no significant change in the accumulation of HIF-1a protein and expression of HIF target genes as *TPR* knockdown.

Although the expression of NPC as the structural protein has no tissue specificity, its tissue-specific function has been widely reported (Raices and D'Angelo, 2012). In this study, we found that the chromatin condensation and organization were specifically disrupted in erythrocytes in *tprb*^{cas7} mutant. On the one hand, this may be the process of nuclear condensation and globally chromatin aggregation specific to erythrocytes, and erythroid terminal differentiation highly depends on this. Therefore, the erythroid cells in *tprb*^{cas7} mutant are more sensitive to chromatin changes. On the other hand, studies have identified different molecules involved in chromatin reorganization during terminal differentiation in different types of cells. Such as in terminally differentiating myotubes, methyl CpG–binding protein MeCP2 and MBD2 are important for the aggregation of pericentric heterochromatin (Brero et al., 2005). Our finding that the chromatin condensation in muscular cells was not affected in *tprb*^{cas7} mutant is consistent with the previous research.

In different species, there are various molecular mechanisms involved in chromatin condensation during terminal erythropoiesis. In chicken erythrocytes, two architectural factors, linker histone H5 and nuclear serpin MENT, accumulate at repressed chromatin domains and promote chromatin condensation (Verreault and Thomas, 1993; Istomina et al., 2003). Also, in mammalian erythrocytes, histone deacetylation and caspase-3 may be the greatest players (Zermati et al., 2001; Popova et al., 2009; Ji et al., 2011; Zhao et al., 2016). In this study, we first showed that nucleoporin Tpr, which faces the nucleoplasm, was essential for chromatin condensation and erythroid maturation in zebrafish embryogenesis. Also, we found that the human TPR was important for K562 erythroid cell maturation. It is still intriguing to explore whether the histones and their modifications are involved in this process and how they can corporate with Tpr. One clue is that Tpr can specifically interact with histone H1.1 and H1.2 to regulate the stability of these replication-dependent linker histones (Zhang et al., 2016).

At present, there are some human diseases associated with TPR. In several different cancers, TPR is present through fusion genes, which is formed by coiled-coil motif in TPR with some kinase partner genes such as *MET* (gastric cancer) (Soman et al., 1991), *NTRK1* (thyroid carcinoma) (Greco et al., 1992), *FGFR1* (myeloproliferative syndromes) (Li et al., 2012), and *ALK* (lung adenocarcinoma) (Choi et al., 2014). In all fusion proteins, TPR N-terminal coiled-coil domain is maintained and fused to the partner kinase domain, resulting to allow dimerization that aberrantly activates kinases and drives the cancer progression. In addition, patients with Hutchinson–Gilford Progeria Syndrome (HGPS) premature aging had abnormal cytoplasm localization of TPR protein. HGPS is caused by a mutation in *LMNA* gene that generates a mutant lamin A protein, which is a major component of the nuclear lamina. Fibroblasts from HGPS patients have defects in the Ran GTPase system that cause a nuclear import defect in TPR and mislocalized in the cytoplasm, not the nuclear side of the nuclear pore complex (Snow et al., 2013). However, it is not clear how the abnormal localization of TPR affects the development of the HGPS.

Previous studies have reported that the chromatin structure can determine the expression of specific genes (Deng et al., 2012; Deng et al., 2014). During terminal erythropoiesis, nuclear and chromatin are gradually condensed and associated with wide downregulation of gene expression (Wong et al., 2011). In *tprb*^{cas7} mutant, chromatin condensation was destroyed, accompanied by a significant increase in euchromatin ratio. This was consistent with the increased total mRNA amount as *tprb* knockdown (data not shown). However, the relationship between chromatin organization and gene expression is still unclear in *tprb*^{cas7} mutant. It is necessary to investigate how the chromatin state and the transcriptome changed.

NPCs have emerged as a crucial regulator of chromatin organization and gene expression (Ibarra and Hetzer, 2015). As an architectural component of NPCs, although Tpr can directly bind to 25% of the genome, most functions of Tpr depend on its interaction with Nup153 to locate at the NPC (Vaquerizas et al., 2010). It is believed that the nuclear envelope is associated with heterochromatin, whereas NPCs are surrounded by euchromatin. The maintenance of these heterochromatin exclusion zones was shown to involve Tpr (Krull et al., 2010). And recently, Tpr is reported to be necessary for SAHF formation, which also relies on its association with the NPC (Boumendil et al., 2019). Nup62 is an element of central channel of NPC (Grossman et al., 2012). We found that the WISH result of *ae1-globin* was increased in zebrafish *nup62l* mutant (**Supplementary Figure 14**), which was identical to *tprb*^{cas7} mutant. It was suggested that the function of Tpr in regulation of erythroid gene expression might be associated with NPC. It will be interesting to clarify the precise mechanism of Tpr in maintenance of chromatin condensation and gene expression. Also, our study would not only uncover

the important role of Tpr in chromatin condensation but also facilitate *ex vivo* production of erythrocytes and regulation of chromatin status to change the cell fate.

MATERIALS AND METHODS

Zebrafish Feeding and Maintenance

The zebrafish facility and study were approved by the Animal Research Advisory Committee of Institute of Nutrition and Health, SIBS, CAS, and zebrafish were maintained according to the guidelines of the Institutional Animal Care and Use Committee. Wild-type (WT) zebrafish strains Tubingen (Vinciguerra et al., 2005) and WIK, the transgenic zebrafish line *Tg(gata1: DsRed)* (Traver et al., 2003), and *Tg(kdrl: EGFP)* (Cross et al., 2003) were described previously. To prevent melanin pigment formation, embryos were incubated in egg water containing 0.045% 1-phenyl-2-thiourea (PTU; Sigma) after 1 dpf and the egg water was changed every day. The embryos were collected at the desired stages (Kimmel et al., 1995).

ENU Mutagenesis and Positional Cloning

ENU mutagenesis and positional cloning were performed as previously described (Bahary et al., 2004). The *cas7* (Tu background) allele was mapped by out-crossing Tu background heterozygous fish into polymorphic WIK background wild-type strain. The mutant^{cas7} was first mapped on chromosome 20 by linked SSLP markers by bulk segregation analysis (BSA) (Knapik et al., 1998; Shimoda et al., 1999). Simple sequence-length polymorphism (SSLP) markers used for BSA were selected from the Massachusetts General Hospital Zebrafish Server website (MGH)[1]. Fine mapping using mainly SSLP markers was carried out to narrow down the genetic interval within a 225-kb region between two markers 294-04 and 297-01. The cDNAs of three candidate genes in the interval were cloned and sequenced from mutants. The sequence *of tprb* gene in mutants^{cas7} had a C to G missense mutation, while other genes were normal. Also, the C to G missense mutation was confirmed by sequencing genomic DNA. All primers used for this study are provided in **Supplementary Table**.

Microinjection and CRISPR-Cas9 Mutagenesis

Morpholino oligonucleotides (MOs) used for microinjection were ordered from Gene Tools. The MOs were microinjected into one-cell-stage embryos as previously described (Nasevicius and Ekker, 2000). Transient *tprb* transgene construct within Tol2 vectors (40 pg) was microinjected into one-cell-stage embryos with Tol2 transposase mRNA (50 pg). CRISPR-Cas9–mediated generation of zebrafish mutants ($tprb^{-3+1}$ and *vhl*) were performed as previously described (Xiao et al., 2013). The gRNAs (50 pg) and Cas9 protein (500 pg) were co-microinjected into one-cell-stage embryos.

[1]http://zebrafish.mgh.harvard.edu

Plasmid Construction

The zebrafish cDNA of *tprb* gene was amplified from reverse transcription products and cloned into pCS2$^+$ vector with *Bam*HI and *Eco*RI restriction sites. To construct Tol2 transgenesis vectors, the *ubiquitin* promoter followed by P2A and in-frame mCherry was cloned into modified Tol2 backbone. Also, the zebrafish $tprb^{WT}$ was amplified from *tprb*-pCS2$^+$ plasmid and inserted between the *ubiquitin* promoter and P2A with *Bam*HI restriction site. We changed several bases of the first 30 bases in the $tprb^{WT}$ gene, to mismatch the *tprb* ATG MO sequence. Changes in these bases would not affect the *tprb* amino acid sequence, for these bases are all changes in synonymous amino acids.

Conventional Whole-Mount *in situ* Hybridization and FISH Analysis

The antisense RNA probes were transcribed *in vitro* by T3 or T7 polymerase (Ambion) with Digoxigenin RNA Labelling Mix (Roche). Conventional and fluorescence whole-mount *in situ* hybridization (WISH and FISH) was described previously (Jowett and Lettice, 1994). In WISH, NBT/BCIP (Sigma) was used for staining and images were captured by Olympus SZX16 microscope. In FISH, embryos were stained with Cy5 (TSA system; Perkin Elmer) and DAPI (1:500; Beyotime) and imaged by Olympus FV1000 confocal microscope.

Giemsa Staining

Zebrafish embryos at indicated time points were anesthetized in calcium-free and magnesium-free PBS (pH 7.4) containing 0.02% tricaine (Sigma) and 1% BSA. Circulating blood cells were collected by cutting tails and cytospined onto slides by centrifugation at 1,000 rpm for 3 min. Then the cells were air-dried and stained by Giemsa solutions (Nanjing Jiancheng) according to the manufacturer's protocol. Images were finally captured by Zeiss Axio Imager A2 microscope. Nuclear area, and nuclear and cytoplasmic diameters of at least 100 randomly selected erythrocytes were measured by using ImageJ software, and nucleo-cytoplasmic ratio was calculated through spherical volume formula.

Flow Cytometry, RNA Extraction, and Quantitative PCR Analysis

The analysis and sorting of *gata1*$^+$ erythrocytes from *Tg(gata1: DsRed; kdrl: EGFP)* embryos were carried out with flow cytometer (Beckman) as previously described (Traver et al., 2003). For total RNA extraction, 10–20 zebrafish embryos or the sorted erythrocytes or cultured human cells were dissolved by TRIzol (Invitrogen), and then transcribed into cDNA by PrimerScript RT Master Mix (TaKaRa). The SYBR Green Real-time PCR Master Mix (TOYOBO) was used to perform quantitative PCR system with ABI Q7 real-time PCR instrument. The primers are listed in **Supplementary Table**.

Cell Culture and siRNA Transfection

HEK293T and Hep3B cells were cultured in DMEM with 10% fetal bovine serum (FBS) and 1% penicillin and streptomycin.

O_2 (1%) was generated by flushing a 94% N_2/5% CO_2 mixture into the incubator and sustained for 48 h until cell confluence. For siRNA transfection, Lipofectamine RNAiMAX Reagent (Invitrogen) was used following the manufacturer's protocol.

Protein Extraction and Immunoblotting

To extract the protein from zebrafish embryos, the embryos were de-membraned and de-yolked first, then homogenized in lysis buffer [20 mM Tris–HCl (pH 7.4), 150 mM NaCl, 5 mM EDTA, 10% glycerol, 0.1% Triton X-100, and protease inhibitor cocktail] and boiled with 2 × SDS buffer for 10 min. To obtain the protein from cultured cells, the cells were homogenized directly with 2 × SDS buffer and boiled for 10 min. Nuclear and cytoplasmic extracts were prepared from cultured cells with Nuclear and Cytoplasmic Extraction Kit (CWBIO) according to the manufacturer's instruction. The immunoblotting was carried out as previously described (Gao et al., 2015), with rabbit anti-Tpr antibody (immunized by 461-710 amino acids of zebrafish Tpr protein; Abclonal), mouse anti-a-tubulin (Sigma), mouse anti-HIF-1a (NOVUS), rabbit anti-TPR (human) (Bethyl Laboratory), goat anti-Lamin B (Santa Cruz), mouse anti-H3 (CST), and goat-anti-rabbit/mouse and donkey-anti-goat secondary antibodies (LIANKE).

Immunofluorescence

Zebrafish embryos at indicated time points were anesthetized in calcium-free and magnesium-free PBS (pH 7.4) containing 0.02% tricaine (Sigma) and 1% BSA. Circulating blood cells were collected by cutting tails and cytospined onto slides by centrifugation at 1,000 rpm for 3 min. Immunofluorescence was carried out as previously described (Gao et al., 2015). The cells were stained with rabbit anti-Tpr antibody, fluorescence was detected with goat-anti-rabbit Alexa Fluor 488 secondary antibody (Invitrogen) and DAPI (Beyotime) was used for nucleus staining.

Low Cell Quantitative ChIP

Quantitative ChIP was performed as previously described (Wardle et al., 2006; Wong et al., 2011) with modifications. Briefly, about 300,000 *gata1*$^+$ erythrocytes from Tg(*gata1*:DsRed) embryos at 3 dpf were sorted and cross-linked with 1% formaldehyde for 10 min at room temperature, followed by glycine (0.125 M) treatment for 5 min. Then the cells were homogenized in lysis buffer [50 mM Tris–HCl (pH8.0), 10 mM EDTA (pH8.0), 0.2% SDS, and Cocktail proteinase inhibitor] and sonicated by Bioruptor to yield fragments. Each sample was incubated with RNA Pol II antibody (clone CTD4H8, Millipore) overnight at 4°C, followed by washing and elution with magnetic beads, and reverse cross-linked for 6 h at 65°C. DNA was purified using MinElute PCR Purification Kit (QIAGEN). The primers used in qChIP are shown in **Supplementary Table**.

Transmission Electron Microscopy

For sample preparation, the tails of zebrafish embryos at 4 dpf were fixed with PBS solution containing 2% paraformaldehyde and 2.5% glutaraldehyde overnight at 4°C, followed by 2% osmium tetroxide. The tails were dehydrated in ethanol and infiltrated in acetone, then embedded in epon 812, and sections were analyzed using a FEI Tecnai G2 Spirit electron microscope. Quantification of certain chromatin was performed as previously described (Baarlink et al., 2017) with modifications. Briefly, each nucleus of erythrocyte was manually segmented and generated a binary mask by ImageJ. Then, the certain chromatin state was classified by the different gray threshold values. Finally, the proportion of certain chromatin was subsequently analyzed by measuring the chromatin area and nucleus area.

Construction TPR Knockdown K562 Cell Line

The shRNA sequences for human *TPR* gene knockdown and the scrambled control shRNA sequence are supplied in **Supplementary Table**. The shRNA sequences were cloned into pLSLG lentiviral vector, which contained the EGFP for detecting transfection efficiency. The respective lentiviral vectors and helper vectors were transfected to 293T cells for viral packaging. Then 60 h after transfection, virus was collected to infect K562 cells in the presence of 10 mg/ml polybrene (Sigma-Aldrich). After 4 days, the cells were used in the experiments as described.

Hemin Induced Erythroid Differentiation in Human K562 Cell Line

The K562 cells were treated with hemin (Sigma) at 0.04 mM for 48 h to induce erythroid differentiation. For immune-fluorescence staining, 1×10^6 cells suspended into PBS were simultaneously incubated for 30 min of anti-APC-conjugated CD235a at 4°C avoiding light. The cells were then washed in PBS to remove unbound antibody for immediate flow cytometry analysis.

Statistical Analysis

Statistical analysis was performed by GraphPad Prism 6 software using two-tailed Student's *t*-test and *p* value of less than 0.05 was considered significant. Error values were calculated by SEM.

DATA AVAILABILITY STATEMENT

The raw data supporting the conclusion of this article will be made available by the authors, without undue reservation.

ETHICS STATEMENT

The animal study was reviewed and approved by the Animal Research Advisory Committee of Institute of Nutrition and Health, SIBS, CAS.

AUTHOR CONTRIBUTIONS

SW, KC, WP, and XJ designed the research, analyzed the data, and wrote the manuscript. SW, KC, and TX performed the

experiments. KM, LG, CF, WZ, CJ, CR, MD, and YC assisted with the experiments. CJ, XJ, LG, KM, YC, and MD contributed to the forward genetics screen. WP and YZ gave suggestions for experiment design. All authors contributed to the article and approved the submitted version.

FUNDING

This work was supported by National Natural Science Foundation of China (81901918, 81660204 to XJ, 31571505 to WP) and Inner Mongolia Science Foundation (2019MS08060); and Innovative and Entrepreneurial Talents in the "Prairie Talents" Project of Inner Mongolia (Q2017047), local science and technology projects guided by the central government (2020ZY0040), and CAS "Light of West China" Program to XJ.

ACKNOWLEDGMENTS

We would like to thank Jun Zhu for *hif-2a* morpholino; Ying Cao for zebrafish *nup62l* mutant; and Xiaolan Peng, Zhiwei Dong, Tingxi Liu, Jiang Zhu, Jun Zhu, and Lan Wang for technical support and suggestions.

SUPPLEMENTARY MATERIAL

The Supplementary Material for this article can be found online at: https://www.frontiersin.org/articles/10.3389/fcell.2021.709923/full#supplementary-material

Supplementary Figure 1 | Developmental serial analysis of α*e1-globin* expression in mutant^{cas7}. Embryos were fixed at time points as indicated, followed by WISH analysis of α*e1-globin* expression. Expression of α*e1-globin* is shown in siblings and mutants at 36 hpf **(A,B)**, 2 dpf **(C,D)**, 3 dpf **(E,F)**, and 4 dpf **(G,H)**. The number and percentage of het-het incross embryos with the *in situ* pattern are listed at the bottom of the mutant^{cas7} panels.

Supplementary Figure 2 | WISH analysis of hematopoietic lineages at 3/4 dpf. WISH analysis of *cmyb* **(A,B)**, *mpx* **(C,D)**, *lyz* **(E,F)**, and *rag-1* **(G,H')** expression shows no significant difference between sibling and mutant^{cas7} at 3/4 dpf. After WISH and photographing, all embryos were extracted for genomic DNA and genotyped by sequencing, then the mutant percentage was evaluated. The percentages of embryos in a het-het incross clutch with the expression pattern as shown in the mutant^{cas7} column is listed at the bottom of each panel. **(I)** The relative expression of α*e3-globin*, β*e1-globin*, β*e2-globin*, *hebp2*, *sdhb*, *fth1a*, *cmyb*, *mpo*, *lyz*, *kdrl*, and *rag1* in sibling and mutant^{cas7} embryos at 3 dpf. Error bars represent SEM. ns, not significant; $^{*}p \leq 0.05$; $^{**}p \leq 0.01$; $^{***}p \leq 0.001$.

Supplementary Figure 3 | Normal primitive hematopoiesis and vascular morphogenesis in mutant^{cas7}. Sibling and mutant^{cas7} embryos were fixed at 22 or 26 hpf, followed by WISH analysis of *scl*, *gata1*, *pu.1*, *mpx*, and *kdrl* expression. Expressions of *scl* **(A,B)**, *gata1* **(C,D)**, *pu.1* **(E,F)**, *mpx* **(G,H)**, and *kdrl* **(I,J)** show no significant difference between wild-type siblings and mutants. Insets in panels **(E,F)** show dorsal views of the head staining region. After WISH and photographing, all embryos were extracted for genomic DNA and genotyped by sequencing, then the mutant percentage was evaluated. The number and percentage of het-het incross embryos with the *in situ* pattern are listed at the bottom of the mutant^{cas7} panels.

Supplementary Figure 4 | The point mutation (C-G) in mutant^{cas7} was not found in all five wild-type strains, indicating that C-G transition at the site is not a SNP. Sequencing electropherogram of the mutation site of *tprb* genomic DNA from five wild-type strains. Genomic DNA were extracted each from 20 to 30 embryos of TU, AB, WIK, Longfin, and Shanghai strains, and then sequenced for *tprb* gene. This point mutation (C-G) in mutant^{cas7} was not found in all five wild-type strains.

Supplementary Figure 5 | WISH analysis of hematopoietic lineages in *tprb* morphants at 3/4 dpf. **(A)** Representative immunoblotting images of Tpr in control and *tprb* morphants. WISH analysis of *cmyb* **(B,C)**, *mpx* **(D,E)**, *lyz* **(F,G)**, and *rag-1* **(H,I')** expression show no significant difference between control and *tprb* morphants at 3/4 dpf. After WISH and photographing, all embryos were extracted for genomic DNA and genotyped by sequencing, then the mutant percentage was evaluated. The percentage of indicated phenotype is listed at the bottom of each panel. **(J)** The relative expression of α*e1-globin*, *alas2*, *band3*, α*e3-globin*, β*e1-globin*, β*e2-globin*, *gata1*, *hebp2*, *sdhb*, *fth1a*, *cmyb*, *mpo*, *lyz*, *kdrl*, and *rag1* at 3 dpf in *tprb* morphants. Error bars represent SEM. ns, not significant; $^{**}p \leq 0.01$; $^{***}p \leq 0.001$.

Supplementary Figure 6 | Giemsa staining in circulating erythroid cells in control and *tprb* morphants at different time stages. **(A)** Quantitative analysis of each erythroid cell nuclear area. **(B)** Quantitative analysis of nucleus-to-cytoplasm (N/C) ratio. Error bars represent SEM. ns, not significant; $^{****}p \leq 0.0001$; $^{**}p \leq 0.01$; $^{***}p \leq 0.001$. **(C–G)** Representative images of Giemsa staining in circulating erythroid cells at different stages: 30 hpf **(C,D)**, 2 dpf **(E,F)**, 3 dpf **(G,H)**, and 4 dpf **(I,J)**. Scale bars represent 20μm.

Supplementary Figure 7 | The result of *tprb*^{cas7} rescue experiment at 4 dpf. Transient expression of wild-type *tprb* under the *ubiquitin* promoter in mutant^{cas7} could rescue the phenotypes. Mutant^{cas7} embryos at one-cell stage were injected the tol2 plasmid with *tprb*^{WT} expression driven by ubiquitin promoter. Then embryos with mCherry fluorescence would be selected for downstream analysis. At 4 dpf, every embryo was cut off in head for genotyping, then the trunk and tail of the embryo was taken for RNA or protein extraction. After genotyping the mutant embryos, we pooled three to five of the same phenotype embryo RNA extraction and took the qPCR experiments. **(A)** The relative expression of α*e1-globin*, *alas2*, *band3*, α*e3-globin*, β*e1-globin*, and β*e2-globin* at 4 dpf. Error bars represent SEM. $^{**}p \leq 0.01$; $^{***}p \leq 0.001$. **(B)** Representative immunoblotting images of Tpr in *tprb* mutants rescued by tol2 plasmid with *tprb*^{WT} expression.

Supplementary Figure 8 | Expression pattern of *tprb* mRNA during zebrafish embryogenesis. **(A–J)** WT (TU strain) embryos were fixed at the time points as indicated in each panel, followed by WISH analysis of *tprb* mRNA expression.

Supplementary Figure 9 | The endogenous Tpr protein is located on the nuclear membrane and Tpr protein is missing in *tprb* mutant or morphant. Representative images of Tpr immunofluorescence in sibling **(A,B)** and mutants **(C,D)** at 3 dpf. All embryos were extracted for genomic DNA and genotyped by sequencing. Representative images of Tpr immunofluorescence in control morphants **(E,F)** and *tprb* morphants **(G,H)** at 3 dpf. Scale bars represent 20 μ m.

Supplementary Figure 10 | Flow cytometry analysis of erythrocytes from control and *tprb* morphants. Flow cytometry analysis of *gata1*$^{+}$ cells from *Tg(gata1: DsRed; kdrl: EGFP)* transgenic line in control and *tprb* morphants at different time points. The ratio of *gata1*$^{+}$ erythrocytes between control and *tprb* morphants was similar.

Supplementary Figure 11 | Generation and phenotype characterization of zebrafish *vhl* mutant. **(A,B)** Generation of *vhl* mutant *via* CRISPR-Cas9 technique. The alignment of WT and mutated sequences is listed. The underlined sequence is *vhl* gRNA target site. The sequencing result of *vhl* genomic DNA showed changed bases (shown in red) at exon 1 (A), which caused a premature stop codon leading to the production of a truncated 31-amino-acid Vhl protein **(B)**. **(C–F)** WISH analysis of *ae1-globin* expression in sibling and *vhl* mutants at 3 dpf under the control and *hif-2a* morpholino **(E,F)** injection, indicating that the *hif-2a* MO can partially rescue the increased expression of *ae1-globin* in *vhl* mutant.

Supplementary Figure 12 | The other tissue cells in *tprb*^{cas7} mutant have normal chromatin organization. **(A–F)** Representative TEM images of chromatin organization within the tissue cells show no obvious difference between sibling and *tprb*^{cas7} mutants at 4 dpf, including neural cells **(A,B)**, endothelial cells **(C,D)**, and muscular cells **(E,F)**.

Supplementary Figure 13 | TPR is also important for erythroid differentiation in mammalian. **(A)** Representative immunoblotting images of TPR shRNA and scramble shRNA in K562 cell line. Tubulin serves as the loading control. **(B)** The

relative expression of *TPR* in different groups. **(C)** Representative FACS images of the ratio of CD235a-positive cells with or without hemin treatment. **(D)** Quantitative analysis of panel **(C)**. **(E)** The relative expression of α/β/γ/δ-globins with or without hemin treatment. Error bars represent SEM. ns, not significant; $^{*}p \leq 0.05$; $^{**}p \leq 0.01$; $^{***}p \leq 0.001$.

Supplementary Figure 14 | Zebrafish *nup62l* mutants represent similar phenotype with *tprb*^{cas7} mutants. **(A,B)** WISH analysis of *ae1-globin* show the increased expression in *nup62l* mutants compared with sibling at 3.5 dpf. The number and percentage of het-het incross embryos with the *in situ* pattern in a clutch are listed at the bottom of the mutant panels.

REFERENCES

Baarlink, C., Plessner, M., Sherrard, A., Morita, K., Misu, S., Virant, D., et al. (2017). A transient pool of nuclear F-actin at mitotic exit controls chromatin organization. *Nat. Cell Biol.* 19, 1389–1399. doi: 10.1038/ncb3641

Bahary, N., Davidson, A., Ransom, D., Shepard, J., Stern, H., Trede, N., et al. (2004). The zon laboratory guide to positional cloning in zebrafish. *Methods Cell Biol.* 77, 305–329. doi: 10.1016/s0091-679x(04)77017-x

Bertrand, J. Y., Chi, N. C., Santoso, B., Teng, S., Stainier, D. Y., and Traver, D. (2010). Haematopoietic stem cells derive directly from aortic endothelium during development. *Nature* 464, 108–111. doi: 10.1038/nature08738

Boumendil, C., Hari, P., Olsen, K. C. F., Acosta, J. C., and Bickmore, W. A. (2019). Nuclear pore density controls heterochromatin reorganization during senescence. *Genes Dev.* 33, 144–149. doi: 10.1101/gad.321117.118

Brero, A., Easwaran, H. P., Nowak, D., Grunewald, I., Cremer, T., Leonhardt, H., et al. (2005). Methyl CpG–binding proteins induce large-scale chromatin reorganization during terminal differentiation. *J. Cell Biol.* 169, 733–743. doi: 10.1083/jcb.200502062

Bunn, H. F. (2013). Erythropoietin. *Cold Spring Harb. Perspect. Med.* 3:a011619. doi: 10.1101/cshperspect.a011619

Chen, A. T., and Zon, L. I. (2009). Zebrafish blood stem cells. *J. Cell Biochem.* 108, 35–42. doi: 10.1002/jcb.22251

Choi, Y.-L., Lira, M. E., Hong, M., Kim, R. N., Choi, S.-J., Song, J.-Y., et al. (2014). A novel fusion of TPR and ALK in lung adenocarcinoma. *J. Thorac. Oncol.* 9, 563–566. doi: 10.1097/jto.0000000000000093

Cordes, V. C., Reidenbach, S., Rackwitz, H. R., and Franke, W. W. (1997). Identification of protein p270/Tpr as a constitutive component of the nuclear pore complex-attached intranuclear filaments. *J. Cell Biol.* 136, 515–529. doi: 10.1083/jcb.136.3.515

Cross, L. M., Cook, M. A., Lin, S., Chen, J.-N., and Rubinstein, A. L. (2003). Rapid analysis of angiogenesis drugs in a live fluorescent zebrafish assay. *Arterioscler. Thromb. Vasc. Biol.* 23, 911–912. doi: 10.1161/01.ATV.0000068685.72914.7E

Deng, W., Lee, J., Wang, H., Miller, J., Reik, A., Gregory, P. D., et al. (2012). Controlling long-range genomic interactions at a native locus by targeted tethering of a looping factor. *Cell* 149, 1233–1244. doi: 10.1016/j.cell.2012.03.051

Deng, W., Rupon, J. W., Krivega, I., Breda, L., Motta, I., Jahn, K. S., et al. (2014). Reactivation of developmentally silenced globin genes by forced chromatin looping. *Cell* 158, 849–860. doi: 10.1016/j.cell.2014.05.050

Drexler, H. G., Matsuo, Y., and MacLeod, R. A. F. (2004). Malignant hematopoietic cell lines: in vitro models for the study of erythroleukemia. *Leuk. Res.* 28, 1243–1251. doi: 10.1016/j.leukres.2004.03.022

Dzierzak, E., and Philipsen, S. (2013). Erythropoiesis: development and differentiation. *Cold Spring Harb. Perspect. Med.* 3:a011601. doi: 10.1101/cshperspect.a011601

Fraser, S. T., Isern, J., and Baron, M. H. (2007). Maturation and enucleation of primitive erythroblasts during mouse embryogenesis is accompanied by changes in cell-surface antigen expression. *Blood* 109, 343–352. doi: 10.1182/blood-2006-03-006569

Galy, V., Gadal, O., Fromont-Racine, M., Romano, A., Jacquier, A., and Nehrbass, U. (2004). Nuclear retention of unspliced mRNAs in yeast is mediated by perinuclear Mlp1. *Cell* 116, 63–73. doi: 10.1016/s0092-8674(03)01026-2

Gao, L., Li, D., Ma, K., Zhang, W., Xu, T., Fu, C., et al. (2015). TopBP1 governs hematopoietic stem/progenitor cells survival in zebrafish definitive hematopoiesis. *PLoS Genet.* 11:e1005346. doi: 10.1371/journal.pgen.1005346

Greco, A., Pierotti, M. A., Bongarzone, I., Pagliardini, S., Lanzi, C., and Della Porta, G. (1992). TRK-T1 is a novel oncogene formed by the fusion of TPR and TRK genes in human papillary thyroid carcinomas. *Oncogene* 7, 237–242.

Green, D. M., Johnson, C. P., Hagan, H., and Corbett, A. H. (2003). The C-terminal domain of myosin-like protein 1 (Mlp1p) is a docking site for heterogeneous nuclear ribonucleoproteins that are required for mRNA export. *Proc. Natl. Acad. Sci. U.S.A.* 100, 1010–1015. doi: 10.1073/pnas.0336594100

Grossman, E., Medalia, O., and Zwerger, M. (2012). Functional architecture of the nuclear pore complex. *Annu. Rev. Biophys.* 41, 557–584. doi: 10.1146/annurev-biophys-050511-102328

Hase, M. E., Kuznetsov, N. V., and Cordes, V. C. (2001). Amino acid substitutions of coiled-coil protein Tpr abrogate anchorage to the nuclear pore complex but not parallel, in-register homodimerization. *Mol. Biol. Cell* 12, 2433–2452. doi: 10.1091/mbc.12.8.2433

Ibarra, A., and Hetzer, M. W. (2015). Nuclear pore proteins and the control of genome functions. *Genes Dev.* 29, 337–349. doi: 10.1101/gad.256495.114

Istomina, N. E., Shushanov, S. S., Springhetti, E. M., Karpov, V. L., Krasheninnikov, I. A., Stevens, K., et al. (2003). Insulation of the chicken β-globin chromosomal domain from a chromatin-condensing protein, MENT. *Mol. Cell. Biol.* 23, 6455–6468. doi: 10.1128/mcb.23.18.6455-6468.2003

Ji, P., Murata-Hori, M., and Lodish, H. F. (2011). Formation of mammalian erythrocytes: chromatin condensation and enucleation. *Trends Cell Biol.* 21, 409–415. doi: 10.1016/j.tcb.2011.04.003

Jong, J. L. O. D., and Zon, L. I (2005). Use of the zebrafish system to study primitive and definitive hematopoiesis. *Annu. Rev. Genet.* 39, 481–501. doi: 10.1146/annurev.genet.39.073003.095931

Jowett, T., and Lettice, L. (1994). Whole-mount in situ hybridization on zebrafish embryos using a mixture of digoxigenin- and fluorescein-labelled probes. *Trends Genet.* 10, 73–74. doi: 10.1016/0168-9525(94)90220-8

Kimmel, C. B., Ballard, W. W., Kimmel, S. R., Ullmann, B., and Schilling, T. F. (1995). Stages of embryonic development of the zebrafish. *Dev. Dyn.* 203, 253–310. doi: 10.1002/aja.1002030302

Kissa, K., and Herbomel, P. (2010). Blood stem cells emerge from aortic endothelium by a novel type of cell transition. *Nature* 464, 112–115. doi: 10.1038/nature08761

Knapik, E. W., Goodman, A., Ekker, M., Chevrette, M., Delgado, J., Neuhauss, S., et al. (1998). A microsatellite genetic linkage map for zebrafish (*Danio rerio*). *Nat. Genet.* 18, 338–343. doi: 10.1038/ng0498-338

Koh, M. Y., and Powis, G. (2012). Passing the baton: the HIF switch. *Trends Biochem. Sci.* 37, 364–372. doi: 10.1016/j.tibs.2012.06.004

Krull, S., Dorries, J., Boysen, B., Reidenbach, S., Magnius, L., Norder, H., et al. (2010). Protein Tpr is required for establishing nuclear pore-associated zones of heterochromatin exclusion. *EMBO J.* 29, 1659–1673. doi: 10.1038/emboj.2010.54

Krull, S., Thyberg, J., Bjorkroth, B., Rackwitz, H. R., and Cordes, V. C. (2004). Nucleoporins as components of the nuclear pore complex core structure and Tpr as the architectural element of the nuclear basket. *Mol. Biol. Cell* 15, 4261–4277. doi: 10.1091/mbc.E04-03-0165

Lee, F. S., and Percy, M. J. (2011). The HIF pathway and erythrocytosis. *Annu. Rev. Pathol.* 6, 165–192. doi: 10.1146/annurev-pathol-011110-130321

Lelek, M., Casartelli, N., Pellin, D., Rizzi, E., Souque, P., Severgnini, M., et al. (2015). Chromatin organization at the nuclear pore favours HIV replication. *Nat. Commun.* 6:6483. doi: 10.1038/ncomms7483

Li, D., Xue, W., Li, M., Dong, M., Wang, J., Wang, X., et al. (2018). VCAM-1(+) macrophages guide the homing of HSPCs to a vascular niche. *Nature* 564, 119–124. doi: 10.1038/s41586-018-0709-7

Li, F., Zhai, Y.-P., Tang, Y.-M., Wang, L.-P., and Wan, P.-J. (2012). Identification of a novel partner gene, TPR, fused to FGFR1 in 8p11 myeloproliferative syndrome. *Genes Chromosomes Cancer* 51, 890–897. doi: 10.1002/gcc.21973

Menon, V., and Ghaffari, S. (2021). Erythroid enucleation: a gateway into a "bloody" world. *Exp. Hematol.* 95, 13–22. doi: 10.1016/j.exphem.2021.01.001

Metelo, A. M., Noonan, H. R., Li, X., Jin, Y., Baker, R., Kamentsky, L., et al. (2015). Pharmacological HIF2α inhibition improves VHL disease–associated phenotypes in zebrafish model. *J. Clin. Invest.* 125, 1987–1997. doi: 10.1172/JCI73665

Murayama, E., Kissa, K., Zapata, A., Mordelet, E., Briolat, V., Lin, H. F., et al. (2006). Tracing hematopoietic precursor migration to successive hematopoietic organs during zebrafish development. *Immunity* 25, 963–975. doi: 10.1016/j.immuni.2006.10.015

Nasevicius, A., and Ekker, S. C. (2000). Effective targeted gene 'knockdown' in zebrafish. *Nat. Genet.* 26, 216–220. doi: 10.1038/79951

Paik, E. J., and Zon, L. I. (2010). Hematopoietic development in the zebrafish. *Int. J. Dev. Biol.* 54, 1127–1137. doi: 10.1387/ijdb.093042ep

Palis, J. (2014). Primitive and definitive erythropoiesis in mammals. *Front. Physiol.* 5:3. doi: 10.3389/fphys.2014.00003

Popova, E. Y., Krauss, S. W., Short, S. A., Lee, G., Villalobos, J., Etzell, J., et al. (2009). Chromatin condensation in terminally differentiating mouse erythroblasts does not involve special architectural proteins but depends on histone deacetylation. *Chromosome Res.* 17, 47–64. doi: 10.1007/s10577-008-9005-y

Qian, F., Zhen, F., Xu, J., Huang, M., Li, W., and Wen, Z. (2007). Distinct functions for different scl isoforms in zebrafish primitive and definitive hematopoiesis. *PLoS Biol.* 5:e132. doi: 10.1371/journal.pbio.0050132

Raices, M., and D'Angelo, M. A. (2012). Nuclear pore complex composition: a new regulator of tissue-specific and developmental functions. *Nat. Rev. Mol. Cell Biol.* 13, 687–699. doi: 10.1038/nrm3461

Schwartz, T. U. (2016). The structure inventory of the nuclear pore complex. *J. Mol. Biol.* 428, 1986–2000. doi: 10.1016/j.jmb.2016.03.015

Shimoda, N., Knapik, E. W., Ziniti, J., Sim, C., Yamada, E., Kaplan, S., et al. (1999). Zebrafish genetic map with 2000 microsatellite markers. *Genomics* 58, 219–232. doi: 10.1006/geno.1999.5824

Snow, C. J., Dar, A., Dutta, A., Kehlenbach, R. H., and Paschal, B. M. (2013). Defective nuclear import of Tpr in Progeria reflects the Ran sensitivity of large cargo transport. *J. Cell Biol.* 201, 541–557. doi: 10.1083/jcb.201212117

Soman, N. R., Correa, P., Ruiz, B. A., and Wogan, G. N. (1991). The TPR-MET oncogenic rearrangement is present and expressed in human gastric carcinoma and precursor lesions. *Proc. Natl. Acad. Sci. U.S.A.* 88, 4892–4896. doi: 10.1073/pnas.88.11.4892

Traver, D., Paw, B. H., Poss, K. D., Penberthy, W. T., Lin, S., and Zon, L. I. (2003). Transplantation and in vivo imaging of multilineage engraftment in zebrafish bloodless mutants. *Nat. Immunol.* 4, 1238–1246. doi: 10.1038/ni1007

van Rooijen, E., Voest, E. E., Logister, I., Korving, J., Schwerte, T., Schulte-Merker, S., et al. (2009). Zebrafish mutants in the von Hippel-Lindau tumor suppressor display a hypoxic response and recapitulate key aspects of Chuvash polycythemia. *Blood* 113, 6449–6460. doi: 10.1182/blood-2008-07-167890

Vaquerizas, J. M., Suyama, R., Kind, J., Miura, K., Luscombe, N. M., and Akhtar, A. (2010). Nuclear pore proteins nup153 and megator define transcriptionally active regions in the *Drosophila* genome. *PLoS Genet.* 6:e1000846. doi: 10.1371/journal.pgen.1000846

Verreault, A., and Thomas, J. O. (1993). Chromatin structure of the beta-globin chromosomal domain in adult chicken erythrocytes. *Cold Spring Harb. Symp. Quant. Biol.* 58, 15–24. doi: 10.1101/sqb.1993.058.01.005

Vinciguerra, P., Iglesias, N., Camblong, J., Zenklusen, D., and Stutz, F. (2005). Perinuclear Mlp proteins downregulate gene expression in response to a defect in mRNA export. *EMBO J.* 24, 813–823. doi: 10.1038/sj.emboj.7600527

Wardle, F. C., Odom, D. T., Bell, G. W., Yuan, B., Danford, T. W., Wiellette, E. L., et al. (2006). Zebrafish promoter microarrays identify actively transcribed embryonic genes. *Genome Biol.* 7:R71. doi: 10.1186/gb-2006-7-8-r71

Wickramasinghe, S. N., and Wood, W. G. (2005). Advances in the understanding of the congenital dyserythropoietic anaemias. *Br. J. Haematol.* 131, 431–446. doi: 10.1111/j.1365-2141.2005.05757.x

Wong, P., Hattangadi, S. M., Cheng, A. W., Frampton, G. M., Young, R. A., and Lodish, H. F. (2011). Gene induction and repression during terminal erythropoiesis are mediated by distinct epigenetic changes. *Blood* 118, e128–e138. doi: 10.1182/blood-2011-03-341404

Xiao, A., Wang, Z., Hu, Y., Wu, Y., Luo, Z., Yang, Z., et al. (2013). Chromosomal deletions and inversions mediated by TALENs and CRISPR/Cas in zebrafish. *Nucleic Acids Res.* 41:e141. doi: 10.1093/nar/gkt464

Zermati, Y., Garrido, C., Amsellem, S., Fishelson, S., Bouscary, D., Valensi, F., et al. (2001). Caspase activation is required for terminal erythroid differentiation. *J. Exp. Med.* 193, 247–254. doi: 10.1084/jem.193.2.247

Zhang, P., Branson, O. E., Freitas, M. A., and Parthun, M. R. (2016). Identification of replication-dependent and replication-independent linker histone complexes: Tpr specifically promotes replication-dependent linker histone stability. *BMC Biochem.* 17:18. doi: 10.1186/s12858-016-0074-9

Zhao, B., Mei, Y., Schipma, M. J., Roth, E. W., Bleher, R., Rappoport, J. Z., et al. (2016). Nuclear condensation during mouse erythropoiesis requires caspase-3-mediated nuclear opening. *Dev. Cell* 36, 498–510. doi: 10.1016/j.devcel.2016.02.001

Conflict of Interest: The authors declare that the research was conducted in the absence of any commercial or financial relationships that could be construed as a potential conflict of interest.

Publisher's Note: All claims expressed in this article are solely those of the authors and do not necessarily represent those of their affiliated organizations, or those of the publisher, the editors and the reviewers. Any product that may be evaluated in this article, or claim that may be made by its manufacturer, is not guaranteed or endorsed by the publisher.

frontiers in Cell and Developmental Biology

ORIGINAL RESEARCH
published: 21 December 2021
doi: 10.3389/fcell.2021.723804

Functional Verification of Novel *ELMO1* Variants by Live Imaging in Zebrafish

Rongtao Xue[1], Ying Wang[2], Tienan Wang[3], Mei Lyu[4], Guiling Mo[5], Xijie Fan[5], Jianchao Li[6], Kuangyu Yen[2], Shihui Yu[5]*, Qifa Liu[1]* and Jin Xu[4]**

[1]Department of Hematology, Nanfang Hospital, Southern Medical University, Guangzhou, China, [2]Department of Developmental Biology, School of Basic Medical Sciences, Southern Medical University, Guangzhou, China, [3]Beigene Ltd., Shanghai, China, [4]Laboratory of Immunology and Regeneration, School of Medicine, South China University of Technology, Guangzhou, China, [5]GuangZhou KingMed Center For Clinical Laboratory Co., Ltd., International Biotech Island, Guangzhou, China, [6]Laboratory of Molecular and Structural Biology, School of Medicine, South China University of Technology, Guangzhou, China

OPEN ACCESS

Edited by:
Anskar Y.H. Leung, The University of Hong Kong, Hong Kong SAR, China

Reviewed by:
Zhihao Jia, Purdue University, United States
Marcel Tawk, Neurogénération et Remyélinisation, France

***Correspondence:**
Kuangyu Yen
kuangyuyen@smu.edu.cn
Shihui Yu
zb-yushihui@kingmed.com.cn
Qifa Liu
liuqifa628@163.com
Jin Xu
xujin@scut.edu.cn

Specialty section:
This article was submitted to Stem Cell Research, a section of the journal Frontiers in Cell and Developmental Biology

Received: *11 June 2021*
Accepted: *17 November 2021*
Published: *21 December 2021*

Citation:
Xue R, Wang Y, Wang T, Lyu M, Mo G, Fan X, Li J, Yen K, Yu S, Liu Q and Xu J (2021) Functional Verification of Novel ELMO1 *Variants by Live Imaging in Zebrafish. Front. Cell Dev. Biol. 9:723804. doi: 10.3389/fcell.2021.723804*

ELMO1 (Engulfment and Cell Motility1) is a gene involved in regulating cell motility through the ELMO1-DOCK2-RAC complex. Contrary to DOCK2 (Dedicator of Cytokinesis 2) deficiency, which has been reported to be associated with immunodeficiency diseases, variants of *ELMO1* have been associated with autoimmune diseases, such as diabetes and rheumatoid arthritis (RA). To explore the function of *ELMO1* in immune cells and to verify the functions of novel *ELMO1* variants *in vivo*, we established a zebrafish *elmo1* mutant model. Live imaging revealed that, similar to mammals, the motility of neutrophils and T-cells was largely attenuated in zebrafish mutants. Consequently, the response of neutrophils to injury or bacterial infection was significantly reduced in the mutants. Furthermore, the reduced mobility of neutrophils could be rescued by the expression of constitutively activated Rac proteins, suggesting that zebrafish *elmo1* mutant functions *via* a conserved mechanism. With this mutant, three novel human *ELMO1* variants were transiently and specifically expressed in zebrafish neutrophils. Two variants, p.E90K (c.268G>A) and p.D194G (c.581A>G), could efficiently recover the motility defect of neutrophils in the *elmo1* mutant; however, the p.R354X (c.1060C>T) variant failed to rescue the mutant. Based on those results, we identified that zebrafish *elmo1* plays conserved roles in cell motility, similar to higher vertebrates. Using the transient-expression assay, zebrafish *elmo1* mutants could serve as an effective model for human variant verification *in vivo*.

Keywords: *ELMO1*, neutrophil, variants, cell motility, zebrafish

INTRODUCTION

The *ELMO1* protein is known to interact with DOCK2 and participates in the regulation of cell motility by regulating the activity of the Rac proteins (Chang et al., 2020; Federici and Soddu, 2020). *DOCK2* deficiency has been reported to be associated with immunodeficiency diseases (Dobbs et al., 2015). Conversely, analyses of genetic polymorphisms in different human populations around the world found that *ELMO1* was associated with autoimmune diseases such as diabetes, rheumatoid arthritis, and nephropathy, but not immunodeficiency diseases (Hironori Katoh, 2006; Arandjelovic et al., 2019; Bayoumy et al., 2020). In addition to DOCK2, ELMO1 also interacts with DOCK180 to

regulate cell migration (Grimsley et al., 2004). Through the interaction with DOCK proteins or RhoG and subsequent activation of the small GTPase such as RACs, ELMO1 involves in regulating lymphocyte migration or promoting cancer cells invasion (Katoh et al., 2003; Jiang et al., 2011; Capala et al., 2014; Stevenson et al., 2014; Gong et al., 2018; Park et al., 2020). Studies in mice and cell cultures have revealed reduced cell migration speeds due to *Elmo1* deficiency. In *Elmo1*-deficient mice, the number of neutrophils at chronic inflammation sites was significantly lower than that in wild-type mice. This neutrophil chemotaxis defect leads to reduced inflammation and the relief of autoimmune diseases in mice (Arandjelovic et al., 2019). Recently, ELMO1 protein has also been found to negatively regulate thrombus formation in mice (Akruti Patel et al., 2019). Moreover, *Elmo1* has been reported to regulate the vascular morphogenesis, the peripheral neuronal numbers and myelination, and the structure formation of kidney during zebrafish development (Epting et al., 2010; Epting et al., 2015; Sharma et al., 2016; Mikdache et al., 2020).

In a study of inflammatory bowel disease caused by *Salmonella* infection, bacterial internalization by macrophages was weakened in *Elmo1*-deficient mice, and led to a decrease in the bacterial load in mice intestines and reduced the level of intestinal inflammation (Das et al., 2015). Thus, studies on *Elmo1* in mouse models indicated that altered *Elmo1* functions changed the function of immune cells and regulated the progression of autoimmune diseases (Hathaway et al., 2016).

Previous studies of clinical samples indicated that *ELMO1* affected the progression of disease by affecting the chemotaxis of immune cells to sites of inflammation (Janardhan et al., 2004; Das et al., 2015; Hathaway et al., 2016). In some studies, neutrophils were directly isolated from patients who carried *ELMO1* variants, and their migration abilities were evaluated *in vitro* (Arandjelovic et al., 2019). However, direct functional verification of *ELMO1* variants *in vivo* has not been performed. Additional *ELMO1* variants are routinely identified by high-throughput genome sequencing of human genomes. However, whether such *ELMO1* variants over-activate or reduce the function of immune cells remains unknown. Therefore, it is necessary to generate a convenient animal model to directly test the functions of *ELMO1* variants *in vivo*.

Recently, zebrafish have been established as an excellent model for the verification of variants of heart and hematopoietic diseases due to their short reproduction cycle, transparent larvae, and relatively low maintenance/drug management costs (Dooley and Zon, 2000). In those studies, target genes containing variants of interest were expressed in zebrafish, and functional analyses were performed *in vivo* to assess the susceptibility of such variants to cardiac and hemostatic diseases (Hu et al., 2017; Hayashi et al., 2020). For *elmo1*, previous studies focused on its functions in the development of peripheral neurons, vessel, and kidney (Epting et al., 2010; Epting et al., 2015; Sharma et al., 2016; Mikdache et al., 2020). On the other hand, previous study showed that *elmo1* knocked-down macrophages present defective engulfment of apoptotic cells and abnormal morphology (Van Ham et al., 2012). Therefore, with the *elmo1* mutation zebrafish, more functions of zebrafish *elmo1* in immune cells need to be further explored.

In our work, we generated zebrafish *elmo1* mutants. Using time-lapse live imaging to directly record the dynamic immune cells, we found that the zebrafish *elmo1* gene was involved in regulating the motility of neutrophils and T-cells, suggesting a conserved role for *elmo1* from fish to humans. Using the *elmo1* mutant model, we evaluated three novel *ELMO1* variants found in the GuangZhou KingMed Center For Clinical Laboratory Co., Ltd genetics database: p.E90K (c.268G>A), p.D194G (c.581A>G), and p.R354X (c.1060C>T). While p.E90K and p.D194G rescued the motility defect of neutrophils in *elmo1* mutants, the p.R354X variant did not.

In summary, we generated a zebrafish model to study the *elmo1* gene and verified the functions of three novel human *ELMO1* variants *in vivo*.

MATERIALS AND METHODS

Zebrafish Lines

The zebrafish AB and SR strains, *elmo1* heterozygous fish, and transgenic fish lines were raised and maintained at 28.5°C in E2 media (Dahm, 2002) and staged as previously reported (Kimmel et al., 1995). Transgenic lines, including *Tg(globin:DsRedx),* which is short for *Tg(globin:LoxP-DsRedx-LoxP-GFP)* (Tian et al., 2017), *Tg(lyz:DsRed)* (Li et al., 2012), *Tg(lck:DsRedx),* which is short for *Tg(lck:LoxP-DsRedx-LoxP-GFP)* (Tian et al., 2017), and *Tg(mpeg1:DsRedx),* which is short for *Tg(mpeg1:LoxP-DsRedx-LoxP-GFP)* (Lin et al., 2019), were used for fluorescence imaging and flow cytometry analyses. $elmo1^{szy103}$ mutant was generated by TALEN technology in the ABSR background. The primers used for genotyping are listed in **Supplementary Table S1**. DdeI digestion was performed following PCR, and while the wild-type allele could be digested, the mutant allele could not. Zebrafish embryos were acquired by natural spawning.

The cDNA Synthesis and Quantitative RT-PCR (qRT-PCR)

In experiments of whole embryos, TRIzol reagent (15596026; Thermo Fisher Scientific) was used to extract total RNA from the wild-type, $elmo1^{+/-}$ and $elmo1^{-/-}$ from the offspring of the heterozygous intercrosses. Reverse transcription was performed with M-MLV (M1701; Promega) to obtain the cDNA library. qRT-PCR was used to detect *elmo1* gene expression using the SYBR Green master mix (04707516001; Roche). In experiments with the cells of a specific lineage, we used 3 days post fertilization (dpf) *Tg(globulin: DsRedx)*, *Tg(lyz:DsRed)* and *Tg(mepg1: DsRedx)*, and 5 dpf *Tg(lck:DsRedx)* to label erythrocytes, neutrophils, macrophages and T-cells, respectively. The cells labeled with DsRed were sorted by flow cytometry, and collected into TRIzol reagent for total RNA extraction. Glycogen (R0551; Thermo Fisher Scientific) was added during RNA precipitation to improve efficiency. The SuperScript™ IV (18091200; Invitrogen) kit was used to obtain the cDNA library. In this process, all of the obtained RNA was added to the reverse transcription PCR. SYBR Green master mix (11198ES03; Yeasen) was used for qRT-PCR and the expressions of *elf* and *elmo1* were

determined. The primers used for qRT-PCR are listed in **Supplementary Table S1**.

Whole-Mount *In Situ* Hybridization and Probe Synthesis

Whole-mount *in situ* hybridization (WISH) assays with zebrafish embryos were conducted as previously described (Thisse and Thisse, 2008) using probes against *elmo1*, *cmyb*, *lyz*, *mpeg1* and *rag1*. Antisense *elmo1* RNA probes were synthesized using the full length *elmo1* CDS (NM_213091.1) cloned into the PCS2 vector.

Immunofluorescence Staining

Immunofluorescence staining assays with zebrafish larvae were conducted as previously described (Barresi Mj and Devoto, 2000; Jin et al., 2006). In brief, 3 dpf larvae were fixed in 4%PFA for 2 h at room temperature. After washing, the larvae were incubated in primary antibody against ELMO1 (ab155775; Abcam) 1:50 diluted and primary antibody against GFP (ab6658; Abcam) 1: 400 diluted in 5%FBS/1xPBS at 4°C overnight. After washing, the larvae were incubated in secondary antibody of Alexa Fluor 555-anti-rabbit (A31572; Invitrogen) and Alexa Fluor 488-anti-goat (A11055; Invitrogen) for 2 h at room temperature. Images were taken under Zeiss LSM800 confocal microscope.

Identification of Human Variants From the GuangZhou KingMed Center For Clinical Laboratory Co., Ltd. Genetics Database.

Blood samples were collected from patients, and genomic DNA was extracted with the QIAamp DNA Blood Mini kit (Qiagen, Hilden, Germany) following the manufacturer's protocol. After enrichment and purification, the DNA libraries were sequenced on the NovaSeq 6000 sequencer according to the manufacturer's instructions (Illumina, San Diego, United States). All reads were aligned to the reference human genome (UCSC hg19) using the Burrows-Wheeler Aligner (BWA) (v.0.5.9-r16) (Li and Durbin, 2010). After data annotation using the PriVar toolkit (Zhang et al., 2013), the clinical significance of the variants was identified (Yang et al., 2013).

Expression of Constitutively Activated Racs

To express the constitutively active form of zebrafish Racs, we cloned the zebrafish p.G12V mutation (Nishida et al., 1999) of the *rac1a/1b/2* CDS after the *coro1a* promoter region, and linked it to DsRed protein using *P2A*. The resulting construct, *coro1a:rac1a/1b/2 CA-P2A-DsRed* (40 ng/μL) and transposase mRNA (50 ng/μL) were injected into the single cell stage of *elmo1*$^{-/-}$ and sibling embryos. The *lyz:GFP* was injected into the above-mentioned embryos as the control plasmid. The final volume injected was 1 nL and the embryos were raised to the desired stage for analysis.

FRET Ratio Analysis

In order to analyse the FRET ratio change specific in wild type and *elmo1*$^{-/-}$ neutrophil, we firstly cloned the RacFRET biosensor from pRaichu-Rac1 (Itoh et al., 2002) and inserted it after the *lyz* promoter. The resulting plasmid *lyz:Rac1-FRET* was co-injected with the transposase mRNA into zebrafish embryos at one cell stage. The final concentration of *lyz:Rac1-FRET* and transposase mRNA were 40 and 50 ng/μL, respectively. After microinjection, we raised the embryos to 3 dpf and took the raw images of the CFP (Ex 458nm; Em 454–534 nm), YFP (Ex 514; Em 535–590 nm) and FRET (Ex 458; Em 535–590 nm) by Zeiss LSM880 with an opened pinhole. A 20x objective was used for photograph. The FRET to CFP ratio image was produced from the raw images in a series of processing steps using ImageJ software (Bosch and Kardash, 2019). When the final FRET ratio image was generated, we then analysed the histogram and exported for data performance.

Expression of Zebrafish *elmo1* and its Variants in T-Cells and Neutrophils

To express the zebrafish *elmo1* in neutrophils, we expressed zebrafish *elmo1* (NM_213,091.1) under the control of the *lyz* promoter and used the *P2A* self-cleaving peptide to link the zebrafish Elmo1 and green fluorescent protein (GFP) (Kitaguchi et al., 2009). To express the zebrafish *elmo1* in T-cells, Elmo1 was directly linked with GFP and its expression was controlled by the *lck* promoter (Langenau et al., 2004). For experiments involving the expression of human *ELMO1* variants in neutrophils for *in vivo* functional verification, the wild-type form of the human *ELMO1* (NM_014800.11) CDS and its variants CDS were directly linked to GFP following the *lyz* promoter. The resulting vectors: *lyz:elmo1*^{ze}*-P2A-GFP (lyz:elmo1*^{ze}*)*, *lck:elmo1*^{ze}*-GFP (lck:elmo1*^{ze}*)*, *lyz:ELMO1*^{hu}*-GFP* (hu-WT), *lyz:E90K-GFP* (E90K), *lyz:D194G-GFP* (D194G), and *lyz:R354X-GFP* (R354X), (40 ng/μL), as well as transposase mRNA (50 ng/μL) were injected into the one cell stage of *elmo1*$^{-/-}$ and sibling embryos. *lyz:GFP* and *lck:DsRedx* were injected into the above-mentioned embryos as the control plasmids. The final volume of the microinjection was 1 nL. Following injection, embryos were raised to the desired stage for analysis.

Time-Lapse Imaging and Cell Tracking Analysis

Time-lapse imaging was performed according to a previous report (Xu et al., 2016). In brief, 3 dpf larvae were anesthetized in 0.01% tricaine (A5040; Sigma-Aldrich), mounted in 1% low melting agarose and imaged on a Zeiss 880 confocal microscope with a 28°C thermal chamber. A 10× objective was used for neutrophil tracking, while a 20× objective was used for T-cell tracking in time-lapse images. The Z-step size was set to 3 μm and 15–20 planes were typically taken in the z-stack at <3 min intervals. The images were processed using ImageJ software, and cell tracking analysis was performed using the MTrackJ plugin. The tracking path of individual cells was extracted from the exported tracking results, and merged using Photoshop software.

Tail Injury Assay

Tail fin injury was performed as previously described (Li et al., 2012). Briefly, lesions were induced in the tail fin of embryos anesthetized with 0.01% tricaine (A5040; Sigma-Aldrich) using a blade.

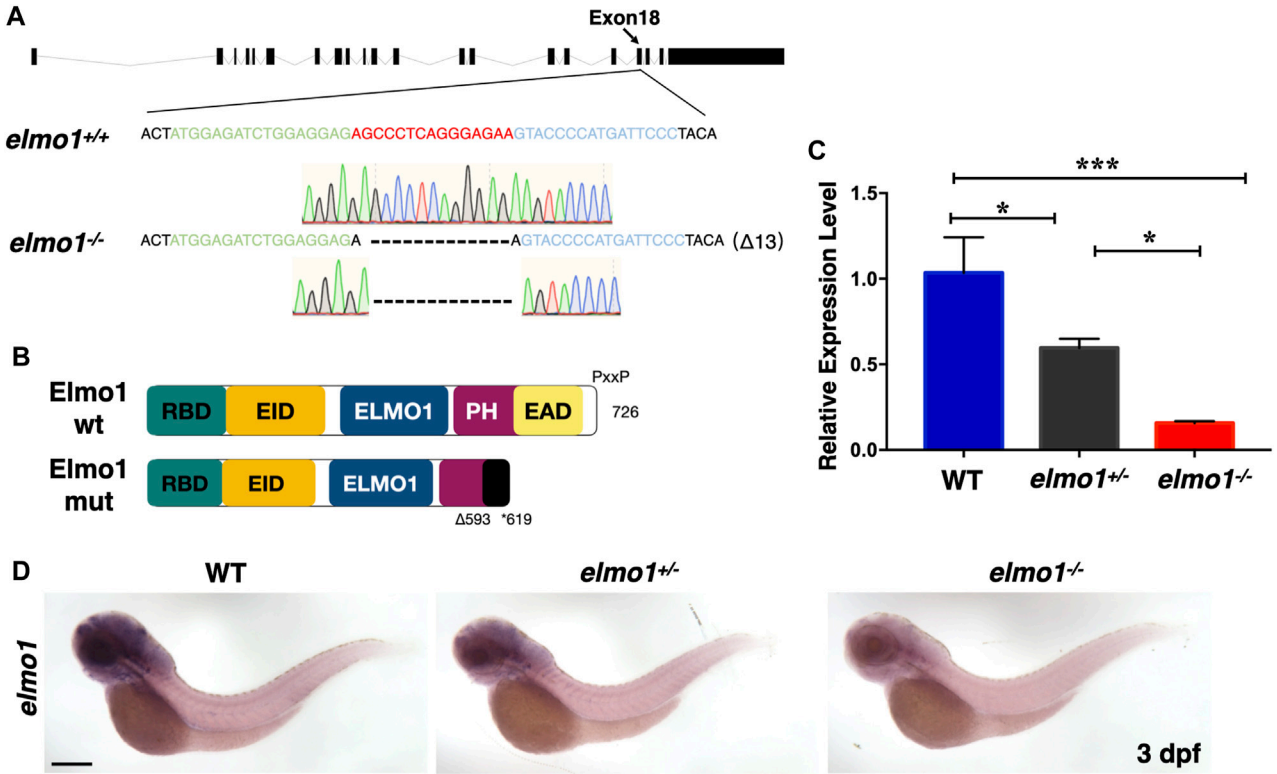

FIGURE 1 | The establishment of the zebrafish *elmo1* mutant. **(A)** Schematic representation of the *elmo1* genomic locus (NC_007130.7). The extended region on exon 18 represents the sequence targeted by the TALEN system. Green: left TALEN arm binding site. Blue: right TALEN arm binding site. Red: spacer site. *elmo1*$^{+/+}$ corresponds to the wild-type allele while *elmo1*$^{-/-}$ represents the loss of function allele in this study. Dashes represent the 13 base pair deletion. **(B)** Schematic view of the wild-type Elmo1 protein (Elmo1 wt) and the mutated Elmo1 protein (Elmo1 mut). The 726 amino acid (aa) Elmo1 wt contains five conserved domains (NP_998,256), while the Elmo1 mut resulting in a truncated protein end up at 619 aa. RBD: RhoG-binding domain; EID: ELMO inhibitory domain; ELMO1: ELMO1 domain; PH: pleckstrin homology; EAD: ELMO auto-regulatory domain. **(C)** The qRT-PCR result showed the relative expression level of the *elmo1* gene in the offsprings of heterozygous intercross at 3 dpf. Three independent experiments were performed. One-way ANOVA, $^{*}p < 0.05$, $^{***}p < 0.005$. **(D)** *elmo1* expression pattern detected by WISH in the offsprings of heterozygous intercross at 3 dpf. Scale bar: 200 μm.

Bacterial Infection Assay

E.coli infection was performed as previously described (Nguyen-Chi et al., 2014). In brief, single colony of *E.coli* which expressing GFP (Olson et al., 2014) were incubated in LB Broth Miller (MKCL4658; Sigma-Aldrich) containing the antibiotic ampicillin (A100339; Sangon Biotech) at 37°C on orbital shaker for at least 24 h before experimentation. After washing cells in 1×PBS and centrifuging at 500 g for 5 min, the *E.coli* were resuspended and diluted to the desired concentration in 1×PBS. *E.coli* were injected into the otic vesicle of zebrafish larvae and observed at the desired developmental stage.

Statistical Analysis

Statistical parameters (mean ± SD) and statistical significance are shown in the figures and described in the Figure Legends. All statistical analyses were performed using GraphPad Prism version 7. Unpaired Student's *t*-tests were used to calculate the *p*-value of pairwise comparisons. For multiple comparisons, significance was calculated using one-way ANOVA followed by the Dunnett's multiple comparisons test. For survival curves, significance was calculated using the Kaplan-Meier curve. Two-tailed *p*-values were calculated for all *t*-tests.

RESULTS

The Establishment of the Zebrafish *elmo1* Mutant

We carried out WISH to examine the expression pattern of *elmo1* in zebrafish. We found that *elmo1* was expressed in vessels at the 20-somites stage. From 22 h post fertilisation (hpf), *elmo1* began to accumulate in the CNS, as was also observed in a prior study (Epting et al., 2010) (**Supplementary Figure S1A**). qRT-PCR revealed that *elmo1* accumulated in leukocytes (**Supplementary Figure S1B**). To establish a zebrafish model to study human variants of *elmo1*, we used TALEN technology (Moore et al., 2012) and targeted exon 18 to disrupt the *elmo1* gene (NC_007130.7) (**Figure 1A**). A frame shift mutation was caused by a 13 bp deletion and resulted in a premature stop codon, which lead to the loss of the PH domain (**Figure 1B**). We

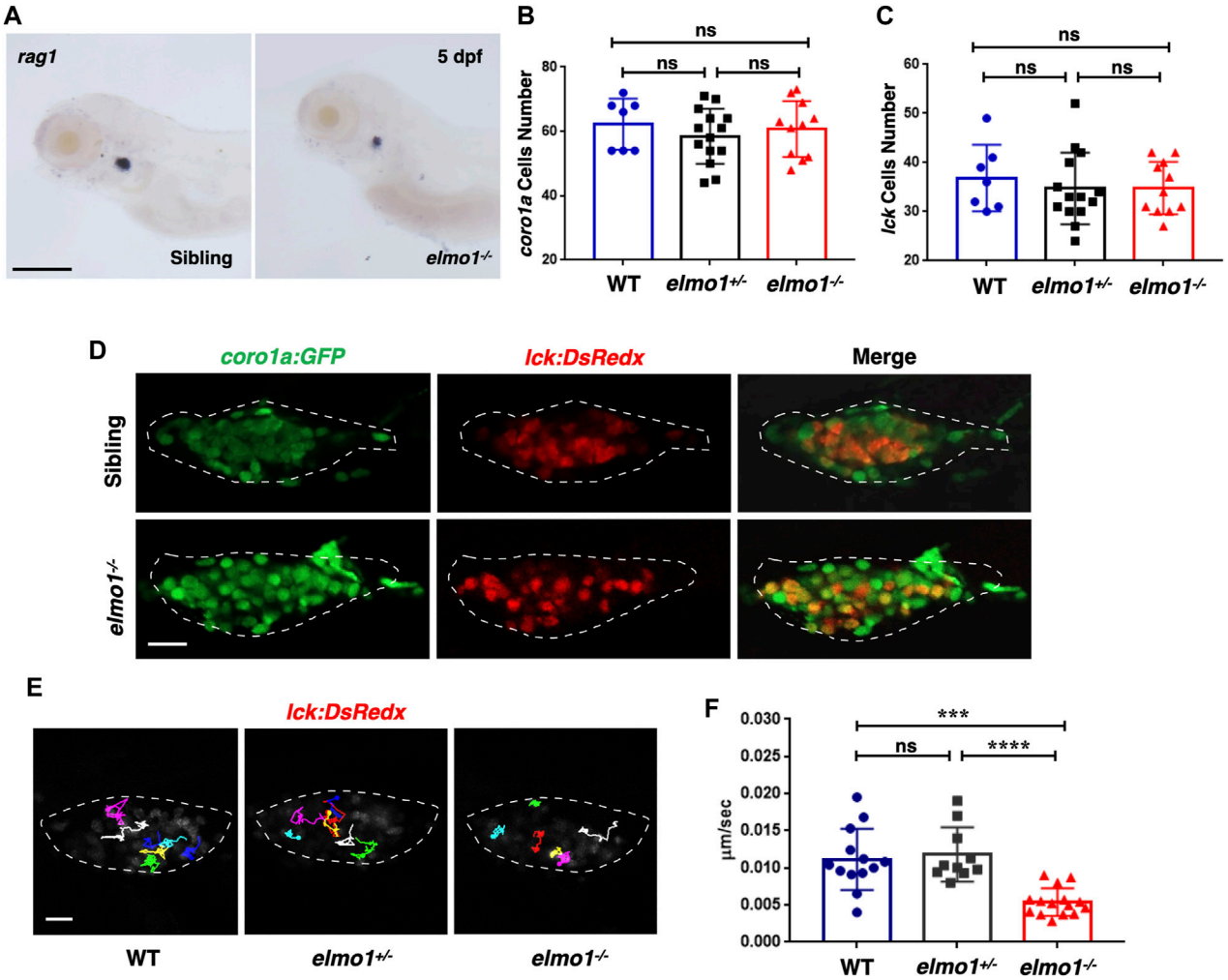

FIGURE 2 | T-cell motility in the thymus was reduced at the larval stage of the *elmo1* mutant. **(A)** *rag1* WISH data indicate a T-cell defect in the *elmo1*$^{-/-}$ larvae at 5 dpf. Scale bar: 200 μm. **(B, C)** Quantification of *coro1a:GFP* positive cells **(B)** represents whole leukocytes and *lck:DsRedx* positive **(C)** cells represent T-cells within the thymus in the wild-type (WT), *elmo1*$^{+/-}$, *elmo1*$^{-/-}$ larvae respectively. There was no significance between them. One-way ANOVA, ns: no significance. **(D)** Fluorescence images show that *coro1a:GFP* represent whole leukocytes and *lck:DsRedx* represent T-cells show no significance between the siblings and *elmo1*$^{-/-}$ larvae in the thymus at 5 dpf. The white dotted region indicates the thymus in the image. Scale bar: 10 μm. **(E)** Track path of *lck:DsRedx* labeled T-cells of the WT, *elmo1*$^{+/-}$ and *elmo1*$^{-/-}$ larvae recorded by live imaging at 5 dpf. The white dotted region indicates the thymus. Each line represents the migration path of one T-cell. Scale bar: 10 μm. **(F)** Quantification of T-cells migration speed in live imaging of the WT (13 cells of 4 larvae), *elmo1*$^{+/-}$ (10 cells of 4 larvae) and *elmo1*$^{-/-}$ (15 cells of 5 larvae) larvae in the thymus at 5 dpf. The migration speed of T-cells dramatically decreased in the *elmo1*$^{-/-}$ larvae. Each dot represents the average speed of one T-cell. Three independent experiments were performed. One-way ANOVA, ns: no significance, ***$p < 0.005$, ****$p < 0.001$.

named this mutant *elmo1*^{szy103} and use *elmo1*$^{-/-}$ for short hereafter. Using qRT-PCR and WISH, the expression level of *elmo1* in the offspring of mutant heterozygote intercrosses was evaluated. A gradient level of expression was observed in the wild-type (WT), *elmo1*$^{+/-}$, and *elmo1*$^{-/-}$ larvae at 3 dpf (**Figures 1C,D**); thus, indicating that the mutant form of the *elmo1* mRNA might be unstable. Furthermore, we directly examined Elmo1 protein in the *elmo1*$^{-/-}$ larvae. We found that Elmo1 protein was readily detected in the siblings by immunofluorescence staining while it was hardly detected in the *elmo1*$^{-/-}$, suggesting a reduced Elmo1 level in mutants (**Supplementary Figure S1D**).

T-Cell Motility in the Thymus was Reduced at the Larval Stage of the *elmo1* Mutant

The *elmo1*$^{-/-}$ larvae survived to adulthood and adult mutants remained healthy throughout the first year compared with their siblings. However, the death rate of adult mutants increased rapidly after 1 year (**Supplementary Figure S1C**). As *Elmo1* has been reported to regulate leukocyte motility in mice, we hypothesized that mutation of *elmo1* might lead to immune dysfunction (Sarkar et al., 2017; Arandjelovic et al., 2019).

We first preformed WISH to examine the development of hematopoietic lineages in the *elmo1*$^{-/-}$ larvae. *cmyb*, *lyz*, and

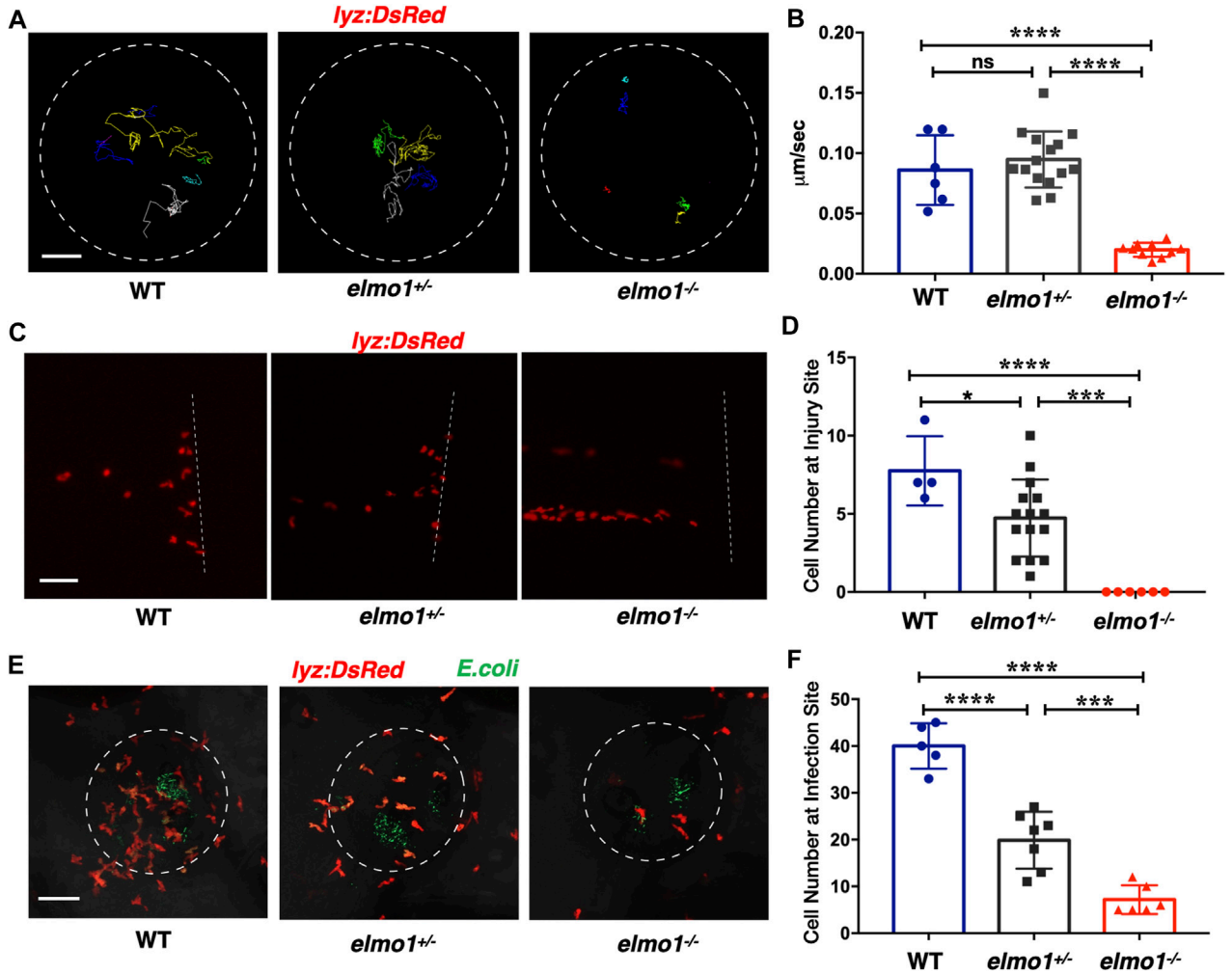

FIGURE 3 | Neutrophils showed attenuated motility and impaired chemotaxis to injury/infection in the *elmo1* mutant. **(A)** Track path of *lyz:DsRed* labeled neutrophils of the WT, *elmo1*$^{+/-}$ and *elmo1*$^{-/-}$ larvae on the yolk sac recorded by live imaging at 3 dpf. The white dotted circle indicates the imaging region of the yolk sac. Each line represents the migration path of individual cells. Scale bar: 50 µm. **(B)** Quantification of neutrophils migration speed of the WT (6 cells of 3 larvae), *elmo1*$^{+/-}$ (15 cells of 5 larvae), and *elmo1*$^{-/-}$ (10 cells of 5 larvae). The *elmo1*$^{-/-}$ showed dramatically decreased speed compared with the WT and *elmo1*$^{+/-}$. **(C)** Fluorescent image of tail fin transection of the WT, *elmo1*$^{+/-}$ and *elmo1*$^{-/-}$ larvae at 3 dpf. The larvae tail region was imaged and the white dotted line represents the transection site. *lyz:DsRed* represents neutrophils failed to accumulate to the injury site in the *elmo1*$^{-/-}$ compared with the WT and *elmo1*$^{+/-}$. Scale bar: 50 µm. **(D)** Quantification of neutrophils accumulated at the tail fin transection site. Neutrophils of the *elmo1*$^{-/-}$ larvae failed to respond to injury compared with the WT and *elmo1*$^{+/-}$. **(E)** Fluorescent image of bacterial infection in the otic vesicle of WT, *elmo1*$^{+/-}$ and *elmo1*$^{-/-}$ larvae at 3 dpf. The white dotted circle represents the infection region. Bacteria of *E.coli* were labeled by GFP. *lyz:DsRed* labeled neutrophils showed a decreasing number at the infection region in the *elmo1*$^{-/-}$ compared with the WT and *elmo1*$^{+/-}$. Scale bar: 50 µm. **(F)** Quantification of *lyz:DsRed* labeled neutrophils accumulated at the infection region. Neutrophils of the *elmo1*$^{-/-}$ larvae failed to respond to infection compared with the WT and *elmo1*$^{+/-}$. In quantification results, each dot represents the neutrophil number in the infected region in individual larvae. Three independent experiments were performed. Here presents one result of three experiments. One-way ANOVA, ns: no significance, *$p < 0.05$, ***$p < 0.005$, ****$p < 0.001$. (B, C, F).

mpeg1 were used as markers in hematopoietic progenitor and stem cell (HSPCs), neutrophils, and macrophages, respectively. The WISH results revealed no significant differences in those markers between WT and *elmo1*$^{-/-}$ larvae at 3 dpf (**Supplementary Figures S2A–C**). Only *rag1,* which represents T-cells, was slightly decreased in *elmo1*$^{-/-}$ larvae at 5 dpf in the thymus (**Figure 2A**). Interestingly, the number of *Tg(coro1a: GFP)*-expressing leukocytes and that of *Tg(lck:DsRedx)*-expressing T-cells in the thymus were similar between homozygous *elmo1*$^{-/-}$ and heterozygous or wild-type siblings (**Figures 2B–D**). Thus, the reduction of *rag1* in mutants might suggest immature T-cell development instead of cellular loss. Similar to the findings at the larval stage, T-cell number in adulthood was not significantly different between *elmo1*$^{-/-}$ and siblings in the kidney, peripheral blood (PB) and spleen (**Supplementary Figures S3A–G**), as determined by flow cytometry.

We next examined whether T-cell motility was affected in the mutant, as suggested in a previous study in which ELMO1 and DOCK2 worked in concert to regulate T-cell motility in

peripheral lymphoid organs (PLOs), including spleen and lymphoid nodes (Stevenson et al., 2014). We carried out live imaging to trace individual T-cells in the thymus of *Tg (lck: DsRedx)* larvae. The results showed that the speed of T-cell migration was drastically decreased in *elmo1*$^{-/-}$ larvae, suggesting impaired mobility of *elmo1* deficient T-cells (**Figures 2E,F**).

Neutrophils Showed Attenuated Motility and Impaired Chemotaxis to Injury/Infection in the *elmo1* Mutant

Previous studies showed that fewer neutrophils responded to inflammation in *Elmo1*-deficient mice (Arandjelovic et al., 2019). Thus, we asked whether defects of neutrophils could be observed in zebrafish *elmo1* mutants. Our WISH data revealed a normal number of neutrophils in *elmo1*$^{-/-}$ larvae (**Supplementary Figure S2B**), and thus, we first examined the motility of neutrophils on the yolk sac using live imaging of *Tg (lyz: DsRed)* larvae at 3 dpf. We found that neutrophils failed to elongate their pseudopodia (**Supplementary Figure S4A**) and exhibited clumsy amoeboid movement in the *elmo1*$^{-/-}$ larvae compared with their siblings (**Supplementary Video S1**). Consequently, the speed of neutrophil movement decreased from 0.08 μm/s in siblings to 0.01 μm/s in *elmo1*$^{-/-}$ larvae (**Figures 3A,B**). In addition, we further examined the motility of macrophage on the yolk sac at 3 dpf. On the contrary to neutrophil, the basal movement of macrophage showed no difference between *elmo1*$^{-/-}$ and siblings suggesting that *elmo1* is not essential for macrophage motility (**Supplementary Figures S4C,D**).

To test whether the attenuated motility would affect an immune response, we performed tail fin transection in 3 dpf *Tg(lyz:DsRed)* larvae. As previously reported, wild-type neutrophils first arrived at the site of injury within 30 min of tail fin transection. Their number peaked at around 6 h post-transection (hpt) and returned to the basal level at 24 hpt (Li et al., 2012). In contrast, the neutrophil number was greatly reduced at the site of injury in *elmo1*$^{-/-}$ larvae from 30 min to 6 hpt after tail fin transection (**Figures 3C,D**; **Supplementary Figure S4B**).

We next examined the chemotaxis of neutrophils under infection conditions. We injected fluorescent *E.coli* into the otic vesicle of 3 dpf *Tg(lyz:DsRed)* larvae so that neutrophil chemotaxis toward bacteria could be observed directly. Since neutrophil count peaked at 3 h post-injection (hpi) (Harvie and Huttenlocher, 2015), we calculated the number of neutrophils in the region of the otic vesicle between 2-4 hpi. We found that neutrophil number was largely reduced in the otic vesicle in *elmo1*$^{-/-}$ larvae, suggesting the *elmo1* deficiency caused defects in the neutrophil response to bacterial infection (**Figures 3E,F**).

The *elmo1* was Cell-Autonomously Required for the Motility of Leukocytes in Zebrafish Larvae

We next investigated whether the impaired motility of leukocytes in the *elmo1*$^{-/-}$ mutant was due to cell-autonomous or non-cell-autonomous effects. We utilized the neutrophil-specific promoter, *lyz*, to transiently express the WT form of zebrafish *elmo1* (*elmo1*^{ze}) in neutrophils of *elmo1*$^{-/-}$ mutants and their siblings. Neutrophils expressing WT *elmo1* were visualized by GFP-linked Elmo1 (*lyz:elmo1*^{ze}). The migration of such neutrophils on the yolk sac was recorded by live imaging and their migration speeds were calculated. We found that the speed of neutrophils largely recovered after neutrophil-specific *elmo1*^{ze} expression (**Figures 4A,B**; **Supplementary Video S2**). We also examined the function of *elmo1* in T-cells using a similar approach. The *elmo1*^{ze} was transiently expressed from the *lck* promoter (*lck:elmo1*^{ze}) in T-cells and the results indicated that the speed of T-cells in *elmo1*$^{-/-}$ larvae was elevated (**Figures 4C,D**). Collectively, our results suggested that *elmo1* was cell-autonomously required for the motility of neutrophils and T-cells in zebrafish larvae.

Constitutively Activated Rac Rescued the Neutrophil Motility Deficiency of the *elmo1* Mutant

Previous studies demonstrated that *ELMO1* regulated cell migration by activating RAC proteins (Grimsley et al., 2004; Gong et al., 2018). There are three *RAC* genes, including *RAC1*, *RAC2*, and *RAC3* in vertebrate. *RAC1* is ubiquitously expressed, while *RAC2* is specifically expressed in hematopoietic cells (Mulloy et al., 2010), and *RAC3* is primarily found in the neurons (Wang and Zheng, 2007). In zebrafish, *RAC1* and *RAC3* have two orthologue: *rac1a/b* and *rac3a/b*, whereas *RAC2* only has one orthologue: *rac2*. From the single-cell transcriptome atlas of zebrafish, *rac1a/b* and *rac2*, but not *rac3a/b*, are expressed in leukocytes (Farnsworth et al., 2020). We employed RacFRET biosensor to examine whether the Rac activation was affected due to Elmo1 deficiency. We cloned the RacFRET biosensor from the Raichu-Rac1 plasmid (Itoh et al., 2002) and constructed it after the *lyz* promoter so that the FRET biosensor can be specifically expressed in neutrophils. As described in previous studies, CFP and YFP was used as the donor and the acceptor, respectively (Itoh et al., 2002). We measure the FRET to CFP change ratio to represent the GTP-bound Rac activity (Aoki and Matsuda, 2009; Bosch and Kardash, 2019), and found that the mean ratio of FRET decreased in *elmo1*$^{-/-}$ neutrophils (**Supplementary Figures S5A–C**). These results indicated that the Elmo1 deficiency resulted in reduced Rac binding to GTP. Next, to investigate whether the cell motility defects of the *elmo1*$^{-/-}$ larvae were caused by reduced Rac activation, we transiently expressed constitutively active *rac1a/b* and *rac2* under the control of the leukocyte-specific *coro1a* promoter in the *elmo1* mutant. We linked DsRed to Racs using the P2A self-cleaving peptide to visualize neutrophils expressing constitutively active Rac protein (p.G12V). Their movement was recorded by live imaging and their speed was calculated. Compared with the control (**Figure 5A**), we found that constitutively active Rac1a (**Figures 5B,E**) and

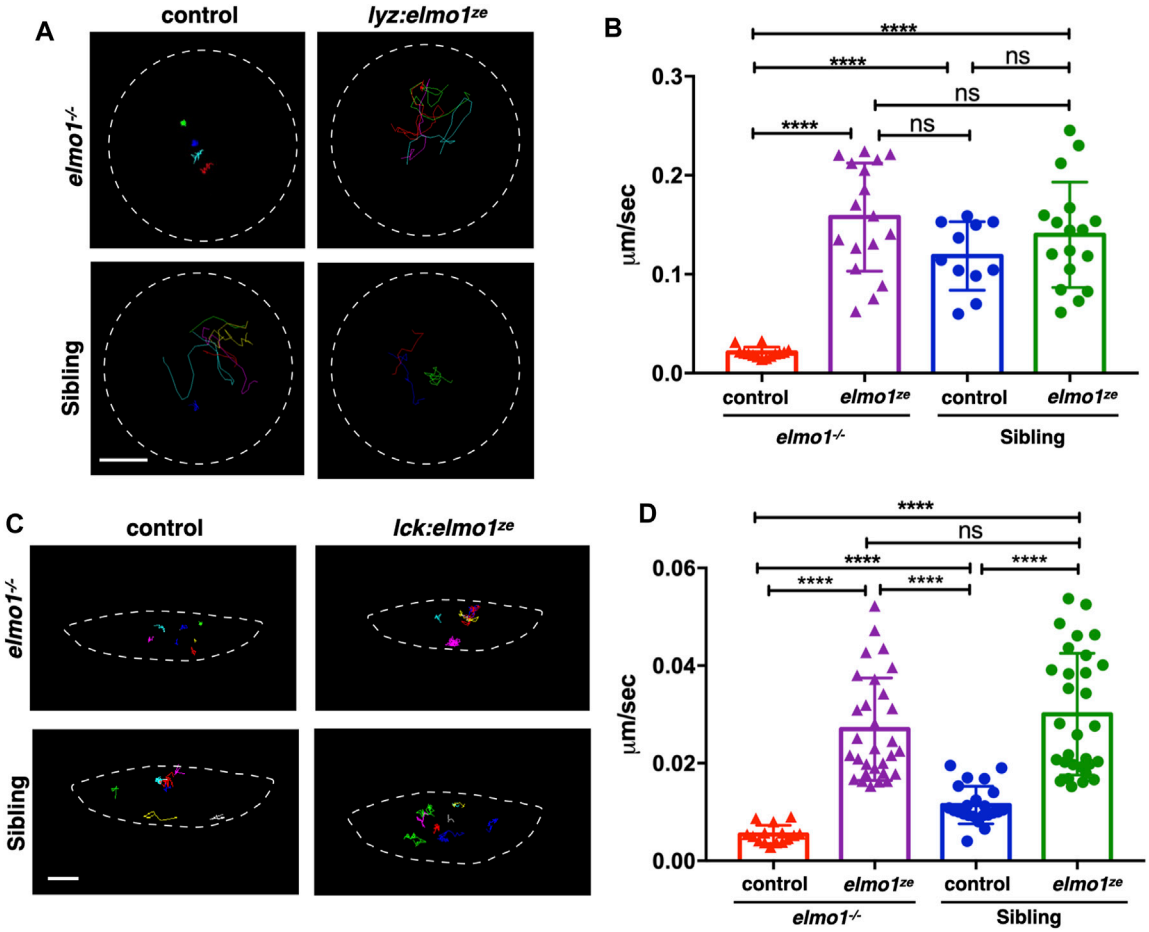

FIGURE 4 | The *elmo1* was cell-autonomously required for the motility of leukocytes in zebrafish larvae. **(A)** Track path of neutrophils expressing *lyz:GFP* (control) or *lyz:elmo1^{ze}-GFP (lyz:elmo1^{ze})* on the yolk sac in the *elmo1$^{-/-}$* and sibling larvae recorded by live imaging at 3 dpf. Each line represents the migration path of a single cell recorded by live imaging. Scale bar: 50 μm. **(B)** Quantification of the neutrophils migration speed of the control and elmo1ze group in *elmo1$^{-/-}$* (14 cells of 4 larvae, 17 cells of 6 larvae) and sibling (11 cells of 4 larvae, 17 cells of 6 larvae) larvae. Compared with the control group, the migration speed of neutrophils expressing *lyz: elmo1^{ze}* was significantly increased in the *elmo1$^{-/-}$* larvae. Each dot represents the average speed of one individual cell. Three independent experiments were performed. Here present the summarized results of three experiments. One-way ANOVA, ns: no significance, ****$p < 0.001$. **(C)** Track path of T-cells expressing *lck:DsRedx* (control) or *lck:elmo1^{ze}-GFP (lck:elmo1^{ze})* within the thymus in *elmo1$^{-/-}$* and sibling larvae recorded by live imaging at 5 dpf. Each line represents the migration path of a single cell recorded by live imaging. Scale bar: 10 μm. **(D)** Quantification of the T-cells migration speed of control and *elmo1^{ze}* group in *elmo1$^{-/-}$* (15 cells of 4 larvae, 30 cells of 9 larvae) and sibling (22 cells of 4 larvae, 31 cells of 9 larvae) larvae. Compared with the control group, the migration speed of T-cells expressing *lck:elmo1^{ze}* was significantly increased in the *elmo1$^{-/-}$* larvae. Each dot represents the average speed of one individual cell. Three independent experiments were performed. Here present the summarized results of three experiments. One-way ANOVA, ns: no significance, ****$p < 0.001$.

Rac2 (**Figures 5D,E**), but not Rac1b (**Figures 5C,E**), could significantly rescue the defective motility of neutrophils in *elmo1$^{-/-}$* larvae (**Supplementary Video S3**).

The Zebrafish *elmo1* Mutant can Serve as an *In Vivo* Model to Verify the Functions of Human Variants

Zebrafish Elmo1 (NP_998256) shares 89.41% identity with human ELMO1 (NP_055615) (Epting et al., 2010). Our data also indicated that zebrafish Elmo1 was similar to higher vertebrates in that it regulated the motility of neutrophils through the Rac proteins. Therefore, we believe that *elmo1* mutant zebrafish can serve as a valuable tool for the *in vivo* functional verification of human *ELMO1* variants. We first verified whether human *ELMO1* could rescue the reduced neutrophil motility in zebrafish *elmo1* mutant by transiently expressing the human ELMO1-GFP fusion protein. The migration of neutrophils expressing human ELMO1 was recorded using time-lapse live imaging. As expected, the expression of wild-type human ELMO1 (hu-WT) effectively rescued the impaired motility of *elmo1* mutant neutrophils, indicating the conservative role of human ELMO1 in zebrafish (**Figures 6B,C,G**; **Supplementary Video S4**). Therefore, *elmo1* mutant zebrafish could be used to verify human variants.

We next identified fourteen novel non-synonymous variants in the coding region of the human *ELMO1* gene from the

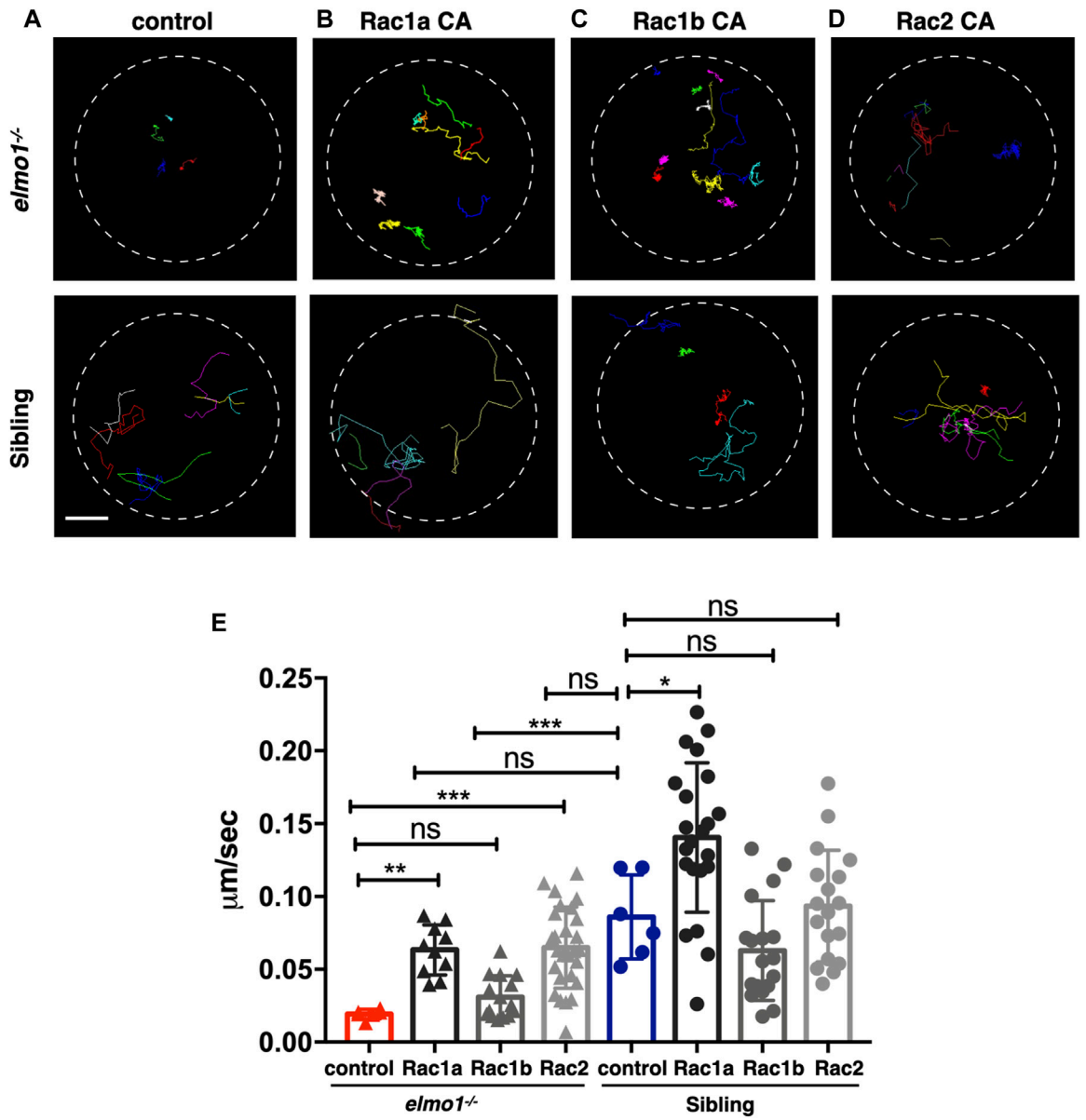

FIGURE 5 | Constitutively activated Rac rescued the neutrophil motility deficiency of the *elmo1* mutant. **(A)** Track path of neutrophils expressing *lyz:GFP* in the *elmo1*$^{-/-}$ and sibling larvae recorded by live imaging at 3 dpf. **(B–D)** Track path of neutrophils expressing constitutively activated Racs (Racs CA) in the *elmo1*$^{-/-}$ and sibling larvae recorded by live imaging at 3 dpf. **(B)** Rac1a CA, **(C)** Rac1b CA, **(D)** Rac2 CA. Each line represents the migration path of individual cells. **(A–D)** Scale bar: 50 μm. **(E)** Quantification of the migration speed of control and neutrophils expressing constitutively activated Racs in the *elmo1*$^{-/-}$ (6 cells of 3 larvae, 10 cells of 6 larvae, 13 cells of 6 larvae, 25 cells of 6 larvae) and sibling (6 cells of 3 larvae, 22 cells of 6 larvae, 18 cells of 6 larvae, 18 cells of 6 larvae) larvae. Compared with the control group, the migration speed of neutrophils expressing Rac1a CA (Rac1a) and Rac2 CA (Rac2) were significantly increased. Neutrophils expressing Rac1a CA (Rac1a) also show an increased the migration speed in sibling. Each dot represents the speed of individual cells. Three independent experiments were performed. Here present the summarized results of three experiments. One-way ANOVA, ns: no significance, *$p < 0.05$, **$p < 0.01$, ***$p < 0.005$, ****$p < 0.001$.

GuangZhou KingMed Center For Clinical Laboratory Co., Ltd genetics database (**Table 1**). Based on the conservation of amino acids, we excluded four variants in which the amino acids differed between human and zebrafish. Furthermore, eight variants were excluded because their amino acid properties were not significantly changed. Of the remaining three variants, p.E90K (c.268G>A) and p.D194G (c.581A>G) changed the amino acid properties, whereas p.R354X (c.1060C>T) resulted in a premature stop codon prior to the PH domain, which interacts with the DOCK protein (**Figure 6A**). To verify the functional changes of p.E90K, p.D194G, and p.R354X *in vivo*, we transiently expressed human *ELMO1* carrying these variants in neutrophils. The ELMO1-positive neutrophils were visualized using GFP, which

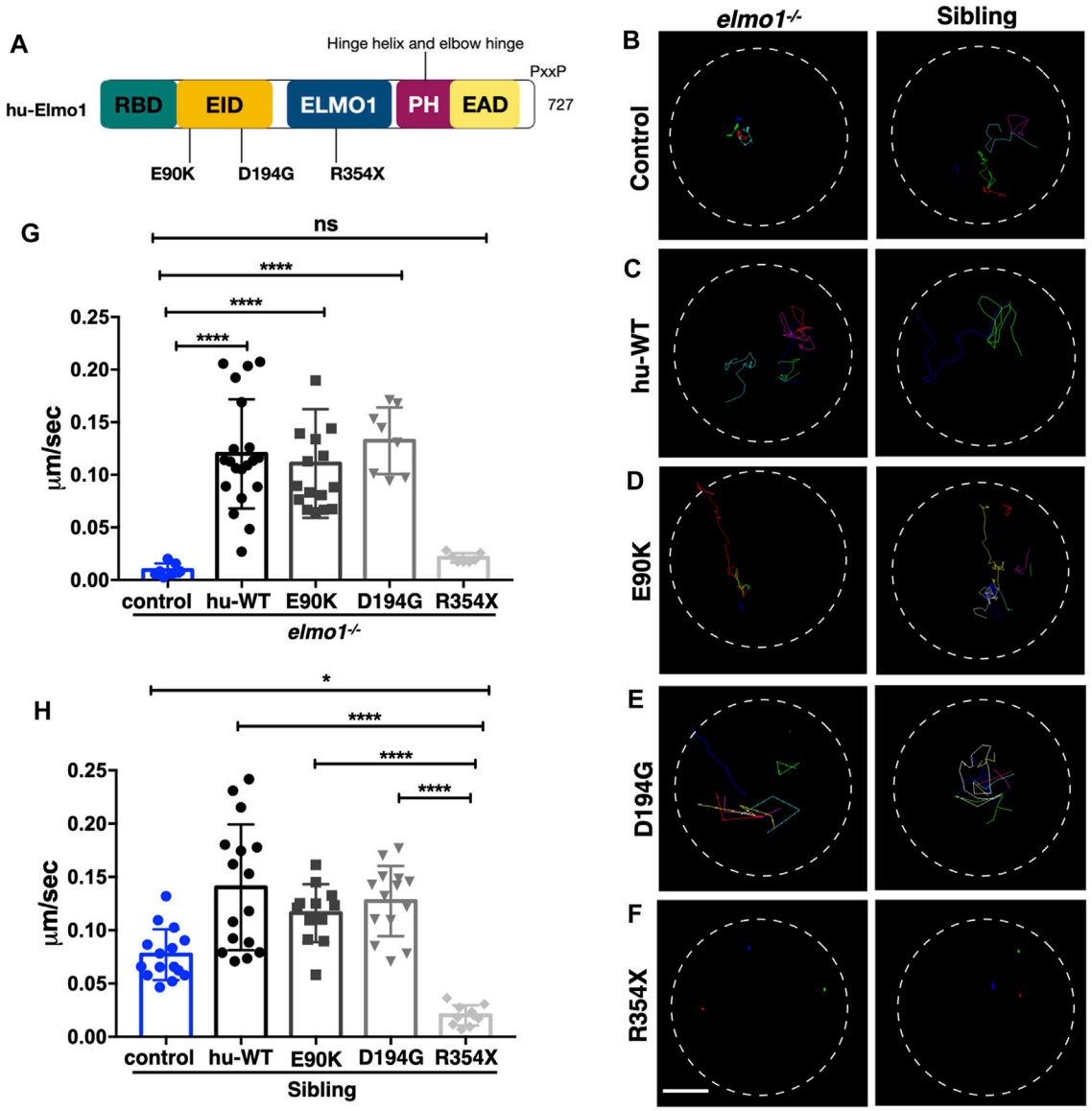

FIGURE 6 | The zebrafish *elmo1* mutant can serve as an *in vivo* model to verify the functions of human variants. **(A)** Schematic view of human ELMO1 protein conserved domains. Position of tested variants: p.E90K (E90K), p.D194G (D194G), and p.R354X (R354X) are indicated. **(B–F)** Track path of neutrophils expressing *lyz:GFP* control **(B)** or human ELMO1 **(C–F)** in the *elmo1*$^{-/-}$ and siblings recorded by live imaging at 3 dpf. Human wild-type (hu-WT) form **(C)**, E90K **(D)**, D194G **(E)**, R354X **(F)**. **(G, H)** Quantification of the migration speed of the control group and neutrophils expressing human ELMO1 variants in the *elmo1*$^{-/-}$ (7 cells of 3 larvae, 20 cells of 6 larvae, 16 cells of 6 larvae, 8 cells of 6 larvae, 7 cells of 3 larvae) **(G)** and sibling (15 cells of 3 larvae, 16 cells of 7 larvae, 12 cells of 8 larvae, 14 cells of 7 larvae, 10 cells of 5 larvae). **(H)**. hu-WT, E90K, and D194G could efficiently rescue the migration speed in the elmo1 mutant compared with control. R354X failed to rescue the defects in *elmo1*$^{-/-}$ and even show a decreased migration speed in siblings. One-way ANOVA, ns: no significance, *$p < 0.05$, ****$p < 0.001$. Scale bar: 50 μm **(B–F)**.

was directly fused to ELMO1. The migration paths of neutrophils were recorded using live imaging and the migration speeds were calculated. Compared with the control group (**Figures 6B,G**), p.E90K and p.D194G (**Figures 6D,E,G**; **Supplementary Video S4**) could effectively restore the migration speed of *elmo1*$^{-/-}$ larvae, while p.R354X (**Figures 6F,G**) failed to do so. Interestingly, the transient expression of p.R354X also significantly reduced the migration speed of neutrophils in siblings (**Figures 6F,H**; **Supplementary Video S5**).

DISCUSSION

As a member of the ELMO1-DOCK2 protein complex, it is known that *DOCK2* deficiency can lead to inherent immunodeficiency diseases in the human population, whereas genetic polymorphism studies have shown that *ELMO1* variants are associated with autoimmune diseases. In mice arthritis model induced by K/BxN serum or collagen, *Elmo1* deficiency can relieve the inflammatory response and cause a better outcome of the disease by reducing the

TABLE 1 | Informations of the human ELMO1 variants. Here list the identified fourteen novel non-synonymous variants in the coding region of the human ELMO1 gene found from the KingMed Diagnostics Group genetics database. (1–10) List the variants in which amino acids are conserved between human and zebrafish. (1–3) p.E90K (c.268G>A) and p.D194G (c.581A>G) changed the amino acid properties, whereas p.R354X (c.1060C>T) resulted in a premature stop codon prior to the pH domain, which interacts with the DOCK protein. (11–14) List the variants in which amino acids are conserved between human and zebrafish.

	cDNA change	Amino acid change	Functional domain	Properties change	Neutrophil motility	Amino acid in zebrafish
1	c.268G>A	p.E90K	EID	acid-basic	Rescued	
2	c.581A>G	p.D194G	EID	acid-nonpolar	Rescued	
3	c.1060C>T	p.R354X	ELMOI	stop	Negative	
4	c.22G>A	p.V8I	RBD	nonpolar-nonpolar	Not available	
5	c.34A>G	p.II2V	RBD	nonpolar-nonpolar		
6	c.610A>G	p.I204V	EID	nonpolar-nonpolar		
7	c.825T>G	p.I275M	EID	nonpolar-nonpolar		
8	c.1771T>G	p.L591V	PH	nonpolar-nonpolar		
9	c.1553G>A	p.R518H	ELMOI	basic-basic		
10	c.1873A>G	p.M625V	PH	nonpolar-nonpolar		
11	c.791A>G	p.N264S	EID	polar-polar		H
12	c.864T>G	p.N288K	EID	polar-polar		D
13	c.2038G>C	p.D680H	PH	acid-acid		E
14	c.2125G>A	p.A709T	PxxP	nonpolar-polar		E

accumulation of neutrophils (Arandjelovic et al., 2019). This study gave us a hint that *elmo1* gene function on regulating the chemotaxis of neutrophils and even other immune cells. So far, most of the works have been done under pathological conditions such as diabetes, bowl inflammation, and RA in the mice model (Arandjelovic et al., 2019; Das et al., 2015; Hathaway et al., 2016). These results indicate that ELMO1 affects the motility of immune cells. In our study, we used the zebrafish model to directly observe the behavior of immune cells affected by Elmo1 through *in vivo* live imaging under physiological conditions. Consistent with previous studies about the ELMO1 participated in regulating cell migration in mice and cell culture (Gumienny et al., 2001; Grimsley et al., 2004; Arandjelovic et al., 2019), we found that the random ameboid migration of neutrophils and T-cells were significantly reduced in *elmo1*$^{-/-}$ larvae, and the chemotaxis of neutrophils was also reduced after injury or infection in *elmo1*$^{-/-}$ larvae by *in vivo* live imaging (**Figure 2**, **Figure3**). Consistent with Mikdache's report in which macrophage activity in the *elmo1* mutant was found normal in the Posterior Lateral Line ganglion, we also found that the motility of macrophage showed no differences between sibling and *elmo1*$^{-/-}$ larvae at 3 dpf (Mikdache et al., 2020). Although, in *elmo1* morphant, macrophages showed abnormal morphology in the brain at 48 hpf and failed to engulf apoptotic cells in *elmo1* knock-down embryos (van Ham et al., 2012), we have observed that macrophages showed normal morphology in *elmo1* mutant embryos on the yolk. The inconsistency between the morphants and mutants is possibly due to the nonspecific effects of morpholino. Alternatively, a genetic compensation response could be provoked in mutant macrophages (Rossi et al., 2015). It warrants further study to distinguish which possibility is true. However, no patients carried *ELMO1* bi-allele mutation have been reported yet. Whether *ELMO1* mutation could lead to immunodeficiency in human warrants further study.

Racs have been reported works as the downstream of DOCK-ELMO1 complex in regulating cell motility (Brugnera et al., 2002; Epting et al., 2015; Chang et al., 2020; Mutsuko Kukimoto-Niino et al., 2021). It is known that, in the case of ELMO1-DOCK2-RAC1, RAC1 directly bind to the DHR2 domain of the DOCK2 protein (Chang et al., 2020). Interestingly, Mutsuko Kukimoto-Niino et al. reported that RAC1 could also interacted with the PH domain on the ELMO1, by which, the PH domain of ELMO1 stabilizes the transition state of the DOCK5 (DHR-2)–Rac1 complex, providing the structural basis for ELMO1-mediated enhancement of the catalytic activity of DOCK5 (Mutsuko Kukimoto-Niino et al., 2021). As expected, the Rac activity was disrupted in *elmo1*$^{-/-}$ larvae. (**Supplementary Figures S5A–C**). Whether the Racs activity in neutrophils is regulated *via* Dock proteins or directly by Elmo1 remains to be clarified. We found that in addition to constitutively activated Rac1a, constitutively activated Rac2 could also effectively rescued the motility defects of neutrophils in *elmo1* mutants; thus, suggesting that Racs functioned downstream of Elmo1 in zebrafish. More importantly, human *ELMO1* could also rescue the defective motility phenotype of mutant neutrophils in zebrafish. These results indicated that *elmo1* acted through a conserved mechanism in zebrafish (Stevenson et al., 2014; Chang et al., 2020); thus, supporting the use of zebrafish as a suitable animal model for identifying functional changes in human *ELMO1* variants.

We performed live imaging on transparent zebrafish larvae to verify the function of the human *ELMO1* variant of neutrophil motility. This assay also provided us a unique opportunity to directly observe the function of *ELMO1* variants *in vivo*. For the three *ELMO1* variants chosen for analysis, p.E90K and p.D194G variants were located in the conserved ELMO inhibitory domain (EID). However, they were not on the ELMO1-DOCK2 interface or the interface with any other known partner of ELMO1, such as RhoG1 or BAI1 (Katoh and Negishi, 2003; Park et al., 2007). Therefore, we hypothesized that these two variants may not substantially interfere with the function of *ELMO1*. Indeed, these two variants successfully rescued the abnormal neutrophil motility of *elmo1* mutant zebrafish. The remaining variant, p.R354X (c.1060C>T), resulted in a stop codon prior to the PH domain, which interacted with the DOCK or RAC, suggesting that it would fail to regulate downstream effecter activities. As expected, the p.R354X variant could not recover the migration speed of neutrophils in the *elmo1* mutant. Interestingly, this variant also

impaired the migration of neutrophils in siblings. We hypothesized that the transiently expressed p.R354X variant may outcompete wild-type ELMO1 for its N-terminal binding partners, including RhoG and BAI1, under over-expression condition. Consequently, the function of wild-type ELMO1 was attenuated in such zebrafish.

Although zebrafish provide a quick and convenient model for testing *ELMO1* variants *in vivo*, we also observed that the transient expression of variants in zebrafish had limitations. For example, we expressed *ELMO1* variants under the control of the *lyz* promoter, which may lead to higher concentrations of *ELMO1* variant proteins in neutrophils than physiological conditions. This may, in turn, cause excessive activation or inhibition of *ELMO1*. To overcome this challenge, we may use the endogenous *elmo1* promoter instead of the *lyz* promoter to drive the expression of *ELMO1* variants. Large-scale clinical analyses with *in vivo* functional studies of *ELMO1* variants should also be combined to better understand the physiological or pathological roles of such variants.

In summary, we found that zebrafish *elmo1* gene functioned in a conserved way in neutrophils. With the zebrafish *elmo1* mutant, we have established a convenient *in vivo* model for the effective analysis of human *ELMO1* variants. This model could facilitate the characterization of *ELMO1* variants and provide valuable suggestions for clinical decision-making. Similar methods could also be applied in zebrafish to *in vivo* evaluations of genetic variants of other genes.

DATA AVAILABILITY STATEMENT

The datasets presented in this study can be found in online repositories. The names of the repository/repositories and accession number(s) can be found below: NCBI [accession: SRR16351675, SRR16351676, SRR16351677].

ETHICS STATEMENT

The studies involving human participants were reviewed and approved by the Ethics Committee of GuangZhou KingMed Center For Clinical Laboratory CO.,Ltd. The patients/participants provided their written informed consent to participate in this study. Ethical review and approval was not required for the animal study because we use the zebrafish as the animal model.

AUTHOR CONTRIBUTIONS

Conceptualization: RX and JX; Data curation: RX and GM; Formal Analysis, RX, and YW; Funding Acquisition, QL, JX, and SY; Investigation: RX, YW, TW, ML, and JL; Resources, RX, GM, XF, and JX; Visualization, RX and JX; Writing-original draft: RX; Writing-review and editing: JX and QL; Supervision, JX, QL, KY, and SY.

FUNDING

This work was supported by the National Natural Science Foundation of China (31771594; 31970763; 81770190), the National Key Research and Development Programs (2018YFA0800200; 2017YFA105500; 2017YFA105504), the Guangdong Science and Technology Plan projects (2019A030317001), and the Program for Entrepreneurial and Innovative Leading Talents of Guangzhou, China (CXLJTD-201603).

ACKNOWLEDGMENTS

We thank Zilong WEN (Hong Kong University of Science and Technology, Hong Kong, China) for sharing the GFP positive *E.coli, Tg(globin:LoxP-DsRedx-LoxP-GFP), Tg(lck:LoxP-DsRedx-LoxP-GFP),* and *Tg(mpeg1:LoxP-DsRedx-LoxP-GFP)*. We thank M.D. Michiyuki Matsuda (Laboratory of Bioimaging and Cell Signaling, Graduate School of Biostudies, Kyoto University, Kyoto, Janpa) for the kindly sharing the Raichu-Rac1 plasmid.

SUPPLEMENTARY MATERIAL

The Supplementary Material for this article can be found online at: https://www.frontiersin.org/articles/10.3389/fcell.2021.723804/full#supplementary-material

REFERENCES

Aoki, K., and Matsuda, M. (2009). Visualization of Small GTPase Activity with Fluorescence Resonance Energy Transfer-Based Biosensors. *Nat. Protoc.* 4, 1623–1631. doi:10.1038/nprot.2009.175

Arandjelovic, S., Perry, J. S. A., Lucas, C. D., Penberthy, K. K., Kim, T.-H., Zhou, M., et al. (2019). A Noncanonical Role for the Engulfment Gene ELMO1 in Neutrophils that Promotes Inflammatory Arthritis. *Nat. Immunol.* 20, 141–151. doi:10.1038/s41590-018-0293-x

Barresi, M. J., Stickney, H. L., and Devoto, S. H. (2000). The Zebrafish Slow-Muscle-Omitted Gene Product Is Required for Hedgehog Signal Transduction and the Development of Slow Muscle Identity. *Development* 127, 2189–2199. doi:10.1242/dev.127.10.2189

Bayoumy, N. M. K., El-Shabrawi, M. M., Leheta, O. F., Abo El-Ela, A. E. M., and Omar, H. H. (2020). Association of ELMO1 Gene Polymorphism and Diabetic Nephropathy Among Egyptian Patients with Type 2 Diabetes Mellitus. *Diabetes Metab. Res. Rev.* 36, e3299. doi:10.1002/dmrr.3299

Bosch, M., and Kardash, E. (2019). *In Vivo* Quantification of Intramolecular FRET Using RacFRET Biosensors. *Methods Mol. Biol.* 2040, 275–297. doi:10.1007/978-1-4939-9686-5_13

Brugnera, E., Haney, L., Grimsley, C., Lu, M., Walk, S. F., Tosello-Trampont, A.-C., et al. (2002). Unconventional Rac-GEF Activity Is Mediated through the Dock180-ELMO Complex. *Nat. Cel Biol* 4, 574–582. doi:10.1038/ncb824

Capala, M. E., Vellenga, E., and Schuringa, J. J. (2014). ELMO1 is Upregulated in AML CD34+ Stem/Progenitor Cells, Mediates Chemotaxis and Predicts Poor Prognosis in Normal Karyotype AML. *PLoS One* 9, e111568.

Chang, L., Yang, J., Jo, C. H., Boland, A., Zhang, Z., Mclaughlin, S. H., et al. (2020). Structure of the DOCK2–ELMO1 Complex Provides Insights into Regulation of the Auto-Inhibited State. *Nat. Commun.* 11, 3464. doi:10.1038/s41467-020-17271-9

Dahm, C. N.-V. A. R. (2002). *Zebrafish – A Practical Approach*. Oxford: Oxford University Press.

Das, S., Sarkar, A., Choudhury, S. S., Owen, K. A., Derr-Castillo, V. L., Fox, S., et al. (2015). Engulfment and Cell Motility Protein 1 (ELMO1) Has an Essential Role in the Internalization of Salmonella Typhimurium into Enteric Macrophages that Impact Disease Outcome. *Cell Mol. Gastroenterol. Hepatol.* 1, 311–324. doi:10.1016/j.jcmgh.2015.02.003

Dobbs, K., Domínguez Conde, C., Zhang, S.-Y., Parolini, S., Audry, M., Chou, J., et al. (2015). Inherited DOCK2 Deficiency in Patients with Early-Onset Invasive Infections. *N. Engl. J. Med.* 372, 2409–2422. doi:10.1056/nejmoa1413462

Dooley, K., and Zon, L. I. (2000). Zebrafish: a Model System for the Study of Human Disease. *Curr. Opin. Genet. Dev.* 10, 252–256. doi:10.1016/s0959-437x(00)00074-5

Epting, D., Slanchev, K., Boehlke, C., Hoff, S., Loges, N. T., Yasunaga, T., et al. (2015). The Rac1 Regulator ELMO Controls Basal Body Migration and Docking in Multiciliated Cells through Interaction with Ezrin. *Development* 142, 1553. doi:10.1242/dev.124214

Epting, D., Wendik, B., Bennewitz, K., Dietz, C. T., Driever, W., and Kroll, J. (2010). The Rac1 Regulator ELMO1 Controls Vascular Morphogenesis in Zebrafish. *Circ. Res.* 107, 45–55. doi:10.1161/circresaha.109.213983

Farnsworth, D. R., Saunders, L. M., and Miller, A. C. (2020). A Single-Cell Transcriptome Atlas for Zebrafish Development. *Dev. Biol.* 459, 100–108. doi:10.1016/j.ydbio.2019.11.008

Federici, G., and Soddu, S. (2020). Variants of Uncertain Significance in the Era of High-Throughput Genome Sequencing: a Lesson from Breast and Ovary Cancers. *J. Exp. Clin. Cancer Res.* 39, 46. doi:10.1186/s13046-020-01554-6

Gong, P., Chen, S., Zhang, L., Hu, Y., Gu, A., Zhang, J., et al. (2018). RhoG-ELMO1-RAC1 Is Involved in Phagocytosis Suppressed by Mono-Butyl Phthalate in TM4 Cells. *Environ. Sci. Pollut. Res.* 25, 35440–35450. doi:10.1007/s11356-018-3503-z

Grimsley, C. M., Kinchen, J. M., Tosello-Trampont, A.-C., Brugnera, E., Haney, L. B., Lu, M., et al. (2004). Dock180 and ELMO1 Proteins Cooperate to Promote Evolutionarily Conserved Rac-dependent Cell Migration. *J. Biol. Chem.* 279, 6087–6097. doi:10.1074/jbc.m307087200

Gumienny, T. L., Brugnera, E., Tosello-Trampont, A. C., Kinchen, J. M., Haney, L. B., Nishiwaki, K., et al. (2001). CED-12/ELMO, a Novel Member of the CrkII/Dock180/Rac Pathway, is Required for Phagocytosis and Cell Migration. *Cell* 107, 27–41.

Harvie, E. A., and Huttenlocher, A. (2015). Neutrophils in Host Defense: New Insights from Zebrafish. *J. Leukoc. Biol.* 98, 523–537. doi:10.1189/jlb.4mr1114-524r

Hathaway, C. K., Chang, A. S., Grant, R., Kim, H.-S., Madden, V. J., Bagnell, C. R., Jr., et al. (2016). High Elmo1 Expression Aggravates and Low Elmo1 Expression Prevents Diabetic Nephropathy. *Proc. Natl. Acad. Sci. USA* 113, 2218–2222. doi:10.1073/pnas.1600511113

Hayashi, K., Teramoto, R., Nomura, A., Asano, Y., Beerens, M., Kurata, Y., et al. (2020). Impact of Functional Studies on Exome Sequence Variant Interpretation in Early-Onset Cardiac Conduction System Diseases. *Cardiovasc. Res.* 116, 2116–2130. doi:10.1093/cvr/cvaa010

Hu, Z., Liu, Y., Huarng, M. C., Menegatti, M., Reyon, D., Rost, M. S., et al. (2017). Genome Editing of Factor X in Zebrafish Reveals Unexpected Tolerance of Severe Defects in the Common Pathway. *Blood* 130, 666–676. doi:10.1182/blood-2017-02-765206

Itoh, R. E., Kurokawa, K., Ohba, Y., Yoshizaki, H., Mochizuki, N., and Matsuda, M. (2002). Activation of Rac and Cdc42 Video Imaged by Fluorescent Resonance Energy Transfer-Based Single-Molecule Probes in the Membrane of Living Cells. *Mol. Cel Biol* 22, 6582–6591. doi:10.1128/mcb.22.18.6582-6591.2002

Janardhan, A., Swigut, T., Hill, B., Myers, M. P., and Skowronski, J. (2004). HIV-1 Nef Binds the DOCK2-ELMO1 Complex to Activate Rac and Inhibit Lymphocyte Chemotaxis. *Plos Biol.* 2, E6. doi:10.1371/journal.pbio.0020006

Jiang, J., Liu, G., Miao, X., Hua, S., and Zhong, D. (2011). Overexpression of Engulfment and Cell Motility 1 Promotes Cell Invasion and Migration of Hepatocellular Carcinoma. *Exp. Ther. Med.* 2, 505–511.

Jin, H., Xu, J., Qian, F., Du, L., Tan, C. Y., Lin, Z., et al. (2006). The 5′ Zebrafishscl Promoter Targets Transcription to the Brain, Spinal Cord, and Hematopoietic and Endothelial Progenitors. *Dev. Dyn.* 235, 60–67. doi:10.1002/dvdy.20613

Katoh, H., Fujimoto, S., Ishida, C., Ishikawa, Y., and Negishi, M. (2006). Differential Distribution of ELMO1 and ELMO2 mRNAs in the Developing Mouse brainGenetic Variations in the Gene Encoding ELMO1 Are Associated with Susceptibility to Diabetic Nephropathy. *BRAIN RESEARCH* 1073-1074, 103–108. doi:10.1016/j.brainres.2005.12.085

Katoh, H., and Negishi, M. (2003). RhoG Activates Rac1 by Direct Interaction with the Dock180-Binding Protein Elmo. *Nature* 424, 461–464. doi:10.1038/nature01817

Kimmel, C. B., Kimmel, W. W. B., Ballard, W. W., Kimmel, S. R., and Schilling, T. F. (1995). Stages of Embryonic Development of the Zebrafish. *Dev. Dyn.* 203, 253–310. doi:10.1002/aja.1002030302

Kitaguchi, T., Kawakami, K., and Kawahara, A. (2009). Transcriptional Regulation of a Myeloid-Lineage Specific Gene Lysozyme C during Zebrafish Myelopoiesis. *Mech. Dev.* 126, 314–323. doi:10.1016/j.mod.2009.02.007

Langenau, D. M., Ferrando, A. A., Traver, D., Kutok, J. L., Hezel, J.-P. D., Kanki, J. P., et al. (2004). *In Vivo* tracking of T Cell Development, Ablation, and Engraftment in Transgenic Zebrafish. *Proc. Natl. Acad. Sci.* 101, 7369–7374. doi:10.1073/pnas.0402248101

Li, H., and Durbin, R. (2010). Fast and Accurate Long-Read Alignment with Burrows-Wheeler Transform. *Bioinformatics* 26, 589–595. doi:10.1093/bioinformatics/btp698

Li, L., Yan, B., Shi, Y.-Q., Zhang, W.-Q., and Wen, Z.-L. (2012). Live Imaging Reveals Differing Roles of Macrophages and Neutrophils during Zebrafish Tail Fin Regeneration. *J. Biol. Chem.* 287, 25353–25360. doi:10.1074/jbc.m112.349126

Lin, X., Zhou, Q., Zhao, C., Lin, G., Xu, J., and Wen, Z. (2019). An Ectoderm-Derived Myeloid-like Cell Population Functions as Antigen Transporters for Langerhans Cells in Zebrafish Epidermis. *Dev. Cel* 49, 605–617. e605. doi:10.1016/j.devcel.2019.03.028

Mikdache, A., Fontenas, L., Albadri, S., Revenu, C., Loisel-Duwattez, J., Lesport, E., et al. (2020). Elmo1 Function, Linked to Rac1 Activity, Regulates Peripheral Neuronal Numbers and Myelination in Zebrafish. *Cell. Mol. Life Sci.* 77, 161–177. doi:10.1007/s00018-019-03167-5

Moore, F. E., Moore, D. R., Sander, R. D., Martinez, Sarah. A., Blackburn, Jessica. S., Cyd, K., et al. (2012). Improved Somatic Mutagenesis in Zebrafish Using Transcription Activator-like Effector Nucleases (TALENs). *PLoS One* 7, e37877. doi:10.1371/journal.pone.0037877

Mulloy, J. C., Cancelas, J. A., Filippi, M.-D., Kalfa, T. A., Guo, F., and Zheng, Y. (2010). Rho GTPases in Hematopoiesis and Hemopathies. *Blood* 115, 936–947. doi:10.1182/blood-2009-09-198127

Mutsuko Kukimoto-Niino, K. K., Kaushik, Rahul., Ehara, Haruhiko., Yokoyama, Takeshi., Uchikubo-Kamo, Tomomi., Nakagawa, Reiko., et al. (2021). Cryo-EM Structure of the Human ELMO1-DOCK5-Rac1 Complex. *SCIENCE ADVANCES* 7, eabg3147. doi:10.2210/pdb7dpa/pdb

Nguyen-Chi, M., Phan, Q. T., Gonzalez, C., Dubremetz, J.-F., Levraud, J.-P., and Lutfalla, G. (2014). Transient Infection of the Zebrafish Notochord with *E. coli* Induces Chronic Inflammation. *Dis. Model. Mech.* 7, 871–882. doi:10.1242/dmm.014498

Nishida, K., Kaziro, Y., and Satoh, T. (1999). Anti-apoptotic Function of Rac in Hematopoietic Cells. *Oncogene* 18, 407–415. doi:10.1038/sj.onc.1202301

Olson, E. J., Hartsough, L. A., Landry, B. P., Shroff, R., and Tabor, J. J. (2014). Characterizing Bacterial Gene Circuit Dynamics with Optically Programmed Gene Expression Signals. *Nat. Methods* 11, 449–455. doi:10.1038/nmeth.2884

Park, D., Tosello-Trampont, A.-C., Elliott, M. R., Lu, M., Haney, L. B., Ma, Z., et al. (2007). Bai1 Is an Engulfment Receptor for Apoptotic Cells Upstream of the ELMO/Dock180/Rac Module. *Nature* 450, 430–434. doi:10.1038/nature06329

Park, Y. L., Choi, J. H., Park, S. Y., Oh, H. H., Kim, D. H., Seo, Y. L., et al. (2020). Engulfment and Cell Motility 1 Promotes Tumor Progression Via the Modulation of Tumor Cell Survival in Gastric Cancer. *Am. J. Transl. Res.* 12, 7797–7811.

Patel, A., Kostyak, J., Dangelmaier, C., Badolia, R., Bhavanasi, D., Aslan, J. E., et al. (2019). ELMO1 Deficiency Enhances Platelet Function. *Blood Adv.* 3, 575–587. doi:10.1182/bloodadvances.2018016444

Rossi, A., Kontarakis, Z., Gerri, C., Nolte, H., Hölper, S., Krüger, M., et al. (2015). Genetic Compensation Induced by Deleterious Mutations but Not Gene Knockdowns. *Nature* 524, 230–233. doi:10.1038/nature14580

Sarkar, A., Tindle, C., Pranadinata, R. F., Reed, S., Eckmann, L., Stappenbeck, T. S., et al. (2017). ELMO1 Regulates Autophagy Induction and Bacterial Clearance during Enteric Infection. *J. Infect. Dis.* 216, 1655–1666. doi:10.1093/infdis/jix528

Sharma, K. R., Heckler, K., Stoll, S. J., Hillebrands, J.-L., Kynast, K., Herpel, E., et al. (2016). ELMO1 Protects Renal Structure and Ultrafiltration in Kidney Development and under Diabetic Conditions. *Sci. Rep.* 6, 37172. doi:10.1038/srep37172

Stevenson, C., De La Rosa, G., Anderson, C. S., Murphy, P. S., Capece, T., Kim, M., et al. (2014). Essential Role of Elmo1 in Dock2-dependent Lymphocyte Migration. *J.I.* 192, 6062–6070. doi:10.4049/jimmunol.1303348

Thisse, C., and Thisse, B. (2008). High-resolution *In Situ* Hybridization to Whole-Mount Zebrafish Embryos. *Nat. Protoc.* 3, 59–69. doi:10.1038/nprot.2007.514

Tian, Y., Xu, J., Feng, S., He, S., Zhao, S., Zhu, L., et al. (2017). The First Wave of T Lymphopoiesis in Zebrafish Arises from Aorta Endothelium Independent of Hematopoietic Stem Cells. *J. Exp. Med.* 214, 3347–3360. doi:10.1084/jem.20170488

Van Ham, T. J., Kokel, D., and Peterson, R. T. (2012). Apoptotic Cells Are Cleared by Directional Migration and Elmo1- Dependent Macrophage Engulfment. *Curr. Biol.* 22, 830–836. doi:10.1016/j.cub.2012.03.027

Wang, L., and Zheng, Y. (2007). Cell Type-specific Functions of Rho GTPases Revealed by Gene Targeting in Mice. *Trends Cel Biol.* 17, 58–64. doi:10.1016/j.tcb.2006.11.009

Xu, J., Wang, T., Wu, Y., Jin, W., and Wen, Z. (2016). Microglia Colonization of Developing Zebrafish Midbrain Is Promoted by Apoptotic Neuron and Lysophosphatidylcholine. *Dev. Cel* 38, 214–222. doi:10.1016/j.devcel.2016.06.018

Yang, Y., Muzny, D. M., Reid, J. G., Bainbridge, M. N., Willis, A., Ward, P. A., et al. (2013). Clinical Whole-Exome Sequencing for the Diagnosis of Mendelian Disorders. *N. Engl. J. Med.* 369, 1502–1511. doi:10.1056/nejmoa1306555

Zhang, L., Zhang, J., Yang, J., Ying, D., Lau, Y. l., and Yang, W. (2013). PriVar: a Toolkit for Prioritizing SNVs and Indels from Next-Generation Sequencing Data. *Bioinformatics* 29, 124–125. doi:10.1093/bioinformatics/bts627

Conflict of Interest: TW was employed by the Beigene Ltd. and GM, XF, and SY were employed by the company GuangZhou KingMed Center For Clinical Laboratory Co., Ltd.

The remaining authors declare that the research was conducted in the absence of any commercial or financial relationships that could be construed as a potential conflict of interest.

Publisher's Note: All claims expressed in this article are solely those of the authors and do not necessarily represent those of their affiliated organizations, or those of the publisher, the editors and the reviewers. Any product that may be evaluated in this article, or claim that may be made by its manufacturer, is not guaranteed or endorsed by the publisher.

frontiers in Cell and Developmental Biology

ORIGINAL RESEARCH
published: 31 January 2022
doi: 10.3389/fcell.2021.760480

Role of SVEP1 in Stroma-Dependent Hematopoiesis *In vitro*

Vinson Tran[1] *and Helen C. O'Neill*[2]*

[1]Research School of Biology, Australian National University, Canberra, ACT, Australia, [2]Clem Jones Centre for Regenerative Medicine, Bond University, Gold Coast, QLD, Australia

Study of the microenvironment that supports hematopoietic stem cell (HSC) development *in vivo* is very difficult involving small numbers of interacting cells which are usually not well defined. While much is known about HSC niches located within the bone marrow in terms of contributing cell types and signalling molecules, very little is known about equivalent niches within spleen. Extramedullary hematopoiesis in spleen contributes myeloid cells important in the mobilisation of an immune response. As a result, it is important to develop *in vitro* models to identify the cells which constitute HSC niches in spleen and to identify the regulatory molecules supporting myeloid cell development. Studies described here document a model system to study the maintenance and differentiation of HSC by splenic stromal cells *in vitro*. The splenic stromal lines 5G3 and 3B5 differ in hematopoietic support capacity. SVEP1 and IGF2 are molecules of interest specifically expressed by 5G3 stroma. Gene knockdown technology using shRNA plasmids has been used to reduce gene expression in 5G3 and to determine specific effects on myeloid cell development following co-culture with overlaid hematopoietic progenitors *in vitro*. Knockdown of *Svep1* gave specific inhibition of a dendritic cell (DC) population described previously in spleen (L-DC). Knockdown of *Igf2* resulted in loss of production of a minor subset of conventional (c) DC. SVEP1 is now considered a marker of mesenchymal stromal cells with osteogenic differentiative capacity reflective of perivascular stromal cells. The power of this *in vitro* model is evidenced by the fact that it has been used to define SVEP1 as a specific adhesion molecule that regulates the hematopoietic process dependent on stromal niche interaction. The identification of stromal cells and molecules that contribute to the hematopoietic process in spleen, brings us closer to the realm of therapeutically regulating hematopoiesis *in vivo*, and to inhibiting niches which support cancer stem cells.

Keywords: myelopoiesis, stroma, spleen, SVEP1, hematopoietic stem cell

OPEN ACCESS

Edited by:
Valerie Kouskoff,
The University of Manchester, United Kingdom

Reviewed by:
Olga Pershina,
Research Institute of Pharmacology and Regenerative Medicine named ED Goldberg (RAS), Russia
Gerard Hoyne,
University of Notre Dame Australia, Australia

***Correspondence:**
Helen C. O'Neill
honeill@bond.edu.au

Specialty section:
This article was submitted to Stem Cell Research, a section of the journal Frontiers in Cell and Developmental Biology

Received: *18 August 2021*
Accepted: *28 December 2021*
Published: *31 January 2022*

Citation:
Tran V and O'Neill HC (2022) Role of SVEP1 in Stroma-Dependent Hematopoiesis In vitro. *Front. Cell Dev. Biol. 9:760480. doi: 10.3389/fcell.2021.760480*

INTRODUCTION

Hematopoietic stem cells (HSC) are supported by the "stem cell niche," a tightly regulated environment comprising stromal cells and molecules that control HSC self-renewal, quiescence, differentiation, proliferation and migration (Oh and Kwon, 2010; Raaijmakers, 2010). Stromal adhesion molecules maintain close proximity between stem cells and stromal cells comprising the niche. In adults, the main HSC niche in bone marrow has been described in terms of three interconnected cellular microenvironments, namely the endosteal, perivascular and vascular niches (Kiel and Morrison, 2008; Bianco, 2011; Nagasawa et al., 2011). A combination of cells including

osteoblasts, perivascular reticular cells, endothelial cells, macrophages and adipocytes all contribute to the hematopoietic niche in bone marrow and to hematopoietic differentiation (Morrison and Scadden, 2014). The spleen supports extramedullary hematopoiesis and specifically myelopoiesis, and in the steady-state also contains HSC (Wolber et al., 2002; Dor et al., 2006; Tan and O'Neill, 2010; Morita et al., 2011; Hara et al., 2014). In mice, perisinusoidal cells in contact with HSC have been identified in the red pulp region of spleen and described as mesenchymal cells expressing molecules including PDGFR, CXCL12 and KITL which support hematopoiesis (Kiel et al., 2005; Inra et al., 2015; Oda et al., 2018). Stromal cells which function *in vitro* as a splenic niche for HSC have now been described (Tan and O'Neill, 2007; O'Neill et al., 2011).

Long-term cultures (LTC) comprising splenic stroma were developed in this lab in order to investigate potential hematopoietic niche elements in spleen. These cultures reflect an *in vitro* microenvironment which supports restricted myelopoiesis with continuous production of progenitors, myeloid/dendritic cells, and a novel dendritic-like cell type, referred to as "long-term culture-derived dendritic cells" or "L-DC" (Wilson et al., 2000; O'Neill et al., 2004). The long-term production of L-DC, but not other cell types, was found to be dependent on stromal cell contact (Wilson et al., 2000; Periasamy et al., 2013). The possibility that HSC in spleen arise from endogenous progenitors laid down during embryogenesis, as opposed to bone marrow-derived progenitors entering spleen through blood, has also been considered (O'Neill et al., 2004; O'Neill et al., 2011).

In order to investigate stromal elements supporting hematopoiesis, stroma was isolated and cloned from the STX3 spleen LTC that had ceased production of cells due to loss of progenitors over time and passage (Despars et al., 2004). The overlay of lineage negative (Lin^-) bone marrow cells on to STX3 stroma in co-cultures led to myelopoiesis and production of cells very similar to LTC (Periasamy et al., 2009). These stromal co-cultures produce progenitors, myeloid cells/precursors and dendritic-like cells including the novel L-DC subset (Periasamy et al., 2009; Periasamy et al., 2013; Periasamy and O'Neill, 2013; Petvises and O'Neill, 2014). Analysis of over a hundred distinct clonal lines derived from STX3 identified 5G3 as a rapidly growing clone which was also a supporter of hematopoiesis. 3B5 was selected as a non-supporter (Despars and O'Neill, 2006a). Further studies questioned which hematopoietic stem/progenitor cell (HSPC) subsets gave rise to L-DC. This study employed known progenitor subsets from bone marrow including long-term HSC (LT-HSC) with self-renewal capacity (Kiel et al., 2005), as well as multipotential progenitors (MPP) with more limited self-renewal capacity and high differentiative potential (Christensen and Weissman, 2001). Both gave rise to L-DC when overlaid on 5G3 in co-cultures such that both subsets appear to contain distinct L-DC progenitors which may be developmentally linked (Petvises and O'Neill, 2014a). Other less well defined progenitors tested included myeloid/dendritic progenitors [MDP] and the common dendritic progenitor (CDP) downstream of the common myeloid progenitor (CMP) (Onai et al., 2007; Liu et al., 2009), but these produced dendritic cells (DC) resembling conventional (c) DC or myeloid DC (Petvises and O'Neill, 2014a). This evidence clearly defined the lineage origin of L-DC as distinct from other dendritic and myeloid cells, and identified a self-renewing HSC as the L-DC progenitor. Furthermore, L-DC development was shown to occur independently of macrophage-colony stimulating factor (M-CSF/CSF1), FMS-like tyrosine kinase-3 ligand (Flt3L) or granulocyte macrophage-colony stimulating factor (GM-CSF) (Petvises and O'Neill, 2014a) which are known regulators of myelopoiesis (Onai et al., 2007; Xu et al., 2007).

A number of splenic stromal cell lines isolated from STX3, including 5G3 and 3B5, have been shown to have similar cell surface marker profile reflecting mesenchymal stem cells (MSC) since they express known markers including CD29, VCAM1, LY6A and Thy1.2 (Lim et al., 2018; O'Neill et al., 2019). They also closely resemble a perivascular subset of MSC in bone marrow known as CXCL12- abundant reticular (CAR) cells due to their marker expression of CD51 and CD140A (Omatsu et al., 2010; Pinho et al., 2013). Further evidence that 5G3 and 3B5 reflect a perisinusoidal/perivascular reticular cell type is ability to undergo osteogenesis when cultured under mineralisation conditions (Askarinam et al., 2013; O'Neill et al., 2019). The functional role of 5G3 as a hematopoietic niche is supported by data from transcriptome analysis showing that 5G3 expresses genes which regulate hematopoiesis, including *Cxcl12*, *Vcam1* and *Spp1* (Periasamy et al., 2018). Inhibition of the CXCL12 and VCAM1 signalling in 5G3 co-cultures was found to give a general reduction in cell production (Lim et al., 2018; Periasamy et al., 2018) consistent with the literature which shows that stromal cells in hematopoietic niches produce CXCL12 that binds to CXCR4 (C-X-C chemokine receptor type 4) and CXCR7 (C-X-C chemokine receptor type 7) on HSC, so directing cells to the stromal cell surface and signalling their differentiation (Sugiyama et al., 2006; Sánchez-Martín et al., 2013). Once HSC come into close proximity with the stromal niche, adhesion molecules like VCAM1 interact with VLA-4 expressed by HSC, so allowing HSC to adhere to stroma and to receive signals which support their maintenance and differentiation (Ulyanova et al., 2005; Martinez-Agosto et al., 2007). The blocking of SPP1 binding to CD44 was shown to specifically decrease L-DC production and to restrict the HSC pool by maintaining HSC in a quiescent state (Periasamy et al., 2018), consistent with the previously published role of SPP1 in bone marrow niches (Nilsson et al., 2005; Stier et al., 2005). Inhibition of interactions like these between stroma and HSC may lead to exhaustion of the HSC pool, so affecting the later production of differentiated cells.

Despite the similar lineage origin of 5G3 and 3B5, only 5G3 is a supporter of *in vitro* hematopoiesis, and specifically of L-DC development. Transcriptome analysis was used to identify genes specifically expressed by stromal lines like 5G3 over 3B5. This study identified a number of genes specifically expressed by 5G3 which are candidates for hematopoietic support. Genes investigated here include *Svep1* (sushi, von Willebrand factor type A, EGF and pentraxin containing 1) and *Igf2* (insulin-like growth factor 2) (Periasamy et al., 2018). Of particular interest is

SVEP1, a selectin-like molecule identified as specifically and highly expressed by 5G3, but for which no specific antibodies exist. Integrin $\alpha_9\beta_1$ is a known ligand for SVEP1 (Sato-Nishiuchi et al., 2012), and antibody to integrin $\alpha_9\beta_1$ inhibited production of cells in 5G3 stromal co-cultures (Periasamy et al., 2018). However, VCAM1 is also a receptor for integrin $\alpha_9\beta_1$ (Ross et al., 2006; Saldanha-Gama et al., 2010). In order to confirm a role for SVEP1 in *in vitro* hematopoiesis and L-DC development, it was therefore necessary to knockdown *Svep1* expression in 5G3 cells.

This work is further justified by recent reports which associate SVEP1 with early hematopoiesis. Evidence favouring a role for SVEP1 in hematopoiesis comes from transcriptomic analysis of the embryonic aorta, which shows conservation across species of molecules which regulate HSC, one of which is SVEP1 (Yvernogeau et al., 2020). Furthermore, a subset of mesenchymal stem/stromal cells in human bone marrow has been identified through expression of low affinity nerve growth factor receptor (CD271) (Kuçi et al., 2010; Kuçi et al., 2019). This subset of stroma is distinct through expression of genes supporting hematopoiesis including *Cxcl12*, *Flt3l*, *Il-3*, *Tpo* and *KitL*, and also through specific expression of several adhesion molecules including *Svep1* (Kuçi et al., 2019).

Here, gene knockdown in splenic stromal lines has been used to specifically test the role of genes in *in vitro* hematopoiesis in stromal co-cultures. Several strongly expressed genes including *Svep1*, *Igf2* and *Csf1*, have been knockdown in 5G3 stroma using short hairpin RNA (shRNA) plasmids. Co-cultures were then established using sorted subsets of HSPC as overlays above knockdown stroma.

MATERIALS AND METHODS

Tissue Culture

Cells were cultured at 37°C in 5% CO_2 in air in Dulbecco's modified Eagle's medium (DMEM) supplemented with 10% fetal calf serum, 5×10^{-4}M 2-mercaptoethanol, 10mM HEPES, 100U/ml penicillin, 100ug/ml streptomycin, 4 g/l glucose, 6 mg/l folic acid, 36 mg/l L-asparagine, 116 mg/l L-asparagine hydrochloric acid (sDMEM).

The 5G3 and 3B5 stromal lines were cloned from STX3 splenic stroma derived from a long-term culture of spleen from B10. A (2R) mice (H-2K^k) (Despars et al., 2004; Despars and O'Neill, 2006a). The original stromal cell lines, as well as transfected stromal lines, were grown from frozen stocks and passaged up to five times by transfer of cells to new flasks following trypsinization using 0.25% trypsin-EDTA treatment to dissociate cells. Stromal cells in culture were maintained by passage every 4 days by scraping and transferring cells to a new flask (Periasamy et al., 2009).

The BCL1 B cell line and P815 mastocytoma cell line were cultured in sDMEM and passaged every 3–4 days.

Animals

Specific pathogen-free C57BL/6J (*H-2K^b*) mice at 6 weeks of age were obtained from the John Curtin School of Medical Research (JCSMR: Canberra, ACT, Australia). Mice were housed and handled according to protocols approved by the Animal Experimentation Ethics Committee at the Australian National University (ANU: Canberra, ACT, Australia).

Preparation of Murine Cells

Mice were euthanized, followed by sterile dissection of tissues. Cell suspensions were dissociated by forcing tissue through a fine wire sieve. Lysis of red blood cells involved hypertonic treatment as described previously (Petvises and O'Neill, 2014). For separation of stromal cells from leukocytes in spleen, thymus and lymph node, the non-suspendable stromal fraction was treated with collagenase IV (1 mg/ml) and DNase (40 μg/ml) in DMEM, with incubation at 37°C for 20 min and slow rotation. This was followed by two further treatments with DMEM containing collagenase D (1 mg/ml) and DNase (40 μg/ml) with slow rotation for 20 min. Collagenase was then inactivated by addition of EDTA (500 mM). Stromal cells were then washed by centrifugation, passed through a 100 μm cell strainer, and resuspended into medium.

Bone marrow was flushed from the bone cavity with sDMEM. Bone marrow was depleted of Lin$^+$ cells using a lineage depletion antibody kit supplemented with antibody to CD11c (Miltenyi Biotec, Bergisch Gladbach, GL, Germany) and MACS® magnetic bead technology (Miltenyi Biotec) as described previously (Periasamy et al., 2009; Periasamy et al., 2013). Over multiple separations, efficiency of depletion was shown to be ~95%.

In preparation for osteogenic differentiation, bone marrow cells were cultured at 10^7 cells/mL in sDMEM. After 24 h, medium containing non-adherent cells was removed and replaced. Adherent MSC were maintained in cultures by medium replacement every 3 days. After 14–18 days, cells were dissociated using 0.25% trypsin-EDTA treatment for 2 min at 37°C. Cells were then plated at a concentration of 10^5 cells/mL in preparation for culture under conditions that stimulate osteogenesis.

Osteogenic Differentiation

Cultures of bone marrow-derived MSC, or of 5G3 and 3B5 stroma, were maintained for up to 4 weeks in sDMEM, containing 10^{-8} M dexamethasone, 100 μM ascorbic acid 2-phosphate (AA2P) and 10 mM β-glycerophosphate to induce mineralisation or osteogenesis (O'Neill et al., 2019). Medium was replaced every 4 days. 5G3 and 3B5 cultures were maintained at a concentration of 10^5 cells/mL by passaging cells every 4 days using 0.25% trypsin-EDTA treatment to dissociate cells. Parallel cultures were maintained in sDMEM medium as undifferentiated control cells. After 8, 16 and 24 days of culture under mineralization conditions, RNA was prepared and qRT-PCR performed.

Establishment of Co-Cultures

Stromal cell lines were grown as a monolayer to 80–90% confluency. Lin$^-$ bone marrow cells were added at 1-5 x 10^4 cells/ml as an overlay. Progenitor cells sorted from bone marrow were plated at 10^3 cells/5ml/flask. Co-cultures were

held at 37°C, 5% CO_2 in air and 97% humidity. Medium changes were performed every 3–4 days by removal of half volume and replacement with sDMEM. At 7-day intervals, non-adherent cells were collected through removal and replacement of supernatant. Cell yield was determined and cell subsets identified through analysis of surface marker expression by antibody staining and flow cytometry.

Flow Cytometry

The procedure used to stain cells with multiple fluorochrome-conjugated antibodies has been described in detail previously (Petvises and O'Neill, 2014; Petvises and O'Neill, 2014a). "Fc block" specific for FcγII/IIIR (eBioscience, Parkville, VIC, Australia) was absorbed to cells ahead of antibody to block non-specific Fc receptor binding. Antibodies were purchased from Biolegend (San Diego, CA, United States). Those used to stain murine myeloid cells were specific for CD11c (N418), CD11b (M1/70), MHC-II(AF6-120.1) and F4/80 (A3-1). Antibodies used to stain bone marrow progenitors for sorting were specific for Sca-1 (D7, PB), cKit (2B8), Flt3 (A2F10), CD150 (TC15-12F12.2) and CD115 (AFS98). Dead cell discrimination involved addition of 1 μg/ml of propidium iodide (PI) to cells prior to flow cytometric analysis. To stain lineage $(Lin)^+$ cells for gating during flow cytometry, a lineage depletion antibody kit supplemented with antibody to CD11c was employed (Miltenyi Biotec). Flow cytometry was performed on an LSRII FACS machine (Becton Dickinson: Franklin Lakes, NJ, United States). Voltage, parameter and event counts were programmed using BD FACSDIVA software (Becton Dickinson). Single colour controls were used to set compensation. FlowJo® software (Ashland, OR, United States) was used to analyse data. Live cells were gated by the absence of PI staining (PI^-), and then gated on the basis of forward scatter (FSC) and side scatter (SSC). Fluorescence-minus-one controls (FMOCs) were used to set gates to distinguish specific antibody binding.

Microscopy

Photographs of stromal cells were taken using an EVOS® FL digital fluorescence microscope (Electron Microscope Sciences: Hatfield, PA, United States), equipped with a Sony® ICX445 CCD camera (Sony: Minato, TKY, JP). Fluorescent micrographs were taken using a Leica TCS SP5 Confocal microscope (Leica Microsystems: Weitziar, HE, GER) at 40X magnification.

Use of SmartFlare ™ Probes for RNA Detection

SmartFlare™ probes (Merck Millipore: Billerica, MA, United States) comprise a gold nanoparticle bound to multiple capture strands. A reporter strand that carries a fluorescent "flare" is hybridized to the capture strand. Upon endocytosis by cells of interest, target mRNA binds to the capture strand, so displacing the reporter strand, which can be detected by its ability to fluoresce once removed from the quenching influence of the gold nanoparticle (Seferos et al., 2007). Probes were obtained from Merck Millipore and included *Actb* Cy5 (SF-781) and *Svep1* Custom Cy5 (SFC-565), a Scrambled Target Control Cy5 (SF-102) and an Uptake Control Cy5 (SF-137) to act as negative and uptake controls, respectively.

Cells of interest were plated at 80% confluency (3×10^5 cells/200 μL) in sDMEM medium. The SmartFlare™ reagent was diluted in sterile PBS to a concentration of 500 pM, and 4 μL added to each well containing cells. Cultures were incubated for up to 24 h at 37°C, 5% CO_2 and 95% humidity. Fluorescent cells were detected through flow cytometric analysis or Confocal microscopy.

Quantitative Realtime-Polymerase Chain Reaction

RNA was extracted from stromal cells using the Qiagen RNeasy minikit (SABiosciences, Valencia, CA, United States) and reverse transcribed into cDNA using the RT^2 First Strand Synthesis kit (SABiosciences) as described previously (Periasamy et al., 2018). Equal amounts of cDNA and primers (10uM) were used. Primers were purchased from SABiosciences: *Svep1* (PPM05259A), *Actb* (PPM02945A), *Csf1* (PPM03116C), *Igf2* (PPM03655A) and *Ms4a4d* (PPM24747A). cDNA and primer mix were added to RT^2 SYBR Green Mastermix and RNase-free water in a ratio of 1: 6.25:5.25. Samples were then run in a LightCycler 480 (Roche, Penzberg, BAV, Germany). A single run involved: 1 cycle of 10 min at 95°C to activate polymerase, 45 cycles of 15 s at 95°C for extension, and 1 min at 60°C for detection of fluorescence.

Data analysis involved LightCycler 480 software v. 1.2.9.11 (Roche). To obtain a cross point value (C_p), also referred to as the cycle threshold (C_t), the Absolute Quantification (second derivative max) method was used. C_p is the point where maximal increase in fluorescence emitted by a single PCR reaction within the log-linear phase occurs. C_t values for genes of interest (GOI) along with housekeeping genes (HKG) were imported into Excel (Microsoft: Redmond, WA, United States) for further analysis. Change in $\Delta C_t = C_t$ (GOI)—C_t (HKG) was calculated, and the average ΔC_t taken from quadruplicate experiments. To calculate the fold change between two samples, the calculation $2^{-\Delta Ct}$ (Sample 1)/$2^{-\Delta Ct}$ (Sample 2), was used. The resulting value corresponds to the relative difference in mRNA quantity between two samples for a GOI. The presence of an amplified product was confirmed by gel electrophoresis.

Transfection of Cells With shRNA

5G3 was transfected with shRNA to establish knockdown lines. The pLKO.1-puro plasmid vector (Sigma-Aldrich: St Louis, MO, United States) contains both ampicillin resistance *AmpR* and puromycin resistance *PurR* genes for selection of bacterial and mammalian cell transfectants, respectively. The sensitivity of 5G3 to puromycin was assessed initially in order to identify the minimum effective concentration of drug and treatment times for stromal cells.

All shRNA plasmids were purchased from Sigma-Aldrich. Each of the shRNA was supplied as glycerol stocks of transformed bacteria. These included: *Svep1* [TRCN0000351057 (shRNA1); TRCN0000340274 (shRNA2);

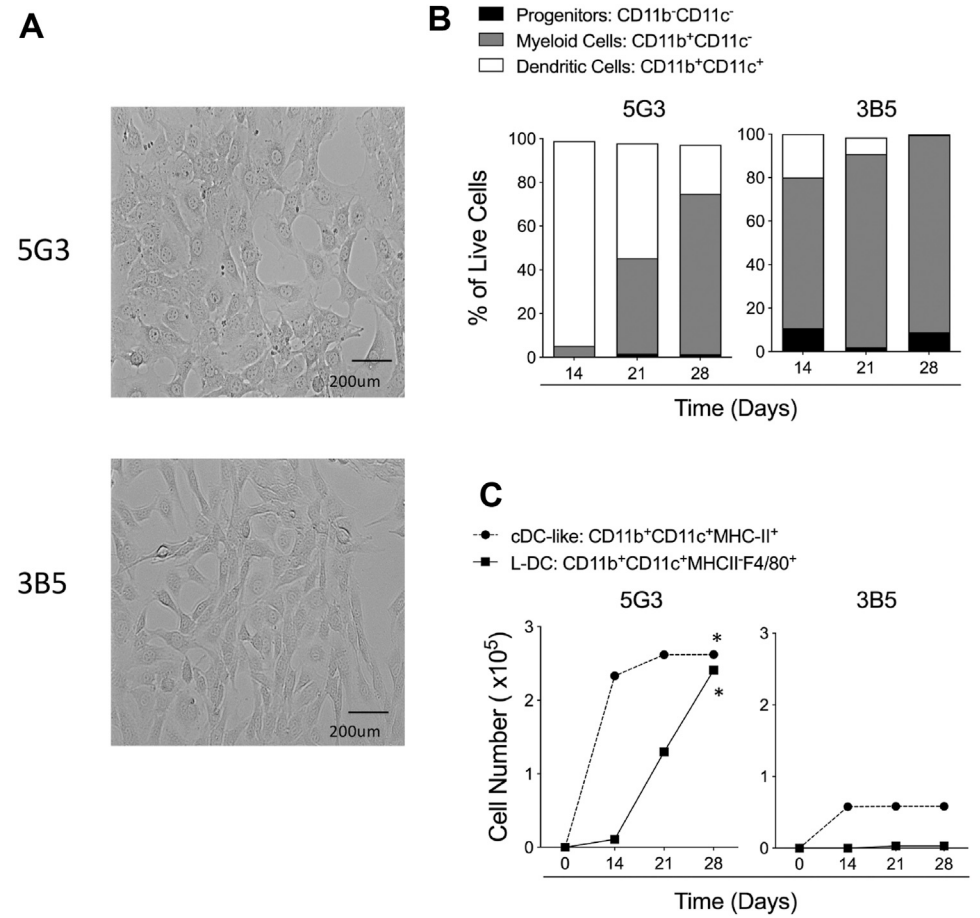

FIGURE 1 | Hematopoietic support capacity of splenic stroma. 5G3 and 3B5 are distinct stromal cell lines cultured to confluence over 28 days **(A)**. Lin$^-$ bone marrow was co-cultured above stroma for 28 days and non-adherent cells collected at medium change weekly for flow cytometric analysis of cell types present. Antibodies used were specific for CD11c, CD11b, F4/80 and MHC-II in order to gate broad subsets of CD11b$^-$CD11c$^-$ progenitor cells, CD11b$^+$CD11c$^-$ myeloid cells and CD11b$^+$CD11c$^+$ DC. Proportion of each of these subsets amongst live (PI$^-$) non-adherent cells over time in shown in **(B)**. DC were further gated as MHC-II$^+$ cDC-like cells, and MHC-II$^-$F4/80$^+$ L-DC. Data are presented as cumulative cell production over time. Cultures showing significant (p = 0.0417) increasing subset production over 4 time points are shown by *__(C)__.

TRCN0000340211 (shRNA3); TRCN0000340213 (shRNA4); TRCN0000340212 (shRNA5)], *Csf1* [TRCN0000065908 (shRNA1); TRCN0000065909 (shRNA2); TRCN0000065910 (shRNA3); TRCN0000065911 (shRNA4); TRCN0000065912 (shRNA5)], and *Igf2* [TRCN0000071147 (shRNA1); TRCN0000071149 (shRNA2); TRCN0000071150 (shRNA3)]. The control vector was supplied as a plasmid, and was firstly transformed into *E. coli* JM109 and plated out on agar containing Carbenicillin (CB; 0.1 mg/ml) to select transformants. Bacterial glycerol stocks of shRNA were streaked on CB agar plates. A single colony from each of the control and shRNA CB agar plates was inoculated into Luria broth (LB) containing 0.1 mg/ml of CB. A plasmid miniprep kit (Pureyield™ plasmid miniprep system; Promega: Madison, WI, United States) was used to prepare plasmid DNA for frozen storage according to the manufacturer's instructions.

On the day prior to transfection, 8×10^4 cells were plated in 500 µL sDMEM with overnight incubation. Transfection mix for each shRNA plasmid, comprised 400 ng of DNA/60 µL sDMEM. Attractene Transfection Reagent (Qiagen: Venio, LI, NA) (1.5 µL) was added to each transfection mix and incubated at 20°C for 20 min. Medium on cells was replaced, and the cells allowed to recover through incubation for 24 h. Transfectants were then selected for 72 h by replacing medium with 1 ml of sDMEM containing 1 µg/ml puromycin. Cells were then grown to 100% confluency with sDMEM changes every 24 h.

Statistical Analysis

When replicates could be prepared, data are presented as mean ± S.E. for sample size n. The Wilcoxon Rank Sum test was used to assess significance ($p \leq 0.05$).

In co-culture experiments where only low numbers of progenitors are seeded and cell production is low, cumulative cell production was measured at several time points in preference to replication of cells produced at one time point. A significant effect is indicated by increasing cell production across 4 time

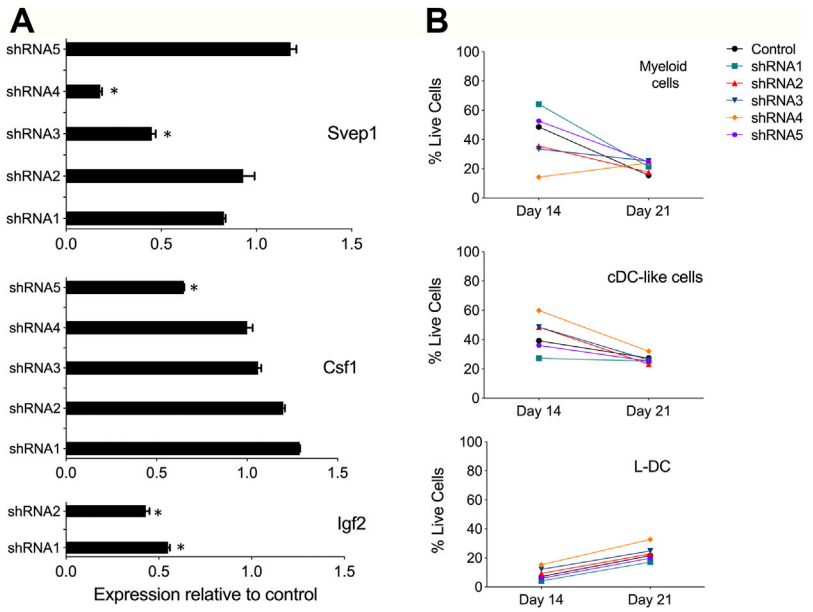

FIGURE 2 | Evidence for gene knockdown in 5G3 stroma. **(A)** Knockdown plasmids containing up to 5 distinct shRNA specific for *Svep1*, *Csf1* or *Igf2*, or an empty plasmid vector as control, were transfected into 5G3 followed by 3 days of puromycin selection (1 mg/ml). Cells were collected and RNA prepared for qRT-PCR to detect changes in gene expression. Data represent gene expression measured by qRT-PCR for each of the shRNA transfected lines relative to the control. Data represent mean ± S.E. from 4 independent PCR reactions. * identifies gene expression significantly less than control ($p \leq 0.05$). **(B)** Hematopoietic support capacity of confluent cultures of each of the *Svep1* knockdown lines, and the control line, was tested by capacity for cell production from overlaid Lin^- bone marrow cells. Non-adherent cells were collected on Days 14 and 21 of co-culture. Cells were counted and stained with fluorochrome-conjugated antibodies specific for CD11b, CD11c, MHC-II and F4/80. "Fluorescence minus one" controls were used to set gates to identify specific antibody binding. All co-cultures produced equal numbers of cells. Subsets were identified as $CD11b^+CD11c^-$ myeloid cells, $CD11b^+CD11c^+MHC\text{-}II^+$ cDC-like cells, and $CD11b^+CD11c^+MHC\text{-}II^-$ L-DC. Data are presented as % of each cell type produced in co-cultures.

points. The null hypothesis is that cell production is random over time, and the alternative hypothesis is that increasing cell production occurs with increasing time. The probability of an ordered expanding sequence for cell production over 4 time points is 1/24 or 0.0417 which reflects significant cell production ($p \leq 0.05$).

RESULTS

Spleen Stromal Lines Support *In vitro* Hematopoiesis

The 5G3 and 3B5 splenic stromal lines reflect morphologically distinct clonal lines of similar lineage origin cloned from stroma isolated from a single spleen LTC (Despars and O'Neill, 2006b; Periasamy et al., 2018) (**Figure 1A**). The two stromal lines differ in terms of hematopoietic support capacity after establishment of co-cultures with overlaid Lin^- bone marrow cells (**Figures 1B,C**). Non-adherent cells were collected on Days 14, 21 and 28, and antibody staining and flow cytometric analysis used to distinguish subsets amongst cells produced over time. Here, progenitors were identified as $CD11b^-CD11c^-$, myeloid cells/precursors as $CD11b^+CD11c^-$, cDC-like cells as $CD11b^+CD11c^+MHC\text{-}II^+$ and L-DC as $CD11b^+CD11c^+MHC\text{-}II^-F4/80^+$. The clear identification of the novel L-DC subset on the basis of F4/80 staining was recently introduced into subset analyses (Petvises and O'Neill, 2014).

All data show that 5G3 is a stronger supporter of hematopoiesis than 3B5, and also produces L-DC, while 3B5 does not. 3B5 co-cultures produced more myeloid cells than DC (**Figure 1B**), but with lower cell production compared with 5G3 (**Figure 1C**). Only 5G3 showed significant production of L-DC and numbers increased over 28 days (**Figure 1C**). Both 5G3 and 3B5 co-cultures produced cDC-like cells initially, but production was transient and decreased over time (**Figure 1C**).

Svep1 Gene Knockdown in 5G3

The gene knockdown procedure was optimised to determine the functional importance of SVEP1 in the hematopoietic support function of 5G3 stroma. Other genes investigated included *Igf2* also expressed by just 5G3, as well as *Csf1* which is strongly expressed by both cell lines. Transfection with shRNA plasmids was chosen over siRNA since shRNA allows generation of stable knockdown cell lines and is more suited to continuously growing lines. Furthermore, the concentration of shRNA remains stable as cells divide so maintaining a constant gene knockdown effect (Taxman et al., 2010).

Multiple *Svep1* shRNA plasmids were tested for each gene. The shRNA plasmids and a control (empty vector) plasmid were transfected into separate cultures of 5G3. qRT-PCR was

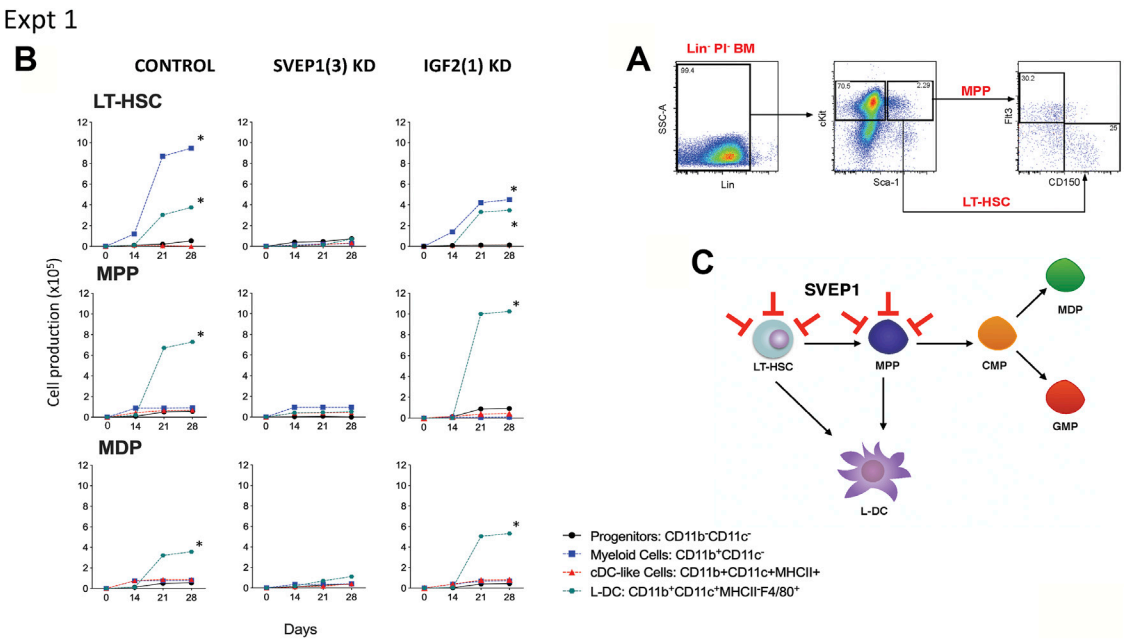

FIGURE 3 | Effect of *Svep1* knockdown on 5G3 hematopoietic support capacity. **(A)** The sorting strategy to isolate LT-HSC and MPP is shown. Lin$^-$ bone marrow cells were prepared by antibody depletion using MACS® column technology and anti-biotin microbeads (Miltenyi Biotec). For sorting progenitor subsets, cells were stained with lineage antibodies as well as fluorochrome-conjugated antibodies specific for progenitors: Sca-1, cKit, Flt3, and CD150. Cells were gated initially as Lin$^-$ PI$^-$ (live) cells. "Fluorescence minus one" controls were used to set gates to identify specific antibody binding. LT-HSC were gated as cKit$^+$Sca-1$^+$Flt3$^-$CD150$^+$ cells, and MPP as cKit$^+$Sca-1$^+$Flt3$^+$CD150$^-$ cells. **(B)** Co-cultures were established by overlay of equal numbers (1×10^3 cells/flask) of sorted LT-HSC and MPP above control 5G3 stroma, *Svep1* knockdown stroma (SVEP1 (3) KD), and *Igf2* knockdown stroma (IGF2 (1) KD). Non-adherent cells were collected weekly and stained with fluorochrome-conjugated antibodies specific for CD11c, CD11b, MHC-II and F4/80 to identify subsets of CD11b$^-$CD11c$^-$ progenitor cells, CD11b$^+$CD11c$^-$ myeloid cells, CD11b$^+$CD11c$^+$MHC-II$^+$ cDC-like cells and CD11b$^+$CD11c$^+$MHC-II$^-$ L-DC. Data are presented as cumulative cell production over time. Cultures showing significant (p = 0.0417) increasing subset production over 4 time points are shown by *. **(C)** A model for the role of *Svep1* in hematopoiesis is shown. Red bars show blocking effects of *Svep1* knockdown on LT-HSC and MPP.

performed on all transfectants and compared with the control (empty vector) transfectants after 7 days to verify gene knockdown. For *Svep1*, cell lines transfected with shRNA3 and shRNA4 showed significant reduction in *Svep1* expression, with values of gene expression relative to control of 0.45 and 0.18, respectively (**Figure 2A**). For *Csf1* transfections, the greatest knockdown effect was seen with shRNA5 (0.65), and for *Igf2* transfection, both shRNA1 and shRNA2 were very effective with expression relative to control of 0.45 and 0.55, respectively (**Figure 2A**).

Initially, selected *Svep1* shRNA transfected lines and the control transfected (empty vector) line were cultured as a monolayer and then overlaid with Lin$^-$ bone marrow to observe any effect of knockdown on the ability of 5G3 to support hematopoiesis. This was assessed in terms of production of myeloid and dendritic subsets through flow cytometry. Myeloid cells and precursors were identified after 14 and 28 days as a CD11b$^+$CD11c$^-$ subset, cDC-like cells as CD11b$^+$CD11c$^+$MHC-II$^+$ and L-DC as CD11b$^+$CD11c$^+$MHC-II$^-$. Apart from some partial changes in number of cells produced in co-cultures using shRNA4 transfectants, cell production was relatively constant across all cultures (**Figure 2B**). While the shRNA protocol was effective in knocking down of *Svep1* expression in 5G3, this change did not dramatically alter the hematopoietic support function of 5G3 in Lin$^-$ bone marrow co-cultures. Similar results were also obtained for *Csf1* and *Igf2* knock down stromal lines (data not shown).

Gene Knockdown in Stromal Co-Cultures of Hematopoietic Progenitors

One hypothesis is that the co-culture of a heterogeneous population of Lin$^-$ bone marrow cells may mask any specific effect of gene knockdown on particular hematopoietic progenitors. Co-cultures were therefore established with knockdown stromal lines overlaid with highly purified LT-HSC sorted as Lin$^-$Sca1$^+$ckit$^+$Flt3$^-$CD150$^+$ cells (Kiel et al., 2005), the broad MPP subset of Lin$^-$Sca1$^+$ckit$^+$Flt3$^+$CD150$^-$ cells (Christensen and Weissman, 2001), and the subset of Lin$^-$Sca1$^+$ckit$^-$Flt3$^+$CD115$^+$ cells which includes MDP (Petvises and O'Neill, 2014). Cell sorting procedures are shown in **Figures 3A**, **4A**. The number of cells available for establishment of co-cultures was very low so that optimisation of conditions was needed to obtain a fully controlled experiment. Preliminary investigations showed that single larger (25 ml) cultures were more supportive of cell production than replicate smaller cultures, so that replication of distinct controlled experiments was chosen over replication within experiments. Single co-

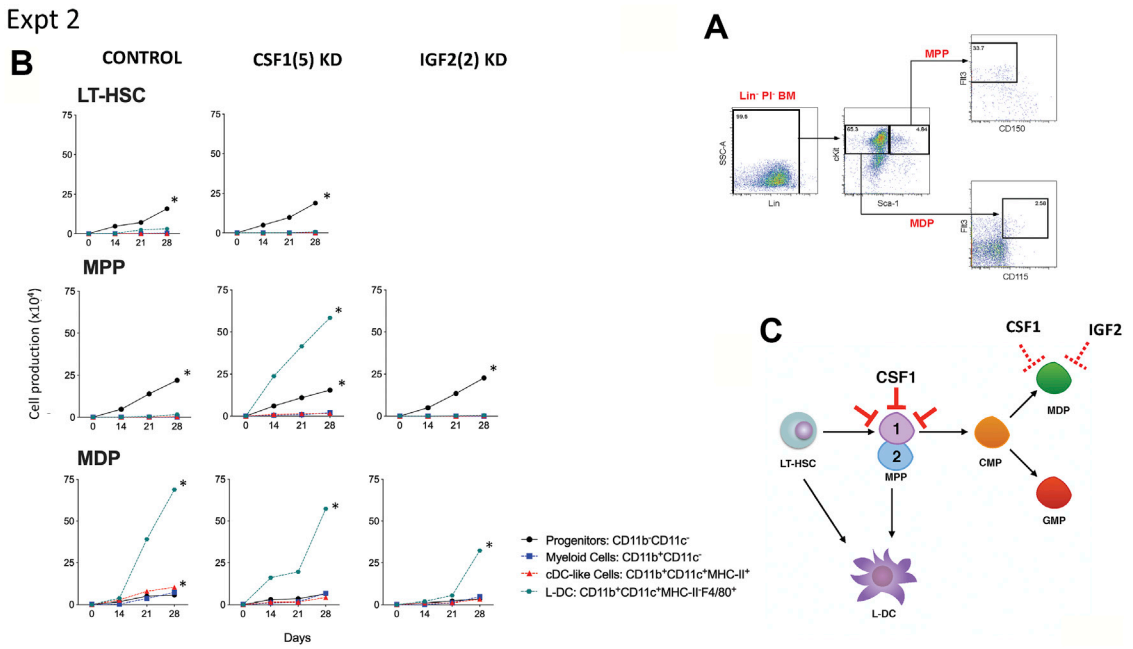

FIGURE 4 | Effect of *Csf1* knockdown on 5G3 hematopoietic support capacity. **(A)** The sorting strategy to isolate MPP and MDP is shown. Lin$^-$ bone marrow cells were prepared by antibody depletion using MACS® column technology and anti-biotin microbeads (Miltenyi Biotec). For sorting progenitor subsets, cells were stained with lineage antibodies as well as fluorochrome-conjugated antibodies specific for progenitors: Sca-1, cKit, Flt3, CD150 and CD115. Cells were gated initially as Lin$^-$ PI$^-$ (live) cells. "Fluorescence minus one" controls were used to set gates to identify specific antibody binding. MPP were gated as cKit$^+$Sca-1$^+$Flt3$^+$CD150$^-$ cells, and MDP were further gated as cKit$^+$Sca-1$^-$Flt3$^+$CD115$^-$ cells. **(B)** Co-cultures were established by overlay of equal numbers (1×10^3 cells/flask) of sorted MDP and MPP above control 5G3 stroma, *Csf1* knockdown stroma (CSF1(5) KD), and *Igf2* knockdown stroma (IGF2 (2) KD). Non-adherent cells were collected weekly and stained with fluorochrome-conjugated antibodies specific for CD11c, CD11b, MHC-II and F4/80 to identify subsets of CD11b$^-$CD11c$^-$ progenitor cells, CD11b$^+$CD11c$^-$ myeloid cells, CD11b$^+$CD11c$^+$MHC-II$^+$ cDC-like cells and CD11b$^+$CD11c$^+$MHC-II$^-$ L-DC. Data are presented as cumulative cell production over time. Cultures showing significant (p = 0.0417) increasing subset production over 4 time points are shown by *. **(C)** A model for the role of *Csf1* in hematopoiesis is shown. Red bars show blocking effects of *Csf1* knockdown on one of two subsets of MPP.

cultures were established for each transfected line, using equal numbers of cells and were maintained equivalently over 28 days through weekly medium change and cell collection. The long-term nature of experiments also precluded comparison of outcomes across experiments since sorted cells vary with preparation, and co-culture differences are amplified over such a long culture period.

Two similar experiments are shown here. In the first, LT-HSC, MPP and MDP were sorted from bone marrow and overlaid on 5G3 transfected with the control (empty) vector, the *Svep1* shRNA3 knockdown stroma and the *Igf2* shRNA1 knockdown stroma. Control co-cultures seeded with LT-HSC showed significant increasing production of CD11b$^+$CD11c$^-$ myeloid cells, most likely reflecting myeloid progenitors and precursors, along with the CD11b$^+$CD11c$^+$MHCII$^-$F4/80$^+$ L-DC subset (**Figure 3B**). Significant cell production was determined by the production of increasing numbers of a cell subset across 4 time points in the assay (p = 0.0417). Co-cultures established with the MPP and MDP populations showed significant production of only the novel L-DC subset. The *Svep1* knockdown line showed no significant cell production of any cell type, implicating a role for the SVEP1 protein in myelopoiesis involving the production of both L-DC and myeloid progenitors/precursors. The *Igf2* knockdown line gave similar results as the control, indicating no effect of IGF2 on cell production. Knockdown of *Svep1* can block the development of myeloid cells from progenitors within the sorted LT-HSC and the MPP subsets (**Figure 3C**), each of which has been shown previously to contain a direct progenitor of the L-DC subset (Petvises and O'Neill, 2014).

A second experiment compared the effects of *Csf1* and *Igf2* knockdown. LT-HSC gave rise to significant production of progenitor cells which was not blocked by knockdown of *Csf1*. A similar finding was reported previously (Petvises and O'Neill, 2014a). MPP co-cultured over control stroma also gave significant production of myeloid progenitors in this experiment, which was not lost through either *Csf1* or *Igf2* knockdown (**Figure 4B**). *Csf1* knockdown stroma however supported significant production of L-DC. The best explanation for this result is that L-DC progenitors are a subset of MPP and are not the cells dependent on CSF1 (**Figure 4C**), so that when this gene is knocked down, there is a rebound effect with increased significant production of L-DC (**Figure 4B**). In contrast, MDP co-cultures gave significant production of only the L-DC subset which was not inhibited by knockdown of either *Csf1* or *Igf2* in 5G3 stroma (**Figure 4B**). The production of L-DC, suggests the presence of an L-DC progenitor within the sorted MDP population (Lin$^-$Sca1$^+$ckit$^-$

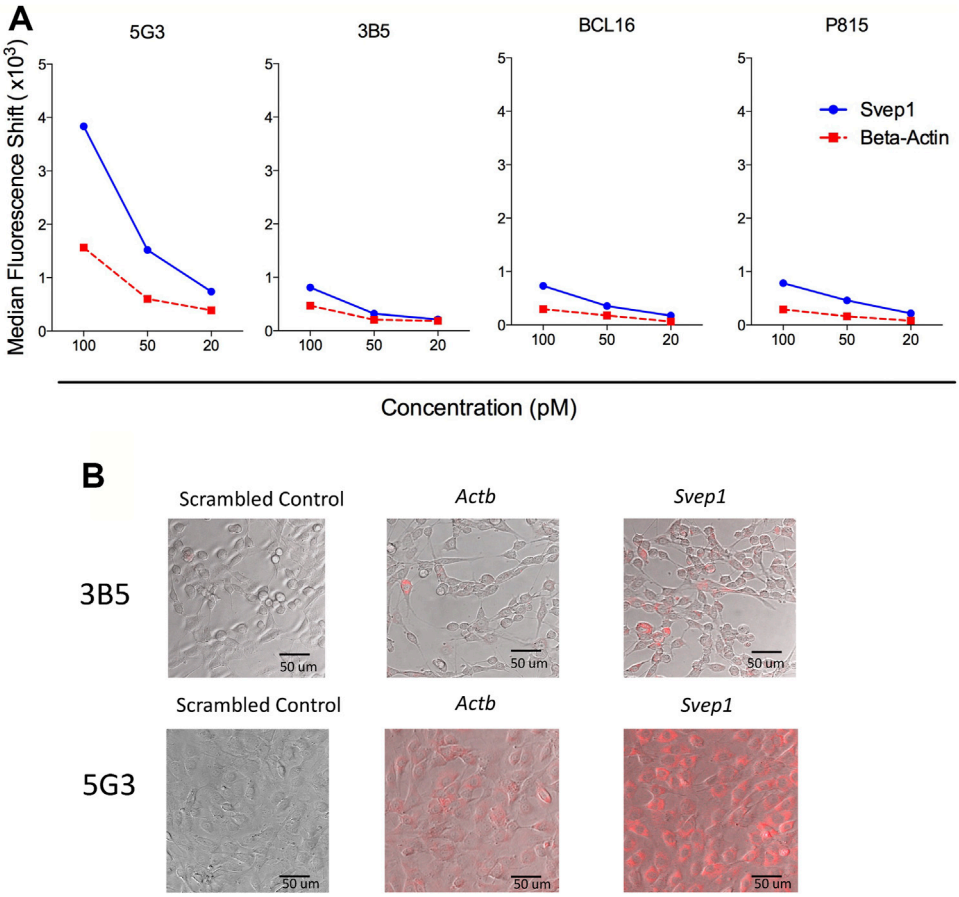

FIGURE 5 | Homogeneous expression of *Svep1* by 5G3 stromal cells. **(A)** Cell lines were cultured to 80% confluency and then supplemented with SmartFlares ™ with the SmartFlare™ Scrambled Target Control Cy5, SmartFlare™ *Actb* Cy5 (housekeeping gene) or SmartFlare™ *Svep1* Cy5 (target gene) at concentrations of 100, 50 and 20 pM. After 16 h, flow cytometric analysis was performed, with the Scrambled Target Control used to set gates to identify fluorescence due to specific gene expression. Data are expressed as shift in median fluorescence above background. **(B)** Cells prepared in **(A)** were photographed by Confocal microscopy at 16 h after labelling.

Flt3$^+$CD115). In Experiment 2, significant but low production of cDC-like cells was evident in control MDP co-cultures which was not lost from the *Csf1* and *Igf2* knockdown co-cultures. This suggests a role for CSF1 and IGF2 in the production of cDC-like cells in 5G3 co-cultures.

Use of SmartFlare™ Technology to Detect *Svep1*-Expressing Cells in Murine Tissues

Further attempts to identify *Svep1* expression on cells in the absence of specific antibodies, involved the use of SmartFlare™ probes combined with flow cytometry. Optimisation of the uptake method in terms of concentration and exposure time utilised several continuous cell lines; 5G3, 3B5, BCL1 and P815. Cells were cultured with the SmartFlare™ Scrambled Target Control and the specific *Svep1* or *Actb* control SmartFlare™ probe. This showed that only 5C3 and no other cell lines tested stained for *Svep1*, with low *Actb* staining. Optimal staining was obtained using 100pM of probe in a 16-hour uptake assay (**Figure 5A**). Confocal microscopy identified homogeneous fluorescent staining for *Svep1* in all 5G3 cells, with a lower level of *Actb* staining (**Figure 5B**). In contrast, 3B5 showed very few cells labelled for either marker. This method confirmed the uniform expression of *Svep1* across all 5G3 cells and with an absence of staining in 3B5 cells. *Svep1* is expressed by a range of tissue types, although any marker positive subsets within tissue are not known. Attempts to stain subsets isolated from dissociated tissues using SmartFlare™ probes gave limited success.

Expression of *Svep1* by 5G3 Stroma is Related to Osteogenic Potential

Svep1 expression was detected using qRT-PCR on cells from dissociated whole organs including thymus, spleen, lymph node, bone marrow, liver, kidney and heart. Expression was measured relative to *Actb* in triplicate reactions. Kidney and heart had the highest expression of *Svep1* at 1.62 and 2.78 fold greater than spleen (**Figure 6A**). In contrast, lymph node had a similar expression level to spleen, while liver, thymus and bone

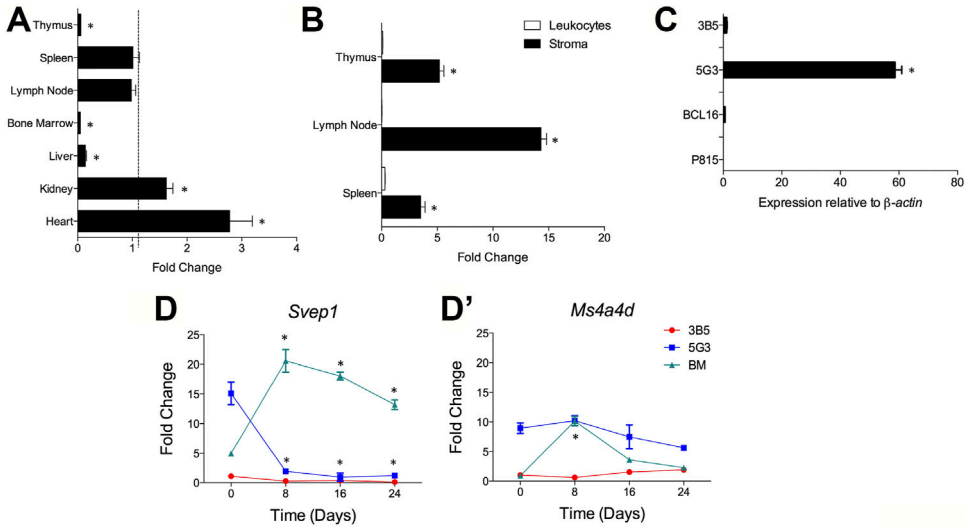

FIGURE 6 | *Svep1* expression is restricted to stromal cells. The expression of *Svep1* was measured by qRT-PCR relative to *Actb* in each sample. Data are presented as mean ± S.E. for 4 independent PCR reactions. **(A)** *Svep1* expression was assessed in multiple organs and is presented in terms of fold change relative to spleen expression. Gene expression significantly different ($p \leq 0.05$) to spleen is shown by *. **(B)** *Svep1* expression was compared in the stromal cell and leukocyte fractions prepared from lymphoid tissues. Significant difference ($p \leq 0.05$) in gene expression between fractions is shown by *. Data represent *Svep1* expression in stromal cells relative to leukocytes for each organ. **(C)** Comparison is made of expression in several cell lines including 5G3 and 3B5 stromal lines, where 5G3 expression is significantly higher ($p \leq 0.05$) than all others *. **(D)** Expression of *Svep1* is related to osteogenesis. The 5G3 and 3B5 cell lines were cultured for 28 days under mineralisation conditions which induce osteogenesis. *Svep1* expression **(D)** and the control gene *Ms4a4d* **(D')** was measured at 8-day intervals. Controls included bone marrow progenitors induced to undergo osteogenesis over 24 days. Data represent the average fold change in gene expression in samples relative to 3B5 measured on Day 0. Gene expression significantly different ($p \leq 0.05$) to the fold change value at Day 0 is shown by *.

marrow showed 10-fold lower levels of *Svep1* expression (**Figure 6A**). Using qRT-PCR only stromal cells and not leukocytes in dissociated lymph node, thymus and spleen expressed *Svep1* (**Figure 6B**). Consistent with this is expression in 5G3 although not in 3B5 (**Figure 6C**). No expression was detected for the P815 mastocytoma line or the BCL1 B lymphoid cell line.

Previous studies have identified 5G3, as a stromal cell line with osteogenic differentiative potential (O'Neill et al., 2019). *Svep1* expression has been identified here as a marker of osteogenic progenitors which is lost on mineralisation. Following culture under mineralisation conditions, both 5G3 and 3B5 undergo osteogenesis with upregulation of genes like *Sp7* (Osterix), *Alp* (Alkaline phosphatase), *Oc* (Osteocalin), *Spp1* (Osteopontin) and *Bsp* (Bone sialoprotein). The expression of *Svep1,* and *Ms4a4d* (used as a control gene), was measured on 5G3 and 3B5 cells over 24-days of culture under mineralisation conditions. qRT-PCR was performed every 8 days to quantify gene expression. No *Svep1* or *Ms4a4d* gene expression was seen with the 3B5 control stromal line. Gene expression is therefore assessed relative to 3B5 cells at Day 0 (**Figures 6D,D'**). *Svep1* gene expression was readily detectable at Day 0 in 5G3 cells but reduced significantly to near zero by Day 8 as cells underwent mineralisation and became osteoblastic (**Figure 6D**). In contrast, *Ms4a4d* did not modulate expression in 5G3 under increasing mineralisation conditions (**Figure 6D'**). Both *Svep1* and *Ms4a4d* increased expression in BM-derived MSC by Day 8 when osteoprogenitors form, significantly reducing in level with mineralisation (**Figures 6D,D'**). *Svep1* and *Ms4a4d* therefore appear to be specific markers of stromal cells which are osteoprogenitors.

DISCUSSION

Stromal niches for HSC utilise multiple cell adhesion molecules. Since SVEP1 is an adhesion molecule that interacts with integrin $\alpha_9\beta_1$ (Sato-Nishiuchi et al., 2012), a reduction in *Svep1* expression could prevent progenitors from binding to 5G3, and so reduce hematopoiesis and the development of myeloid cells within co-cultures. After *Svep1* shRNA was used to produce *Svep1* knockdown lines of 5G3 stroma, highly purified progenitor subsets were needed to show a change in the production of myeloid and DC subsets in co-cultures involving knockdown stroma. Selectins like SVEP1 would appear to anchor HSC on to stroma so ensuring their maintenance, quiescence, and supporting their later differentiation and mobilisation (Oh and Kwon, 2010).

The preparation of stable 5G3 knockdown cell lines was chosen over transient knockdown lines, since the co-culture system of HSPC over stroma assesses cell production over an extended period of 4 weeks. This strategy was applied for two reasons. Firstly, the stable transfectants produced are considered a heterogeneous population and the generation of a heterogeneous population is more time-efficient and achieves an average knockdown effect. However, this can lead to differences between experiments in the cell population

produced over an extended culture period out to 28 days as seen in the two experiments shown here. Secondly, the generation of a single cloned knockdown cell line for each gene would be time-consuming and complex in terms of the assay methods needed to screen for single clonal transfectants. The knockdown procedure used here gave reduced expression of three genes, namely *Svep1*, *Csf1* and *Igf2*. The impact of knockdown was evident by differences in cell production and the clear capacity of shRNA transfected lines to reduce or change hematopoiesis.

Replicate co-cultures established with LT-HSC, MPP and MDP, showed reproducible changes in cell production within an experiment despite variation between experiments in terms of the type of cells produced. HSPC sorting procedures were held consistent between replicate experiments using equal numbers of mice and the same concentration of antibodies. Cell yield was always low, with variation in the number of LT-HSC and MPP recovered from each sort. Experiments were however standardised so that equal numbers of each progenitor type were added to each stromal type under test. Despite experimental difficulty, well controlled replicate experiments have been achievable.

Selectins and integrins are known to be essential in the hematopoietic process. For example, E-selectin expression by stroma drives HSC proliferation, such that a deficiency in E-selectin leads to HSC quiescence and greater capacity for HSC self-renewal (Winkler et al., 2012). P-selectin has been found to regulate myelopoiesis, such that transplantation of $Lin^{-}Sca1^{+}cKit^{+}$ (LSK) cells from P-selectin$^{-/-}$ mice produced higher numbers of myeloid progenitors *in vivo* compared with wild type controls (Sullivan et al., 2011). Based on the known function of selectins and integrins, it is hypothesised that SVEP1 adheres HSPC to 5G3 stroma *via* interaction with integrin $\alpha_9\beta_1$. Once adherent, 5G3 may utilise signalling pathways that maintain HSPC and drive differentiation. If *Svep1* expression is reduced, HSPC may bind only weakly to stroma, leading to reduced differentiation and lower or delayed differentiation in co-cultures, perhaps with greater accumulation of progenitors.

The MDP population of $Lin^{-}Sca1^{+}ckit^{-}Flt3^{+}CD115^{+}$ cells used here contains a progenitor/precursor of L-DC. It is not equivalent to the $CX3CR1^{+}$ subset of these cells which was previously shown to lack progenitors of L-DC (Petvises and O'Neill, 2014a). Recent studies have also found that the MDP subset is not restricted in development to monocytes and DC as previously reported (Sathe et al., 2014). Agar colony assays performed on $Lin^{-}cKit^{hi}Sca1^{-}CD16/32^{hi}CX_3CR1^{+}$ MDP were unexpectedly found to give rise to granulocytes, and very few MDP produced both macrophages and DC in colony assays (Sathe et al., 2014). These studies by others raise doubt about the existence of a single progenitor within the MDP subset with restricted differentiative capacity for just monocytes and DC.

Since *Svep1* expression by 5G3 was directly linked to L-DC development, the possibility that *Svep1* encodes a specific marker for the *in vivo* cell equivalent to 5G3 was considered. In an attempt to identify *Svep1*-expressing cells *in vivo*, SmartFlare™ probes were employed. These served to show that all 5G3 cells expressed *Svep1*. Preliminary experiments using the SmartFlare™ technology indicated limitations for detecting *Svep1*-expressing cells *in vivo*. Several studies were therefore undertaken to assess the cell type in spleen which expresses *Svep1*. Expression was detected in several murine tissues by qRT-PCR, and shown to be restricted to the stromal fraction of lymphoid organs. This is consistent with earlier evidence that SVEP1 is a cell surface protein on mesenchymal and osteoblastic cells (Shur et al., 2006; Sato-Nishiuchi et al., 2012). It was also found to be specific to resting 5G3 cells, and was lost upon culture under mineralisation conditions which induce osteogenesis. *Svep1* expression therefore appears to be limited to stromal cells with osteoprogenitor characteristics, consistent with the phenotype of 5G3 as a perisinusoidal/perivascular reticular cell (Periasamy et al., 2018).

These results identify SVEP1 as another potential adhesion pathway for maintenance of self-renewing HSPC to hold them in close proximity with stromal cells (Martinez-Agosto et al., 2007; Chen et al., 2013). It is also well known that integrin-ligand binding generates intracellular signals that result in changes in gene expression, cell proliferation, survival and differentiation (Legate et al., 2009). SVEP1 is therefore potentially a very important regulator of stem/progenitor cell self-renewal and may have future therapeutic importance in terms of manipulation or supplementation of hematopoiesis.

Although IGF2 is a growth factor for HSC, knockdown of *Igf2* did not significantly impact L-DC production and gave only a partial or transitory knockdown effect on cDC-like cell production. Previously it was shown to weakly inhibit production of cDC-like cells developing from myeloid progenitors (Petvises and O'Neill, 2014a). IGF2 has been shown to be important in the maintenance and expansion of early HSC in the aorta gonad mesonephros (AGM), the fetal liver and in bone marrow (Zhang and Lodish, 2004; Mascarenhas et al., 2009). However, IGF2 function is not restricted to one cell type, and the IGF1R receptor which binds IGF2 is commonly expressed by numerous cell types (Brown et al., 2008; Chao and D'Amore, 2008). Interaction of IGF2 with IGF1R leads to phosphorylation of signalling molecules including mitogen-activated protein kinase and protein-kinase B, which function together to drive cell survival and differentiation (Prince et al., 2007). In co-cultures shown here involving LT-HSC and MDP, knockdown of *Igf2* in 5G3 stroma gave a reduction in production of only cDC-like cells.

CSF1 was also investigated as a regulator of *in vitro* hematopoiesis and is strongly expressed by both 5G3 and 3B5. CSF1 was originally described as a promoter of monocyte and DC development (MacDonald et al., 2005; Hume and MacDonald, 2012). However, here it is more specifically shown to act as a factor driving a subset of progenitors within the MPP population, such that when *Csf1* was knocked down in 5G3, a subset of MPP proceeded towards L-DC development. Evidence for a decrease in the development of cDC-like cells due to CSF1 inhibition serves to reinforce former evidence that CSF1 is a growth factor required for production of cDC-like cells rather than L-DC in *in vitro* co-cultures (Petvises and O'Neill, 2014; Petvises and O'Neill, 2014a). One explanation for this result is that CSF1 may be important for self-renewal or proliferation of a subset of MPP progenitors, although not the L-DC progenitors, such that knockdown of CSF1 gave preferential production of L-DC. The importance of

CSF1 in cDC development *in vivo* has also been reported previously such that the administration of CSF1 to *Flt3*$^{-/-}$ mice increases cDC numbers by 2-fold in spleen, confirming that cDC development depends on CSF1 (Fancke et al., 2008).

Delineation of molecules here represents a significant contribution to the characterisation of hematopoietic niches, how they function and how they are regulated. The identification of stromal cells, growth factors and molecules that contribute to the hematopoietic process, brings us closer to the realm of regulating hematopoiesis *in vivo*, and to inhibiting niches which support cancer stem cells. In terms of the therapeutic importance of the findings made here, it is important to emphasise that the knockdown studies described here directly link gene expression to the function of SVEP1 in early hematopoiesis involving HSPC. The finding that a subset of human bone marrow stroma expresses *Svep1* (Kuçi et al., 2010; Kuçi et al., 2019), emphasises the significance of this result. These cells represent the perivascular reticular cells of the HSC niche in human bone marrow. In future it will be very important to investigate more fully the expression and function of SVEP1 by human bone marrow and spleen stromal subsets, and to determine whether changes in SVEP1 expression is associated with myeloid leukemias or myeloproliferative disorders. The opportunity exists to identify molecules as potential regulators of myelopoiesis. Molecular mimics of SVEP1 could be used therapeutically to enhance myelopoiesis, and inhibitors of SVEP1 binding to HSPC could be used to treat myeloproliferative disorders and leukemia.

CONCLUSION

This study identifies SVEP1 expressed by stromal cells in spleen as an important regulator of hematopoiesis in spleen. In well-controlled experiments, *Svep1*, *Csf1* and *Igf2* knockdown cell lines of the 5G3 mesenchymal stromal line were co-cultured with purified subsets of bone marrow-derived HSPC. These experiments identified *Svep1* as critical to the development of L-DC from progenitors from sorted populations of LT-HSC, MPP and also the MDP from bone marrow. *Csf1* and *Igf2* knockdown was effective in reducing the low level production of cDC-like cells from progenitors within the MDP subset. *Csf1* knockdown was found to enhance the production of L-DC probably through indirect inhibition of a subset of myeloid progenitors within the MPP subset.

DATA AVAILABILITY STATEMENT

The raw data supporting the conclusion of this article will be made available by the authors, without undue reservation.

ETHICS STATEMENT

The animal study was reviewed and approved by Animal Experimentation Ethics Committee at the Australian National University (ANU: Canberra, ACT, Australia).

AUTHOR CONTRIBUTIONS

Conceptualisation: All authors. Data curation: All authors. Formal analysis: All authors. Funding acquisition: All authors. Investigation: All authors. Methodology: VT. Project administration: HO'N. Resources: All authors. Supervision: HO'N. Validation: All authors. Visualisation: All authors. Writing original draft: All authors. Writing, reviewing, editing: All authors.

FUNDING

This work was supported by project grants to HO from the Australian Research Council (#DP13010307) and the National Health and Medical Research Foundation of Australia (#585443). VT was supported by an Australian National University Postgraduate Scholarship. The funders had no role in the study design, data collection and analysis, decision to publish, or preparation of the manuscript.

REFERENCES

Askarinam, A., James, A. W., Zara, J. N., Goyal, R., Corselli, M., Pan, A., et al. (2013). Human Perivascular Stem Cells Show Enhanced Osteogenesis and Vasculogenesis with Nel-like Molecule I Protein. *Tissue Eng. A* 19 (11-12), 1386–1397. doi:10.1089/Ten.Tea.2012.0367

Bianco, P. (2011). Bone and the Hematopoietic Niche: a Tale of Two Stem Cells. *Blood* 117 (20), 5281–5288. doi:10.1182/blood-2011-01-315069

Brown, J., Delaine, C., Zaccheo, O. J., Siebold, C., Gilbert, R. J., van Boxel, G., et al. (2008). Structure and Functional Analysis of the IGF-II/IGF2R Interaction. *Embo J.* 27 (1), 265–276. doi:10.1038/sj.emboj.7601938

Chao, W., and D'Amore, P. A. (2008). IGF2: Epigenetic Regulation and Role in Development and Disease. *Cytokine Growth Factor. Rev.* 19 (2), 111–120. doi:10.1016/j.cytogfr.2008.01.005

Chen, S., Lewallen, M., and Xie, T. (2013). Adhesion in the Stem Cell Niche: Biological Roles and Regulation. *Development* 140 (2), 255–265. doi:10.1242/dev.083139

Christensen, J. L., and Weissman, I. L. (2001). Flk-2 Is a Marker in Hematopoietic Stem Cell Differentiation: A Simple Method to Isolate Long-Term Stem Cells. *Proc. Natl. Acad. Sci.* 98 (25), 14541–14546. doi:10.1073/pnas.261562798

Despars, G., Ni, K., Bouchard, A., O'Neill, T. J., and O'Neill, H. C. (2004). Molecular Definition of an *In Vitro* Niche for Dendritic Cell Development. *Exp. Hematol.* 32, 1182–1193. doi:10.1016/j.exphem.2004.08.013

Despars, G., and O'Neill, H. C. (2006). Heterogeneity Amongst Splenic Stromal Cell Lines Which Support Dendritic Cell Hematopoiesis. In Vitro *Cel Dev Biol Anim* 42 (7), 208–215. doi:10.1290/0602016.1

Despars, G., and O'Neill, H. C. (2006). Splenic Endothelial Cell Lines Support Development of Dendritic Cells from Bone Marrow. *Stem Cells* 24, 1496–1504. doi:10.1634/stemcells.2005-0530

Dor, F. J. M. F., Ramirez, M. L., Parmar, K., Altman, E. L., Huang, C. A., Down, J. D., et al. (2006). Primitive Hematopoietic Cell Populations Reside in the Spleen: Studies in the Pig, Baboon, and Human. *Exp. Hematol.* 34 (11), 1573–1582. doi:10.1016/j.exphem.2006.06.016

Fancke, B., Suter, M., Hochrein, H., and O'Keeffe, M. (2008). M-CSF: a Novel Plasmacytoid and Conventional Dendritic Cell Poietin. *Blood* 111 (1), 150–159. doi:10.1182/blood-2007-05-089292

Hara, H., Lin, Y. J., Tai, H.-C., Ezzelarab, M., Quader, M. A., Houser, S. L., et al. (2014). Hematopoietic Chimerism Following Allotransplantation of the Spleen, Splenocytes or Kidney in Pigs. *Transpl. Immunol.* 31 (3), 125–133. doi:10.1016/j.trim.2014.09.006

Hume, D. A., and MacDonald, K. P. A. (2012). Therapeutic Applications of Macrophage colony-stimulating Factor-1 (CSF-1) and Antagonists of CSF-1 Receptor (CSF-1R) Signaling. *Blood* 119 (8), 1810–1820. doi:10.1182/blood-2011-09-379214

Inra, C. N., Zhou, B. O., Acar, M., Murphy, M. M., Richardson, J., Zhao, Z., et al. (2015). A Perisinusoidal Niche for Extramedullary Haematopoiesis in the Spleen. *Nature* 527 (7579), 466–471. doi:10.1038/nature15530

Kiel, M. J., and Morrison, S. J. (2008). Uncertainty in the Niches that Maintain Haematopoietic Stem Cells. *Nat. Rev. Immunol.* 8 (4), 290–301. doi:10.1038/nri2279

Kiel, M. J., Yilmaz, Ö. H., Iwashita, T., Yilmaz, O. H., Terhorst, C., and Morrison, S. J. (2005). SLAM Family Receptors Distinguish Hematopoietic Stem and Progenitor Cells and Reveal Endothelial Niches for Stem Cells. *Cell* 121 (7), 1109–1121. doi:10.1016/j.cell.2005.05.026

Kuçi, S., Kuçi, Z., Kreyenberg, H., Deak, E., Pütsch, K., Huenecke, S., et al. (2010). CD271 Antigen Defines a Subset of Multipotent Stromal Cells with Immunosuppressive and Lymphohematopoietic Engraftment-Promoting Properties. *Haematologica* 95 (4), 651–659. doi:10.3324/haematol.2009.015065

Kuçi, S., Kuçi, Z., Schäfer, R., Spohn, G., Winter, S., Schwab, M., et al. (2019). Molecular Signature of Human Bone Marrow-Derived Mesenchymal Stromal Cell Subsets. *Sci. Rep.* 9 (1), 1774. doi:10.1038/s41598-019-38517-7

Legate, K. R., Wickström, S. A., and Fässler, R. (2009). Genetic and Cell Biological Analysis of Integrin Outside-In Signaling. *Genes Dev.* 23 (4), 397–418. doi:10.1101/gad.1758709

Lim, H. K., Periasamy, P., and O'Neill, H. C. (2018). *In Vitro* Murine Hematopoiesis Supported by Signaling from a Splenic Stromal Cell Line. *Stem Cell Int.* 2018, 1–9. doi:10.1155/2018/9896142

Liu, K., Victora, G. D., Schwickert, T. A., Guermonprez, P., Meredith, M. M., Yao, K., et al. (2009). *In Vivo* analysis of Dendritic Cell Development and Homeostasis. *Science* 324 (5925), 392–397. doi:10.1126/science.1170540

MacDonald, K. P. A., Rowe, V., Bofinger, H. M., Thomas, R., Sasmono, T., Hume, D. A., et al. (2005). The Colony-stimulating Factor 1 Receptor Is Expressed on Dendritic Cells during Differentiation and Regulates Their Expansion. *J. Immunol.* 175, 1399–1405. doi:10.4049/jimmunol.175.3.1399

Martinez-Agosto, J. A., Mikkola, H. K. A., Hartenstein, V., and Banerjee, U. (2007). The Hematopoietic Stem Cell and its Niche: a Comparative View. *Genes Dev.* 21, 3044–3060. doi:10.1101/gad.1602607

Mascarenhas, M. I., Parker, A., Dzierzak, E., and Ottersbach, K. (2009). Identification of Novel Regulators of Hematopoietic Stem Cell Development through Refinement of Stem Cell Localization and Expression Profiling. *Blood* 114 (21), 4645–4653. doi:10.1182/blood-2009-06-230037

Morita, Y., Iseki, A., Okamura, S., Suzuki, S., Nakauchi, H., and Ema, H. (2011). Functional Characterization of Hematopoietic Stem Cells in the Spleen. *Exp. Hematol.* 39 (3), 351–359. doi:10.1016/j.exphem.2010.12.008

Morrison, S. J., and Scadden, D. T. (2014). The Bone Marrow Niche for Haematopoietic Stem Cells. *Nature* 505 (7483), 327–334. doi:10.1038/nature12984

Nagasawa, T., Omatsu, Y., and Sugiyama, T. (2011). Control of Hematopoietic Stem Cells by the Bone Marrow Stromal Niche: the Role of Reticular Cells. *Trends Immunol.* 32 (7), 315–320. doi:10.1016/j.it.2011.03.009

Nilsson, S. K., Johnston, H. M., Whitty, G. A., Williams, B., Webb, R. J., Denhardt, D. T., et al. (2005). Osteopontin, a Key Component of the Hematopoietic Stem Cell Niche and Regulator of Primitive Hematopoietic Progenitor Cells. *Blood* 106 (4), 1232–1239. doi:10.1182/blood-2004-11-4422

O'Neill, H. C., Griffiths, K. L., Periasamy, P., Hinton, R. A., Hey, Y.-Y., Petvises, S., et al. (2011). Spleen as a Site for Hematopoiesis of a Distinct Antigen Presenting Cell Type. *Stem Cell Int.* 2011, 1–8. doi:10.4061/2011/954275

O'Neill, H. C., Wilson, H. L., Quah, B., Abbey, J. L., Despars, G., and Ni, K. (2004). Dendritic Cell Development in Long-Term Spleen Stromal Cultures. *Stem Cells* 22 (4), 475–486. doi:10.1634/stemcells.22-4-475

Oda, A., Tezuka, T., Ueno, Y., Hosoda, S., Amemiya, Y., Notsu, C., et al. (2018). Niche-induced Extramedullary Hematopoiesis in the Spleen Is Regulated by the Transcription Factor Tlx1. *Sci. Rep.* 8 (1), 8308. doi:10.1038/s41598-018-26693-x

Oh, I. H., and Kwon, K. R. (2010). Concise Review: Multiple Niches for Hematopoietic Stem Cell Regulations. *Stem Cells* 28, 1243–1249. doi:10.1002/stem.453

Omatsu, Y., Sugiyama, T., Kohara, H., Kondoh, G., Fujii, N., Kohno, K., et al. (2010). The Essential Functions of Adipo-Osteogenic Progenitors as the Hematopoietic Stem and Progenitor Cell Niche. *Immunity* 33, 387–399. doi:10.1016/j.immuni.2010.08.017

Onai, N., Obata-Onai, A., Schmid, M. A., Ohteki, T., Jarrossay, D., and Manz, M. G. (2007). Identification of Clonogenic Common Flt3+M-CSFR+ Plasmacytoid and Conventional Dendritic Cell Progenitors in Mouse Bone Marrow. *Nat. Immunol.* 8 (11), 1207–1216. doi:10.1038/ni1518

O'Neill, H. C., Lim, H. K., Periasamy, P., Kumarappan, L., Tan, J. K. H., and O'Neill, T. J. (2019). Transplanted Spleen Stromal Cells with Osteogenic Potential Support Ectopic Myelopoiesis. *PLoS One* 14 (10), e0223416. doi:10.1371/journal.pone.0223416

Periasamy, P., and O'Neill, H. C. (2013). Stroma-dependent Development of Two Dendritic-like Cell Types with Distinct Antigen Presenting Capability. *Exp. Hematol.* 41 (3), 281–292. doi:10.1016/j.exphem.2012.11.003

Periasamy, P., Petvises, S., and O'Neill, H. C. (2013). Development of Two Distinct Dendritic-like APCs in the Context of Splenic Stroma. *Front. Immunol.* 4, 73. doi:10.3389/fimmu.2013.00073

Periasamy, P., Tan, J. K. H., Griffiths, K. L., and O'Neill, H. C. (2009). Splenic Stromal Niches Support Hematopoiesis of Dendritic-like Cells from Precursors in Bone Marrow and Spleen. *Exp. Hematol.* 37, 1060–1071. doi:10.1016/j.exphem.2009.06.001

Periasamy, P., Tran, V., and O'Neill, H. C. (2018). Identification of Genes Which Regulate Stroma-dependent *In Vitro* Hematopoiesis. *PLoS One* 13 (10), e0205583. doi:10.1371/journal.pone.0205583

Petvises, S., and O'Neill, H. C. (2014). Characterisation of Dendritic Cells Arising from Progenitors Endogenous to Murine Spleen. *PLOS One* 9, 1–10. doi:10.1371/journal.pone.0088311

Petvises, S., and O'Neill, H. C. (2014). Distinct Progenitor Origin Distinguishes a Lineage of Dendritic-like Cells in Spleen. *Front. Immunol.* 4, 501. doi:10.3389/fimmu.2013.00501

Pinho, S., Lacombe, J., Hanoun, M., Mizoguchi, T., Bruns, I., Kunisaki, Y., et al. (2013). PDGFRα and CD51 Mark Human Nestin+ Sphere-Forming Mesenchymal Stem Cells Capable of Hematopoietic Progenitor Cell Expansion. *J. Exp. Med.* 210 (7), 1351–1367. doi:10.1084/jem.20122252

Prince, S. N., Foulstone, E. J., Zaccheo, O. J., Williams, C., and Hassan, A. B. (2007). Functional Evaluation of Novel Soluble Insulin-like Growth Factor (IGF)-II-specific Ligand Traps Based on Modified Domain 11 of the Human IGF2 Receptor. *Mol. Cancer Ther.* 6 (2), 607–617. doi:10.1158/1535-7163.MCT-06-0509

Raaijmakers, M. H. G. P. (2010). Regulating Traffic in the Hematopoietic Stem Cell Niche. *Haematologica* 95, 1439–1441. doi:10.3324/haematol.2010.027342

Ross, E. A., Douglas, M. R., Wong, S. H., Ross, E. J., Curnow, S. J., Nash, G. B., et al. (2006). Interaction between Integrin α9β1 and Vascular Cell Adhesion Molecule-1 (VCAM-1) Inhibits Neutrophil Apoptosis. *Blood* 107 (3), 1178–1183. doi:10.1182/blood-2005-07-2692

Saldanha-Gama, R. F., Moraes, J. A., Mariano-Oliveira, A., Coelho, A. L., Walsh, E. M., Marcinkiewicz, C., et al. (2010). α9β1 Integrin Engagement Inhibits Neutrophil Spontaneous Apoptosis: Involvement of Bcl-2 Family Members. *Biochim. Biophys. Acta (Bba) - Mol. Cel Res.* 1803 (7), 848–857. doi:10.1016/J.Bbamcr.2010.03.012

Sánchez-Martín, L., Sánchez-Mateos, P., and Cabañas, C. (2013). CXCR7 Impact on CXCL12 Biology and Disease. *Trends Molecular Medicine* 19 (1), 12–22. doi:10.1016/j.molmed.2012.10.004

Sathe, P., Metcalf, D., Vremec, D., Naik, S. H., Langdon, W. Y., Huntington, N. D., et al. (2014). Lymphoid Tissue and Plasmacytoid Dendritic Cells and Macrophages Do Not Share a Common Macrophage-Dendritic Cell-Restricted Progenitor. *Immunity* 41 (1), 104–115. doi:10.1016/j.immuni.2014.05.020

Sato-Nishiuchi, R., Nakano, I., Ozawa, A., Sato, Y., Takeichi, M., Kiyozumi, D., et al. (2012). Polydom/SVEP1 Is a Ligand for Integrin α9β1. *J. Biol. Chem.* 287, 25615–25630. doi:10.1074/jbc.M112.355016

Seferos, D. S., Giljohann, D. A., Hill, H. D., Prigodich, A. E., and Mirkin, C. A. (2007). Nano-flares: Probes for Transfection and mRNA Detection in Living Cells. *J. Am. Chem. Soc.* 129 (50), 15477–15479. doi:10.1021/ja0776529

Shur, I., Socher, R., Hameiri, M., Fried, A., and Benayahu, D. (2006). Molecular and Cellular Characterization of SEL-OB/SVEP1 in Osteogenic Cells *In Vivo* and *In Vitro*. *J. Cel. Physiol.* 206, 420–427. doi:10.1002/jcp.20497

Stier, S., Ko, Y., Forkert, R., Lutz, C., Neuhaus, T., Grünewald, E., et al. (2005). Osteopontin Is a Hematopoietic Stem Cell Niche Component that Negatively Regulates Stem Cell Pool Size. *J. Exp. Med.* 201 (11), 1781–1791. doi:10.1084/Jem.20041992

Sugiyama, T., Kohara, H., and Noda, M. (2006). Maintenance of the Hematopoietic Stem Cell Pool by CXCL12-CXCR4 Chemokine Signaling in Bone Marrow Stromal Cell Niches. *Immunity* 25, 977–988. doi:10.1016/j.immuni.2006.10.016

Sullivan, C., Chen, Y., Shan, Y., Hu, Y., Peng, C., Zhang, H., et al. (2011). Functional Ramifications for the Loss of P-Selectin Expression on Hematopoietic and Leukemic Stem Cells. *PLoS One* 6 (10), e26246. doi:10.1371/journal.pone.0026246

Tan, J. K., and O'Neill, H. C. (2007). Concise Review: Dendritic Cell Development in the Context of the Spleen Microenvironment. *Stem Cells* 25, 2139–2145. doi:10.1634/stemcells.2007-0244

Tan, J. K. H., and O'Neill, H. C. (2010). Investigation of Murine Spleen as a Niche for Hematopoiesis. *Transplantation* 89. doi:10.1097/tp.0b013e3181c42f70

Taxman, D. J., Moore, C. B., Guthrie, E. H., and Huang, M. T.-H. (2010). Short Hairpin RNA (shRNA): Design, Delivery, and Assessment of Gene Knockdown. *Methods Mol. Biol.* 629, 139–156. doi:10.1007/978-1-60761-657-3_10

Ulyanova, T., Scott, L. M., Priestley, G. V., Jiang, Y., Nakamoto, B., Koni, P. A., et al. (2005). VCAM-1 Expression in Adult Hematopoietic and Nonhematopoietic Cells Is Controlled by Tissue-Inductive Signals and Reflects Their Developmental Origin. *Blood* 106 (1), 86–94. doi:10.1182/blood-2004-09-3417

Wilson, H. L., Ni, K., and O'Neill, H. C. (2000). Identification of Progenitor Cells in Long-Term Spleen Stromal Cultures that Produce Immature Dendritic Cells. *Proc. Natl. Acad. Sci.* 97 (9), 4784–4789. doi:10.1073/pnas.080278897

Winkler, I. G., Barbier, V., Nowlan, B., Jacobsen, R. N., Forristal, C. E., Patton, J. T., et al. (2012). Vascular Niche E-Selectin Regulates Hematopoietic Stem Cell Dormancy, Self Renewal and Chemoresistance. *Nat. Med.* 18, 1651–1657. doi:10.1038/nm.2969

Wolber, F. M., Leonard, E., Michael, S., Orschell-Traycoff, C. M., Yoder, M. C., and Srour, E. F. (2002). Roles of Spleen and Liver in Development of the Murine Hematopoietic System. *Exp. Hematol.* 30 (9), 1010–1019. doi:10.1016/s0301-472x(02)00881-0

Xu, Y., Zhan, Y., Lew, A. M., Naik, S. H., and Kershaw, M. H. (2007). Differential Development of Murine Dendritic Cells by GM-CSF versus Flt3 Ligand Has Implications for Inflammation and Trafficking. *J. Immunol.* 179 (11), 7577–7584. doi:10.4049/jimmunol.179.11.7577

Yvernogeau, L., Klaus, A., Maas, J., Morin-Poulard, I., Weijts, B., Schulte-Merker, S., et al. (2020). Multispecies RNA Tomography Reveals Regulators of Hematopoietic Stem Cell Birth in the Embryonic Aorta. *Blood* 136 (7), 831–844. doi:10.1182/blood.2019004446

Zhang, C. C., and Lodish, H. F. (2004). Insulin-like Growth Factor 2 Expressed in a Novel Fetal Liver Cell Population Is a Growth Factor for Hematopoietic Stem Cells. *Blood* 103 (7), 2513–2521. doi:10.1182/blood-2003-08-2955

Conflict of Interest: The authors declare that the research was conducted in the absence of any commercial or financial relationships that could be construed as a potential conflict of interest.

Publisher's Note: All claims expressed in this article are solely those of the authors and do not necessarily represent those of their affiliated organizations, or those of the publisher, the editors and the reviewers. Any product that may be evaluated in this article, or claim that may be made by its manufacturer, is not guaranteed or endorsed by the publisher.

Advantages of publishing in Frontiers

OPEN ACCESS
Articles are free to read for greatest visibility and readership

FAST PUBLICATION
Around 90 days from submission to decision

HIGH QUALITY PEER-REVIEW
Rigorous, collaborative, and constructive peer-review

TRANSPARENT PEER-REVIEW
Editors and reviewers acknowledged by name on published articles

Frontiers
Avenue du Tribunal-Fédéral 34
1005 Lausanne | Switzerland

Visit us: www.frontiersin.org
Contact us: frontiersin.org/about/contact

REPRODUCIBILITY OF RESEARCH
Support open data and methods to enhance research reproducibility

DIGITAL PUBLISHING
Articles designed for optimal readership across devices

FOLLOW US
@frontiersin

IMPACT METRICS
Advanced article metrics track visibility across digital media

EXTENSIVE PROMOTION
Marketing and promotion of impactful research

LOOP RESEARCH NETWORK
Our network increases your article's readership